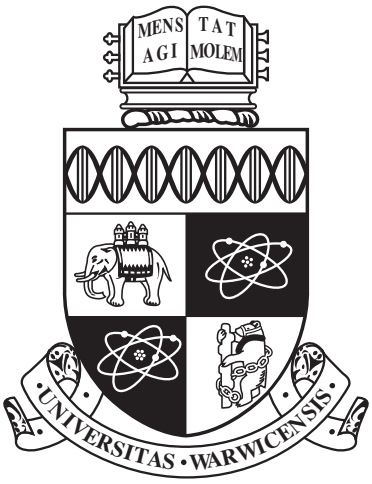

High Sensitivity Electromagnetic Testing of Hi-Tech and Safety Critical Metal Components

by

Amanda L. To

Thesis

Submitted to the University of Warwick

for the degree of

Doctor of Philosophy

The Department of Physics

August 2021

Contents

List of Tables

List of Figures

Acknowledgments

I would like to thank foremostly my supervisor, Steve Dixon. I could not have done this project without his help. I would like to thank my colleague, Zhichao Li, for his work collecting the edge defect results. I would like to acknowledge EPSRC for the DTA, RCNDE for the studentship, and Rolls Royce and EDF for sponsoring my PhD project. Also, thank you to Robert Day and David Greenshields for help with the electronics, and Jonathan Harrington for the mechanical advice and assistance.

Furthermore, I would like to thank my family and friends for their support throughout my PhD.

Declarations

This thesis is submitted to Warwick University for the degree of Doctor of Philosophy. I declare that the work presented in this thesis is my original research and have to the best of my ability clearly indicated any contribution from others. No part of this work has been previously submitted to Warwick University or any other academic institution for another degree or qualification.

Papers

- A To, Z Li, and S Dixon. Improved eddy current testing sensitivity using phase information. *Insight - Non-Destructive Testing & Condition Monitoring*, 63(10): 578–584, 2021.
- A To, Z Li, and S Dixon. Improved detection of surface defects at sample edges using high-frequency eddy current amplitude and phase measurements. *Nondestructive Testing and Evaluation*, pages 1–25, 2022.

Abstract

Eddy current testing is widely used to inspect safety-critical components, where it is important to find surface-breaking defects and fatigue cracks at their earliest stage of growth. This requires finding sub-millimetre defects, which usually means the electromagnetic skin depth of the eddy current must be $< 1\,\text{mm}$. To achieve skin depths of $< 1\,\text{mm}$ on low conductivity metals such as Ti and TiAl, the frequency of the excitation current needs to be greater than several MHz. Eddy current sensor frequencies of up to 40 MHz, which provide good signal-to-noise ratios, have been achieved by positioning circuitry directly behind the coils [1]. However, even when locating the electronics close to the coils, increasing frequency will always lead to an increase in electrical noise as inductance in the wires increases and stray capacitances become more significant. As an alternative, lower frequency ($< 1\,\text{MHz}$) Parametric approaches have been investigated [2], where the magnitude and phase of the eddy current signal are independently measured.

In this thesis, a combination of these approaches is used. A two coil transmit-receive eddy current sensor was built that operates at 1 MHz where the sensor electronics were located behind the coils and simultaneously measure magnitude and phase of the eddy current signal. The approach can improve sensitivity to defects in experimental 2D scans of the sample surface.

In addition, work has been performed that involves changing various parameters such as defect orientation and the lift-off of the eddy current coils. Through this, it was found that this new approach can improve lift-off performance and the ability to measure defects close to the edge of a sample. Experimental results and

finite element modelling are presented to support these findings.

The standard experimental approach was one where software-based digital signal processing was used to measure the magnitude and phase difference of various signals, which is relatively time-consuming. A new approach was designed and tested using a low-cost, specialised chip to measure phase difference. This new meter is capable of measuring both the magnitude and phase of the signal using an inexpensive AD8302 chip, which produces good results from eddy current signals, decreasing system complexity and cost whilst also reducing measurement time.

Abbreviations

Alternating current (AC)

Computer-aided design (CAD)

Carbon fibre-reinforced polymer (CFRP)

Direct current (DC)

Eddy current (EC)

Eddy current testing (ECT)

Electromagnetic acoustic transducers (EMATs)

Fast Fourier transform (FFT)

Finite element analysis (FEA)

Finite element method (FEM)

Foreign Object Damage (FOD)

Howland current source (HCS)

Infinite element domain (IED)

Intergranular stress corrosion cracking (IGSCC)

Liquid penetrant (LP)

Magnetic particle inspection (MPI)

Magnitude (mag.)

Non-destructive testing (NDT)

Nuclear power plants (NPPs)

Printed circuit board (PCB)

Radio frequency (RF)

Receiver (Rx)

Signal-to-noise ratio (SNR)

Stainless steel (SS)

Titanium aluminide (TiAl)

Transmitter (Tx)

Ultrasound testing (UT)

Visual testing (VT)

Chapter 1

Introduction

1.1 General background

Detecting small cracks at the earliest stage of development is very important for safety-critical components, particularly if frequently subjected to high stress or temperature such as is experienced with jet engine turbine blades. Aircraft engines are susceptible to Foreign Object Damage (FOD). Ingested objects can range in size and hardness, and the resulting damage can range from minor to very severe. The most serious cases of FOD may involve the failure of components, which can be disastrous with a great financial and human cost. Nonetheless, even non-catastrophic damage can be costly as it reduces the engine's operating efficiency and lifetime of the blade [3]. In fact, the costs associated with FOD was estimated to be $4 billion annually by the Boeing [4].

There is much attention and social awareness around the FOD damage caused by bird strike events, not least because of events such as the Hudson River landing in 2009, also know as "Miracle on the Hudson" [5]. Bird strikes are a fairly common occurrence such that the Federal Aviation Administration (FAA) requires full-scale bird ingestion tests with the engine running at full speed to pass certification [6]. However, while bird strike events can cause significant damage to the engine, the majority of FOD involves damage less than 2 mm in depth [7] and the operational life of an aircraft is largely determined by the growth of small cracks [8]. FOD often originates from hard millimeter-sized object such as sand or gravel, which at high speeds, up to $300\,\mathrm{m\,s^{-1}}$, can cause small indentation that are sites for fatigue crack initiation and can cause severe damage to thermal barrier coatings [9].

High cycle fatigue is a major cause of failure in gas turbine engine blades and such failures are largely associated with surface damage, which includes FOD [10].

Here, a combination of high-frequency vibratory loading and prior in-service damage such as FOD has caused the part to fail. FOD is of particular concern because of how detrimental it can be to rotating components even if the damage is smaller than what is detectable by the human eye [7]. As such, it is of interest to find small defects in these turbine engines.

However, advances in materials and manufacturing techniques are currently pushing the capabilities of inspection. Advance materials can come with benefits such as being stronger and lighter, but for these materials to be used safely, it must be possible to inspect them with confidence. Being able to perform a comprehensive inspections on such materials also allows for parts to be designed with a lower "factor of safety". This means reduced cross-sectional area, with weight and material saving [11].

Advances in material technology include the increasing use of low electrical conductivity metal alloys such as titanium aluminide (TiAl). TiAl is lightweight and has good mechanical properties even at high temperatures making it appealing for use in a range of applications, including turbine blades where General Electric's GEnx engine is the first commercial aircraft engine to use TiAl (Ti-48Al-2Nb-2Cr) for their low-pressure turbine blades, which entered service in 2011 and has been used in Boeing aircraft [12]. This move has been followed by other aircraft engine manufacturers including Pratt & Whitney and Rolls Royce [13].

Jet engines can be separated into three main parts: the compressor, the combustor and the turbines as illustrated in figure 1.1. Furthermore, most modern jet engines are turbofans with their higher fuel efficiency [14]. Turbofans have, in addition, a distinct fan stage before the compressor.

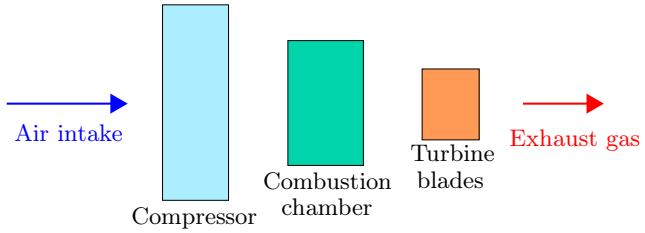

Figure 1.1: Schematic of engine.

Titanium (Ti) alloys are widely used for the fans and early parts of the compressor, where the temperature is relatively low ($< 600°C$) [15, 16]. In the compressor, titanium alloys can be used for the blades and the development of strong titanium alloys has allowed it to also be used for the compressor discs and shafts. The push for weight savings has, however, lead to a shift towards composites being

used these cooler parts, for example, General Electric introduced the GE90 engine, which has carbon fibre reinforced composite fan blades strengthen by titanium alloy leading edges [17]. While, Titanium has migrated to hotter parts of the engine.

Until recently, the compressor was the only internal part of a gas turbine engine where titanium alloys were used since prior Ti alloys were unable to withstand temperatures in hotter parts of the engine [17]. The development of TiAl with its good high temperature (600°C-800°C) oxidation and creep resistance [13], makes it suitable for turbine blades and divergent flaps in nozzles. It is light compared to nickel-based superalloys (density is half of Nickel) and replacing Nickel-based superalloy parts with TiAl could reduce the structural weight of a gas turbine engines by 20%-30%, which would improve performance and fuel efficiency [18]. In particular, the use of TiAl for GEnx's low-pressure turbine blades has helped reduced fuel consumption by 20%, peak noise by 50% and NOx emissions by 80%. TiAl would also be suitable for hotter part of the compressor, the afterburners, and the nozzle in the case of military engines, but is not currently economical to implement [17].

Apart from aerospace materials, this thesis covers stainless steel (SS), which is widely used in the power generation industry. There is a dependancy on energy from nuclear power plants (NPPs), which supplies 16% of the global electrical power capacity, and this is compounded by the need to move away from more volatile and polluting sources of energy such as oil, coal and gas. However, many NPPs constructed in the 1965–80 "boom-era" are approaching the end of their original planned life [19] and few new NPPs have been built [20], which has brought about discussions on operating NPPs beyond their planned lives and the management of ageing assets has become a "hot" topic in the nuclear industry [21]. NPPs have generally been designed to operate for up to 40 years [22], which is the original length of operating licences for NPPs in the US. However, the average age of NPPs worldwide was close to 30 years in 2015 [23], as such there is wide discussion over life extension. There is even some argument as to operate NPPs for up to 100 years, but at the least, it is expected that most NPPs will renew their license as the alternative (decommisioning) would be unfavourable [21].

In NPPs, austenistic stainless steels are extensively used for their "ductility, formability, toughness and weldability" as well as its suitability to corrosive environments. Moreover, often Molybdenum is added to form 316 steel, which has better corrosion resistance. Intergranular stress corrosion cracking (IGSCC) is the largest cause of damage for austenitic stainless steels in oxidising BWR conditions. IGSCC are cracks that have been caused by localised corrosion along grain boundaries in the material [24]. In austenitic stainless steel, it is caused by the migration of car-

bide and formation of chromium carbide at the grain boundaries, which results in the depletion of chromium and the corrosion of the material [25], while its growth is driven by inelastic deformation at the crack [24]. A significant contributor to IGSCC is sensitisation, which is reduced by decreasing the carbon content to form 316L, 316LN and 316NG stainless steels [26]. IGSCC is a major concern and an increasingly important one as nuclear power plants age. To prolong the age of nuclear power plants, it has become paramount to find such cracks [27].

An important tool in detecting defects, such as FOD or cracks, is non-destructive testing (NDT). This is a term that was adopted during the Second World War, used to describe inspection using techniques that do not cause damage to the inspected part [28]. A part is usually only considered to be damaged if usability is affected or its integrity is compromised, and thus techniques that alter the part can still potentially be considered non-destructive. The extent of what constitutes NDT has no definitive boundaries; it can be something as simple as examining a sample visually [29] or in the early days of NDT in industry, wheeltappers on railways would check for defects in wheels by listening to the sound they made after simply tapping them with a hammer [30]. A caveat is that the term "NDT" is usually used within the engineering industry, gaining less traction outside of this. For example, techniques such as ultrasound and radiography are well used in NDT but many are familiar with them because of their use in medicine, where they would not usually be referred to as NDT techniques.

A wide range of information can be gathered from NDT, from finding the dimensions of an item to determining the properties of a material, but as mentioned already, the focus of this thesis will be on detecting defects [31]. Not maintaining a component or anticipating when it will break is of little consequence in many circumstances, for example when a light bulb breaks. Here, it is appropriate to allow the item to fail before maintenance, otherwise known as breakdown maintenance. However, sometimes the unexpected failure of a component can have serious repercussions. This may be unplanned interruptions, expensive replacements or even a catastrophic incident where there is the potential for loss of life. In these circumstances, it is beneficial, or even imperative, to detect early deterioration using methods such as NDT, which can allow components to be repaired or replaced more conveniently in order to prevent more serious incidents. This is known as condition-based maintenance, and it is an important strategy when dealing with critical systems [32], which are prevalent in aviation.

In aviation, safety is a high priority and the sudden breakdown of safety-critical components can be disastrous, particularly with a growth in passenger travel

putting more lives at risk and increased social awareness over issues like safety [33]. In such industries, it is mandatory to perform regular inspections involving NDT. The problem of damage resulting from ageing in aircrafts in particular was brought to the attention of the public with the the Aloha Airlines accident in April 1989. In response to the accident, the Federal Aviation Administration (FAA) established the Aging Aircraft Program [34].

For NPPs, while the risks differ from aerospace, the risks are significant with their, for example, being a risk of radioactivity leaking to the environment or a burst [35], and thus, in-service inspections are routinely performed [36]. Also, the Nuclear industry faces enhanced scrutiny, where part of maintaining its position amongst the public is to remain a safe, reliable source of energy [21]. This means avoiding incidents and maintaining high safety standards.

1.2 NDT techniques

Modern non-destructive testing has advanced through our understanding of electromagnetism, imaging, piezoelectricity, radioscopy and ultrasound [29] These have all contributed to what are now the six main forms of NDT [37], which are covered in the following subsections.

1.2.1 Visual

Visual Testing (VT) is one of the oldest NDT techniques and one of the most widely used. It accounts for as much as 90% of inspections in aircraft maintenance according to some estimates [38] and its wide usage can be attributed to it being generally the cheapest inspection to perform with it being intuitive to understand and relatively straightforward to apply since specialist equipment is not always necessary. It is a technique that can be underestimated as it may not be as sophisticated as some of the other techniques but the technique is needed to avoid gross errors and any comprehensive inspection should include one [39]. VT in its most basic form consists of inspecting for signs of damage by eye or a light-sensitive device such as a photocell. VT is used to inspect for surfaces features and it works well for large area damage. For engine components, features that can be inspected for include larger cracks, holes, corrosion, blisters and impact damage [40].

There are, however, significant limitations to VT and in some areas, VT has been displaced by other methods. For example, the state of New York challenged the adequacy of visual inspections at the Indian Point Nuclear reactor nearly a decade

ago and the damaged stainless-steel bolts found in 2016 were found by ultrasonic inspection [41].

VT is not suited to volumetric inspection and it is less suitable for finding small defects. While it may be possible to find small defect, it may be difficult to do so with a suitable level of repeatability as conditions vary [42]. Detecting aircraft defects can be challenging due to surface deformation, variations in lighting, dirt and paint quality [43]. Moreover, defect determination with VT is traditionally very subjective and can often result in debates with it sometimes being difficult to tell the difference between a defect and a benign flaw. Even though it is an intuitive technique, inspectors may still require special training and regular testing to ensure inspection are carried out consistently and performed to a high standard [44]. Even then, physiological and psychological factor play a significant role [28].

The human component to inspection can be reduced by using automated detection. An example is machine vision detection technology, which has the advantages of high sensitivity and fast detection speed. It can, however, be difficulty to implement, particularly for onsite inspections, as the varying conditions bring great difficulties to defect detection algorithms [45].

Other advances include optical enhancement by magnification and visual correction, and digital technology allowing images to be enhanced [39]. Additionally, Magnetic Particle and Liquid Penetrant testing including fluorescent penetrant inspection can be seen as extensions of the visual technique [28].

1.2.2 Radiography

Radiography is a volumetric technique, which can be used to image the internal structure of an object allowing embedded defects to be detected [46]. The technique is based on Wilhelm Röentgen's accidental discovery of X-rays in 1895 during experiments involving electric discharges through rarified gases, which earned him the first Nobel Prize in Physics [47, 48].

X-rays are high frequency electromagnetic radiation (10^{18} Hz) and are traditionally produced when high speed electrons are accelerated towards a tungsten target [11]. Röentgen found that X-rays had difficulty passing through bone and metal compared to human tissue [49]. This is the result of X-rays being attenuated differently depending on the structure and material of the specimen. This differential absorption is the bases of radiography and in the context of defect detection, more radiation would pass through a void compared to the intact material. The sensitivity of X-rays is nominally 2% of the thickness of the material such as steel. This would mean for a 25 mm thick sample, the smallest detectable void would be

0.5 mm. Another point to consider is that a crack will not show up unless it produces a thickness change parallel to the X-rays [50].

The resulting radiation pattern can be viewed using photographic film, florescent screens or after processing by a computer, particularly in the case of tomography where the X-ray source and detector are moved around the specimen to produce a 3D image from which any cross-section can be obtained [51]. Acquiring images from different angles helps locating and finding cracks in different orientations. The results can be stored for permanent reference of the internal structure, which is a significant advantage of the technique [50].

A major disadvantage of radiography is the safety risk. While the technique has a good safety record, the safety concerns mean that there are often more restrictions such as it needing to be done in a confined space and it is possible the specimen may need to be dismantled [52]. As such alternative are being used to replace radiography, though it remains one of the two main volumetric methods, alongside ultrasonic testing [42], where X-rays, particularly computed tomography, would be viewed the high fidelity technique and ultrasound as the relatively lower fidelity technique.

The radiographic technique has been developed to include gamma radiography and neutron radiography where gamma and neutron radiation are used respectively as the source instead of X-rays [51]. To penetrate thick metal samples, high energy X-ray sources are required, and at some point, X-rays do not have sufficient penetrating power to pass through a metal sample without introducing problematic health and safety issues. In these situations, one might choose gamma rays, which are able to penetrate deeper into a sample. Accordingly, gamma ray tends to be be used for larger components and X-rays on smaller ones [17].

1.2.3 Ultrasound

Ultrasonic testing (UT) is suited for bulk inspection and is able to detect embedded defects and defects on the back surface with only sided access being being needed [53]. Some surface inspections is possible with UT [54] but the technique is not known for being particularly suitable for surface inspection unlike eddy current testing [55]. The technique has difficulties with detecting sub-millimetre sized surface defects even when samples have significant surface preparation.

UT is similar in principle to the early hammer tests but it uses higher frequency sound waves above the audible range. Typical frequencies for UT range between 1 MHz and 10 MHz [51]. The transition to ultrasound was made possible by improvements in understanding how to generate and detect ultrasound through

the work by individuals such as Paul Langevin who developed the first application of ultrasound during World War I. Langevin's extensive knowledge of piezoelectricity allowed him to enhance the piezoelectric effect of quartz crystals allowing ultrasound to be transmitted and detected at levels that could be used in submarine detection [56, 57].

Conventional ultrasound uses piezoelectric transducers and it is the most common transducer type used. It is, however, limited by the need for direct contact and the transmission of ultrasound is usually aided by a coupling fluid, since the propagation of elastic waves through the air is very inefficient. In the last decade, there has been a focus on developing non-contact sensors and air-coupled probes [58]. Non-contact probes include Electromagnetic Acoustic Transducers (EMATs) and lasers.

EMATs create ultrasound either through: generating eddy currents in the surface of the sample and using a static magnetic field from a magnet to generate a Lorentz force or through magnetostriction, whereby dimensional changes in ferromagnetic materials are caused by an alternating magnetic field [59]. Although contact is not required, the probe should be within a few millimetres as the magnetic field strength falls rapidly with lift-off, this is the distance between the probe and the sample.

Laser Ultrasonics allows inspections to be carried out from further away. Pulsed laser beam generation of ultrasound works between two extreme regimes: the ablative regime and the thermoelastic regime [60]. In the ablative regime, a the high energy density, pulsed laser beam heats a point on the sample's surface, such that a plasma is formed above or the surface is partially ablated, which then generates ultrasound by the recoil effect [61]. In the thermoelastic regime, a lower energy density laser beam heats a region of the sample surface, which is constrained by the cooler surrounding material. This rapid change in stress generates ultrasonic waves that are generally lower energy and with different properties to those generated in the ablative regime.

There has been a trend in industry to replace inspections where radiography has been typically used due to safety concerns. Ultrasound is natural to consider as it is also a volumetric technique, but it is important to remember they are distinct methods with considerably different physics and thus, ultrasound would not always be suitable as a replacement [62]. For example, generally in-planar defects (i.e. defects are plane parallel to the face) are more suited for UT as this is the orientation where a defect would intercept the ultrasonic beam maximally while transverse defects (i.e. defects that lie across the face) are more suited to radiography as this is

the orientation where the defect crosses the X-ray path maximally [11]. Additionally, ultrasound can be less effective if the geometry of the specimen is complex or the surface is rough [63]. Moreover, X-rays are not impeded the way ultrasound is by air gaps.

1.2.4 Magnetic particle inspection

Magnetic particle inspection (MPI) is a technique that can be seen as an extension of the visual technique. Defects are enhanced by magnetising a section of the specimen and covering it in magnetic particles suspended in a liquid. In a flawless specimen, the magnetic flux resulting from magnetisation stays largely within the sample. However, if a defect is present, the magnetic flux will be distorted with defects near the surface forcing the magnetic flux to 'leak' out of the surface. This magnetic flux leakage attracts magnetic particles, which can be seen by visual examination. As the technique depends on magnetising the specimen, the technique only works on magnetic materials [37, 51] thus it is not suitable for non-ferrous and most austenitic stainless steels [64].

The surface may need to prepared prior to inspection. The surface should be cleaned to prevent contamination, and paint may need to be removed as the force of the magnetic field is proportional to the distance from the poles. Consequently only non-magnetic coatings less than 0.025 mm can be left on prior to inspection for critical components [65].

1.2.5 Liquid penetrant testing

Liquid penetrant testing (LP) is another technique that can be considered an extension of visual testing. LP is used to enhance the appearance of surface-breaking defects and it is more more suitable for sub-millimetre defects compared to visual testing. In fact, its main draw is the sensitivity of the method, where defects with an opening width of 0.5 mm can be safely detected. Furthermore, it is suited to complex geometries and it is a low cost method [66].

In LP inspections, a liquid is applied to the surface of the specimen and drawn into defects by capillary action, and sometimes heat. The surplus liquid is removed after allowing sufficient time for the liquid to penetrate the flaws, otherwise known as the 'dwell' time. The defect should then be clearly visible after a developer is applied to draw out penetrant left in flaws. It can be visible either directly or using some aid such as ultraviolet light if the liquids are florescent [47]. Such fluorescent dyes were used in aircraft production in World War II and continue to be the penetrant

typically used in the aerospace industry [28].

Prior to the application of the liquid, the surface needs to be prepared and cleaned. This can involve several steps as any residue can hinder the entry of the penetrant. For example, the contamination may need to be removed by chemicals, but these chemicals may adversely affect the penetrants and thus need to be thoroughly removed. A typical sequence might consist of alkaline cleaning followed by a tap water rinse, a pickling tap water rinse and then a deionized water rinse before drying with a hot air knife [67]. Care needs to be taken with these potentially harmful chemicals.

The disadvantages of the method are that it does not work well on rough surfaces and only surface breaking cracks can be detected, even defects through paint cannot be detected as the dye must enter the defect itself. Information about the full extent of the defect is also not provided, for example, its depth and shape. Moreover, the process can be time-consuming and labour intensive, especially if small defects need to be found [66]. However, a large area can be inspected and it can be done so relatively quickly after preparation.

1.2.6 Eddy current testing

Eddy current testing (ECT) is technique based on the phenomena of eddy currents, which were first observed by François Arago in 1824 [68]. The technique is based on magnetically inducing current loops in the test material, usually through driving a nearby coil with an alternating current. The loops generated are called eddy currents. The resulting magnetic field can then be detected using various magnetometers, but usually the electrical voltage signal across the existing coil or another nearby coil is just measured. The signal gives information about the properties of the test material, and changes in the measured signals can be an indication of a discontinuity like a defect.

Eddy currents are, by their nature, localised mainly under the generation coil, which means that the sensor can only detect defects in the immediate vicinity. This means that only surface and near-surface defects can be found, and the sensor needs to be scanned over the whole test surface, which can be time-consuming. However, this also means the determination of the defect location is more straightforward compared to a technique like ultrasound, where defect positions may need to be extracted from complicated traces. ECT is also very sensitive to surface variations, where it can detect small sub-millimetre sized defects.

1.2.7 Choosing an NDT method

The optimal technique for any NDT requirement is completely application-specific. This thesis will focus on surface-breaking defects on TiAl, Ti and stainless steel (SS) 316L. Whilst the Institute of Metals [47] found that ultrasound and X-rays account for about a third of NDE techniques in use, these techniques are better suited to volumetric inspection rather than surface inspection, although there are reports of the successful use of ultrasound to defect small surface-breaking defects [69]. X-rays can also be used, but usually dismantling of the component is needed and there are safety considerations with the ionising radiation from the X-rays.

Techniques such as visual testing, MPI, liquid penetrant testing and ECT are more suitable for surface breaking defect. These are naturally surface selective techniques. Inherently "visual" inspection methods such as liquid penetrant and magnetic particle testing account for 50% of testing [47]. However, MPI is not suitable for the austenistic metals such as 316L as the material must be magnetisable [70], and visual testing is less suitable for the small defects. This leaves liquid penetrant testing and ECT as the main candidates. That being said, there is considerable surface preparation needed to carry out LP inspections. As such, this thesis will focus on eddy current testing, which according to the aforementioned Institute of Metals study [47] accounts for approximately 10% of NDE inspections.

ECT has certain advantages that make it well suited to the detection of surface defects, and the use of electromagnetic induction means that defects can be inspected without touching the sample and a relatively fast, quantitative indication of defect size can be given. The use of electromagnetic induction obviously limits its applicability to electrically conductive materials, but this is not a problem for the majority of engineering applications since many engineering structures are metallic. As such, ECT is one of the standard methods for detecting defects in aircraft jet engine turbine blades.

Eddy current testing can overcome some of the limitations associated with visual testing. While it is not suited to volumetric inspection either, it is able to detect subsurface defects in addition to surface defects, and detect defects through paint. It is not susceptible to to lighting conditions and it is inherently a more quantitative technique.

1.3 Background to Eddy Current Testing (ECT)

Eddy currents were first observed by François Arago in 1824 [68] and electromagnetic induction, which underpins the phenomena, was discovered by Michael Faraday [71] in 1831. However, it was not until 1878 that D. E. Hughes developed a device capable of sorting metals, which is usually credited as the first application of eddy current NDT. He found that the electrical properties of a coil would change when placed near metals of different conductivity and permittivity [72]. The apparatus used may be considered antiquated by today's standard, but he had demonstrated the utility of the method.

Modern ECT is largely attributed to Friedrich Föerster, who was responsible for developing much of the underpinning theory and technology. His contributions to the development of quantitative test equipment and methods were an important factor in the wide acceptance of ECT during the early years (the 1950s - 1960s) where it was taken up by the aircraft and nuclear industries [73]. Much work in ECT was inspired by his efforts, with his research being acknowledged by several early works [74, 75].

These seminal papers that established the underlying scientific description and mathematics behind ECT included the paper from Dodd and Deeds (1968) [76], which found the first closed-form solution for a practical ECT sensor. They derived the magnetic vector potential for an air-cored coil situated near a conductor in various geometries. Calculating the magnetic vector potential allows "any physically observable electromagnetic quantity" to be calculated. Though perhaps more importantly for ECT, it allowed a sample's properties to be determined from measurements through an inverse calculation of the electromagnetic response of an eddy current coil. The Dodd and Deeds paper formed the basis for more complex models by Cheng, Dodd and Deeds (1971) [77], who had multi-layered conductive slab as the sample, and another paper by Uzal, Moulder, Mitra and Rose (1993) [78], who made the sample a layered material whose conductivity and permeability profile vary arbitrarily. However, the Dodd and Deeds (1968) paper remain one of the most important analytical solutions in the field, and it continues to be one of the most highly cited papers in ECT.

ECT is now a well-established technique, with more recent developments being less about establishing the technique and more about addressing the existing limitations. These developments have included pulsed eddy current techniques and eddy current arrays. Pulsed ECT allows information about a range of depths to be gained by using an excitation current that is a step function and thus contains

multiple frequencies which correspond to different penetration depths [79], while eddy current arrays multiplex between multiple sensors to provide wider coverage and faster scanning times [80].

While ECT has been used in various applications such as thickness measurements, surface treatment and sorting [81], the focus of this thesis is the detection of defects on low conductivity metals. The F. Hughes, R. Day, N. Tung, and S. Dixon (2016) [82] paper focussed on addressing this issue by operating at higher frequencies. They demonstrated that the operating frequency of ECT can be increased by mounting parts of the electrical circuitry directly behind the coils. This helps reduce noise caused by the cables as they move and interact with nearby objects, which they can electrically couple with. By mounting the circuitry in this way, they show that frequencies of over 15 MHz can be reached, inspecting both low conductivity metals and carbon fibre composites. There is, however, a limit to how much of the electronics can fit directly behind the coils to reduce the use of connecting cables and the noise associated with higher frequencies.

Additionally, high frequencies help with both smaller defects and lower conductivity materials. The benefits of higher frequency to detecting small defect stem from the penetration depth generally reducing with higher frequencies. This can be seen in the work of Heuer et al. (2011) [83], where the EddyCus system is used to detect flaws in the range of a few millimetres by operating at 2 MHz to 10 MHz.

The skin effect also means that higher electrical conductivity materials tends to be inspected with higher frequencies and lower electrical conductivity materials tend to be inspected with lower frequencies. Metals generally have a high electrical conductivity. Thus, the eddy current penetration depth in metals is generally lower and frequencies from low kHz up to single digit MHz tend to be used [84]. As such, commercial eddy current testing equipment generally goes up to 10 MHz as higher frequencies are not needed for most applications [85].

However, in the special circumstance of low conductivity materials, higher frequencies up to 50 MHz or even 80 MHz may be needed [84]. In low-conductivity engine alloys, the penetration depth cannot be reduced below below 0.2 mm without using frequencies above 10 MHz and frequencies of at least 50 MHz are needed to capture the important part of the near-surface residual stress profile [85]. While, frequencies of 5 MHz or higher must be used for carbon fibre-reinforced polymer (CFRP) with the optimal frequency being 5 MHz to 25 MHz for uncured prepreg using the EddyCus MPECS system. Here, the conductivity of CFRP is significantly lower than the conductivity observed in metal despite the carbon fibres being highly conductive [86].

For sub-millimetre defect inspection of aerospace material, such as titanium alloy, the operating frequency should often be between 5 and 10 MHz [87]. Though frequencies above 10 MHz may also be beneficial [82]. In fact, Ernt et al. (2016) notes that high frequencies are needed for small surface defects on TiAl, where the combination low conductivity and the requirement to detect defects less than 200 µm in depth mean that standard techniques are unsuitable [88].

High-frequency operation on low conductivity materials is also seen in Mook et al. (2009) [89], where a high frequencies probe that operates at frequencies up to 10 MHz is used to detect fibre orientation and local flaws on CFRP [90], and in the R.R. Hughes, B. W. Drinkwater and R. A. Smith (2018) [91] paper, which uses high-frequency (20 MHz) ECT on CFRP. Like F. Hughes, R. Day, N. Tung, and S. Dixon (2016), the Howland current source (HCS) is mounted immediately behind the sensor coil to reduce the effects of connecting cables at high frequencies and the HCS is presumably made to a similar specification, although other parts appear to have to be placed further away. The purpose of the paper was to display the benefits of using Radon Transformation to maintain the correct fibre orientations and stacking sequence in CFRP. The paper may not be focused on high frequencies, but they use high frequencies to produce high-resolution images, and so it nonetheless shows that operating at high frequencies can be useful. In such a scenario, high frequencies are used due to a combination of the low conductivity of CFRP and the high resolution that is desired.

The low conductivity of some materials means that conventional ECT technique is unsuitable, which often means needing to increase the frequency [90, 92]. However, as mentioned in the abstract, increasing the frequency will result in an increase in electrical noise as the cables inductively couple to the surrounding environment and stray capacitances becomes more significant. Such coupling can result in variations in the measured signals that are unrelated to the electromagnetic coupling between the coil and sample [82]. According to Jun Cheng et al. (2016) [93], the "transmission of high frequency signals in coaxial cable tends to introduce serious line-line crosstalk, external interference, as well as the energy loss of received signal due to the dielectric insulation resin, resulting in extra difficulties in the stage of system design and implementation". Additionally, they note that high frequency probes suffer "from higher levels of background noise as it became more susceptible to lift-off, tilt and sample surface condition". This may negatively impact on the signal-to-noise at higher frequencies. Therefore, possibilities at lower frequencies need to be explored.

Alternatives to improve defect detectability at lower frequencies include using

a SQUID magnetometer. This is explored by Ruosi (2005) [94] and Carr et al. (2003) [95]. They use SQUID due to the difficultly detecting small disturbances in the magnetic field, that may result from defects, when the background magnetic noise is large. SQUID is able to do this well even at low frequencies.

Another alternative is presented by A. Egbeyemi's (2018) [2]. His work involved small defects on low conductivity materials such as Ti and TiAl. However, rather that going to higher frequencies, which can be less suitable for arrays. It was found that combining magnitude and phase data by multiplication leads to a significant improvement in the signal-to-noise ratio compared with using each parameter individually in isolation. This approach of measuring magnitude and phase simultaneously will be called the Parametric approach, which will be covered in more detail in section 1.6, and will be explored in this thesis to detect small defects.

There is also an interest in inspecting for defects in complex geometries as FOD damage on air turbine blades often manifests as a dent or notch at or close to the leading edge of the blade [96]. Fatigue cracks tend to be at edge due to the high stress concentrations at sharp geometries [97]. However, inspecting for defects near edges can be more challenging as the edge response has the potential to mask the response to a defect at or close to the edge [97, 98]. As such, some simply recommend avoiding the edge region [99] despite the need to inspect for edge defects.

There are, nevertheless, some papers such as Theodoulidis and Bowler (2009) [100], and Bowler et al. (2012) [101] that seek to better understand the edge effect. These papers seek to aid the inspection of defects near edges by improving the understanding of the edge effect through a more analytical approach. On the other hand, Xie et al. (2020) [102] uses simulations to improve sensor parameters for the purpose of detecting defects close to an edge. This paper, in particular, models a titanium alloy sample using the finite element method.

Moreover, there exists experiments involving defects near an edge. For example, Wang et al. (2017) [103] used an absolute probe for subsurface defects at the edge of a titanium alloy block. Special probes and probe configurations may also be used. T Dogaru et al. (2000) [104] used a magnetoresistance based eddy current sensor to detect edge defects that are several millimetres (1 mm to 15 mm) long on an aluminium plate. While, Fava and Ruch (2004) [105] uses rectangular planar coils to minimise the edge effect. Rectangular planar coils are sensitive to shallow features but bridge balancing is required with half of the coil's area on the sample and the other half off the sample. Eua-Anant et al. (1999) [106] suggests the use of differential probes to reduce the edge effect. Though, it is usually necessary to ensure good alignment with the edge when using such coils. Other solutions include

high magnetic permeability cores, flux focusing and using small coils, which work by spatially localising the eddy current to reduce the response of the eddy current to the edge [107, 108]. Also, shielded probes allow for inspection near edges by focusing the magnetic field [109].

Another solution would be to localise the eddy currents by operating at higher frequencies. Increasing the operating frequency produces eddy currents that are localised to a shallower skin depth, which both provides increased sensitivity to shallow defects and reduces the lateral extent of the eddy current [82]. This may be used to reduce the edge effect. Sasi et al. (2004), for example, uses a dual-frequency technique where they mix signals from two frequencies to suppress the edge effect [97]. The approach of using higher frequencies will be combined with the approach of using small coils to find edge defects in this thesis.

1.4 Principles of ECT

Michael Faraday discovered electromagnetic induction, which is the process that explains the origin of eddy current generation in conductive materials [110]. Maxwell later mathematically described the process, and this is known to many as Faraday's law of induction. Along with Ampère's law, the physics of eddy current testing can be explained. Faraday's and Ampère's law can be respectively be stated in differential form as [111]

$$\nabla \times \mathbf{E} = -\frac{\partial \mathbf{B}}{\partial t}, \tag{1.1}$$

and

$$\nabla \times \mathbf{H} = \mathbf{J} + \frac{\partial \mathbf{D}}{\partial t}, \tag{1.2}$$

where $\mathbf{H}$ is the magnetic field, $\mathbf{J}$ is the current density, $\mathbf{D}$ is the electric displacement field, t is time, $\mathbf{E}$ is the electric field, and $\mathbf{B}$ is the magnetic flux density. Here, the constitutive relation linking $\mathbf{B}$ and $\mathbf{H}$ is $\mathbf{H} = \mathbf{B}/\mu$.

From these equations, it follows that passing an alternating electrical current through an electromagnetic coil to concentrate the field produces an alternating magnetic field through Ampère's law, which can induce a current in a nearby conducting test material through Faraday's law. These currents are called eddy currents and they flow in closed loops plane perpendicular to the magnetic field. The negative sign in Faraday's law is due to Lenz's Law, and means that direction of the induced current is such that the magnetic field produced by the induced current acts to oppose the change in the magnetic field that caused the induced current. Accordingly, the direction of the induced eddy currents opposes that of the current in the exciting

coil [112].

The eddy currents also change based on the properties of the material and the defects in the vicinity of the coil change the eddy current flow as they are forced to go around them. The eddy current itself also produces a magnetic field through Faraday's law, and this magnetic field can be measured in many ways. A simple approach would be to measure the impedance across an electromagnetic coil. The same physics that produced the eddy currents would mean the eddy current themselves would induce an current across the coils. The electromagnetic coil can even be the same as the driving coil such that only one coil is needed for the probe [51, 113]. Through its use of inductive coupling, ECT has the major advantage of being a non-contact technique [114].

Usually, the frequency of the alternating electrical current in the coil, which will be called the operating frequency, is chosen based on the desired skin depth where eddy current density drops to $1/e$ of its value at the surface. When assuming a plane wave solution, the skin depth, δ, can be derived using Ampère's and Faraday's laws.

It can be derived as followed [110], where Ohm's law ($\mathbf{J} = \sigma\mathbf{E}$, where σ is electrical condictivity and $\mathbf{E}$ is the electric field) will be used. Using the vector Laplacian relationship

$$\nabla \times \nabla \times \mathbf{E} = \nabla(\nabla \cdot \mathbf{E}) - \nabla^2\mathbf{E}. \tag{1.3}$$

In a conducting medium, the macroscopic charge density remains zero everywhere, thus $\nabla \cdot \mathbf{E} = 0$ and equation 1.3 becomes

$$\nabla \times \nabla \times \mathbf{E} = -\nabla^2\mathbf{E}. \tag{1.4}$$

Following Faraday's equation (equation 1.1)

$$\nabla \times \nabla \times \mathbf{E} = -\nabla \times \frac{\partial \mathbf{B}}{\partial t} = -\frac{\partial}{\partial t}(\nabla \times \mathbf{B}), \tag{1.5}$$

Combining this with equation 1.4 and ampere's law (equation 1.2), with the displacement current taken to be negligible, results in

$$\nabla^2\mathbf{E} = \sigma\mu\frac{\partial \mathbf{E}}{\partial t}. \tag{1.6}$$

For an attenuated plane wave moving in the z-direction, this becomes

$$\frac{\mathrm{d}^2\mathbf{E}}{\mathrm{d}z^2} = \sigma\mu\frac{\partial \mathbf{E}}{\partial t}, \tag{1.7}$$

Solving this equation using a plane wave solution ($\mathbf{E} = \mathbf{E}_0 \exp[j(\omega t - \beta z)] \exp(-\alpha z)$, where ω is the angular frequency, and α and β are parameters to be determined) gives

$$\alpha = \beta = \sqrt{\frac{\omega\mu\sigma}{2}} \tag{1.8}$$

The skin depth is defined as $\delta = 1/\alpha$ and thus

$$\delta = \sqrt{\frac{2}{\omega\mu\sigma}}. \tag{1.9}$$

In actuality, the coils are of finite size and accordingly, they do not generate a plane magnetic field. With smaller diameters where $R/\delta \approx 1$, the actual penetration depth is smaller that the calculated skin depth, δ. Only with diameters, where $R/\delta > 10$, does the actual penetration depth converge with the skin depth, δ [115]. Nevertheless, the equation 1.9 is widely used to approximate the skin depth and for defects, at the surface, this skin depth should be comparable to the shallowest defect that will need to be detected for optimum detection. Large electromagnetic skin depths mean the sensor is less sensitive to defects near the surface, and too small skin depths mean the sensor is too sensitive to surface roughness. This dependency of skin depth on frequency is why a higher frequency is needed for detecting small defects in low electrical conductivity materials, where high frequencies are required to maintain small penetration depths on lower conductivity materials.

The electrical conductivity of Ti is considered to be low [116] with a value of 2.38×10^6 Sm^{-1} [117]. Thus for a sub-millimetre size defect on Ti, the operation frequency should be about 10 MHz. Apart increasingly sensitivity to the surface by using higher frequencies, the strength of the eddy currents generated is also increased. However, this is countered by an increase electrical noise at higher frequencies [82], as discussed in section 1.3, and at a fundamental level, the sensor is more sensitive to changes in the distance between the sensor and the sample, otherwise known as lift-off [113, 108]. The increased sensitivity to lift-off at higher frequencies is caused by the skin effect being stronger, thus making variations in lift-off more prominent [39].

This may be offset by the Parametric approach, which will be used in this thesis. This approach can be seen to increase the signal-to-noise ratio at well as improve robustness to lift-off. The Parametric approach can be used as an alternative to operating at higher frequencies. As mentioned in the abstract, this thesis will mainly involve work at 1 MHz, though there is also some higher frequency work.

1.5 Challenges that will be addressed

In addition to trying to detect small sub-millimetre sized defects, this thesis will address finding them in some challenging circumstances. This is mainly split into two branches. Firstly, as previously mentioned, components such as turbine blades are increasingly made from low conductivity materials like TiAl. TiAl is an intermetallic, which is a material with an ordered crystallographic structure formed from a combination of metals, where concentration of the alloys exceeds the solubility limit [118]. As an intermetallic, it is expected to be lower conductivity, which was verified by four-point probe measurements. This is a method, where current flows through an outer probe pair and the voltage drop is measured across an inner pair using a voltmeter. The value of the voltage, current and spacing between the probes can then be used to find the conductivity of the material [119]. While uncertainties in, for example, the probe geometry meant one could not be confident in the absolute resistivity, the conductivities of different materials could be ranked, where TiAl was determined to be likely more resistive than Ti.

Low conductivity is a problem for the ECT method, as the eddy currents are generally weaker and less localised in lower conductively materials. The basic logic in ECT suggests higher frequencies are needed to counteract this, but as explained in sections 1.3 and 1.4, noise can be higher at such frequencies. Additionally, intermetallics are often more brittle than conventional structural metals (being between a ceramic and conventional structural metal). Moreover, TiAl is considered a more brittle intermetallic, where the crack-growth response more closely resembles that of ceramics [120]. Here, the crack-growth exponents are extremely high, and thus when a crack is initiated, it will typically grow extremely rapidly. This makes it more important to find these defects at an earlier and smaller stage. This thesis will look at improving the detection of small defects using ECT for use on these low electrical conductivity materials [121].

Another challenge is the detection and characterisation of defects near an edge. This detection of cracks near sharp edges is a problem, especially in the aircraft industry [104]. ECT is a well-established technique and there is much research behind it, and yet, there are only a few studies on edge defect detection. It is often easier to assume the sample is infinite in some dimension. It is more challenging to identify defects near an edge as both the defect and the edge of the material will distort eddy currents, with both affecting the signal. With conventional probes, the large signal associated with the edge can completely mask the signal produced by the crack [104]. However, defects commonly develop at edges and the stress concentration at edges

can aid in the growth of a crack, which makes this an important challenge to tackle.

A quick and compact solution to measuring phase using hardware will also be tackled. Compact solutions are needed in eddy current testing to make testing convenient and efficient to perform. Fortunately, there exists a plethora of compact and inexpensive hardware capable of performing this task, where phase often needs to be measured up to and into GHz frequencies in radio-frequency (RF) applications, such as receiving signals from antennas. To measure phase at such high frequencies, these systems also need to be accurate and precise. One such device is the AD8302 chip, which is an inexpensive and small chip capable of measuring phase in frequencies up to 2.7 GHz, and this will be implemented in this thesis.

1.6 Parametric approach to Eddy Current Testing

An approach that will be called the Parametric approach in this thesis is explained in the following section. Eddy current testing (ECT) is traditionally performed by displaying the magnitude and phase on a Lissajous plot. With the Lissajous plot, the system is generally calibrated by zeroing the probe on the material such that the change in magnitude and phase in shown, then rotating the displayed data to lie along the horizontal as lift-off is changed over a region free from defects [122]. By plotting the measured impedance with the plot rotated such that lift-off is horizontal, signals deviating from the horizontal can then be identified as being an indication [109]. Such plots generally require careful interpretation with small changes being often difficult to reliably detect, let alone quantify. In contrast, our Parametric approach involves measuring the magnitude and phase of the signal independently. To explain what is meant by magnitude and phase, let us start with Ohm's law for AC circuits,

$$\tilde{V} = \tilde{I}\tilde{Z}, \tag{1.10}$$

where $\tilde{V}$, $\tilde{I}$ and $\tilde{Z}$ are the voltage, current and impedance of the transmitter coil respectively. Writing $\tilde{Z}$ in its exponential form results in

$$\tilde{V} = \tilde{I}Z\exp(i\phi), \tag{1.11}$$

Z and ϕ are the magnitude and phase of impedance respectively. This equation implies that ϕ is equal to the phase difference between the voltage and current. If the current is kept constant as is the case for our transmitter coil, any changes in the phase of the impedance must result in an equivalent change in the phase of the voltage. Additionally, constant current also means the magnitude of the voltage is

proportional to the magnitude of the impedance.

Furthermore, the signal can be related to the inductance, L, and resistance, R, of the coil by treating the coil as an inductor with an equivalent series resistance (i.e. $\tilde{Z} = R + i\omega L$) so that $Z = \sqrt{R^2 + \omega^2 L^2}$ and $\phi = \arctan(\omega L/R)$. For an inductor, $\phi = 90°$. This means the voltage leads the current by 90° [123].

The signal in the receiver coil is due to a combination of the magnetic field seen from the transmitter coil (B_{Tx}) and the eddy current (B_{EC}). Modelling the magnetic field from each as a sine wave, the total magnetic field is

$$B = B_{\mathrm{Tx}} + B_{\mathrm{EC}} = B_{\mathrm{Tx0}}\sin(\omega t + \alpha) + B_{\mathrm{EC0}}\sin(\omega t + \beta) = B_0\sin(\omega t + \eta), \quad (1.12)$$

where B_{Tx0}, α, B_{EC0}, β, B_0 and η are constants, ω is the angular frequency and t is time. Here,

$$B_0 = \sqrt{[B_{\mathrm{Tx0}}\cos(\alpha) + B_{\mathrm{EC0}}\cos(\beta)]^2 + [B_{\mathrm{Tx0}}\sin(\alpha) + B_{\mathrm{EC0}}\sin(\beta)]^2} \quad (1.13)$$

while

$$\eta = \arctan\left[\frac{B_{\mathrm{Tx0}}\sin(\alpha) + B_{\mathrm{EC0}}\sin(\beta)}{B_{\mathrm{Tx0}}\cos(\alpha) + B_{\mathrm{EC0}}\cos(\beta)}\right]. \quad (1.14)$$

Since the total magnetic field is a sinusoid, the voltage in the coil is also a sinusoid of the same frequency (i.e. $V_{\mathrm{Rx}} = V_{\mathrm{Rx0}}\sin(\omega t + \gamma)$) through Faraday's law, whereby [124]

$$V = -\frac{\mathrm{d}}{\mathrm{dt}}\iint \mathbf{B}\cdot d\mathbf{s}, \quad (1.15)$$

where V is voltage and $\mathbf{s}$ is a surface. Thus $V_{\mathrm{Rx}} \propto B$.

The analysis of eddy current signals in this manner differs from the usual Lissajous method of viewing the signals. While there are clear similarities between the Lissajous plot information and the Parametric approach, the methodology and quantification used in this thesis are distinctly different and provide the potential for more reliable measurements. Analysing signals with the Parametric approach may help with the identification and characterisation of defects as the results show interesting characteristics such as the phase being potentially to be more robust to lift-off and the edge of the sample. This is important since lift-off variation is known to be one of the main factors that can limit effective eddy current testing (ECT) [125], where variations in lift-off have the potential to mask a defect.

1.7 Eddy current probe configurations

A simple ECT sensor configuration would be to use a single coil to generate and detect the eddy current. This is a well-used and simple configuration. Moreover, the most widely used circuitry for measuring the impedance of the coil is an impedance bridge [108]. To demonstrate the principle behind an impedance bridge, a Wheatstone bridge is shown in figure 1.2. A Wheatstone bridge measures an unknown electrical impedance by balancing two legs of a bridge, where one leg of the bridge has the component whose impedance is to be found. The principle is as followed. For the circuit in figure 1.2, if the potential difference measured at V is zero then

$$\frac{Z_3}{Z_1} = \frac{Z_4}{Z_2}. \tag{1.16}$$

Thus, if say Z_4 was the component whose impedance is to be measured, by varying Z_3 to balance the bridge, the impedance of Z_4 can be found if Z_1, Z_2 and Z_3 are known [126].

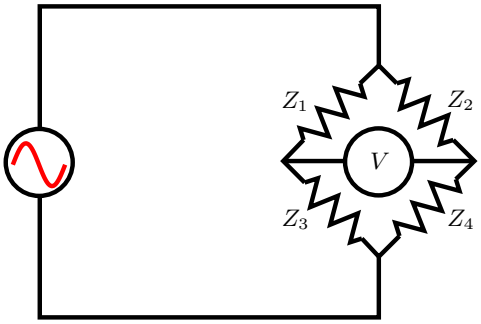

Figure 1.2: Wheatstone Bridge.

Figure 1.3 shows examples of absolute probes in bridge mode. It shows an uncompensated and compensated probe. It is common for absolute probe to be compensated to reduce variations due to thermal fluctuations, a "dummy" coil that is not coupled magnetically to either the main coil or the sample is used as a reference where the difference between the coils can be measured in this bridge configuration.

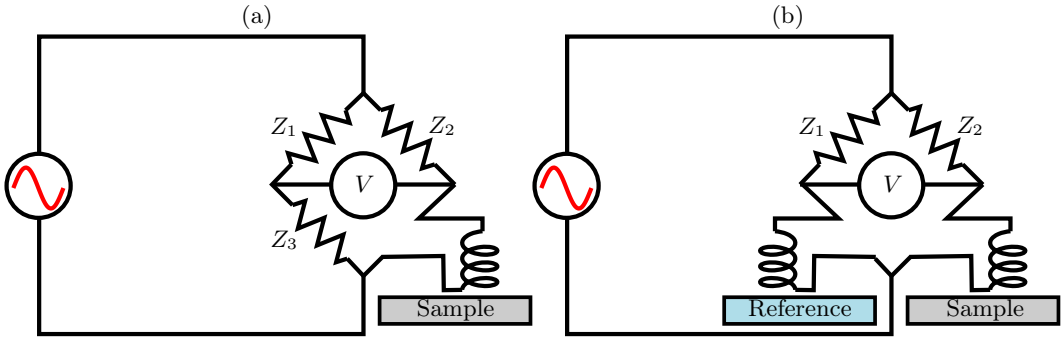

Figure 1.3: Diagram of absolute probe configurations. (a) is uncompensated, (b) is compensated.

Another option is to use a differential probe. Such probes tend to be better for comparing adjacent material sections and more suited to detecting abrupt changes such as those caused by small defects [127, 128, 129]. These can be formed by winding two coils in opposition [129]. It is able to enhance the detection of defects by producing a signal related to the difference in impedance between the two coils. In the differential configuration, a signal is produced when one coil is over a defect and the other is over a flaw-free region, but no signal is produced when both are over a flaw-free region. They have the advantage of being very sensitive to defects, whilst being more robust to material and lift-off variations. It is important to note that they are relatively insensitive to gradual dimension change and can be difficult to interpret: for example if the flaw is longer than the spacing between the coils [127]. Figure 1.4 shows some typical configurations where the most used configuration is the parallel configuration, though the coaxial configuration widely usedsignal-to-noise for tube/rods [130]. An orthogonal arrangement is used in a circumstance when the flaw is best detected by considering the difference between a tangential and normally orientated coil.

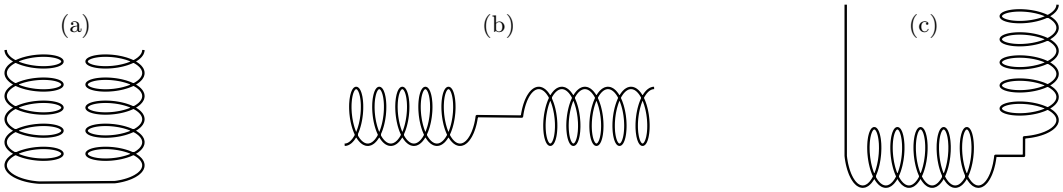

Figure 1.4: Differential eddy current probe configurations where the coils are positioned (a) parallel, (b) coaxially, and (c) orthogonal to one another.

Reflection probes (also know as transmit-receive or driver-pickup) can also be used. In such an arrangement, one coil is used as a transmitter and another coil is

used as a receiver [131]. Obrutsky (1997) [132] worked with laterally displaced transmit and receive probes, which they argued had the advantage of having a greater signal-to-noise in the presence of lift-off and being strongly directional. They reasoned that the signal generated by localised defects between the transmitter and receiver coils was similar to a similar-sized impedance coil, but the low flux linkage between the coils meant that the response to global variations such as lift-off would also be low, while the directional properties can help enhance the detectability of defects such as cracks.

In the work presented in this thesis, two adjacent coils are used. One coils is used as a transmitter, but the magnitude and phase of the signals from both coils are measured. Thus, one benefits from the data that a reflection probe would generate while maintaining the data that would be obtained from an absolute probe.

1.8 Modelling the eddy current sensor

As mentioned, Dodd and Deeds found the first close form solutions for a practical sensor [76]. These solutions were for 1) a coil above a two-conductor plane, and 2) a coil surrounding an infinitely long circular tube/rod. The former was was used to calculate the current density for zinc cladded carbon steel in MATLAB. This was solved as followed, with the model setup shown in figure 1.5.

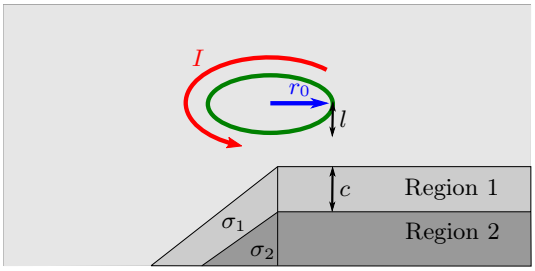

Figure 1.5: Dodd and Deeds model setup.

In the Dodd and Deeds paper, the magnetic vector potential in the top layer (region 1 in figure 1.5) is given by

$$\mathbf{A}_1(r,z) = \mu I r_0 \int_0^\infty J_1(\alpha r_0) J_1(\alpha r) e^{-\alpha l} \alpha \times \left[\frac{(\alpha_2+\alpha_1)\exp(2\alpha_1 c)\exp(\alpha_1 z) + (\alpha_1-\alpha_2)\exp(-\alpha_1 z)}{(\alpha-\alpha_1)(\alpha_1-\alpha_2) + (\alpha+\alpha_1)(\alpha_2+\alpha_1)\exp(2\alpha_1 c)} \right] d\alpha. \tag{1.17}$$

While, the magnetic vector potential in the bottom layer (region 2 in figure 1.5) is

given by

$$\mathbf{A}_2(r,z) = \mu I r_0 \int_0^\infty J_1(\alpha r_0) J_1(\alpha r) e^{-\alpha l} \alpha \times \left[\frac{2\alpha_1 \exp[(\alpha_2+\alpha_1)c]\exp(\alpha_2 z)}{(\alpha-\alpha_1)(\alpha_1-\alpha_2)+(\alpha+\alpha_1)(\alpha_2+\alpha_1)\exp(2\alpha_1 c)} \right] d\alpha \tag{1.18}$$

.

In these equations J_1 is a first order Bessel function, I is the current, r_0 is the coil radius, l is the coil lift-off, c is the thickness of the top layer, α is a continuous variable and $\alpha_i := (\alpha^2 + j\omega\mu\sigma_i)^{1/2}$.

The current density can then be calculated using the magnetic vector potential and Ohm's law,

$$\mathbf{J} = \omega\mathbf{E} = -\sigma\frac{\partial A}{\partial t} = -j\omega\sigma\mathbf{A}, \tag{1.19}$$

which becomes $J = -j\omega\sigma A(r,z)$ due to the axial symmetry, where ω is the angular frequency.

The equations were combined with values for electrical conductivity of $17\,\mathrm{MS\,m^{-1}}$ [133] and $5.9\,\mathrm{MS\,m^{-1}}$ [134] for the conductivities of zinc and carbon steel respectively (values derived from electrical resistivity), a thickness of 0.3 mm for the zinc layer, a lift-off of 0.1 µm, an angular frequency of $2\pi \times 1\,\mathrm{MHz}$ and a current of 2 µA. Furthermore, the principle of superposition was used to model a coil with multiple layers and turns, where the contribution from multiple coils were added. Here, the inner radius is taken to be 0.9 mm, the spacing between coils to be 0.063 mm, the number of the layers to be four and the turns per layer to be 25.

The result is shown in figure 1.6, where r is the radial position, z is the depth, and J is the normalised current density. The apparent lack of eddy currents in the bottom layer is because the eddy currents induced in the top layer are much stronger. This is due to a combination of the difference in electrical conductivity and permeability of the materials, and the multiple windings that concentrate the eddy currents close to the surface.

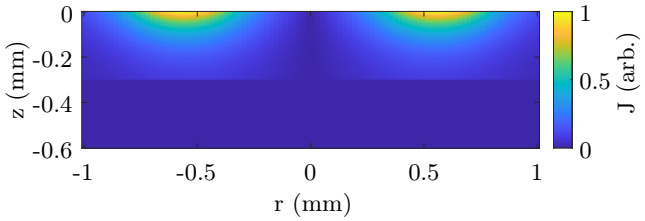

Figure 1.6: Dodd and Deeds solution produced in MATLAB.

Analytical models tend to provide solutions for idealised systems with zero/infinite dimension parts, or simple systems with a good amount of symmetry. For example, Bowler (1994) models a defect as a negligible opening, which is impenetrable to electric current [135], while Skarlatos et al. (2011) [136] model a defect as a hole parallel to the surface. The defects in this thesis are slot defects and while there is analytical work on rectangular defects such as that by Theodoulidis (2005) [137], much analytical work uses truncated domains. In these domains, the space is truncated by an artificial boundary, with the papers mentioned here using a half-space domain. Truncated domains are used since the Green's functions are known and can be more easily evaluated. These are functions are used to solve linear inhomogeneous partial differential equations [138] and they are a solution of

$$LG(x,s) = \delta(x-s), \tag{1.20}$$

where L is a linear differential operator, G is a green function, δ is the dirac delta function and s is a position.

In addition to the complexity introduced by the defect geometry, there are often additional geometries and factors that complicate matters further. Often the complexity of a real system means it is not feasible to calculate closed-form solutions, particularly solutions that require 3-D modelling. Trying to solve complex geometries analytically would be prohibitively difficult, as the entire system would need to be solved at once. In such cases, numerical methods may need to be used. The three main numerical methods that have been adopted to solve eddy current problems are the finite element method (FEM) [139], the boundary element method (BEM) [140], and the finite difference method (FDM) [141].

Out of these methods, the FEM and FDM are more established. The FDM solves differential equations by approximating the derivatives by a differential quotient. Mathematically, this means

$$u'(x) \approx \frac{u(x+h) - u(x)}{h}, \tag{1.21}$$

which is a good approximation so long as h is small but not equal to zero. Steps can be taken to improve the accuracy, which includes centering the quotient like so

$$u'(x) \approx \frac{u(x+h) - u(x-h)}{2h}. \tag{1.22}$$

FEM has risen with advances in computational modelling. The FEM is better suited for complex geometries than the FDM [142], where arbitrary geometries can

be modelled with relative ease. The FEM works by dividing the geometry into elements (connected by nodes) and solving equations for each element, which are then combined to model the system. These elements generally fall under two main shapes: tetrahedral and hexahedral. Tetrahedral elements will mainly be used as these mesh easily and better fit arbitrary geometries. Moreover, the order of the elements used will be quadratic, which allows for quadratic interpolation of variables between nodes (the corners of each element) and better fitting of curved geometries than linear elements. The order of elements could of course be higher (e.g. cubic) but the computation requirements increase with increasing order. A related term is finite element analysis (FEA), which refers to the application of the FEM.

The BEM has risen as an alternative method to the FEM. Instead of dividing the geometry into elements, the problem is reduced to a boundary problem, where only the surface is discretised. By reducing the dimensionality by one order (see figure 1.7 [143]), the computational time is reduced and the technique is suited to infinite domain problems [144].

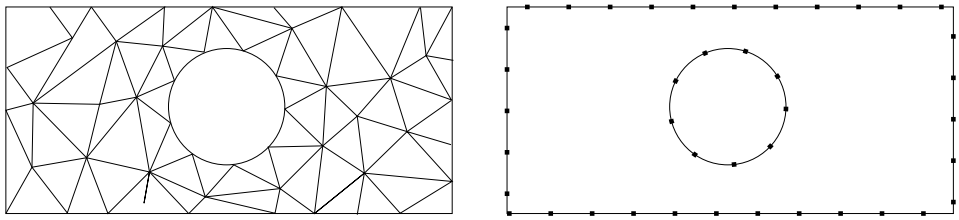

Figure 1.7: Comparison of finite difference and boundary element discretisation.

In this thesis, the finite element method (FEM) will be used. A commercial finite element program is used to build our models and run simulations. More specifically, the magnetic fields interface of COMSOL's AC/DC module will be used. This means the main dependent variable being solved for in the model is the magnetic vector potential, and it is from this the desired variables (e.g. the voltage across each coil) are "probed" for. Furthermore, the model can be solved more efficiently in the frequency domain as linear differential equations can be simplified into algebraic equations. This is suitable for systems that vary sinusoidally over time, as is the case for the systems in this thesis. Conceptually, this means that the Maxwell equations

being solved are of the form:

$$\nabla \times \mathbf{H} = \mathbf{J} \tag{1.23}$$

$$\mathbf{B} = \nabla \times \mathbf{A} \tag{1.24}$$

$$\mathbf{E} = -j\omega\mathbf{A} \tag{1.25}$$

$$\mathbf{J} = \sigma\mathbf{E} + j\omega\mathbf{D} \tag{1.26}$$

The inputs for the equations come from constitutive relations, based on the material properties (e.g. $\mathbf{B} = \mu_0\mu_r\mathbf{H}$ and $\mathbf{D} = \epsilon_0\epsilon_r\mathbf{E}$). The second term in equation 1.26 involves the term $\mathbf{D}$. This is known as the displacement current and it is a correction to Ampère's law made by Maxwell. Furthermore, in our model, the boundary condition used on the outer surface of the system is the magnetic insulation boundary condition and before this there is an infinite element domain, which should stretch the coordinate axis with the effect of approximating an infinitely large domain.

Chapter 2

Methodology

This chapter will begin with discussing the experimental setup and the considerations made before in the final section of the chapter (section 2.8) explaining the simulation setup.

2.1 General setup

The general setup is depicted in figure 2.1, in which the transmitter coil (Tx) is driven at a constant amplitude sinusoidal current, and there is a nearby receiver coil (Rx) that is passive. The coils are placed directly adjacent along the x-direction unless stated otherwise. The constant current is achieved using a Howland current source (HCS), which produces a current proportional to the reference signal that in this case will be a constant amplitude voltage. The specific setup will vary within this thesis as the probe and the measurement system is varied. This is, for example, why the Rx coils do not appear to be connected to anything in figure 2.1.

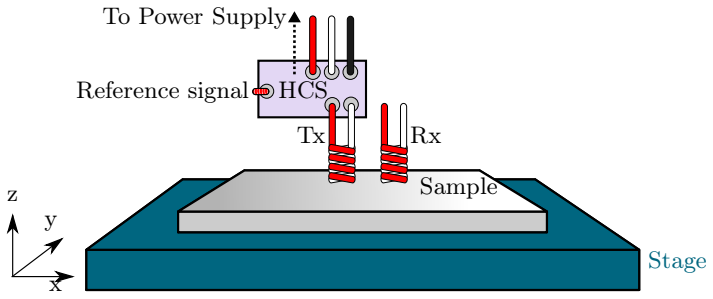

Figure 2.1: General setup.

Also, the equipment used to generate the reference signal will differ, although direct digital synthesis will be used throughout, and the parameters of the coil will

change between the study of defects that are away from and defects close to an edge. The common features along with some of the general considerations and details of the data collecting process used in this chapter are discussed in this section. To make the setup clear for each experiment, each chapter will start with a description of the specific setup used.

2.2 Howland current source for transmitter coils

As seen in section 1.6, a constant current to the coil means that only the voltage needs to be measured, and this also simplifies the interpretation of the results. A current source should generate current independent of the voltage across it and a HCS is used in this system. A HCS consists of a high gain operational amplifier and a balanced resistor bridge, as shown in figure 2.2.

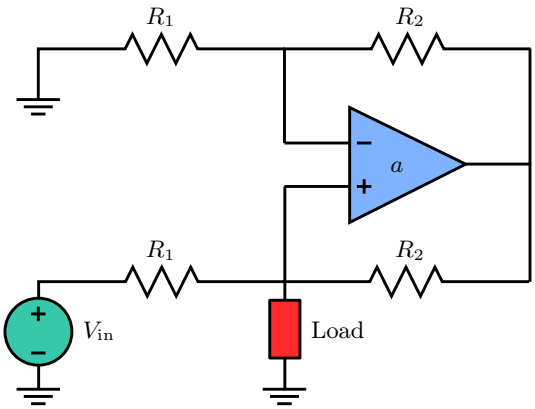

Figure 2.2: Schematic of a basic Howland current source. R_1 and R_2 are the resistances of the resistors. a represents the gain of the op-amp.

The system has the benefit of being able to output current in both directions and having a grounded load. However, the HCS is not expected to work well at high frequencies, because at high frequencies the gain of the op-amp, a, falls, leading to a decrease in its output impedance, R, according to,

$$R = (R_1 \parallel R_2) \times \left(1 + \frac{a}{1 + R_2/R_1}\right). \tag{2.1}$$

When combined with the increase in the impedance of the load up to its resonance frequency, the frequency operated at has to be well below resonance. While there is work regarding eddy current measurements at near resonance, where the behaviour near resonance can help with defect detection as mentioned in section 1.3, the res-

onance can also be affected by a number of other factors that could interfere with defect detection [125]. Above the resonant frequency, the coil is in the capacitive region and thus the system is not dominated by the effects of induction, which ECT depends on.

The voltage across the coils and current can be measured using the setup shown in figure 2.3. There are unity gain op-amps either side of a resistor. The voltage going through an op-amp is the same as the input but their high impedance means they draw little current. The load voltage is monitored from the bottom op-amp. Whereas, the current amplitude can be found by subtracting the voltage signals from each op-amp, finding the amplitude of the resulting waveform, and dividing by the resistance of the resistor.

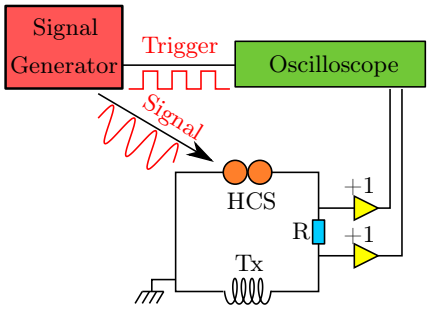

Figure 2.3: The arbitrary function generator (AFG) generates a sinusoidal voltage, which is feed to the Howland current source (HCS). The HCS generates a current proportional its input such that it drives the circuit at a constant amplitude sinusoidal current. The yellow triangles are op amps of unity gain. The signals from the op amps are terminated at $50\,\Omega$ going into the oscilloscope to reduce reflections. The resistor has a resistance of R.

In the setup shown, the voltage measurements is performed using an oscilloscope, but any other voltage measuring device may be used. When using an oscilloscope, the signals from the op-amps are terminated at $50\,\Omega$ going into the oscilloscope, and so the measured signals are also attenuated by a factor of two. Thus, there is a correction factor of two that needs to be applied for both the voltage and current measurements.

As one may appreciate, the measured voltage is not only dependent on the electrical properties of the coils, since there is a resistor on the Tx side and an amplifier on the Rx side, but the measured voltage would be expected to scale proportionately with the voltage without these components. This is key since the defect indication comes from observing changes in the eddy current sensor signals, whilst the absolute value of the voltage is less important.

Moreover, while one might want to take the phase difference of the voltage signal with respect to the current in the Tx coil, this would add extra capacitance to the system and extra components would be needed to measure it accurately. Instead, it is more sensible to trigger from the voltage output of the signal generator, as while this is not necessarily in phase with the current in the Tx coil, it should be phase-locked to the current in the Tx coil when using the HCS.

2.3 Scanning method for positioning of sensor

The coil positions generally fall under three basic probe positions: encircling, internal axial and surface scanning. In this thesis, surface scanning probes will be used throughout, whereby the axis of the coils are held perpendicular to the surface to be inspected. For 2D scans where an eddy current probe is held above a sample and moved to cover a region on the surface, the eddy current probe is mounted on an XY stage. The XY stage moves the sample, such that the coils move across the sample surface. The scanning pattern is such that measurements are taken at 0.1 mm intervals in a square grid-like pattern. Moreover, the scanning pattern implemented is one in which each line would be retraced before going to the next line, to reduce misalignment through backlash. Faster scanning patterns were considered, such as the bidirectional raster scan, whereby alternating lines are scanned in opposite directions, but it was deemed more important to reduce misalignment.

As discussed, taking Parametric measurements was found to improve the robustness to lift-off. While this was initially suspected to be the case after analysing the 2D scans, the natural progression was to perform lift-off measurements to confirm this and better understand the lift-off behaviour. For these lift-off measurements, the probe is mounted onto a vertical positioning micrometer, to move the coils towards and away from the sample surface. Lift-off measurements are taken at 0.1 mm intervals moving toward the sample. This is because if the probe is moved away from the sample surface, the probe may recoil after being initially in contact with the sample.

2.4 Geometry of eddy current probe

ECT probes are generally made by winding a wire into a coil. There are many variations of this design, which can depend on the purpose or type of defect that needs to be detected. This section will discuss different shapes and sizes, before finalising the coil selection that will be used in this thesis.

2.4.1 Shape considerations for coil

The probe sensitivity improves with higher coil inductance, L. For a coil, L can be calculated as [31]

$$L = Kn^2\pi[(r_0^2 - r_c^2) - \mu_r r_c^2]\mu_0/l, \tag{2.2}$$

where r_0 is the mean radius, r_c is the radius of the core, l is the length, n is the number of turns, μ_r is the relative permeability of the core material, μ_0 is the permeability of free space, and K is a dimensionless constant.

K is a correction factor that is based on the shape of the coil. It can help account for the reduction in inductance associated with the coil being finite and is a concept introduced by Nagaoka [145]. Nagaoka's paper contains a look up table of values for the correction factor [146].

From this equation, it can be seen that several variables can be changed to increase L. This includes increasing n, which can be achieved by winding the coil along its length to form a solenoid, or winding the coil into a flat spiral shape to form a pancake coil.

In winding a pancake coil, the cross-sectional area (related to the $r_0^2 - r_c^2$ term) also increases, which further increases the L. However, the distribution of eddy currents in the sample mirrors the footprint of the coil and thus doing so can reduce the spatial resolution. The pancake coil may be suitable for measuring material properties such as conductivity, but the smaller footprint of the solenoid makes it suitable for detecting small defects.

Other details to consider include whether a coil should have multiple layers. Multiple layers increase n without increasing l for solenoids or cross-sectional area for pancake coils. Also, there exist other coil shapes, which are not axisymmetric such as rectangular coils [105] or double-D coils, which is used in differential setups [147].

2.4.2 Size considerations for coil

Choosing the right size coil is a trade-off between many, sometimes competing factors. Smaller probes tend to have a better spatial resolution, as eddy currents tend to follow the coil footprint. As for vertical resolution, when the penetration depth was discussed in section 1.4, a plane wave solution was assumed. In actuality, the electromagnetic penetration depth also depends on the diameter of the coils, which is finite. At high frequencies, the actual penetration depth is more or less accurately approximated by the penetration depth formula for a plane wave solution. In fact, according to Mottl (1990) [148], the equation holds if the mean coil radius divided by the standard depth of penetration is greater than ten, which is a regime that

is not ideal for eddy current testing. As Mottl states, "the coil impedance changes due to eddy current generation are relatively small, so it is not the optimal range for eddy current testing". At lower frequencies, the actual penetration depth and the penetration depth from the formula diverge. This has been studied using finite element models [149, 150], where one sees the penetration depth plateau towards lower frequencies as depicted in figure 2.4. At these lower frequencies, it can be seen that smaller coils have a lower penetration depth.

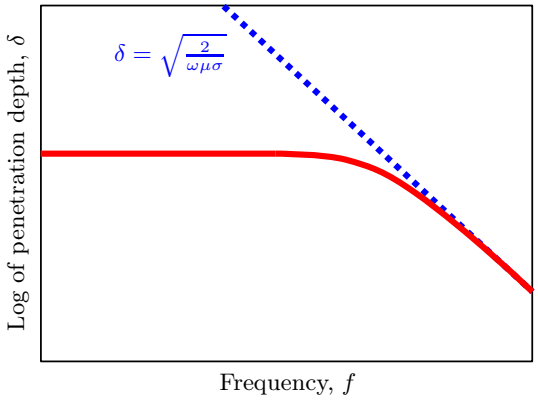

Figure 2.4: Diagram illustrating how the penetration depth differs for a finite coil (red) compared to the penetration depth from a plane wave solution (blue).

Moreover, smaller coils can fit into smaller gaps and the coils need to be small enough that the test surface at any position can be considered flat for surface scanning [31]. Also, inductance, which is linked with larger coils, can be an issue for maintaining a constant current source. This is because a high output impedance compared to the load is needed in order for the current to be relatively unaffected by variations in the load conditions. In fact, an ideal current source would have infinite output impedance [151].

On the flip side, coils that are too small may be overly sensitive to surface variations and suffer more from lift-off induced changes to the electrical properties. Additionally, the spatial coverage will be reduced and so will the potential signal that can be induced due to its lower inductance.

2.4.3 Chosen coil specification

Taking these factors into consideration, the coils used for most of the work in this thesis were solenoidal shaped and wound using 0.063 mm diameter wire on a 0.9 mm diameter rod to have 4 layers with 25 turns per layer. The rod is removed after winding. They were wound with an orthocyclic winding structure, which has the

highest fill factor for round wires. It achieves this by placing the winding of each layer into the groves in the lower layer.

Initially, air-cored coils were used, but this later progressed to using a NiZn ferrite core. There is usually a trade-off where higher permittivity cores help concentrate the magnetic field but their domains tend to switch less easily, which makes them less suitable for high-frequency operation. Accordingly, NiZn ferrite was selected because of its suitability for use at high frequencies although it has a lower permittivity than many other ferrites such as MnZn ferrite.

Ferrites have the chemical formula $MOFe_2O_3$, where MO is one or more divalent metal oxide blended and sintered with 48 to 60 mole percent of iron oxide [152]. The NiZn ferrite rods used are called "67 material" by Fair-Rite. According to the safety data sheet, it is a Nickel Zinc Spinel Ferrite, which by weight is composed of $<$23% Ni, $<$8% Cu, $<$23% Zn and $<$2% Co [153], indicating the material is further doped Cu and Co. Also, according to the data on its permittivity vs frequency, $\mu_r = 35.969 + 0.15i$ at 1 MHz [154].

An impedance analyser was used to characterise the probe. The results for the probe with NiZn cored coils are shown in figures 2.5 and 2.7. Figure 2.5 displays two peaks at about 15 MHz and 20 MHz in the impedance. This arises from the coupling of two adjacent coils within the probe, where the coils have different self-resonances.

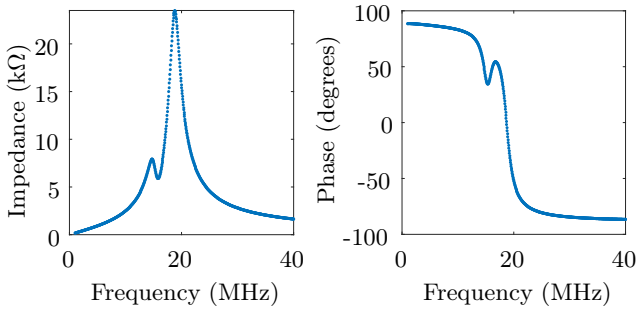

Figure 2.5: Impedance of NiZn cored coils.

The coils are made to the same specification, but it is apparent slight differences have caused the coils to have different resonances. This behaviour is also reported in R. Hughes (2016) [155], which investigates the electrical resonance in eddy current array probes. According to the paper, multiple peaks are caused by coils with different resonances coupling, where variations in the resonance may be caused by any number of parameters, including "turn spacing, coil slippage and ferrite core length/condition". The results for a single NiZn coil made to the same specification as the coils in the probe is shown for comparison in figure 2.6. In this,

only one peak is present since there are no adjacent coils to couple to.

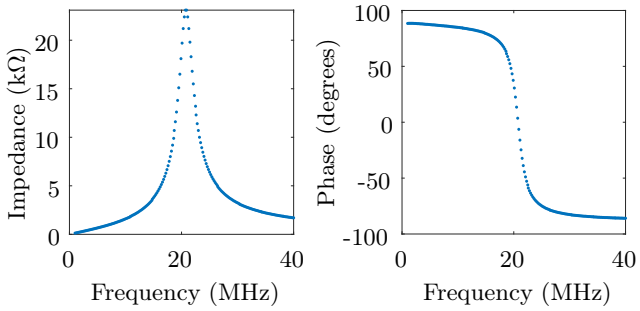

Figure 2.6: Impedance of a single NiZn cored coil.

The series equivalent inductance and resistance are also plotted in figure 2.7. In the resistance plot, it is possible to again see the double peaking characteristic of the coils self-resonances. The inductance on the other hand goes from positive inductance to a negative one. This negative inductance is capacitance. The electrical resonance would be expected to shift to higher frequencies on non-ferromagnetic material and decrease over a crack [155].

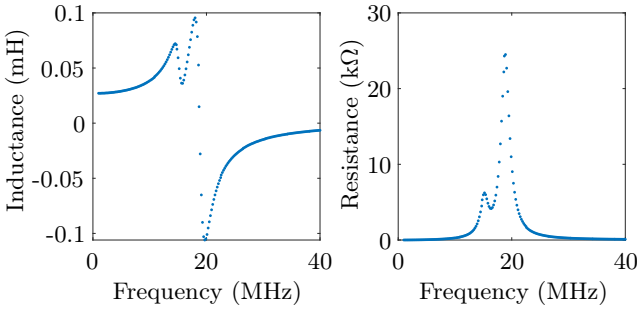

Figure 2.7: Series equivalent inductance and resistance of NiZn cored coils.

The impedance for a single coil can be straightforwardly modelled using Kirchoff's law. This is shown for a coil in free-space in figure 2.8. The figure is calculated from an equivalent circuit model, more specifically a circuit with a resistor and inductor in series and a capacitor in parallel was used resulting in the formula [156, 155].

$$Z = \frac{R + j\omega L}{1 - \omega^2 LC + j\omega RC}. \tag{2.3}$$

This equation can be split into real and imaginary components as followed

$$Z = \left[\frac{R}{(1-\omega^2 LC)^2 + (\omega RC)^2}\right] + j\left[\frac{\omega L(1-\omega^2 LC) - \omega R^2 C}{(1-\omega^2 LC)^2 + (\omega RC)^2}\right]. \tag{2.4}$$

Equation 2.4 was plotted in MATLAB with $R = 6.68\,\Omega$, $C = 0.1\,\text{nF}$ and $L = 19.82\,\mu\Omega$. The resulting plot can be seen to be similar to the measured impedance for the single NiZn cored coil (figure 2.6).

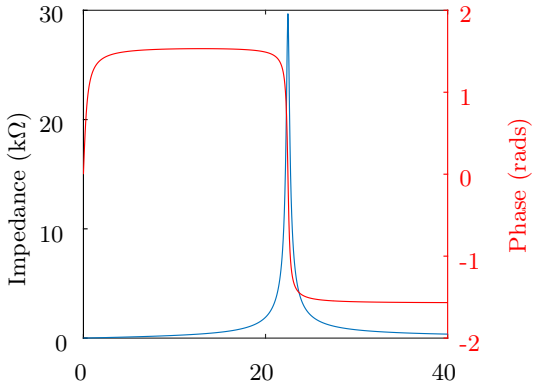

Figure 2.8: Impedance from Kirchoff's law.

For the edge/corner defect part, the geometry of the coils is slightly different. The coils are air-cored as they are designed to operate at higher frequencies and consist of 5 layers, 20 turns per layer to give a total number of 100 turns of wire. The coils are 1 mm long, and the inner and outer diameters of the coils are 0.315 mm and 0.55 mm respectively. These smaller coils should allow for greater localisation of the eddy current as the eddy current footprint follows that of the coils. Also, the smaller coils help allow higher frequencies to be reached as load impedance is lower, which is better for the current source. Higher frequencies in turn reduce the skin depth. By better confining the eddy current, there should be increased sensitivity to shallow defects while reducing the extent that the eddy current is affected by the sample edge. The impedance analyser results are shown in figure 2.9 and were taken by Zhichao Li. The resonance peak is less pronounced and lower than the NiZn cored coils. This can be explained by the coils being uncored and smaller, thus expected to have a lower inductance. In fact, the inductance is calculated to be approximately $1.8\,\mu\Omega$. It can also be seen that the first resonance occurs at 23.1 MHz. Care must be taken to operate below the resonance peak as this the region where inductance dominates.

When dealing with applications such as surface crack detection, it is common to try to confine the magnetic field [157], which can be achieved with ferrite cores or shielding. This can additionally help with reducing the coupling between the inductor and the rest of the circuit. The edge/corner coils were, however, uncored in an attempt to reduce the instability in the current source seen at higher frequencies.

The approach however is agnostic and thus, can be applied to other probes including ferrite-cored/shielded ones.

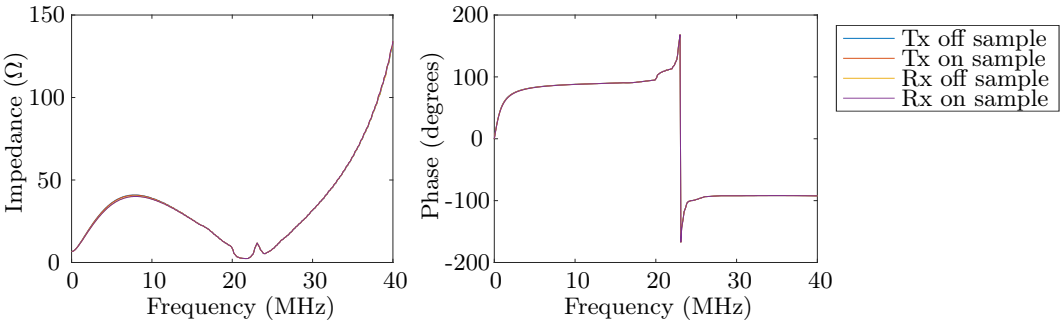

Figure 2.9: Impedance of coils used for edge defects.

2.5 Material selection for samples

Significant properties of the material tested are the permeability and electrical conductivity [158]. On the issue of permeability, non-magnetic materials were chosen, as ECT tends to work well on these materials. With magnetic materials, other techniques such as magnetic particle inspection can be used and thus are potential competition. Also, magnetic materials can have issues that are different from non-magnetic materials, requiring the sample to be tested differently. For example, magnetic materials have the issue that permeability variations generally have a much greater effect than variations in conductivity on the eddy current response, which means that defects may not be possible to detect if there is too much heterogeneity. In particular, ferromagnetic materials tend to have significant variability in magnetic permeability, so difficulties can be experienced in the inspection of ferromagnetic materials and the testing of such materials may need to be altered. For example, it may be beneficial to magnetically saturate such materials during testing to have fewer permeability variations [108].

Taking the requirement for non-magnetic materials into account, three samples were chosen: a sheet of austenitic SS 316L of thickness 2.16(2) mm, a titanium aluminide (TiAl) block of thickness 11.84(2) mm, and a titanium (99.6%+ purity) sheet (Ti) of thickness 6.0 mm. These materials were chosen because of their wide usage or potential usage in safety-critical applications.

Stainless steel (SS) is has been a transformative material since it was commercialised in the early 20th century [159] and is ubiquitous in industries including for power generation applications, where it has superior resistance to corrosion in most environments and it can endure the high temperatures/pressures and radiation

often present. The most commonly used are the austenitic grades, of which 302, 304, and 316 are the most popular wrought grades [160]. 304 grade SS has enjoyed much popularity in the power industry, but the 316L grade that will be tested has a better resistance to chemicals and chlorides.

TiAl is a low-density material with high oxidation resistance and impressive strength retention even at high temperatures. As such, it has great potential in the aerospace and automotive industries for combustion engines and gas turbines. TiAl is becoming an increasingly important alloy for aerospace applications, whereby the Ti-48Al-2Cr-2Nb (4822) version of TiAl has been used in making low-pressure turbine blades for GEnx engines, achieving a 50% weight reduction [14]. This thesis will be using the Ti-45Al-2Mn-2Nb-1B (4522XD) version of TiAl, which is considered to be more suitable for casting with its fine grain size [161]. As TiAl is a more novel material, there are relatively few papers that describe eddy current inspection of titanium aluminide [162]. This makes it an interesting material to look at, but it is also consequently harder to source. Instead of purchasing a standard sheet of material from a supplier, an engine part made from TiAl had to be ground to have a smooth surface.

Often alloys/intermetallics rather than pure materials are used in industrial applications as alloying a material usually confers additional beneficial mechanical properties. However, as a baseline, pure titanium will be tested, as it can be sourced from suppliers to a particular specification. In this case, the sample is a high purity (ASTM B265 Grade 2) and temper annealed sheet sourced from Advent Research Materials under the label "TI2290 titanium Plate". It acts as a comparison sample, which other materials can be compared to. In this vein, compared to other alloys/intermetallics one would expect some general features to be similar, depending on the exact composition, although there would of course be key differences. As an intermetallic, it is expected to be lower in electrical conductivity than Ti, which was confirmed by magnitude of the receiver coil voltage being generally lower in experimental results, where the difference in the magnitude of the receiver coil voltage can be seen in a comparison of the 2D scans. As well as, four-point probe measurements.

The four-point probe measurements were performed using a CROPICO DO5000 Microhmmeter (Seaward, UK). The four-point probe method consists of placing four probes on the material whose conductivity is to be measured (see figure 2.10). An electrical current (I) is then induced across the outer probes and the voltage (V) is measured between the inner probes. The conductivity (σ) can

then be found using [163]

$$V = V_2 - V_3 = \frac{I\rho}{2\pi}\left[\left(\frac{1}{s_1} - \frac{1}{s_2}\right) - \left(\frac{1}{s_3} - \frac{1}{s_4}\right)\right], \tag{2.5}$$

where ρ is the resistivity whereby ($\rho = 1/\sigma$) and s are the spacings. The use of the four-point probe method avoids the problem of contact resistances, but it assumes the sample is semi-finite. In reality, the sample is finite and as such, it was difficult to be confident in the absolute value. The samples could, however, be ranked for conductively in relative to the other samples.

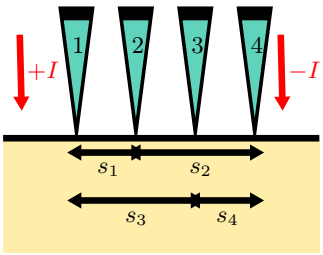

Figure 2.10: Four-point measurement schematic.

SS and Ti are known to be relatively lower in conductivity compared to other metals, and with TiAl being lower in conductivity than Ti, finding small defects in such materials may be more of a challenge since this increases the skin depth, and thus reduces sensitivity to surface variations. However, TiAl is also expected to be more brittle than Ti. Intermetallics are often more brittle than conventional structural metals, being somewhere between a ceramic and a conventional structural metal, and on this scale, TiAl is closer to a ceramic than many other intermetallics [120]. This means that it is even more important to detect defects at the earliest stage of development in safety-critical components, presenting an interesting challenge.

2.6 Defect dimensions used on samples

Defects were laser micro-machined to allow small slots to be produced. The laser micromachined slots simulate idealised defects and will be referred to as such in this thesis. There are obvious differences between real and machined defects. It is unusual for real defects or cracks to have a simple geometrical shape [164]. Cracks can several branches and irregular openings [165] as well as interfacial contact within them [166]. The use of machined slots is, however, common practice [165, 166] with

it is still being useful for benchmarking purposes since their dimensions are better controlled and defined.

There were Ti and TiAl slots that were positioned far from the edge of the sample so that the sample edge would have little to no impact on the results. These were measured using an optical microscope (Zeiss Axio Imager). See figures 2.11 and 2.12 for the images taken, which are produced by focusing the microscope on the top surface of the Ti and TiAl samples respectively. The SS sample was too big to fit under the microscope.

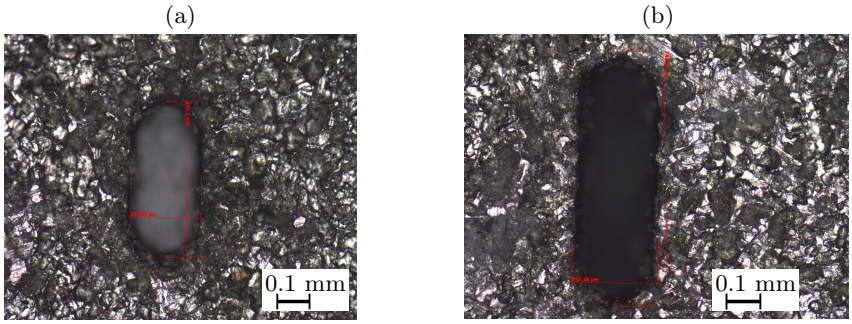

Figure 2.11: Optical microscope image of the surface of the Ti sample. (a) is the region in which the shortest slot (nominally 0.25 mm) is and (b) is the region in which the longest slot (nominally 1 mm) is. The red markings are from when the slot measurements were taken, but there is a scale positioned to the lower right of the slot in each image since the dimensions marked in red are small.

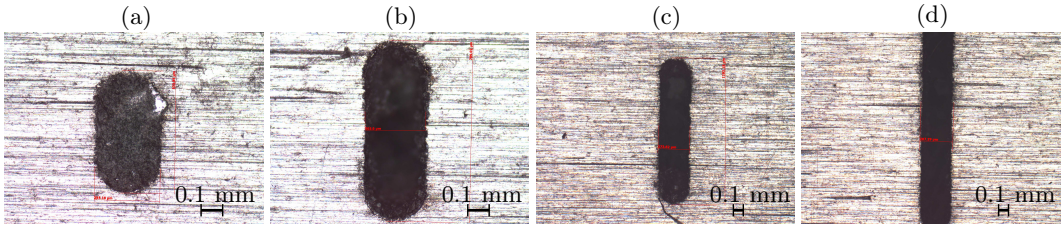

Figure 2.12: Optical microscope image of the surface of the TiAl sample. From (a) to (d) are the regions in which the shortest (nominally 0.25 mm) through to the longest slot (nominally 2 mm) are respectively. For (d), the slot length was too big to both be in focus and to fit on the screen. The red markings are from when the slot measurements were taken, but there is a scale positioned to the lower right of the slot in each image since the dimensions marked in red are small.

It was found that the measured dimensions of the slot at the surface were larger than the nominal ones (see table 2.1), at least at the surface. This was because the kerf was not being appropriately accounted for when the slots were being machined. The laser beam was moved the nominal length, but since the kerf

is 0.25 mm, the outline of the slot from the surface is a locus of 0.125 mm from the laser path, as depicted in figure 2.13. There were difficulties getting light into the crack, which meant that depth could not be measured reliably, and only the opening size of the machined slot could be measured. Regardless, the power of the pulsed laser beam used to do the micro-machining is expected to vary across its cross-section and the slot would not be expected to be cut with a uniform width all the way down.

Sample	**Nominal dimensions (mm)**			**Measured dimensions (mm)**		
	Length	**Width**	**Depth**	**Length**	**Width**	**Depth**
Stainless steel	10	0.1	1.15	*	*	1.15
TiAl	0.25		Half the length	0.55	0.29	***
	0.5			0.79	0.27	
	1			1.28	0.27	
	2			**	0.29	
Ti	0.25			0.46	0.22	
	0.5			0.75	0.25	

Table 2.1: Nominal and measured dimensions of slot on samples tested. The defects were measured at the surface using an optical microscope. * Stainless steel sample was too big to fit under the optical microscope. ** represents a measurement where the slot length was too big to fit for the microscope used. *** represents a depth that could not be measured accurately. The uncertainty in the measured values is 0.05 mm for the optical microscope readings (i.e. all measured values except for the depth of the stainless steel slot depth, which has an uncertainty of 0.1 mm).

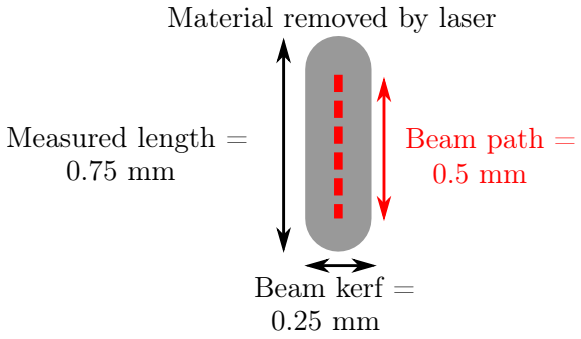

Figure 2.13: Depiction of material removed for a slot with a nominal length of 0.5 mm.

The depth of the SS slot was measured (see figure 2.14) using a piece of metal whose height has been measured with a digital vernier, and a digital vernier placed on a parallel that is on top of two parallels on either side of the slot. The process of measuring the depth starts with zeroing the vernier on the sample surface, the piece of metal of known height is then placed in the slot making sure contact with

the bottom of the slot is made. The depth of the slot can then be found by adding the vernier measurement with the piece of metal in place (the vernier measurement will be negative) from the height of this piece of metal.

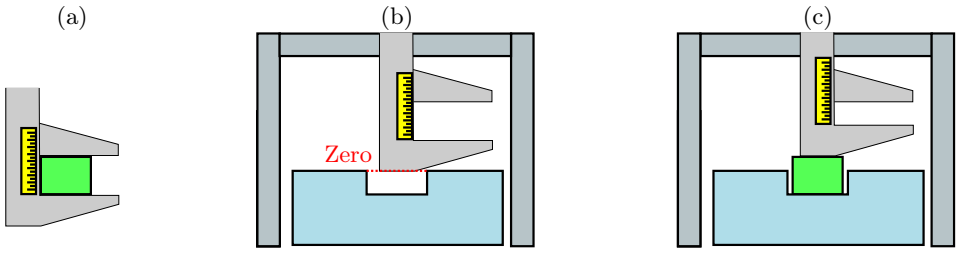

Figure 2.14: Schematic for measuring depth of stainless steel slot.

The measurement of the slots was performed after the simulations and the depth measurement was found to have poor reliability. Consequently, the simulation uses the nominal dimensions that had also been determined from machining calibration cuts at the edges of other samples. This is not a problem for understanding the general behaviour of the eddy current interaction with the defect, as is the purpose in this thesis, but it does mean that nominal dimensions are used for the simulation despite having access to the optically measured results, which is why both dimensions are presented.

The slot machined on the SS sample is relatively large at 10 mm long, but it is consistent with slot sizes that may be of interest in the power generation industry. The slots on the TiAl and Ti samples are much smaller since very small defects need to be detected in aerospace applications. The measured dimensions are larger than the nominal ones, but they still go down to sub-millimetre sizes (0.55 mm and 0.46 mm for TiAl and Ti respectively).

In safety-critical components, there is a requirement to detect surface-breaking defects and fatigue cracks at the earliest stage of growth, with an aspirational target of detecting defects less than 250 µm long. Reasonable detection rates are only seen for defects over a couple of milimeters [167] and thus, 250 µm would represent a very significant improvement on what was currently available. Moreover, as discussed, TiAl has a limitation in that it is relatively brittle [14], meaning that it is even more important to detect defects at the earliest stage of development.

This is of course expected to be difficult, given the lower electrical conductivity of TiAl, which is lower than Ti, a material considered to be a low conductivity material. ECT is very sensitive to small defects and it has certain advantages such as being a non-contact technique, which make it a suitable candidate to find small

defects at an earlier stage. However, its lower conductivity increases the eddy current (EC) electromagnetic skin depth for a given frequency and it means the eddy currents are much smaller in amplitude, making it more difficult to detect surface cracks.

Another observation to note is that in the optical microscope measurements, it can also be seen that the Ti sample has a rougher surface texture than the TiAl sample. This is potentially linked to Ti being much more prone to oxidation. It was observed that the Ti dulls quite quickly on unpacking, and TiAl maintains quite a shiny, flat surface, for longer in air.

Since there are two adjacent coils, the probe is directional, and thus the defect will be considered in two extreme orientations, as portrayed in figure 2.15. These will be called parallel and perpendicular orientations. These are shown from the view of looking down onto the sample's top surface (the surface that the defect is machined onto). There will be a depiction of the scan orientation in the bottom left corner on most figures. This is to remind the reader of the coil positioning relative to the defect. An example of how the depiction will look is in figure 2.15, and these depictions will also be from the view of looking down onto the sample's top surface.

If the probe consisted of just one coil (consider figure 2.15 with just the transmitter coil), the defect response would be expected to be the same when the sample is rotated to change the defect orientation (like in figure 2.15) but with a change in the signal position to reflect change in position of the defect. However, even accounting for the change in position of the defect, the signal will be expected to be difference when considering a probe with two adjacent coils. At least the receiver signal would be affected as the magnetic field from the eddy current would appear to be difference from the receivers perspective for a given transmitter location relative to the defect. This may in turn affect the sensitivity to the defect. Moreover, it is possible that the change in the receiver signal would affect the transmitters signal as they are electrically coupled, but the effect would not be expected to be as strong.

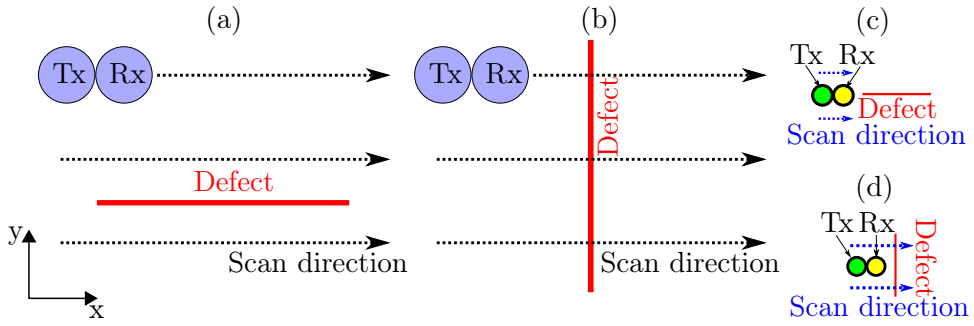

Figure 2.15: Top view of (a) "parallel" and (b) "perpendicular" scanning with respect to a slot on the surface of a sample. The defect is shown in red and the dotted black line represents the direction of scanning. The transmit (Tx) and receive (Rx) probes have the axis perpendicular to the surface. Its circular shape reflects the circular footprint of the probes. Not to scale. (c) and (d) are examples what the depictions look like for the parallel and perpendicular orientations.

Defects can occur in difficult locations such as near edges, and so three slots near the edge of the Ti sample have also been inspected. One slot was placed perpendicular to an edge and was once again a laser machined slot defect. The others were corner defects machined using a small circular abrasive disc of thickness 0.6 mm and were crude in nature. The dimensions are given in table 2.2 and photographs of them are shown in figure 2.16.

Location	**Label**	**Dimensions (mm)**		
		Length	**Width**	**Depth**
Edge	N/A	3	0.5	2
Corner	Notch 1	1	0.8	1
	Notch 2	2		

Table 2.2: Dimensions of edge and corner defects on the Ti sample. The uncertainty in the measured values is 0.1 mm.

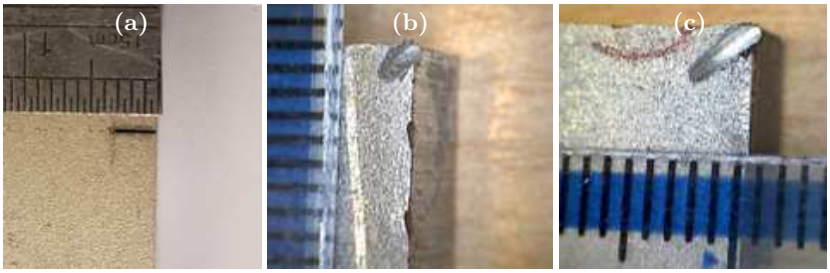

Figure 2.16: Photographs of the edge defects. (a) is the slot defect near the edge, while (b) and (c) are the corner defects labelled notch 1 and notch 2 respectively. They are orientated in a way to aid with comparison with the results.

2.7 Data processing of the signal from the sensor

Data processing was limited to relatively simple approaches. The thesis focuses on improving data collection and the setup where possible. For example, signal background variation was reduced by reducing the tilt of the sample with respect to the probe, rather than background subtraction. This was to avoid getting artefacts in the data due to data processing.

Generally, the only post-processing used after signal averaging was in extracting the magnitude and phase from the signal for the experiments where an oscilloscope is used to directly capture and store the voltage in the coils, after buffering/amplification i.e. where the magnitude/phase is not already extracted by preceding electronics. Only in limited circumstances is more post-processing used, but it will be made clear where this happens. For example, a more complex background subtraction technique is used for just two of the figures, but this is made clear by showing the original data and the background signal to be subtracted in the same figure, and clearly mentioning that background subtraction is applied. This background subtraction still basic whereby a linear fit is applied to the endpoints for each scanning line and subtracted from the original data.

The extraction of the magnitude and phase information from each eddy current coil voltage signal is done by fitting a sinusoidal fit using the "sin1" fit in MATLAB. While the oscilloscope is capable of extracting this data, the MATLAB function was used as the documentation for the function is more accessible.

"sin1" uses the sum of sines model in MATLAB, a model that fits data to the function

$$y = \sum_{i=1}^{n} a_i \sin(b_i x + c_i), \tag{2.6}$$

where a is the amplitude, b is the frequency, and c is the phase. According to the MATLAB documentation that can be found in the software [168], the non-linear least squares method and trust region algorithm is used with the starting points calculated heuristically based on the current data set, and it is constrained so that $b_i > 0$.

The number of terms in the series, n, is set to 1 for the "sin1" fit. Also, the terms x and y in equation 2.6 would be time, t, and voltage, V, for our data. Consequently, the fit used is

$$V = a\sin(bt + c). \tag{2.7}$$

Here, a and c are the values of interest since these are the values used for the magnitude and phase.

To quantify the signal-to-noise ratio (SNR), the following process was performed (see figure 2.17):

1. Select an area away from the defect to represent the background signal, this will be called the "defect-free region". While this is only part of the background signal, it would be expected to be fairly representative of the overall background for the scan of the entire surface, since the sample surface has been processed in the same way.

2. Subtract the mean of the measured value over this "defect-free region" from all the values in the scanned area to produce a background-subtracted data set.

3. Take the noise to be the root mean square of the background-subtracted data in the "defect-free region".

4. Take the signal amplitude to be the average of the largest in magnitude values (i.e. the magnitude of the values with the biggest difference from the background level). Unless otherwise mentioned five values will be averaged to produce a single value for the signal amplitude.

5. The equation
$$\text{SNR} = 20 \log \left(\frac{\text{signal amplitude}}{\text{noise}} \right) \tag{2.8}$$
is used to get the signal-to-noise ratio in decibels.

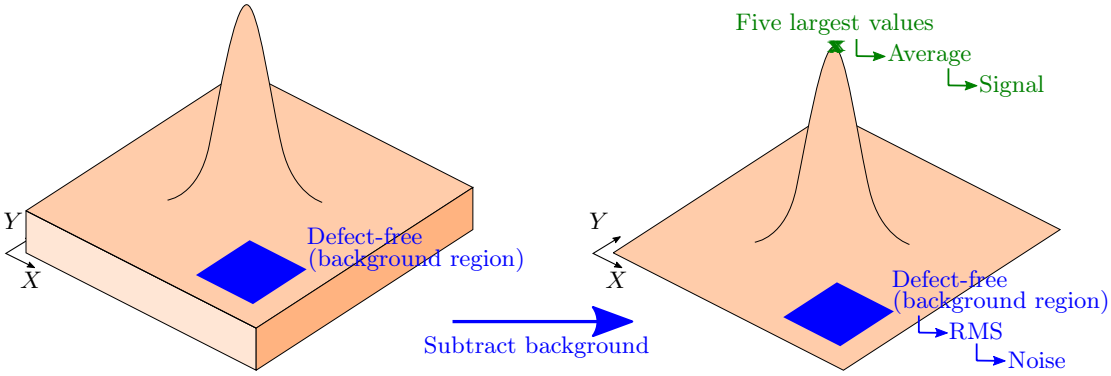

Figure 2.17: Process for extracting signal and noise values to calculate the signal-to-noise ratio.

This is a simple way of calculating the signal-to-noise ratio, but the actual ability to spot the defect is often better than the calculated signal-to-noise ratio would suggest, as it does not take into account the complex ability of humans to

spot patterns and see general changes in morphology, particularly since there are four separate measured parameters that can be taken into consideration. The errors will be calculated using the functional approach [169].

2.8 Simulation methodology

The finite element method (FEM) is used to try to better understand the physics behind the interaction of the eddy current with the defects and coils, and the reason for certain observed behaviours. Simulation of the eddy current probe systems is achieved using the commercial finite element software program COMSOL. The theory behind the model has been summarised in section 1.8. For this thesis, a simplified version of the experimental setup was built. The model has two coils and a sample, which is enclosed in an infinite element domain.

For defects where the edge effect should be negligible, the coils are held stationary, centred on the centre of the sample while a rectangular defect is moved along the sample. Also, $(0, 0)$ mm is the position where the defect's centre and the Tx and Rx coils combined centre coincide. The Tx coil is to the left and the Rx coil to the right. The geometry is shown in figure 2.18. The model geometry is shown for a perpendicular scan, but the geometry is similar for a parallel scan with the defect simply being rotated 90°.

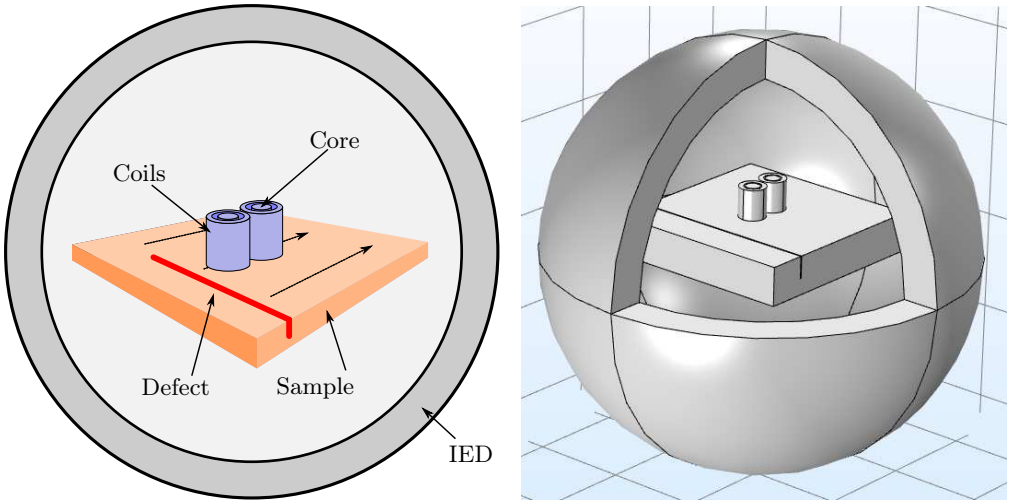

Figure 2.18: Geometry of COMSOL model. Coils are stationary while the defect moves across the sample with the black dotted lines representing the scan direction, which in this case is perpendicular. Model is enclosed in an infinite element domain (IED). (a) shows an artistic depiction of the geometry while (b) shows the geometry implemented in COMSOL.

For the case where a defect is near the edge of the sample, a similar approach is used. In this instance, the rectangular geometry of the defect is attached to another rectangular geometry to represent the area over the sample edge, which are both subtracted from the sample. This forms the geometry shown in figure 2.19. The location $(0, 0)$ mm is where the Tx and Rx coils' combined centre coincides with the edge in the horizontal extent (x-direction) and the centres of the defect in the vertical extent (y-direction). The Rx coil is to the right of the Tx coil. The geometry is shown in figure 2.19.

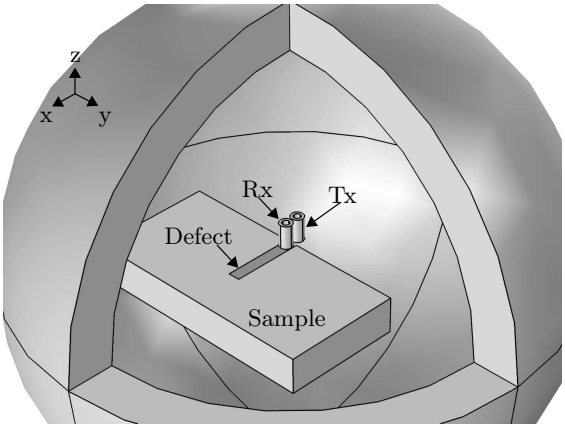

Figure 2.19: Geometry of COMSOL model for edge defect.

The corner defect FE model is similar to the edge defect model, but the cut-out for the area over the sample edge is an L-shaped region (the cut out for the defect is rotated 45° to be attached to the inner corner of the L-shape) as shown in figure 2.20. $(0, 0)$ mm is where the coils combined centre coincides with the corner of the sample. Again, the Rx coil is to the right of the Tx coil as shown in the figure.

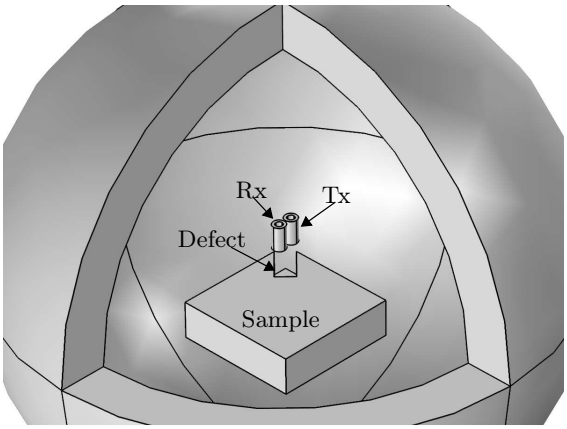

Figure 2.20: Geometry of COMSOL model for corner defect.

The model uses a mixture of the nominal sizes (the coil and defects are based on nominal dimensions) and sensible estimates (the distance between the coils and the lift-off is set to be 0.1 mm for defects where the edge effect should be negligible and 0.05 mm for the edge/corner defects). The stationary location of the coils near the centre of the model's geometry with the defect moving was a conscious choice so that the coil remain the same distance from the boundary of the model. The size of the model's geometry was then chosen based on making it large enough that the values outputted from the simulation (magnitude and phase) were stable. The fast drop off in the magnetic field generated by the coils with distance should mean that the model can be kept to a manageable size. This is important since the computational resources were moderate (16 GB of RAM). With moderate computational resources, a large model geometry would mean the mesh density would need to be lowered or long computational times. Following similar reasoning, the sample dimensions are reduced. The skin depths expected are small (for example, the skin depth is 0.3 mm in Titanium at 1 MHz). Thus, the sample need not be large for the system to be properly modelled. It is more important to ensure the mesh is dense, so that the steep changes in the eddy currents with space are appropriately modelled.

The current used to drive the Tx coils is set to a constant amplitude of 2 mA. The current is set to have no phase shift, such that the value for phase from the model can be thought of as being with respect to the current. As mentioned in section 1.8, a frequency-domain study is performed. In such a study, the frequency is set by the user and all variables that usually vary with time, vary at the chosen frequency.

The current amplitude is from the measured value (see section 2.2). While the setup used to measure current is sufficient to approximate the current amplitude within an order of magnitude, there will be some uncertainty in the precise value. These uncertainties are caused by, for example, the voltages from the op-amps being only subtracted after traversing through the leads instead of using a differential op-amp to subtract the voltages on-board the circuit board. The extra components needed for an accurate measurement would not help with defect detection. After all, what matters is that the current is constant not that it is a particular value. The extra components do, however, adds capacitance, which is known to negatively affect the operation of the sensor.

This means steps such as continuously measuring current so that the effect on the system is consistent, and adding additional components were not taken. The voltage should be proportional to the current in any case, and also the receiver voltage is not amplified in the simulation as is the case in the experiment. As such,

the general behaviour should be similar, although some scaling may be needed.

The main material properties that would be expected to affect the measurements are its electrical conductivity and magnetic permeability [158]. Ti has an electrical conductivity of $2.38 \times 10^6\,\mathrm{S\,m^{-1}}$ [117] as mentioned in section 1.4 and SS 316L has an electrical conductivity of $1.35 \times 10^6\,\mathrm{S\,m^{-1}}$ (derived from a resistivity of $74 \times 10^{-8}\,\Omega\,\mathrm{m}$ [170]). As non-magnetic materials, their relative permeabilities were taken to be 1 (the relative permeability of Ti and 316L are 1.00005 [171] and $1.0-1.3$ respectively [172]).

These material properties are reflected in the model. However, more complex material features are not. For example, the model assumes the material is isotropic and homogeneous, when in fact, titanium and most common alloys suffer from grain noise and have some degree of elastic and electrical anisotropy. As a hexagonal crystal, the axial symmetry around the principal direction allows for the electrical conductivity to be directional, converse to cubic structures, where the electrical resistivity is fully isotropic in a single crystal [173]. In titanium, $\sigma_\perp = 2.08 \times 10^6\,\mathrm{S\,m^{-1}}$ and $\sigma_\parallel = 2.21 \times 10^6\,\mathrm{S\,m^{-1}}$ (derived from $\rho_\perp = 48 \times 10^{-8}\,\Omega\,\mathrm{m}$ and $\rho_\parallel = 45.35 \times 10^{-8}\,\Omega\,\mathrm{m}$ [173]).

This grain noise is a well-known issue. There is a tendency for grains to have anisotropic morphologies, which can lead to differences in grain boundary density in different directions. The resulting variations in the local conductivity within the material causes electrical scatter and increases the noise, which is detrimental to defect detection [173]. The approximations used in the model mean that the results are not expected to be exactly the same as experimental data, but it is used to help understand the physics involved.

The model was automatically meshed using COMSOL's physics controlled mesh and the choice of solver was left to COMSOL. For 2D scans and lift-off measurements, measurements are taken at intervals that match the experiment (i.e. with a scanning step/interval of 0.1 mm). This means multiple simulations are needed for each data set. Thus, care must be taken with the mesh density so that it is sufficiently high to ensure stable results, but not so dense that the simulation would take too much time and computational resources.

The results extracted from the model were the voltage signal from both coils, and checks were done to ensure that the mesh had a suitable mesh density. As validation, the results were checked to make sure they converged numerically at certain coordinates (see figure 2.21). The purpose of the simulation results was to understand behaviour in the experimental measurements. Thus, it was sufficient for the behaviour of the experimental and simulation results to be just similar provided

the differences could be understood. It was a tool to understand the experimental results rather than being the focus of the thesis.

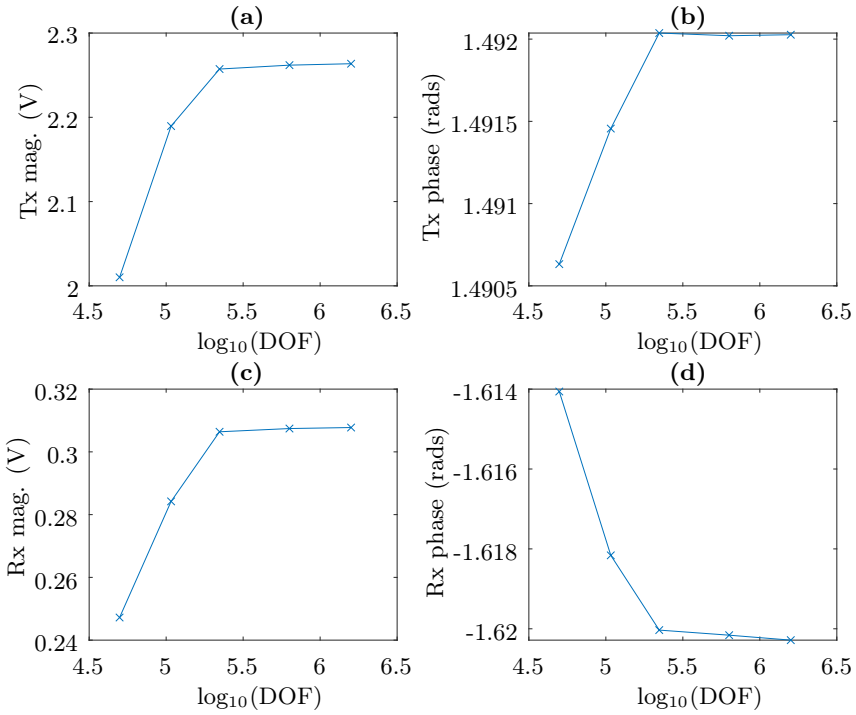

Figure 2.21: Convergence of parameters in stainless steel model. Mesh refinement using different settings: coarse, normal, fine, finer, extra fine. Plotted is the logarithm (base 10) of the degrees of freedom vs the value for each measured parameter.

The gains with increasing mesh density are diminishing so it makes sense to choose a mesh that balances the requirement for stability and the computational resources needed. Accordingly, the second finest mesh in figure 2.21 (i.e. $\log_{10}(\text{DOF}) \approx 5.8$) was chosen. With this mesh density, the returns had greatly diminished with the output values plateauing, but the time taken remained reasonable.

The time taken for a simulation with this mesh density is around 1 minutes 30 seconds for each defect location. Whereas, the highest mesh density ($\log_{10}(\text{DOF}) \approx 6.2$) took around 18 minutes for each defect location. This adds up. For example, to cover a 10 square millimetre area with an interval of 0.1 mm, 10000 simulations would need to be run. This translates to 9 days for the second finest mesh and 125 days for the finest mesh. The time could, however, be hugely reduced with enough computational resource. Since the simulations at different locations are separate, it would be possible to run the simulations in parallel.

COMSOL by default ensures that the result meets a convergence threshold of better than 1% i.e. where the estimated error between the current solution and exact solution is below the defined tolerance (relative tolerance was kept at the default of 0.001). Results below this threshold are disregarded. The final estimated error of the accepted points is often below the tolerance (see figure 2.22). Each simulation took approximately 2.8 iterations with an average final error of 1.2×10^{-4} for the scan on Titanium.

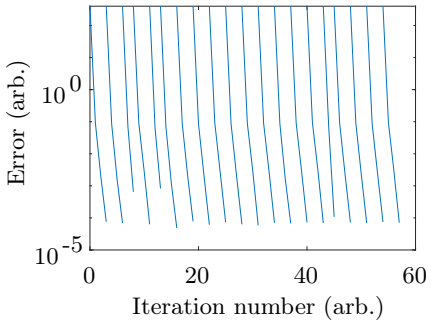

Figure 2.22: Convergence plot for BiCGStab. 20 simulations are shown for a scan of the Ti sample's surface.

Chapter 3

Developing the Sensor system

3.1 Phase difference and signal amplitude measurements with the AD9850 module

3.1.1 Experimental setup for testing probe by performing 2D scans

Chapter 2 outlines the general setup used to test the probe designed throughout this thesis. The initial design of our probe with the setup used to test it is depicted in figure 3.1. This configuration uses the sinusoidal output of a signal generator module (AD9850) as the reference signal for the aforementioned HCS. The module is inexpensive and its small size of approximately $4.5\,\text{cm} \times 2.6\,\text{cm} \times 1.7\,\text{cm}$ makes it extremely portable. The frequency was tuned using an Arduino nano board, and according to the datasheet, it should be capable of generating waveforms up to 40 MHz [174]. The electronics in the dotted box shown in figure 3.1 are mounted directly behind the coils, and the arrows indicate connected electronics that are further away. The voltage across each coil is measured using an oscilloscope (DPO3034), from which both magnitude and phase data are simultaneously extracted. The receiver (Rx) coil voltage is measured after (10×) amplification. The oscilloscope is triggered on the output from the signal generator module.

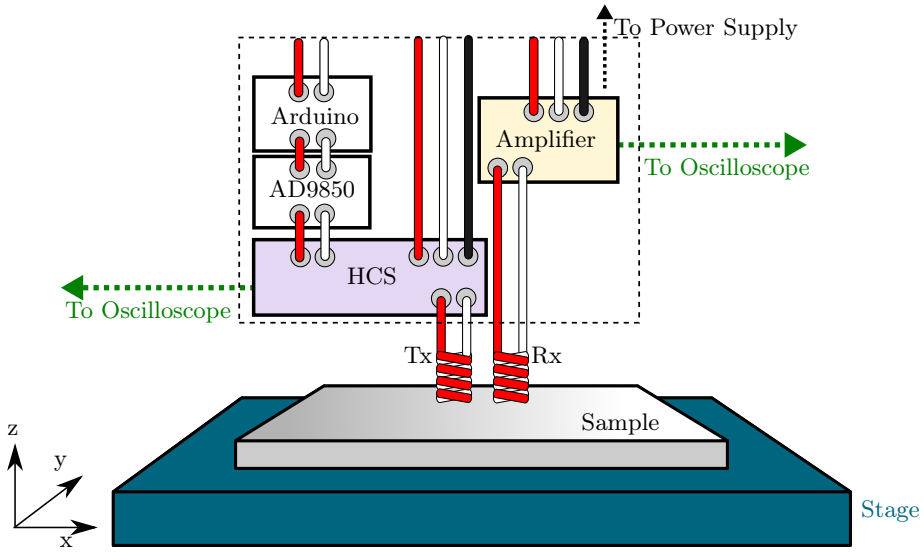

Figure 3.1: Setup using AD9850 module. The part within the dotted box is directly behind the coils. Not to scale - coils are much smaller compared to the rest of the components shown and are in close proximity to each other. The XY stage used is the K8200.

The probe was tested by performing 2D scans over the largest defect that will be studied in this thesis (the slot of length 10 mm, width 60 µm and depth 1.15 mm on the austenitic SS 316L sheet of 2.16(2) mm thickness) since its relatively large size should mean that it is the easiest defect to detect.

3.2 Experimental results from testing probe

A 2D scan over the slot on the the SS sample is shown in figure 3.2. The process established in section 2.7 for calculating SNR was used with the background region being defined to be $[\mathrm{x}, \mathrm{y}, \mathrm{width}, \mathrm{height}] = [1, 1, 5, 5]$ mm i.e. a rectangle with a width and height of 5 mm and its lower left corner located at $(1, 1)$ mm. This yielded an SNR of 15.8(3) dB for Rx mag. For the other parameters, the five values with the biggest difference from the background level were not on the slot due to the data sporadically spiking, and thus are not expected to produce valid results.

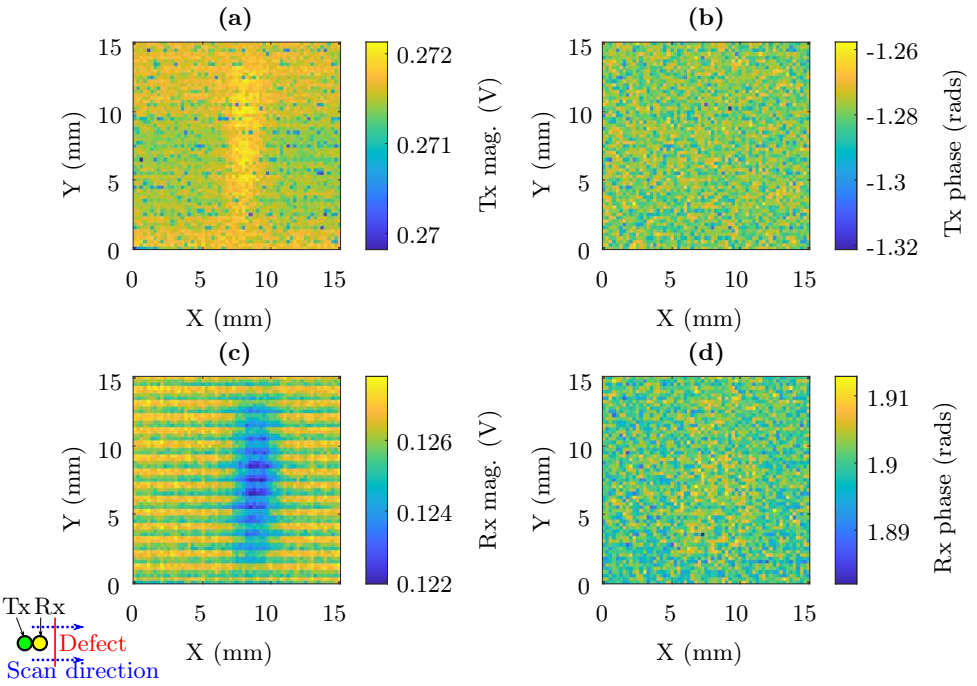

Figure 3.2: Experimental data on stainless steel (316L) of thickness 2.16(2)mm with a single 10 mm long, 60 µm and 1.15 mm deep slot running vertically, taken using signal generator module (AD9850) at 1 MHz. The orientation of the coils is "perpendicular" to the slot (as depicted in the bottom left corner). (a) and (b) are magnitude and phase of the voltage measured on the transmitter coil while (c) and (d) are magnitude and phase of the voltage measured on the receiver coil.

The reliability of this simplistic approach can be improved by using a 2D median filter (the default "medfilt2" function in MATLAB is used, which uses a 3-by-3 neighbourhood), resulting in SNR values of 15.7(3) dB and 19.294(1) dB for Tx mag. and Rx mag. In figure 3.4, it can be seen that the scans do not give a clear indication of a defect around the location where the defect exists for the phase measurements, but they do for the magnitude results. From this, it can be said that using this setup, it is possible to detect the slot in the Tx mag. and Rx mag.

The simulated counterpart is shown in figure 3.3. Since the Tx coil is slightly to the left of the origin, the transmitter signals are also slightly to the left, but it is interesting to note that the receiver signals tends to be centred about the origin, which is where the centre of the two coils and the slot coincide (the Tx coil is to the left and the Rx coil is to the right of the origin). It may be the case that the origin is a compromise between both the Tx coils being around the slot to produce a change in the eddy current and the Rx coil being close enough to see this.

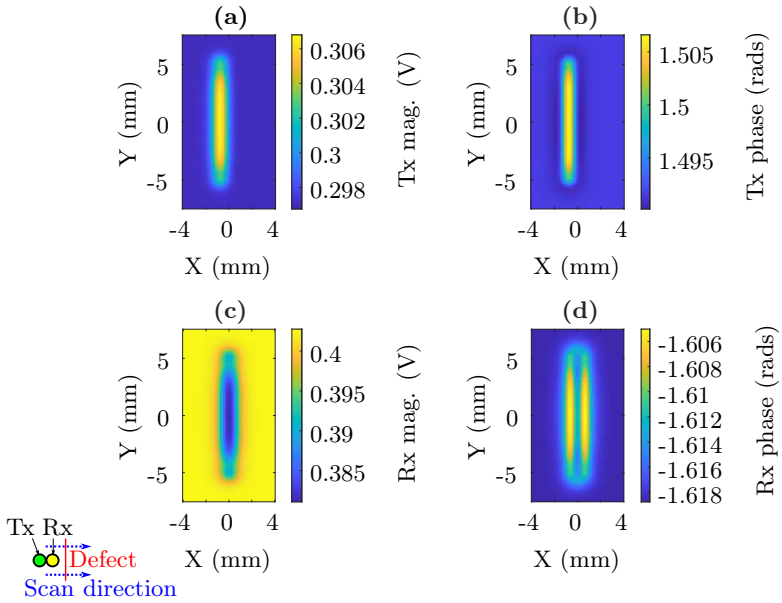

Figure 3.3: Simulation of a slot in a perpendicular orientation (as depicted in the bottom left corner) on stainless steel at 1 MHz. Grouped in columns by frequency and row by measured parameters. Rx mag. values have been multiplied by ten to reflect the amplification of the Rx signal.

In the simulation, the main response to a slot in the Tx mag. is to increase. The Tx mag. measurement increases when the Tx coil is on the slot, although the signal steps down near the ends of the slot. The increase in the Tx mag. measurement is due to the slot disrupting the eddy current, which causes the eddy current to take a longer path around the slot. Consequently, the eddy current is generally weaker and so is the secondary magnetic field [108]. This results in a higher impedance over the slot [175]. The central part of the defect signal is when both coils are on the slot and the steps either side of the slot is due to the slot only partially intersecting the coil as explained in Uchanin (2007) [175]. The eddy currents mainly follow the coil wires. Thus, as the coil intersects the slot, there is a period where the slot is intersecting one side of the eddy current loop but not the other resulting in the steps. The Tx phase follows a similar behaviour to the Tx mag.

Also in the simulation, the Rx mag. dips in response to a slot when the slot is between the two coils. This can be explained by the slot blocking the eddy current. In the Tx coil, the eddy current opposes the current in the coil, but in the Rx coil, the generation of current in the coil comes from the eddy current so blocking of the eddy current results in a reduction of the signal. The Rx phase measurement is more interesting yet, where the defect response is almost more like a raised outline of the slot. The Rx signal arises from how the magnetic field from the Tx coil and from

the eddy current interact, which means that an understanding and explanation of the phase change is more complex. Not only is there a combined effect from the magnetic fields but the eddy current caused by the Tx coil also affects the Tx coil itself, thus creating a feedback loop. This made trying to model each contribution in isolation difficult.

It can be seen that for Tx mag. and Rx mag., the overall response from experiment is in line with the COMSOL simulation results, whereby the Tx mag. value increases in response to the slot and the Rx mag. falls. There, however, appear to be horizontal ridges in the Rx mag. scan data, that are not present in the simulation results, along with some general noise.

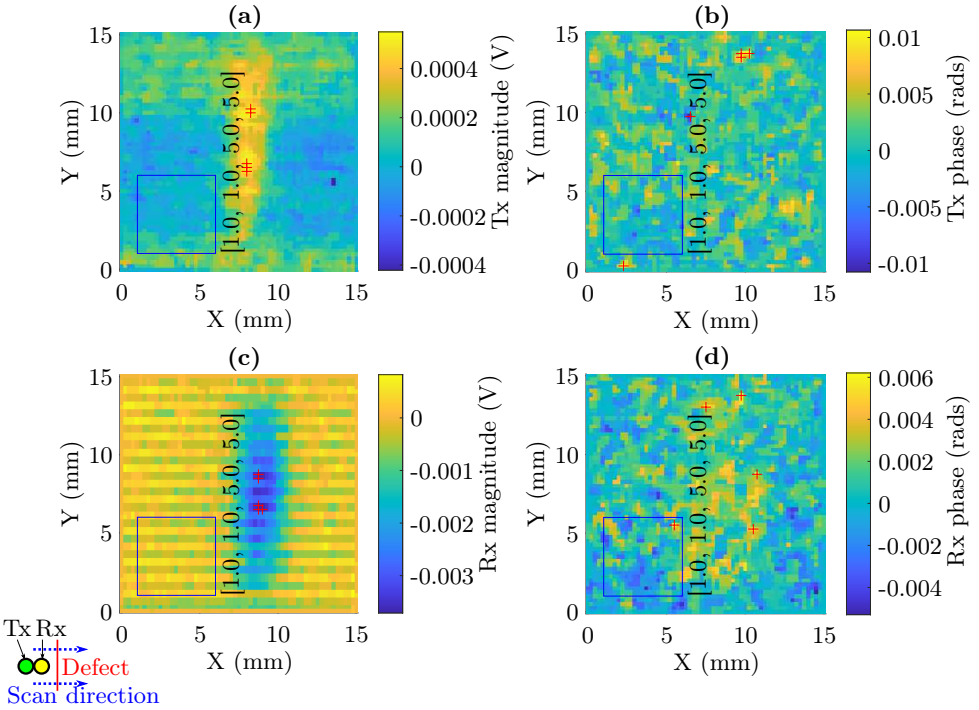

Figure 3.4: Median filtered result for a slot in the perpendicular orientation (as depicted in the bottom left corner) at 1 MHz. The signal-to-noise ratio is determined by selecting an area off the slot (blue) and subtracting the average of this area from the plot followed by taking the noise to be the RMS value of the data in this region and the signal to be the average of the five largest in magnitude points (red crosses).

The slot in the scan is large and yet the SNR values calculated are not particularly high, while the phase measurements cannot be realistically used due to the difficultly in distinguishing any defect signal. This problem was only likely to get worse with increasing frequency, but to confirm this, some measurements were taken at higher frequencies. At 10 MHz, the signal seemed unstable on the oscilloscope

but it was possible to get some results, which are plotted in figure 3.5. It seems that despite the optimum frequency being calculated to be around 10 MHz from the skin depth formula in section 1.4, the electronics used result in an unstable signal (the signal is located at spikes in the scan even with 2D median filtering). When increasing the frequency to 20 MHz, the signal from the module was too unstable to reliably trigger from.

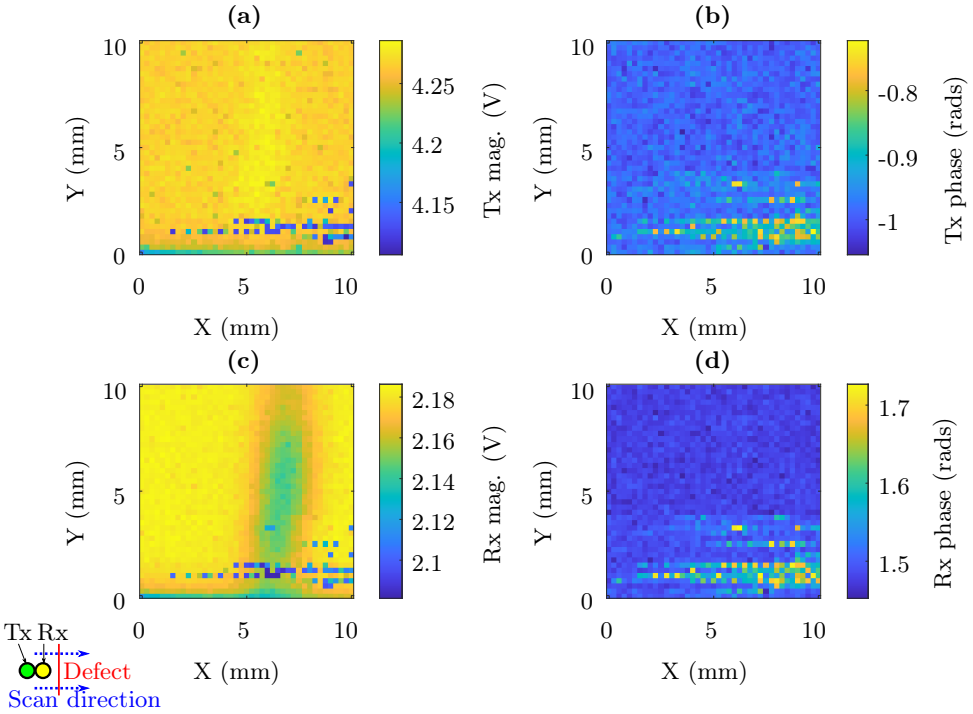

Figure 3.5: Experimental data on stainless steel (316L) of thickness 2.16(2)mm with a single 10 mm long, 60 µm and 1.15 mm deep slot running vertically, taken using signal generator module (AD9850) at 10 MHz. The orientation of the coils is "perpendicular" to the slot (as depicted in the bottom left corner). (a) and (b) are magnitude and phase of the voltage measured on the transmitter coil while (c) and (d) are magnitude and phase of the voltage measured on the receiver coil.

Modifications were made to the probe instead of continuing to the much smaller slots on TiAl and Ti, as they would likely be very difficult to see given the current issues.

3.2.1 Summary of experimental results from testing probe

It was observed that it was possible to detect the slot in the Tx and Rx mag. scan data whose overall response of increasing/decreasing in response to the slot was as expected from the COMSOL simulation results. However, the SNR was

low and phase measurements cannot be realistically used due to the difficultly of distinguishing any defect signal. Modifications were made to the probe design in response (section 3.5), but in the next section (section 3.3), a prototype sensor from EddySense Ltd was tested. The probe is limited to measuring just Rx mag. signals, while the aim of this thesis is to measure mag. and phase for both the Tx and Rx coils, but it serves as a means of benchmarking and testing how the system used by EddySense would compare to the probe designed in this thesis.

3.3 Evaluation of a prototype ECT sensor head from EddySense

3.3.1 Experimental setup for testing probe by performing line and 2D scans

Given the problems experienced in getting a high SNR on the SS slot with the initial iteration of our probe, shown in the previous section (section 3.2), a prototype produced by EddySense was tested. Eddysense is a spin-off company from Warwick University, which produces high-frequency eddy current technology.

The coils used are made to the same specification as the coils used previously, though are not the same coils. The system works using similar principles to our system, but there are some differences in the implementation. The EddySense electronics use the same design of HCS to drive the generation coil, and a similar design of amplifier to amplify the voltage from the Rx coil. However, in the Eddysense sensor, this amplified Rx coil voltage is rectified using a precision rectifier, then integrated using an integrator with a time constant of several microseconds. A microcontroller with a maximum sampling rate of 125 kHz is used to convert the output of the integrator to a digital value that can be stored in memory or transmitted to another device. Only the Rx mag. is measured and recorded. This value of Rx mag. is read by a computer via a USB cable in the setup that was used to test the sensor, which is depicted in figure 3.6.

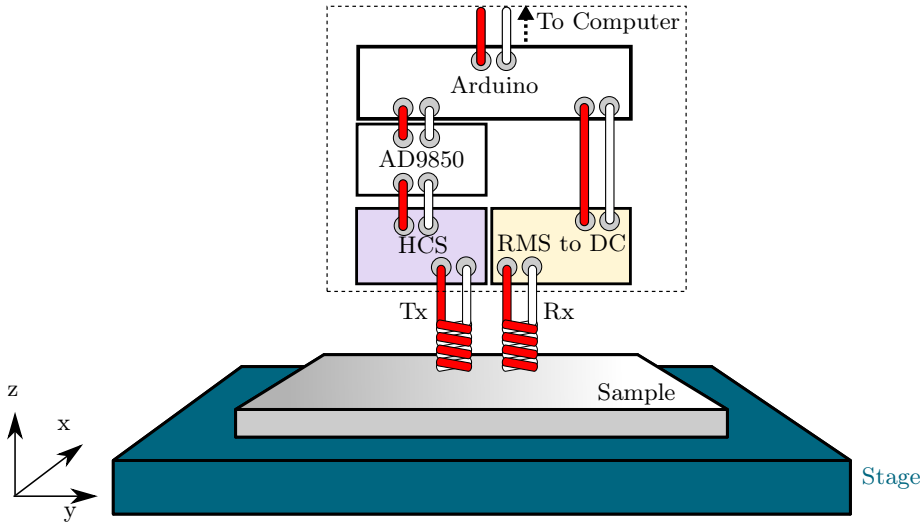

Figure 3.6: EddySense setup. The part within the dotted box is directly behind the coils on a single printed circuit board. Not to scale - coils are much smaller compared to the rest of the components shown and are in close proximity to each other.

The value returned by the microcontroller is an integer value between 0 and 1023, corresponding to a voltage of 0 V to 1 V. There are adjustable potentiometer offsets, which can be used to bias the output of the microcontroller to be midway in its output range when on a defect-free region of the sample. The lack of phase information or measurements from the Tx coils is an immediately obvious trade-off, but the system is capable of a good signal-to-noise ratio performance on the Rx mag. measurement at high frequencies up to 40 MHz.

In the EddySense system, almost all the electronics are integrated onto a single printed circuit board (PCB) that has a design optimised to reduce noise picked up and feedback at radio frequencies; not only is the electrical system, including the whole measurement system, located behind the coils as shown in figure 3.7, but they are carefully laid out to fit on a single board. The AD9850 chip is soldered to the same circuit as all the other components, and the chip is connected via conductive tracks to other components instead of wires. This reduces stray capacitance and inductance that would come from connecting wires/cables. Also, by using a PCB, smaller surface mounted components can be used and electrical components can be organised to reduce path lengths. Additionally, the USB cable used to read the Rx mag. is used to power the circuit, which runs on 5 V.

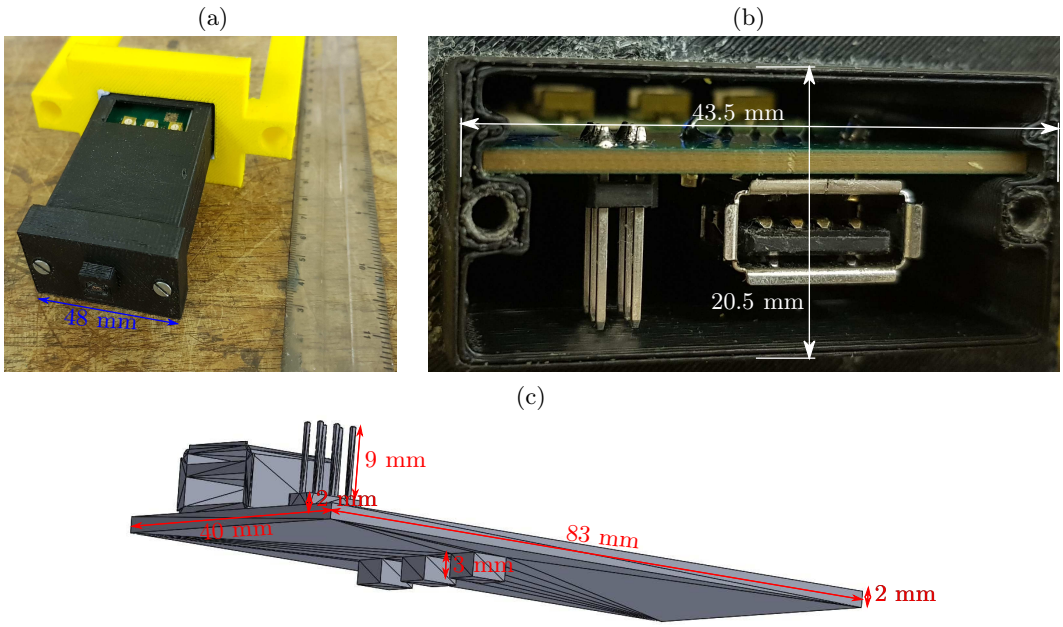

Figure 3.7: (a) and (b) are images of the EddySense integrated circuit board enclosed in a 3D printed holder. There is a ruler for reference in (a). (c) is an image of a computer-aided design (CAD) model that shows the geometry of the printed circuit board. The overall dimensions are 83 mm × 40 mm × 16 mm).

3.4 Experimental results from testing probe

Line scans were taken that cut across the slot's width in the parallel orientation on the SS sample. As mentioned, the slot is a 10 mm long, 60 µm and 1.15 mm deep slot (see table 2.1). The results were taken using coils made to the same specification as before. These coils had an inductance of 19.82 µΩ as seen in subsection 2.4.3.

The initial result is in figure 3.8. There is no result for 1 MHz as the purpose was initially to see the the system could work at higher frequencies first. The behaviour appears to be noisy in the figure. There was a moderate of averaging with the number of averages being set to ten, but the problem seemed to transcend the issue of simply how much averaging there was, especially given the size of the slot. While it appears that there is a transition in the defect response as the frequency increases, which may be due to the coil resonance as the the impedance peaks of the original coils were 15 MHz and 20 MHz (see subsection 2.4.3), even the behaviour at lower frequencies is not ideal. Combined with the recommendation that air-cored coils should be used by someone involved in making the EddySense system, experimentation using ferrite-cored coils ended prematurely.

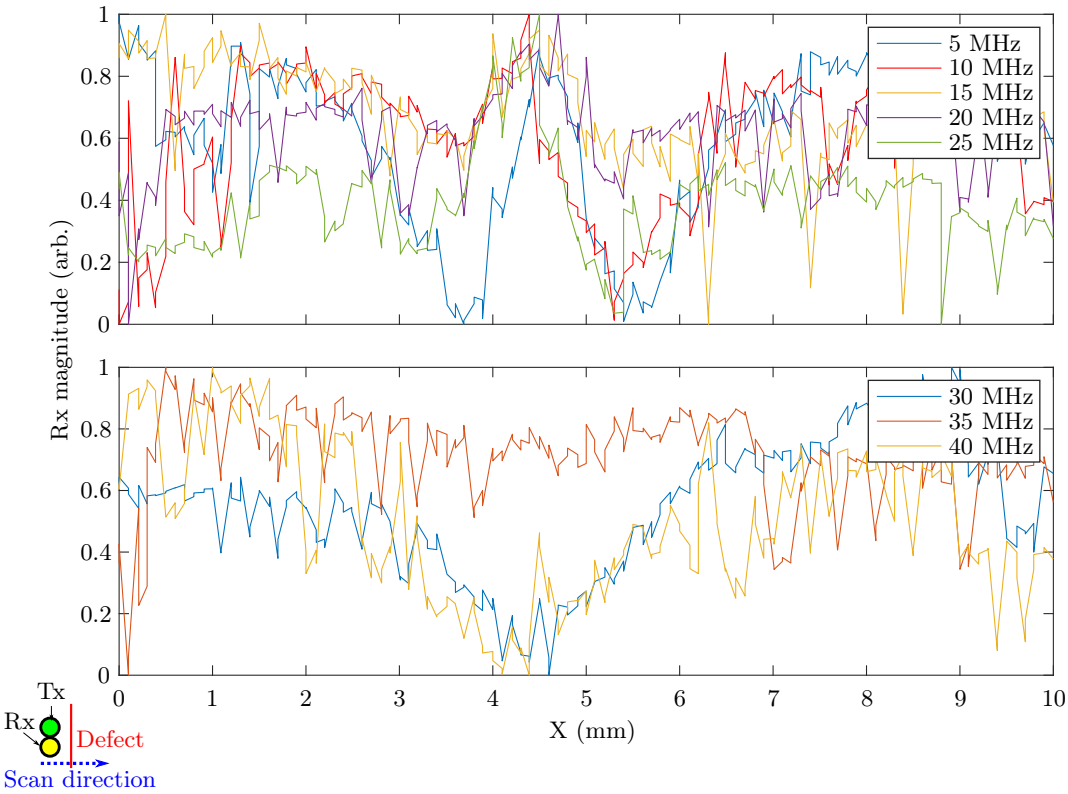

Figure 3.8: Normalised line scans along perpendicular bisector of slot in parallel orientation (as depicted in the bottom left corner) on stainless steel using the EddySense probe with ferrite-cored coils. Each line is taken at a different frequency as given by the legend.

Following the recommendation, coils to the same specification as before but without a ferrite core were used. These coils will only be used in this section and as such, the impedance analyser results for these coils are shown here in figure 3.9. The calculated inductance using from these results is approximately 4.7 µΩ and it can be seen that the resonance is much higher at about 50 MHz, which should help with reaching higher frequencies.

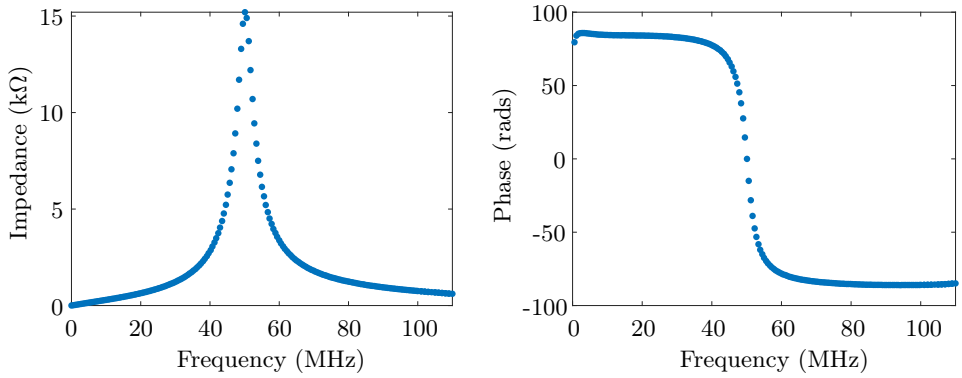

Figure 3.9: Impedance analyser results for air-cored coils.

Using the air-cored coils results in figure 3.10. There is a much stronger signal up to 20 MHz, which is quantified in figure 3.11. The signal quickly drops off at 20 MHz and beyond this there is no discernible defect signal, nevertheless this is an improvement upon using the ferrite-cored coils with the EddySense probe.

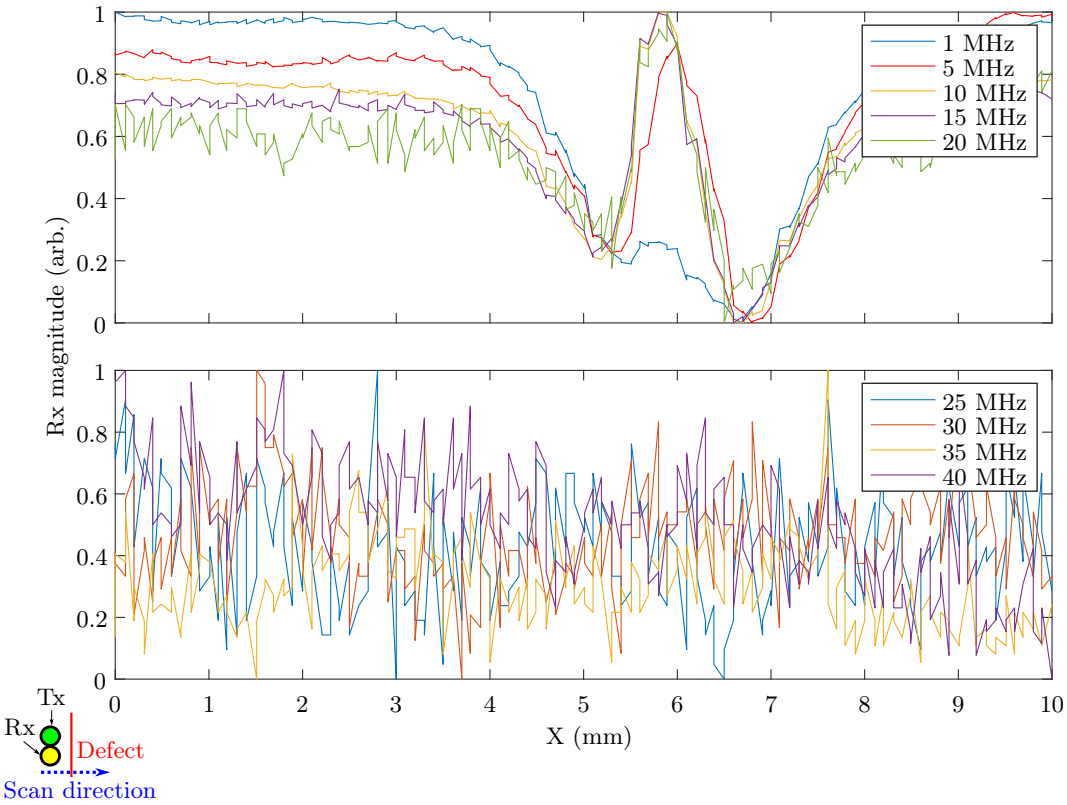

Figure 3.10: Normalised line scans along perpendicular bisector of slot in parallel orientation (as depicted in the bottom left corner) on stainless steel using the EddySense probe with air-cored coils. Each line is taken at a different frequency given by the legend.

Because of the signal's profile, it makes sense to take the signal to be the height of the defect signal. Figure 3.11 shows the signal-to-noise calculated based on the method established in section 2.7 along with the signal-to-noise based on taking the signal to be the height of the defect signal (the difference between the mean of the five largest and the mean of the five smallest values), but otherwise following the same method of calculating signal-to-noise that has been established. The background region is defined to be between $X = 0\,\text{mm}$ and $3\,\text{mm}$.

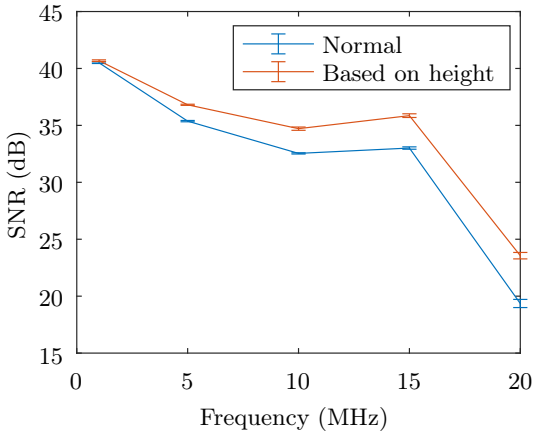

Figure 3.11: Calculated signal-to-noise ratios (SNR) based on the normal approach and the approach using the height of the defect signal.

Based on these SNRs (figure 3.11), it was decided that 2D scans at 1 MHz and 15 MHz would be taken. Its possible to see that there was significant lift-off variation across the scans. Nevertheless, the defect signal can be seen and this can be largely corrected for using background subtraction. The 2D scans are shown in figure 3.12. In the figure, the slots are again parallel in orientation with respect to the coils, but we have changed over to the TiAl sample. For these scans, TiAl sample was orientated so that the slots increase in size going from the bottom to the top of the plot, and the steps taken to subtract the background are shown in the figure.

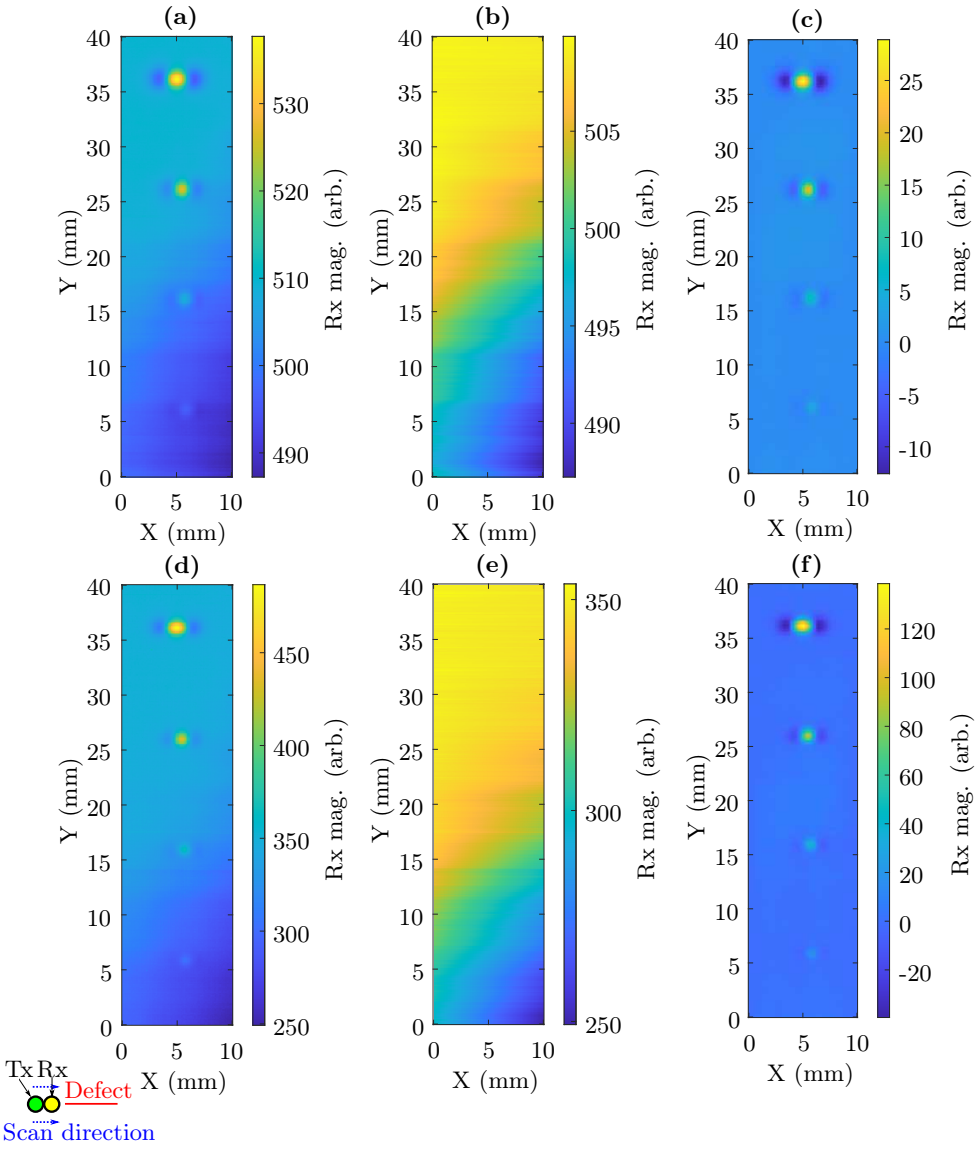

Figure 3.12: Experimental data taken at 1 MHz and 15 MHz using the EddySense probe with air-cored coils on TiAl with the slots in the parallel orientation (as depicted in the bottom left corner). (a)-(c) is the data for 1 MHz while (d)-(f) is the data for 15 MHz. (a) and (d) are the original data, (b) and (e) are the calculated background based on a linear fit between the endpoints for each scanning line, and (c) and (f) are the results after subtraction.

The ridges in the Rx mag. that were present in previous 2D scan data (section 3.2) are not present in the 2D scans here (figure 3.12), suggesting that the ridges were due to the construction of the coils and/or housing of them in the coil holder, rather than the coil specifications themselves. There is, however, significant lift-off variation in these scans. This is likely not helped by the small footprint of

the probe head, but the variation seems to be due to misalignment of the line scans that make up the 2D scan (2D scans are essentially composed of multiple line scans along the x-direction). Drawing a line from the first to the last point in each line and subtracting this from the scan results in a much more level plot. This is a very crude way of dealing with the issue, but it works well because the sample is fairly flat and homogenous, and thus the background signal should not vary significantly. This background-subtracted plot was used in trying to determine the SNR for each slot.

Following this, the process established in section 2.7 was used to calculate the SNR, where the background region is defined to be at $[\mathrm{x}, \mathrm{y}, \mathrm{width}, \mathrm{height}] = [2, 8, 5, 5]$ mm. Since there are multiple slots, the search area is restricted to the quartile of the scan containing the each slot for each SNR. The SNRs are shown in figure 3.13. The high SNR values indicates that the defect signal is clear to see.

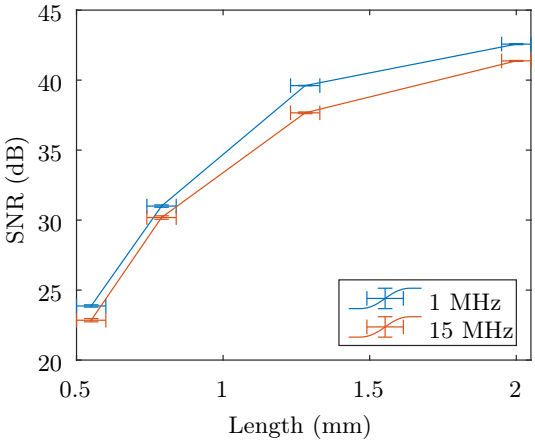

Figure 3.13: Signal-to-noise ratio for TiAl slots in parallel orientation for EddySense probe based on background subtracted data.

3.4.1 Summary of experimental results from testing probe

The purpose of performing these tests was to investigate what level of SNR performance was possible on the Rx mag. measurements when using a circuit designed specifically for low noise at MHz frequencies. The circuit used the same driver and amplifier electronics, and so gives a benchmark of the SNR that could be achieved. The EddySense probe produces some good results for the measurement of Rx mag. with high signal-to-noise ratios that go up to 42.57(4) dB, which is achieved on the largest slot (nominally 2 mm) on the TiAl sample at 1 MHz though the smallest slot (measured to be 0.55(5) mm long) on TiAl can be seen with an SNR of 23.86(8) dB.

Moreover, the system seems to work well up to 20 MHz, where the SNR for the line scan on SS using the air-cored coils is 19.4(4) dB.

3.5 Eddy current sensor measurements using benchtop laboratory equipment

3.5.1 Experimental setup for testing probe by performing 2D scans

A significant contributor to the low SNR in the magnitude and phase data was found to be due to the signal driving the HCS. Because of this, the AD9850 module used in section 3.2 was replaced with the Tektronics AFG3052C function generator as shown in figure 3.14. The function generator has a higher specification and would, accordingly, be expected to produce a more stable signal. The function generator, for example, has a frequency resolution of 1 µHz [176] compared to 0.0291 Hz [174] for the AD9850 module. Additionally, the function generates a 5 V square wave, which provides a sharp edge to trigger from. This will be used as the trigger for the oscilloscope instead of triggering on the reference signal for the HCS to improve the stability of the signal further.

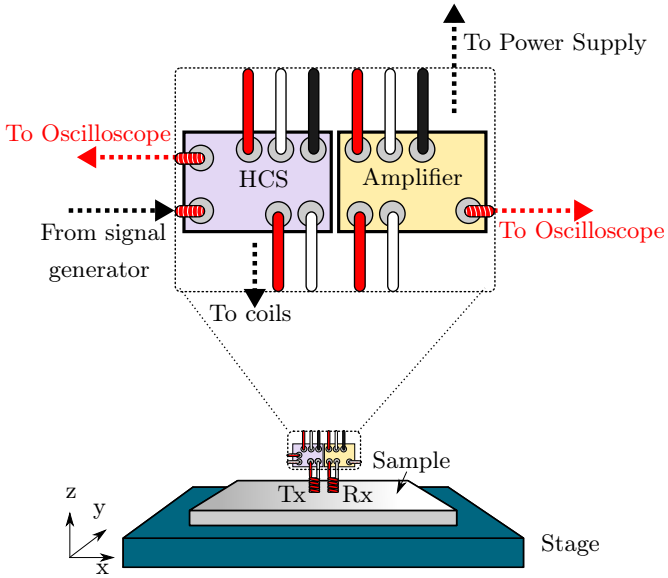

Figure 3.14: Setup with function generator. The part within the dotted box is directly behind the coils. Not to scale - coils are much smaller compared to the rest of the components shown and are in close proximity to each other.

To check the signal quality from the AD9850 module and AFG3052C, the signal was tested using an MDO4054C oscilloscope. This oscilloscope has a sampling

frequency of 2.5 GHz and sampling depth of 8 bits. Waveforms at frequencies from 1 MHz to 20 MHz in 1 MHz intervals were taken to compare the two methods of signal generation. Each waveform was generated from 128 averages. These waveforms were then frequency transformed to analyse their frequency content. From the Fast Fourier transforms (FFT), the peak frequencies were found to align with the expected value to a precision of 25 kHz. Furthermore, to quantify the signal-to-noise, the peak value in the FFT was divided by the sum of the values at all other frequencies resulting in figure 3.15. This uses the full FFT range up to 1.25 GHz. From this, the function generator was found to have a higher SNR compared to the AD9850 module.

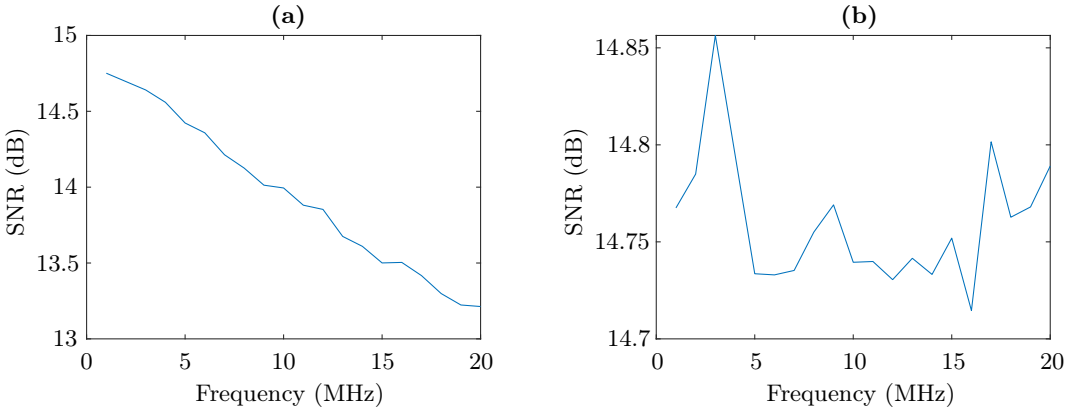

Figure 3.15: Signal-to-noise ratio (SNR) generated using the FFT of the signal, where the FFT goes up to a frequency of 1.25 GHz. In the SNR calculation, the signal amplitude is taken to be the maximum value in the FFT and the noise to be the sum of all values in the FFT. To get the SNR in decibel the formula $\text{SNR} = 20\log(\text{signal amplitude}/\text{noise})$ is used. (a) is the signal from the AD9850 module and (b) is the signal from a function generator (Tektronics AFG3052C).

This is by no means a comprehensive study of the signal quality. Regardless, it would be difficult to tell how much using the function generator would help without using it in its intended application.

3.5.2 Results on stainless steel sample

Going back to testing the system with the new function generator (Tektronics AFG3052C), a 2D scan on SS is shown in figure 3.16. The scan uses new coils made to the same specification as the previous ferrite-cored coils. The defect signal is much clearer in the scans, and it is possible to see the defect in all the measured parameters, including in the phase, which has so far been difficult to do. The calculated SNRs (using the established method in section 2.7) are 21.60(2) dB, 20.0(2) dB,

28.90(2) dB and 16.6743(1) dB for Tx mag., Tx phase, Rx mag. and Rx phase respectively (the background region is set to [x, y, width, height] = [0, 5, 3, 3] mm).

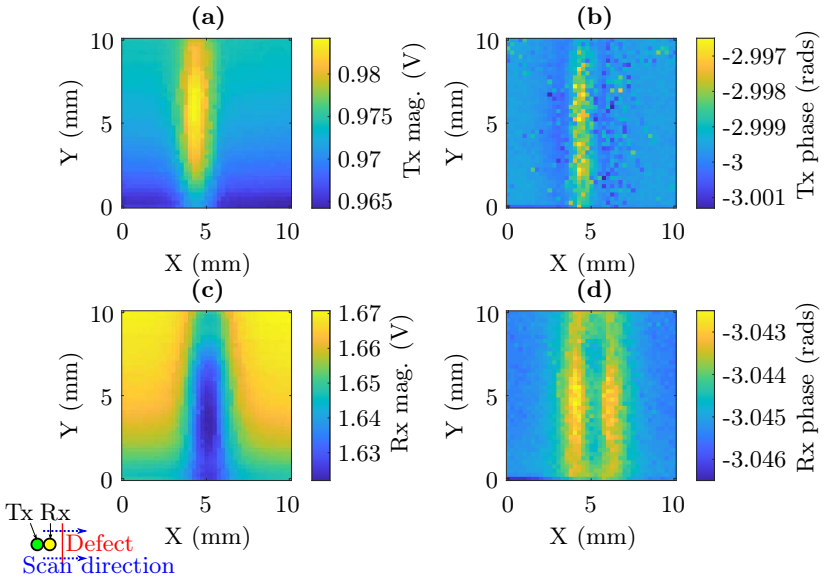

Figure 3.16: Experimental data taken at 1 MHz on stainless steel (316L) sample. The orientation of the coils is "perpendicular" to the slot (as depicted in the bottom left corner). (a) and (b) are magnitude and phase of the transmitter while (c) and (d) are magnitude and phase of the receiver.

As a precursor to performing 2D scans at higher frequencies, a number of line scans were taken resulting in figure 3.17. Voltage into the HCS was lowered but keep constant to prevent distortion of the signal at frequencies where the signal peaks. The calculated SNRs are given in figure 3.18. The noise was taken to be the region between $X = 1$ mm and 2 mm. Starting at the lower frequencies, it can be seen that the Tx mag. initially increases in response to the slot while its SNR drops with the defect signal being difficult to distinguish from the background at 6 MHz to 7 MHz. As the frequency is increased beyond 7 MHz, the Tx mag. seems to then decrease in response to the slot. This behaviour suggests that the system has gone through a resonance.

To confirm this, the frequency of the signal from the function generator was swept and the usual measured parameters (Tx mag., Tx phase, Rx mag. and Rx phase) were recorded. The result of the sweep is shown in figure 3.19 and from this, there appears to be a peak in the magnitude data at 7 MHz while the phase goes from a higher to lower value, which seems to confirm there is a resonance at 7 MHz. There is some noise near the start of the line scans for 5 MHz and 6 MHz. This might be linked to the system being near resonance and thus, being less stable.

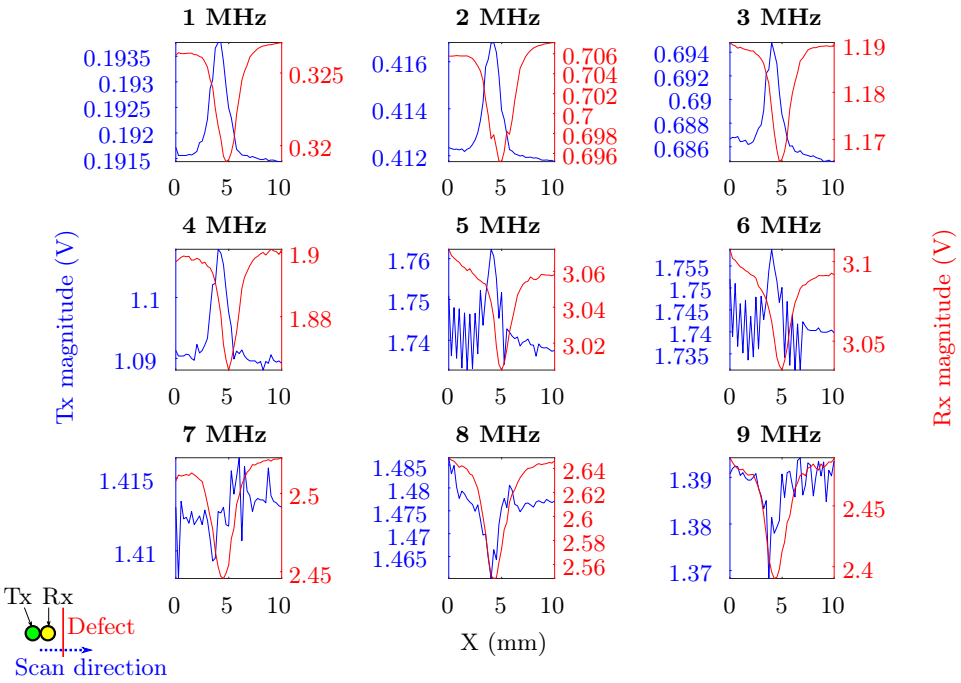

Figure 3.17: Line scans at differing frequencies. A depiction of the scan orientation is in the bottom left corner.

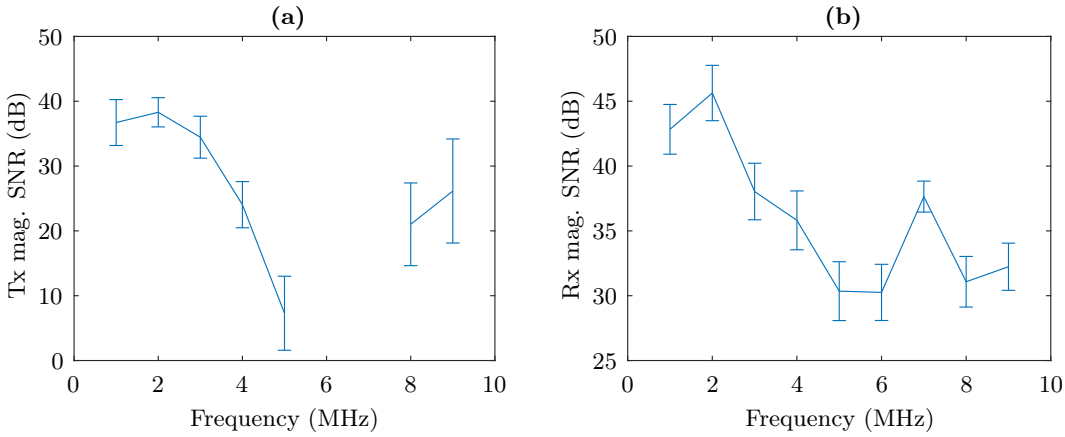

Figure 3.18: Results of signal-to-noise (SNR) calculation for line scans at different frequencies. The results for 6 MHz and 7 MHz are not shown for Rx mag. For these frequencies, the identified signal locations appeared to be spread about the line scan.

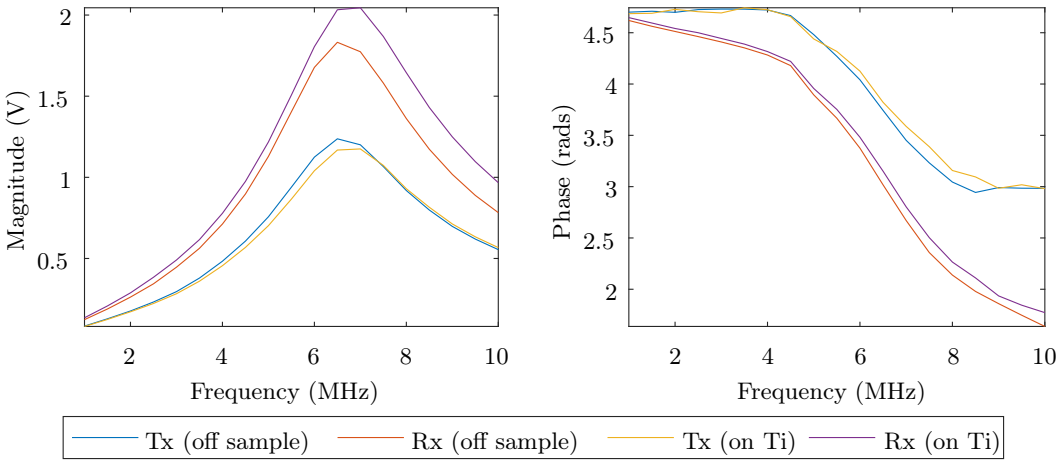

Figure 3.19: Measured parameters with increasing frequency. Input voltage to Howland current source is kept constant. The phase is wrapped to [0 2π].

There appeared to be a slope in many of the scans. This is clearly seen in figure 3.16 going from the top to the bottom of the scan. It appears to be the case even after rotating the sample 90° as shown in figure 3.20. As this slope was thought to be caused by the misalignment of each scan line, the program was changed to scan in the y-direction resulting in a 2D scan that is the composite of scans along the y-direction, instead scans in the x-direction. The result is figure 3.21, which has a slope that is instead in the x-direction, confirming that the slope is due to the misalignment of each line scan. It would be sufficient to fit each line to a linear fit and subtract each one to remove this type of background, but to reduce the lift-off variation in the raw data, an adjustable table was made to mount the sample so that it can be tilted. Additionally, near the start of the scan, there is often a line/a couple of lines where the signal diverges from the background level (scan starts from the origin of the plot). This was found to be caused by the system needing to equilibrate after being switched on and to allow this to happen, the system was left on for about half an hour before starting a scan.

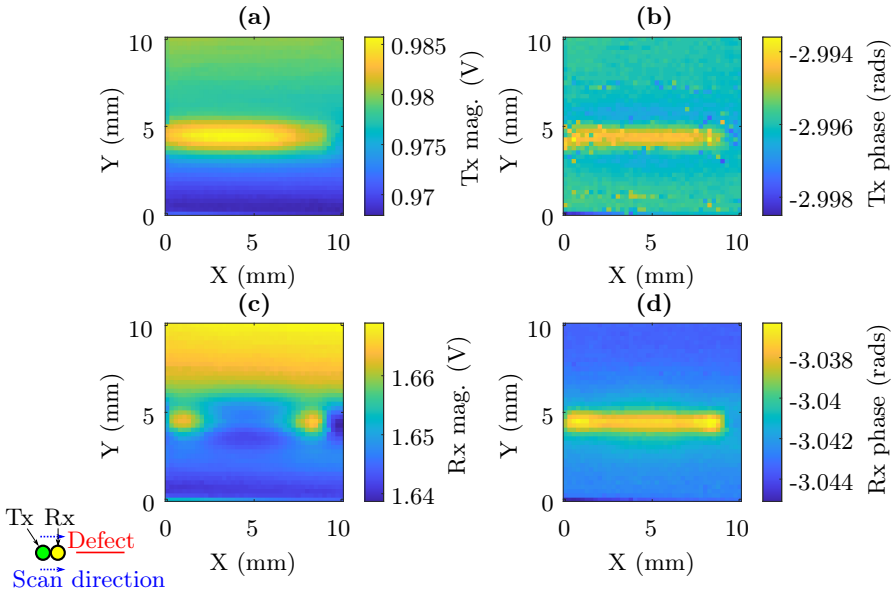

Figure 3.20: Experimental data taken at 1 MHz on stainless steel (316L) sample. The orientation of the coils is "parallel" to the slot (as depicted in the bottom left corner). (a) and (b) are magnitude and phase of the transmitter while (c) and (d) are magnitude and phase of the receiver.

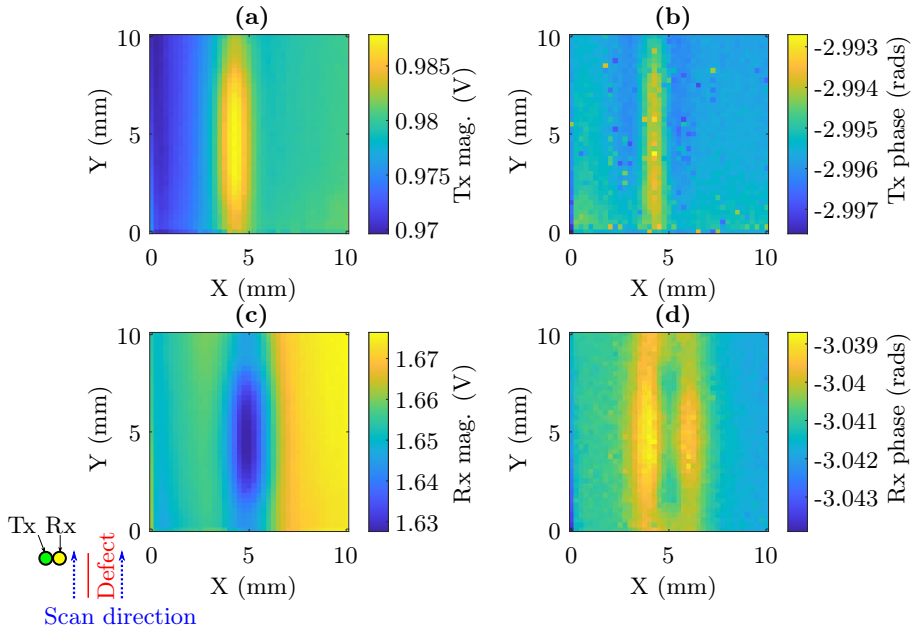

Figure 3.21: Experimental data taken at 1 MHz on stainless steel (316L) sample. The orientation of the coils is "perpendicular" to the slot (as depicted in the bottom left corner). (a) and (b) are magnitude and phase of the transmitter while (c) and (d) are magnitude and phase of the receiver.

With the table reducing the tilt, a larger area of the surface was scanned so that the full slot on the SS sample is scanned over, resulting in figures 3.22 and 3.23. Instead of there being a tilt from top to bottom, there is some horizontal banding in the background. This banding is not ideal, but it is distinct from the defect signal response and the table reduces the general lift-off. The banding is likely caused by errors in the placement of the probe by the XY stage. The calculated values for SNR, using the same process in section 2.7 and the background region $[\mathrm{x}, \mathrm{y}, \mathrm{width}, \mathrm{height}] = [1, 1, 5, 5]$ mm, are 22.505(9) dB, 21.0(3) dB, 27.0558(1) dB and 26.8969(1) dB for the Tx mag., Tx phase, Rx mag. and Rx phase respectively for the perpendicular orientation, while the SNRs are 20.130(2) dB, 20.9(1) dB, 18.30(1) dB and 31.20(5) dB for the same measured parameters in the parallel orientation. While the Rx mag. is expected to have the highest SNR, and it does for the perpendicular orientation, the horizontal banding is stronger in the Rx mag. in the parallel orientation, compared to in the other measured parameters.

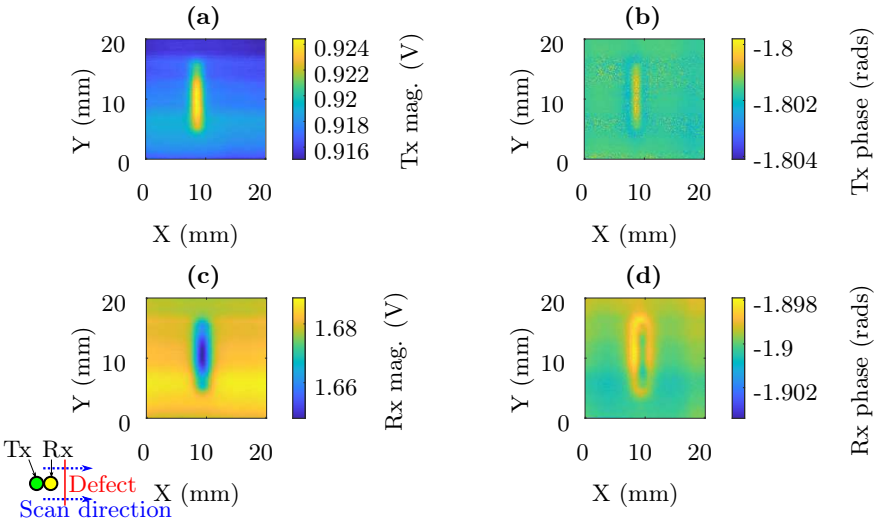

Figure 3.22: Experimental results from 2-by-2 cm perpendicular scan (as depicted in the bottom left corner) over the surface of the stainless steel sample at 1 MHz. (a) is the magnitude of the transmitter, (b) is the phase of the transmitter, (c) is the magnitude of the receiver and (d) is the phase of the receiver. The magnitude and phase are respectively in terms of voltage and radians.

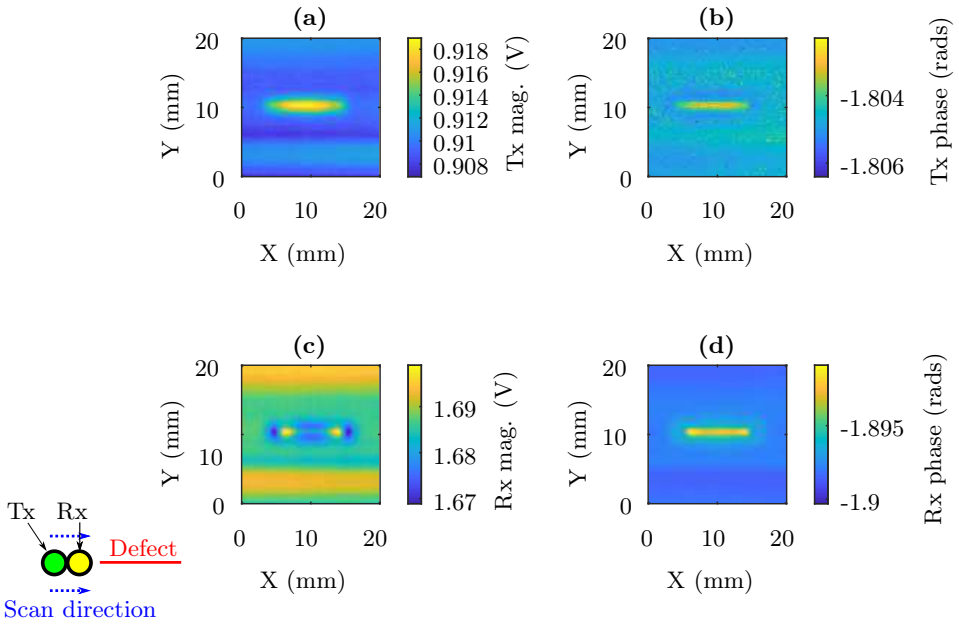

Figure 3.23: Experimental results from 2-by-2 cm parallel scan (as depicted in the bottom left corner) over the surface of the stainless steel sample at 1 MHz. (a) is the magnitude of the transmitter, (b) is the phase of the transmitter, (c) is the magnitude of the receiver and (d) is the phase of the receiver. The magnitude and phase are respectively in terms of voltage and radians.

The response to the slot in these 2D scans are similar to that seen in the simulation results. The simulation results in the perpendicular orientation were introduced in figure 3.3, and the simulation result for parallel orientation can be seen in figure 3.24. In both the perpendicular and parallel scanning orientations, the Tx mag. and Tx phase increase in response to a slot in the experimental (figures 3.22 and 3.23) and simulation (figures 3.3 and 3.24) results. The reasoning for the behaviour in the Tx mag. and phase was discussed in section 3.2 and the same reasoning applies here as well. The defect signal is just rotated to lie along the the horizontal direction for the parallel orientation to reflect the change in the slot position. The experimental and simulation results, however, differ in that that there is horizontal banding present in the experimental results.

The Rx signal is more complicated with it arising due to a combination of the magnetic field directly from Tx and the magnetic field from the eddy current, although again it exhibits a response that is similar to those obtained in the simulation. Like the simulation, in the perpendicular orientation, the signal decreases in the Rx mag. and forms a halo in the Rx phase as discussed in section 3.2.

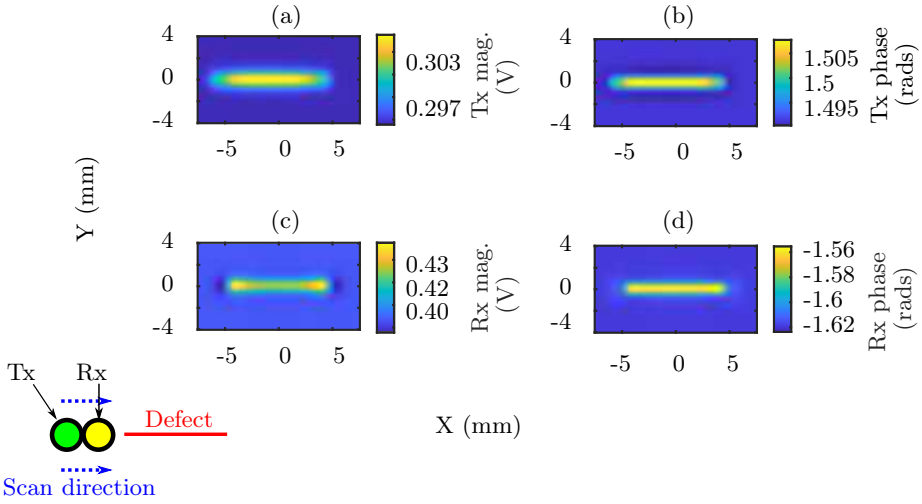

Figure 3.24: Simulation results for 2D scan taken in parallel orientation over stainless steel slot at 1 MHz. Rx mag. values have been multiplied by ten to reflect the amplification of the Rx signal.

In the parallel orientation, the Rx signals differ from the perpendicular orientation, but they are again similar to the simulation. In the Rx mag., there is a double-peaked structure when traversing the slot length, peaking when either the Tx or the Rx coil is near the end of the slot. On first impressions the Rx mag. response to a slot in the parallel orientation may look quite different to that in the perpendicular orientation, as it primarily increases in response to the slot instead of decreasing. However, it is important to note that the main response is not the only response that Rx mag. has to the slot, for example, there is the lower region around the main defect signal in the parallel orientation, which can be seen on closer inspection (see figure 3.25). Thus, the differences in the defect response in the perpendicular and parallel orientations are not incompatible. The Rx phase seems to increase over the slot, although there appears to be slight peaking near either end of the slot on the 2D scan data.

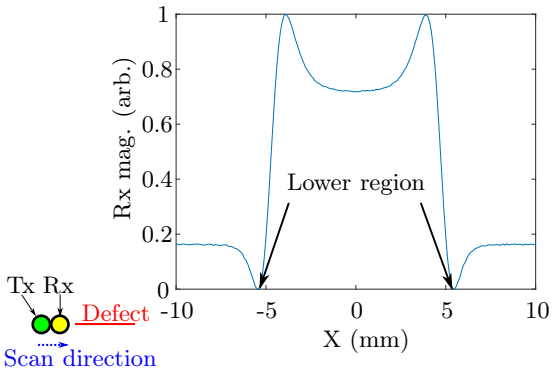

Figure 3.25: Normalised line scan in parallel orientation (as depicted in the bottom left corner) of Rx magnitude at Y = 0 mm for 1 MHz. Scan normalised to be in the range [0 1].

Moreover, the defect signal from Tx also looks shifted to the right of the signal from the Rx for the perpendicular orientation, while in the parallel orientation, there is no apparent shift. This mirrors the simulation results and it is presumably due to the relative positions of the coils.

3.5.3 Results on the titanium aluminide sample

Results taken in the perpendicular and parallel orientation are shown in figures 3.26 and 3.28 respectively. The simulation counterparts are shown in figures 3.27 and 3.29, which have slots based on the TiAl sample but on a material with the electrical properties of Ti since there were uncertainty in the conductivity of TiAl. Nevertheless, it is possible to see that the defect signal have similarities. Although the material is different, the conductivities are not expected to differ so much that the general morphology of the signal would be hugely different. Accordingly, the simulation results can be reasonably compared to the experimental results. The general shape of the signal should be more influenced by other parameters such as the slot size compared to the coil diameter, which is approximately 1 mm. Here, a good range of slot dimensions are tested, with slots shorter and longer than the coil diameter, helping to show how the defect signal evolves with slot size.

Starting with the perpendicular results, for the experimental (figure 3.26) and simulated (figure 3.27) counterpart, the Tx mag. and Tx phase signal for the shortest slot appears as a raised ring. In the simulation, the ring can be seen to form where the slot and the circular footprint of the Tx coil coincide. The defect signal arises from the slot crossing the eddy current induced by the Tx coil, and since the slot is smaller than the coil diameter, the signal is lower when the slot sits completely within the inner diameter of the Tx coil and is raised in a ring shape around this

lower part as the slot intersects with the footprint of the Tx coil. Furthermore, the slot blocks the eddy current more when the current flow is perpendicular to the slot length, leading a rise in the signal near the top and bottom of the ring. As the slot increases in length, the slot goes from being smaller than the coil diameter to being larger. With this increase, the signal elongates, and the dip in the middle of the ring becomes less pronounced as the slot is no longer able to fit completely within the inner diameter of the coil. For the 2 mm long slot, the slot extends beyond the coil diameter, and the signal looks like a continuous raised section as the Tx coil traverses the slot length.

In the Rx mag. and Rx phase, there is a single peak for the smallest slot. In the simulations, the location of the peak appears to be a compromise between the Tx coil being close enough for the slot to disrupt the eddy current and for the Rx coil to be affected by this disruption. There is also dipping in the Rx mag. that is located on either side of the peak along the slot length. There is some horizontal banding that is not in the simulation results, but the higher SNR means it is less visible.

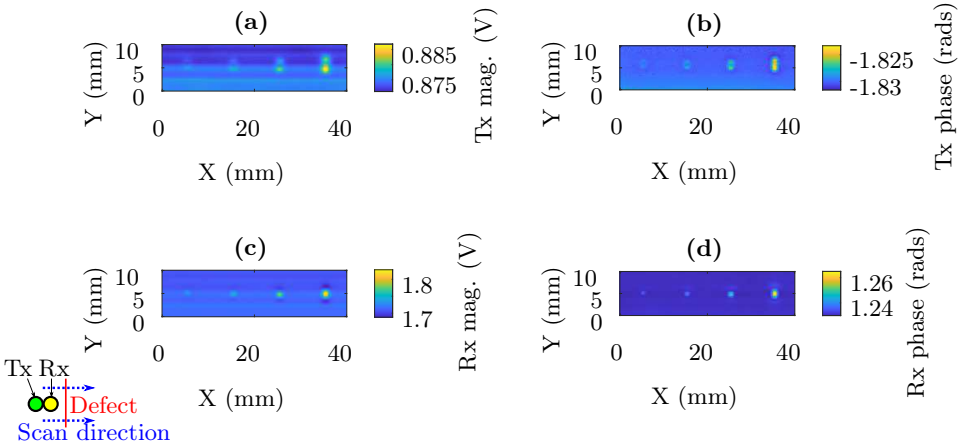

Figure 3.26: Experimental results from 4-by-1 cm perpendicular scan (as depicted in the bottom left corner) over the surface of a titanium aluminide at 1 MHz. Sample with four slots: the shortest to the longest slot from left to right. (a) is the magnitude of the transmitter, (b) is the phase of the transmitter, (c) is the magnitude of the receiver and (d) is the phase of the receiver. The magnitude and phase are respectively in terms of voltage and radians.

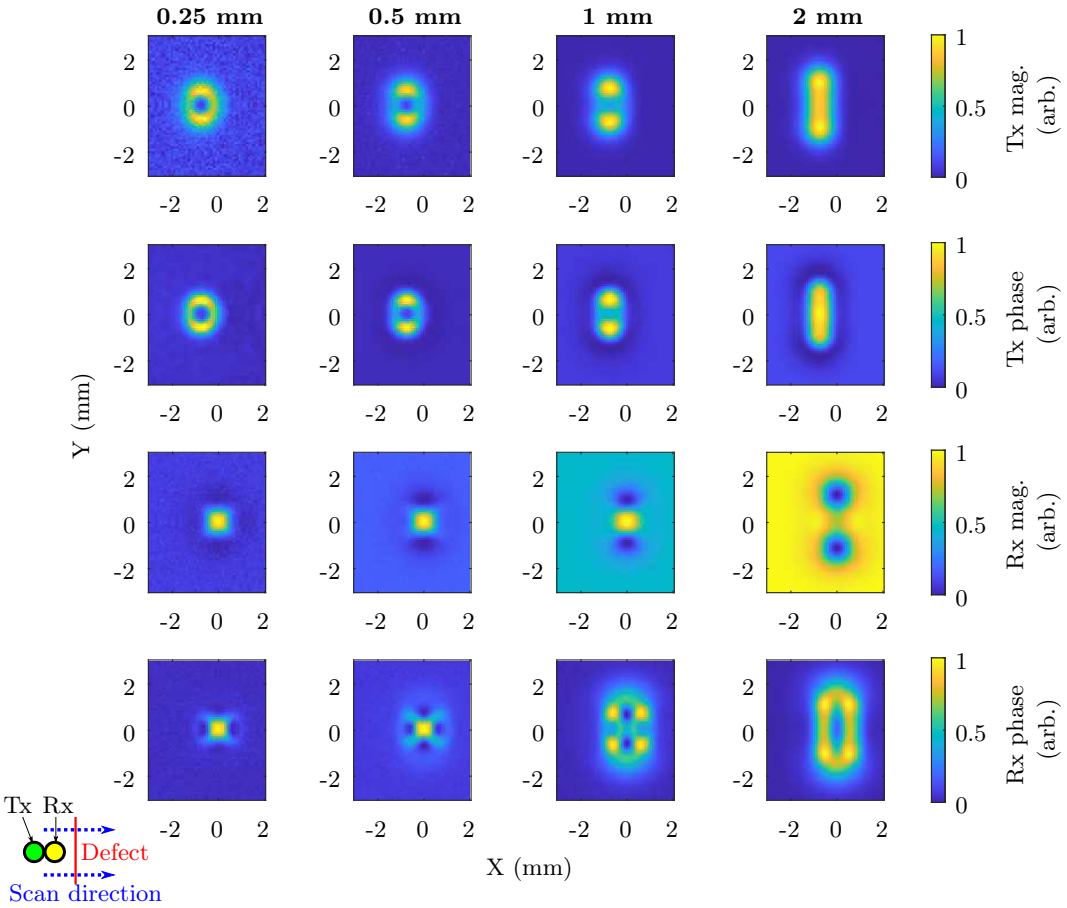

Figure 3.27: Nomalised simulation results for perpendicular orientated slots (as depicted in the bottom left corner) on Ti at 1 MHz. Sorted in columns by slot length and row by the parameter measured.

Moving on to the result in the parallel orientation, the Tx mag. and Tx phase measurements were expected to be similar to that in the perpendicular results, but with the signal rotated to lie along the the horizontal direction to match the change in orientation of the slot. However, the Tx mag. and Tx phase also has visible asymmetry along the slot length. This is seen for both the experimental (figure 3.28) and simulation results (figure 3.29). This asymmetry is likely caused by the ferrite core of the Rx coil pulling the eddy current towards it, as shown in figure 3.30.

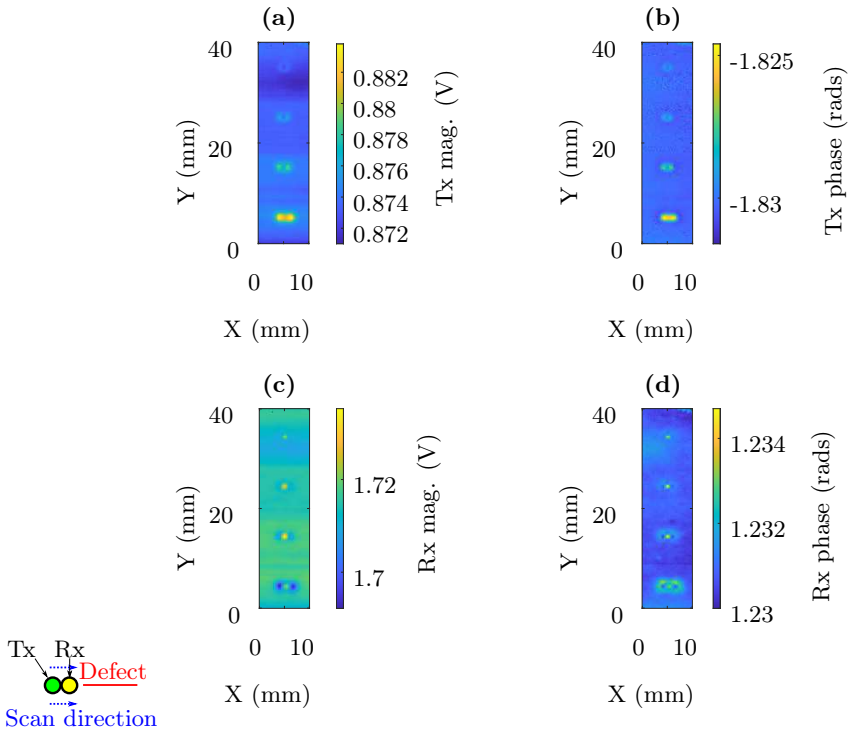

Figure 3.28: Experimental results from 1-by-4 cm parallel scan (as depicted in the bottom left corner) over the surface of a titanium aluminide sample at 1 MHz. Sample has four slots: from the shortest to the longest, from top to bottom. (a) is the magnitude of the transmitter, (b) is the phase of the transmitter, (c) is the magnitude of the receiver and (d) is the phase of the receiver. The magnitude and phase are respectively in terms of voltage and radians.

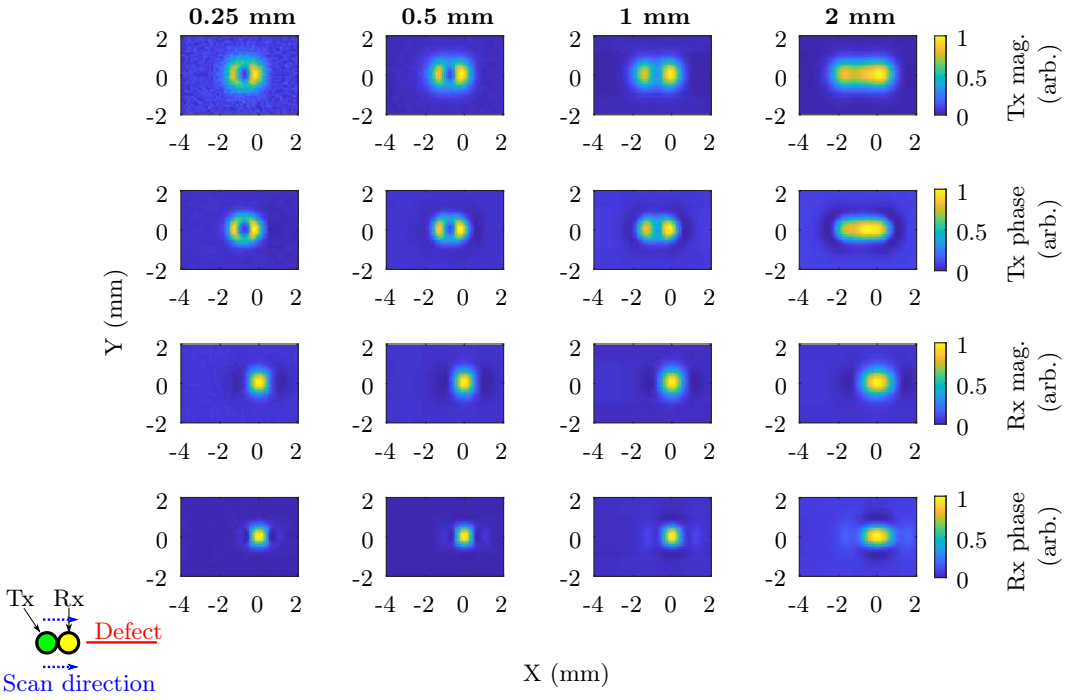

Figure 3.29: Normalised results for parallel orientated slots (as depicted in the bottom left corner) on Ti at 1 MHz. Sorted in columns by slot length and row by the parameter measured.

The asymmetry in the eddy current means that more of the eddy current is disrupted when crossing the right side of the coil. Thus, causing a bigger change in the signal on this side. When the coils are air-cored, the result looks symmetrical as one would expect since, without the core, the Rx coil would not be expected to significantly influence the Tx coil. Ignoring the Rx coil, the system is symmetric whether on the left or right of the slot and thus the signal should also be symmetric. While, defect signal is again a peak in the Rx mag. and Rx phase in the experimental and simulation results.

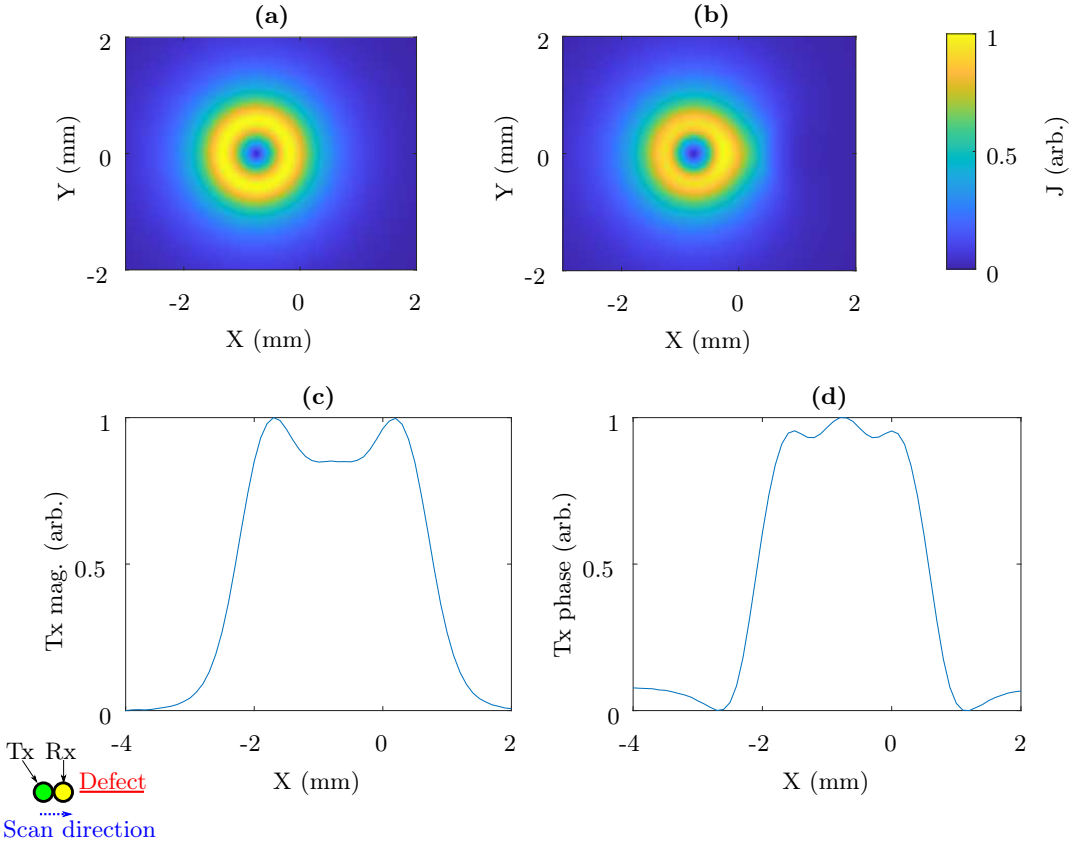

Figure 3.30: Normalised magnitude of the current density at the sample surface under the Tx coil in COMSOL (a) without a core and (b) with a ferrite core. The origin is where the centre of the coils are (the Tx coil is to the left and the Rx coil is to the right). (c) and (d) are the simulated Tx results when traversing in the parallel orientation (as depicted in the bottom left corner) through the slot (i.e. at $Y = 0\,\text{mm}$ in a 2D scan) with air-cored coils, where the results can be seen to be more symmetric.

By dividing the signal search area into quadrants where each slot is in a separate quadrant, the SNR can be calculated for each slot. The results are shown in figures 3.31 and 3.32 for the perpendicular and parallel orientations. The background for the SNR calculation is defined to be $[\mathrm{x}, \mathrm{y}, \mathrm{width}, \mathrm{height}] = [7, 1.5, 5, 5]$ mm and $[2, 7, 5, 5]$ mm for each respective orientation. From this, the signal appears to stand out particularly in the Rx phase with a good SNR of up to 43.0(3) dB, which is achieved on the 2 mm long slot in the perpendicular direction.

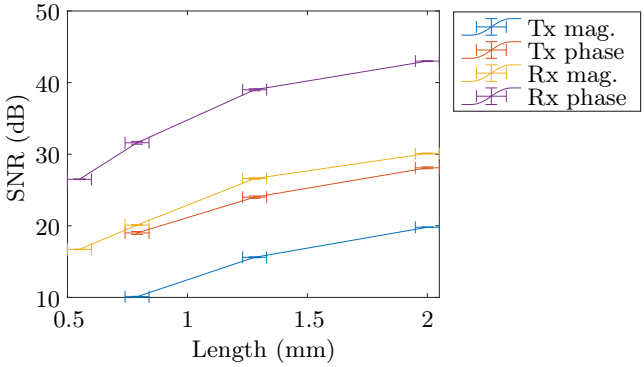

Figure 3.31: Signal-to-noise ratio for TiAl slots in perpendicular orientation. For the shortest slot, the Tx mag. and Tx phase SNRs are not present since the locations with maximum difference from the background average were not located on the slot.

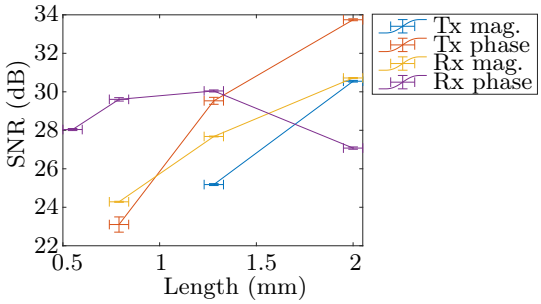

Figure 3.32: Signal-to-noise ratio for TiAl slots in parallel orientation. Points where the maximum difference from the background average are not located on the slot are not included.

Although there is some noise in the Rx phase for both the SS and TiAl samples, the relatively level appearance of the background with the lift-off variation being less apparent, gave rise to the idea that the Rx phase may be more robust to lift-off. This was a driving factor behind performing lift-off experiments, which can be seen later in section 4.3.

3.5.4 Results on the titanium sample

Again, there are similarities in the experimental (figures 3.33 and 3.34) and simulation results (the 0.25 mm and 0.5 mm long slots in figures 3.26 and figure 3.28). However, there is banding in the background of the 2D images in experimental results, which is more visible on results for the Ti sample than on the TiAl sample. This could be because the slots on the Ti sample are smaller than those on the TiAl sample, but it could also because the surface of the titanium sample is particularly uneven (see optical microscope measurements in section 2.6), where the consequently weaker signal results in more visible banding. The banding means that the SNR could not be calculated for many of the results, including the slots in the perpendicular orientation. This is because for these results the banding intersects the slot. But, where the SNR could be calculated, the SNR is calculated based on the method in section 2.7, but with the defect search area split into halves according to where the defect location is. This results in SNRs for the Rx mag. of 25.97(3) dB for the shortest slot (measured to be 0.46(5) mm) and 28.57(6) dB for the longest slot (measured to be 0.75(5) mm), while the SNR for the Rx phase is 25.2(1) dB for the longest slot when the slot is in parallel orientation and when the background is set to $[\mathrm{x}, \mathrm{y}, \mathrm{width}, \mathrm{height}] = [1, 10, 2.5, 2.5]$ mm.

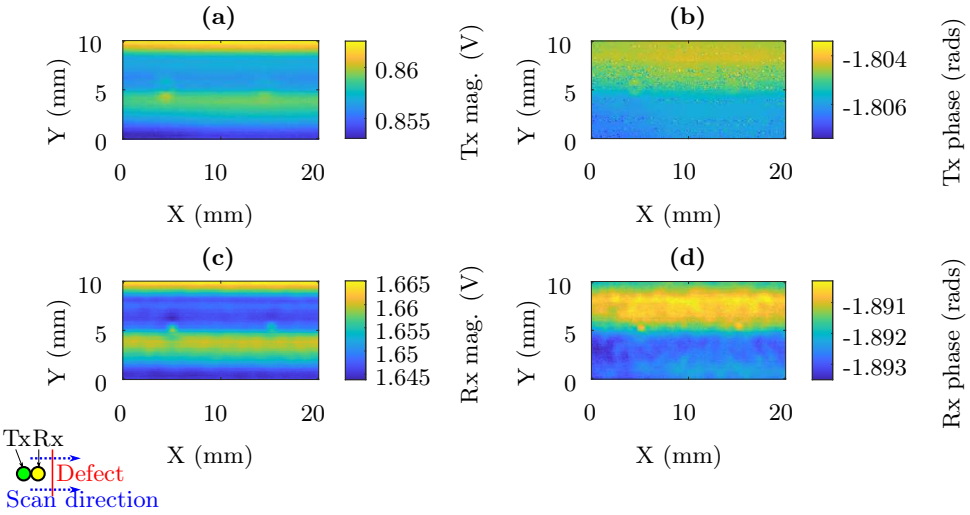

Figure 3.33: Experimental results from 2-by-1 cm perpendicular scan (as depicted in the bottom left corner) over the surface of a titanium sample at 1 MHz. The longer slot (0.75(5) mm) is to the left of the shorter slot (0.46(5) mm). (a) is the magnitude of the transmitter, (b) is the phase of the transmitter, (c) is the magnitude of the receiver and (d) is the phase of the receiver. The magnitude and phase are respectively in terms of voltage and radians.

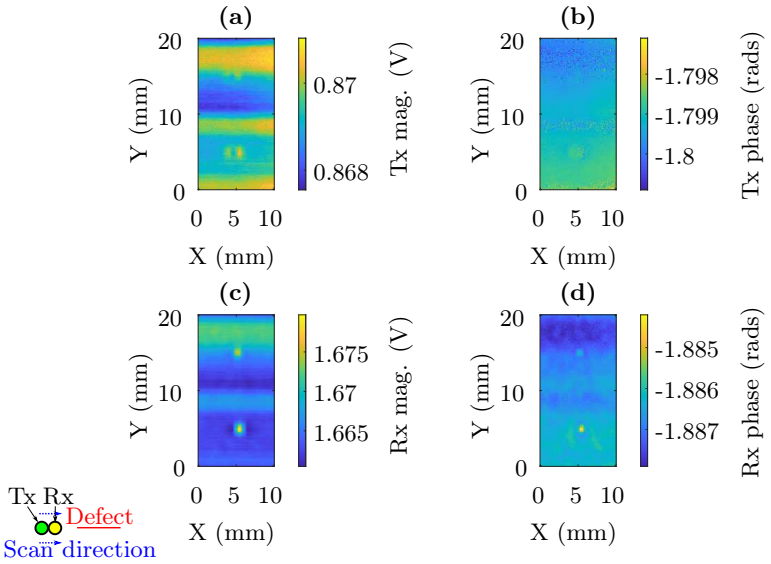

Figure 3.34: Experimental results from 1-by-2 cm parallel scan (as depicted in the bottom left corner) over the surface of a titanium sample at 1 MHz. The shorter slot (0.46(5) mm) is above the longer slot (0.75(5) mm). (a) is the magnitude of the transmitter, (b) is the phase of the transmitter, (c) is the magnitude of the receiver and (d) is the phase of the receiver. The magnitude and phase are respectively in terms of voltage and radians.

To combat the banding in the background, various coil enclosures were experimented with. This included an enclosure that used springs to press the coils to the sample. However, this seemed to result in the coils becoming increasingly tilted when dragged along the scanning direction and when PTFE tape was used to reduce the friction of the coils on the sample, the behaviour only improved to periodic dragging then releasing.

The variation in lift-off during a scan of the sample surface was small, but noticeable in the results. A system that can correct for small lift-offs while not tilting was needed. After several iterations of the coil enclosure, it was decided that an approach where the coil holder was printed using 3D printed resin would be used. This implementation is presented and used in the next chapter (chapter 4). With this improvement and the other improvements implemented during this chapter, higher frequencies up to 20 MHz were also investigated. It was suspected there may be issues, because of the aforementioned resonance at around 7 MHz, but it was also thought that taking 2D scans and lift-off measurement may provide more information.

3.5.5 Summary of experimental results from testing probe

Overall, the defect signal looks much clearer with the improvements made, which have included using a function generator instead of the AD9850 module, a new pair of coils and a new table to mount the sample. There is some visible banding in the 2D scan data, but this has allowed an interesting feature to be seen where the Rx phase seems like it could be more robust to lift-off in the TiAl results. This will be explored later in this thesis in section 4.3, but in the next chapter, lift-off will be reduced by printing a coil holder made using a 3D resin printer where results at higher frequencies will also be taken. Here, there are similarities between the experimental and simulation results, despite the banding, and reducing the lift-off variations should help improve the similarities.

Chapter 4

Control Tests

4.1 2D scans

4.1.1 Experimental setup for performing 2D scans

The same setup as the one used in section 3.5 was used along with the alterations made during the study (i.e. the new ferrite-cored coils and the table to level the sample). Additionally, a resin 3D printed coil holder will be implemented as suggested at near end of the previous chapter (in subsections 3.5.4 and 3.5.5). Figure 4.1 shows the computer-aided design (CAD) model of this resin 3D printed coil holder.

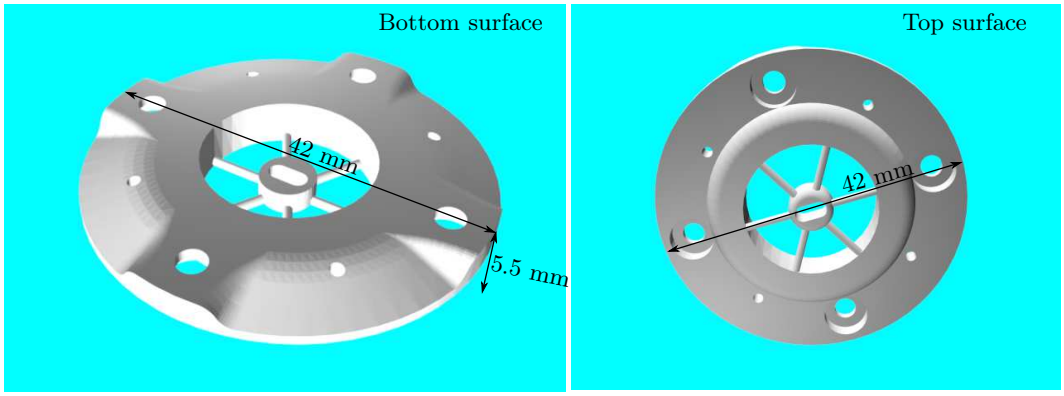

Figure 4.1: CAD model for coil holder 3D printed using resin. The coils are placed in the central cutout and the four holes near the circumference are to attach the coil holder to the main structure where the electronics behind the coils are placed.

In figure 4.1, the "top surface" is the surface that is placed against the sample. The four holes near the circumference are used the attach the coil holder to the main enclosure for the electronics placed directly behind the coils. The coils themselves

are placed into the central cutout and are adhesively bonded in place using epoxy resin.

Resin printing allows fine details to be printed, which is used here to print fine spokes that radiate from the coils at the centre. The spokes are fine so that they are able to flex, allowing the coils to closely follow the surface during a scan. Resin printing also ensures a smooth finish that reduces the friction between the coil holder and the sample surface. There is also slopes cut on the bottom surface and some additional smaller holes. This is to help with the alignment of the coil holder and the main enclosure.

Using this setup, measurements will be taken at higher frequencies, up to 20 MHz, and this is done with the MDO4054C oscilloscope.

4.2 Experimental 2D scan results

4.2.1 Line scans on stainless steel sample

For comparison to the line scans obtained using the EddySense prototype in section 3.4, line scans were taken at different frequencies up to 40 MHz using the experimental setup developed so far. The Rx mag. results from this are shown for comparison in figure 4.2. The x-axis is labelled "Y" since the coils are housed in a different orientation to the results that are shown in section 3.4, and thus the scan needed to be scanned in the y-direction to be comparable; both the scan using the EddySense prototype (figure 3.8) and the setup developed so far (figure 4.2) are scans that cross along the slot's width in the parallel orientation on SS.

The general cross-section in the Rx mag. is w-shaped, where the lobing either side of a central peak dominate such that the overall shape is more of a dip in the frequency range 10 MHz to 30 MHz, and at frequencies above and below, the central peak dominates the response.

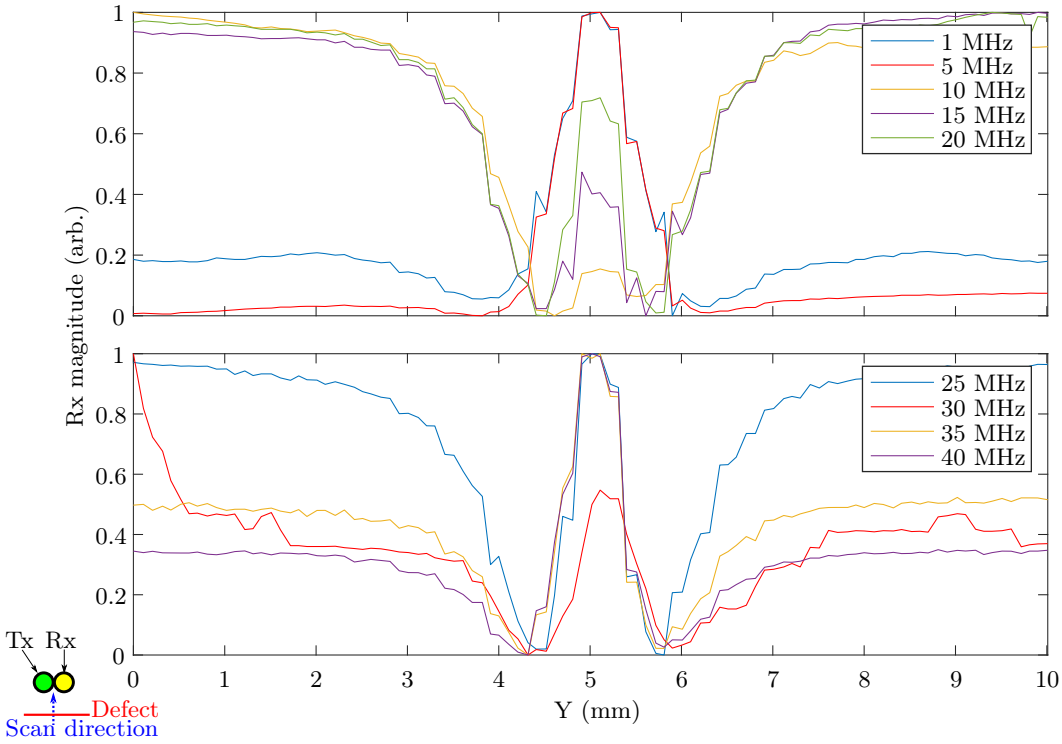

Figure 4.2: Line scans along perpendicular bisector of slot in the parallel orientation (as depicted in the bottom left corner) on stainless steel using a probe that uses a AFG3052C function generator as the reference signal. Each line is taken at a different frequency given by the legend.

The calculated SNR, with the background taken to be the region $Y < 2\,\text{mm}$, is shown in figure 4.3. The Rx mag. SNR is generally improved compared to the result with the EddySense probe, particularly when comparing higher frequencies. The system is, however, capable of also measuring the Tx mag., Tx phase and Rx phase. Parameters such as the Rx mag. and Rx phase seemed to be capable of distinguishing the slot at high frequencies, up to and potentially beyond 40 MHz, despite the aforementioned dip in SNR that is centred around 30 MHz. However, there were issues detecting the slot with the Tx mag. and, even more so, with the Tx phase, at high frequencies. For these parameters, the SNR reduces with increasing frequency until the slot is difficult to distinguish from the noise at 30 MHz for the Tx mag. measurement, and at 25 MHz for the Tx phase measurement, with the SNR not recovering as the frequency is further increased. This could be related to the fact that the HCS is known operate less well at higher frequencies, and considering all the results, it seems that it is not possible to continue beyond 20 MHz if the Tx phase is to be usable.

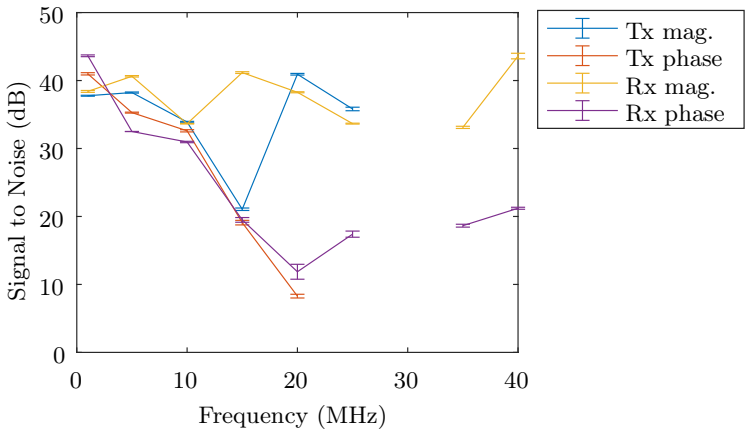

Figure 4.3: Calculated signal-to-noise ratios for line scans on stainless steel. Missing data points represent invalid results where some/all of the identified signal locations are away from the defect region.

4.2.2 2D scans

2D scans were consequently taken at five driving frequencies up to 20 MHz. Scans were taken at 1 MHz, 5 MHz, 10 MHz, 15 MHz and 20 MHz. These 2D scans give a more comprehensive picture of the defect signal and are more likely to show lift-off variations, since lift-off seems to show up between the line scans that the 2D scan is comprised of. The measurements are all taken with a 0.5 V pk-pk reference signal for consistency as the measured waveform distorts around the resonant frequency ($\sim$7 MHz) if a larger reference signal is used (subsection 3.5.2).

Plots showing 2D scans for each sample will presented for the perpendicular and parallel orientations at 1 MHz. The scan area is the same for the other frequencies, but the results will be summarised in selected plots. These selected plots will include plots quantifying the signal, along with some cross-sectional plots.

For the SS sample, the 2D scans in the perpendicular and parallel orientation at 1 MHz are shown in figure 4.4. It can be seen that the behaviour looks similar to previously taken scans in subsection 3.5.2.

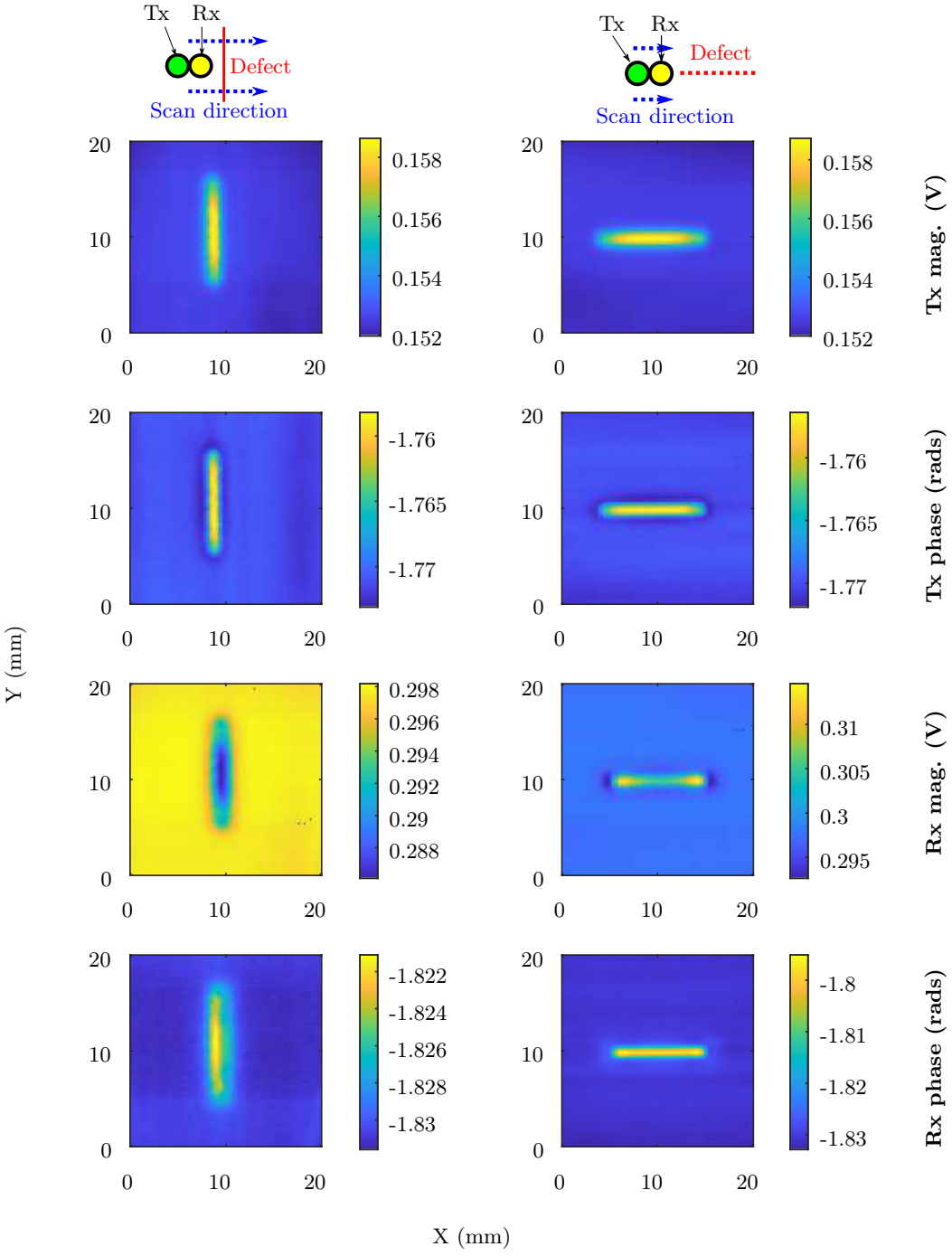

Figure 4.4: 2D scans on stainless steel at 1 MHz. Scan with slot in perpendicular orientation in the first column and scan with slot in the parallel orientation in the second column. The orientation is depicted at the top for each column.

For the TiAl sample, the scan in the perpendicular orientation at 1 MHz is shown in figure 4.5 and the scan in the parallel orientation is shown in figure 4.6. At each frequency, one continuous 2D scan containing all the slots were taken for the experimental results. However, the difference in signal for the longest and shortest slot varied considerably (for example the signal is about eight times greater for the longest slot compared to the shortest slot for the Tx phase in the parallel direction), which makes it difficult to see the shortest slot on the same plot as the longest slot, even if the shortest slot has a good SNR. Consequently, each scan is split into quadrants to form four plots for each variable such that the original data set would be formed from the plots shown, but concatenated.

For the perpendicular orientation, the plots would be concatenated in descending slot length so that the longest slot (2 mm) would be on the far left and the shortest slot (0.55(5) mm) would be on the far right. While, for the parallel orientation, the plots would be concatenated so that shortest slot (0.55(5) mm) would be on the top going up in size to the longest slot (2 mm) on the bottom.

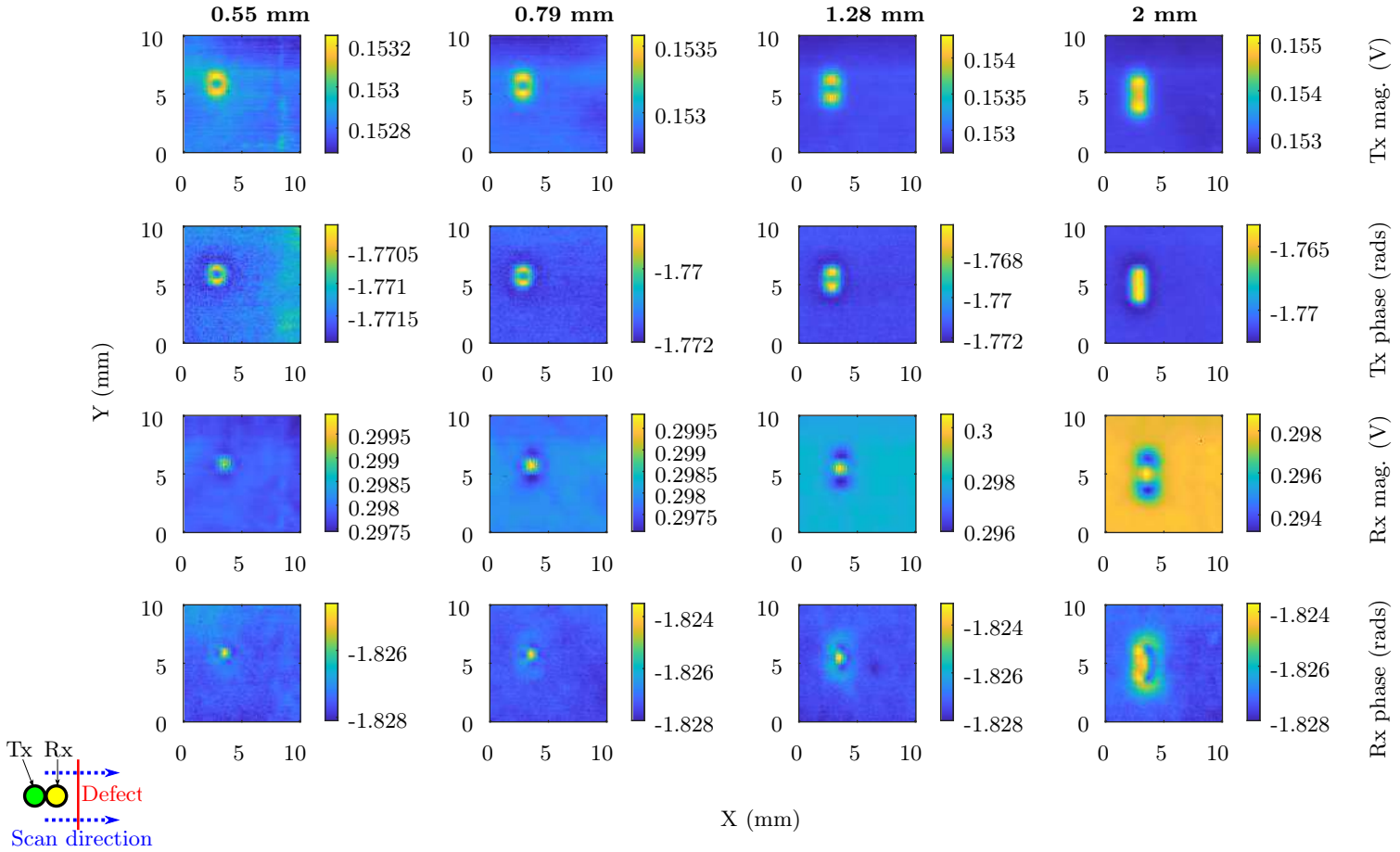

Figure 4.5: TiAl at 1 MHz. Slot is in perpendicular orientation (as depicted in the bottom left corner). Grouped in rows by the measured parameter and columns by the slot length.

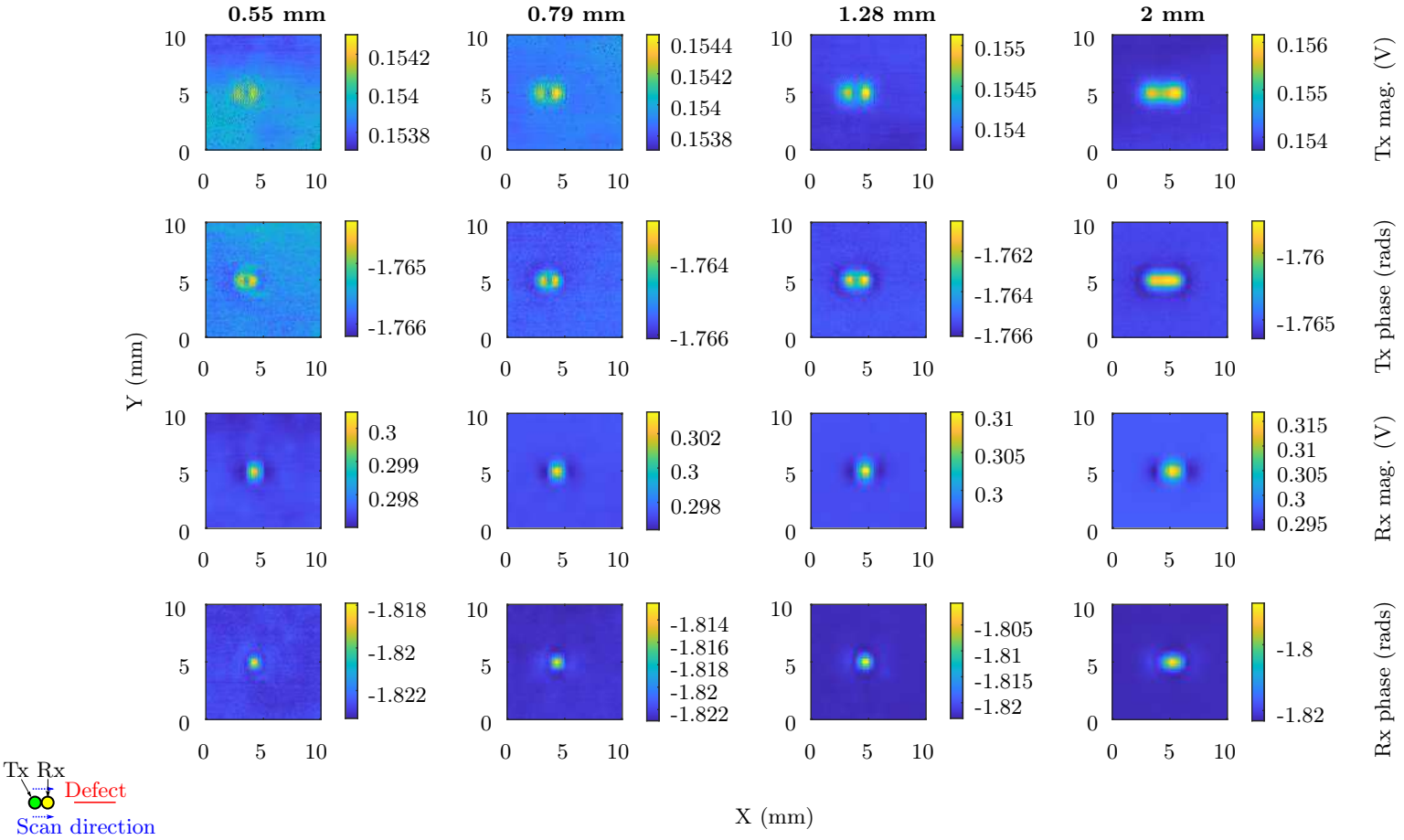

Figure 4.6: TiAl at 1 MHz. Slot is in parallel orientation (as depicted in the bottom left corner). Grouped in rows by the measured parameter and columns by the slot length.

Like for the previously taken results in section 3.5.3, these experimental results (figures 4.5 and 4.6) and its simulated counterparts (figures 3.27 and 3.29 respectively) share similarities such as the Tx mag. and phase forming more of raised ring in appearance for the shorter slots, which morphs into more of a bar for the longer slots for both the perpendicular and parallel orientations. Additionally for both the experimental and simulation results, the Rx mag. evolves from a mainly peaking signal to a dipping signal as the dipping side lobes become more dominant with increased length, while it forms more of a single peak in the parallel orientations. In the Rx phase, the signal evolves from more of a peak to a raised ring in the perpendicular orientation with increased length, while the signal remains peak in the parallel orientation. It is clear that the experimental and simulation results are similar, and the experimental results are repeatable.

The 2D plots for the Ti sample are shown in figures 4.7 and 4.8 for the perpendicular and parallel results respectively. Like the TiAl results, the 2D scan was taken is continuously, but the scan was split. As there are two slots, the plot was split into two. The original plot would be a concatenation. In the the perpendicular orientation, they would be concatenated with the longest slot (0.75(5) mm) on the left and the shortest slot (0.46(5) mm) on the right. In the parallel orientation they would be concatenated with the shortest slot (0.46(5) mm) on the top and the longest slot on the bottom (0.46(5) mm).

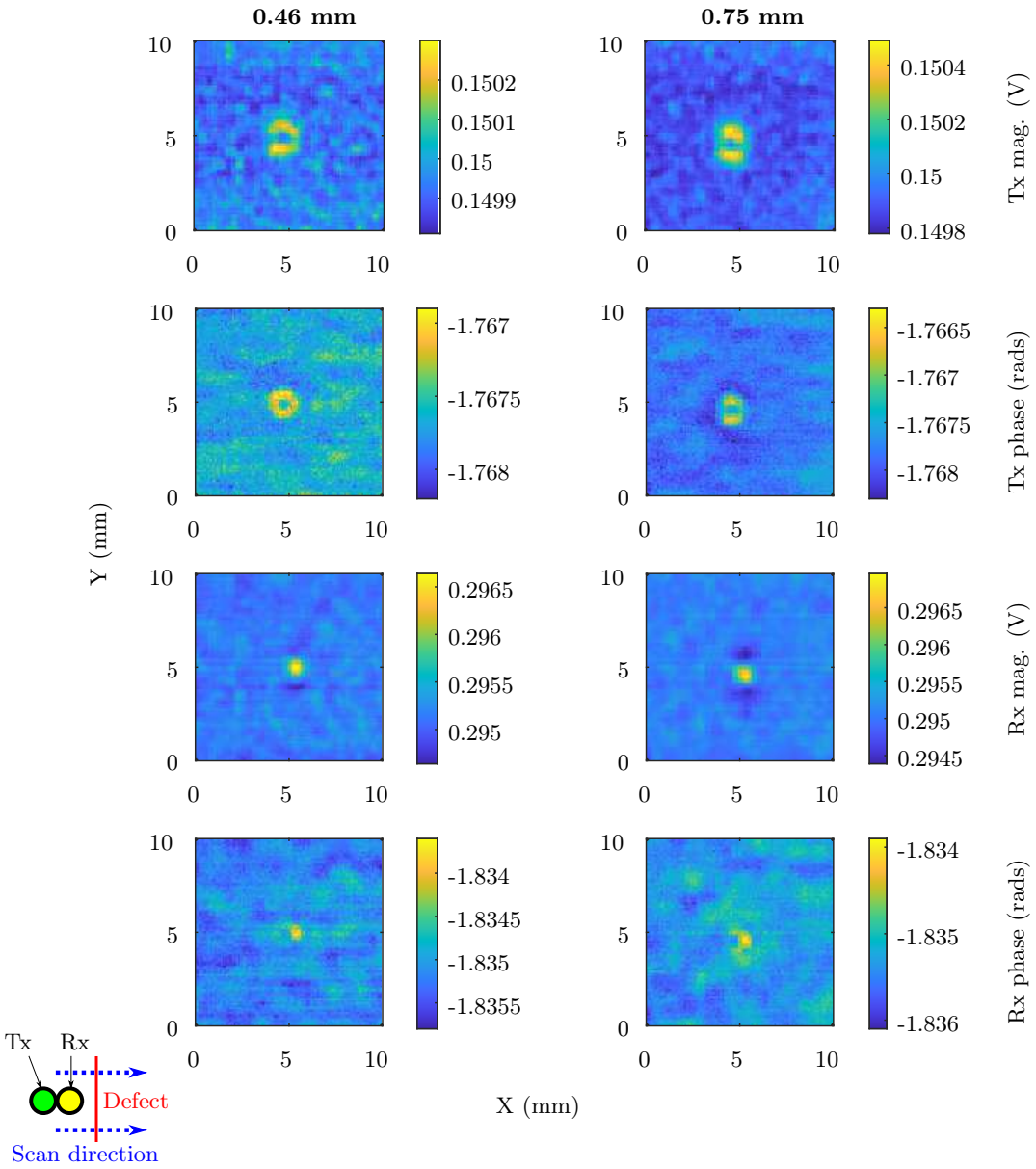

Figure 4.7: Ti at 1 MHz. Slot is in perpendicular orientation (as depicted in the bottom left corner). Grouped in rows by the measured parameter and columns by the slot length.

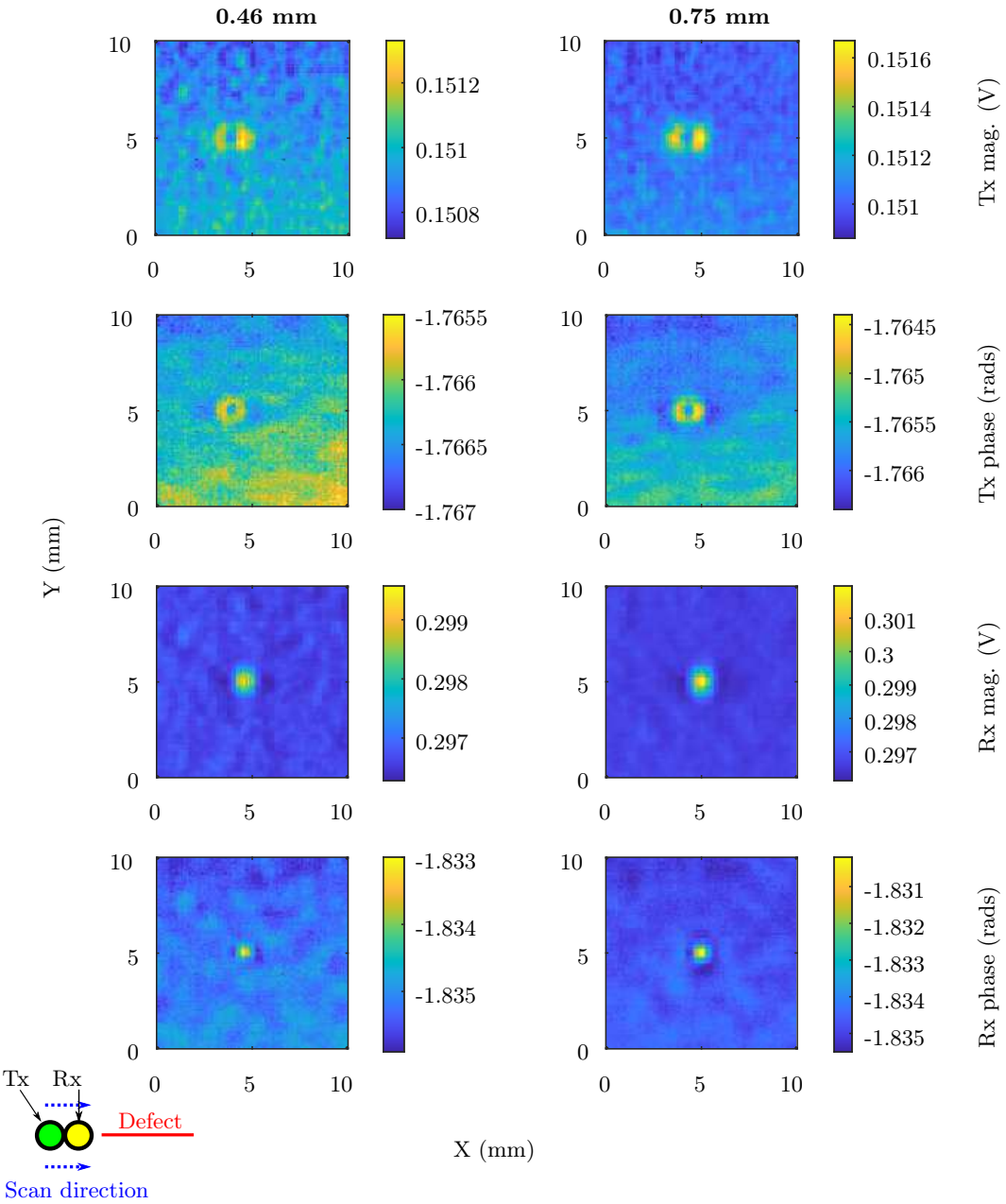

Figure 4.8: Ti at 1 MHz. Slot is in parallel orientation (as depicted in the bottom left corner). Grouped in rows by the measured parameter and columns by the slot length.

From these 2D scan plots, the general response to a slot appears similar to previous experimental results, but with reduced noise and less banding present. It is also possible to see that the background looks mottled in the Ti results, which could reflect surface variations related to the surface roughness. This roughness was noted in the optical microscope measurements (see subsection 2.6) and it is thought that

this may be due to the Ti sample surface being more prone to oxidation. It is much more difficult to observe the slots on the Ti sample compared to the slots on the TiAl sample. This could be due to various factors such as the higher conductivity of the Ti compared to the TiAl sample making the sensor more sensitive to surface variations, the greater surface roughness of the Ti sample and the slightly larger size of the Ti slots. Also, there is the possibility that Ti suffers more from grain noise and TiAl is better behaved.

To try to quantify the defect signal, the SNR will be calculated as well as the signal response as a percentage of the background value. The results in the perpendicular orientation from this analysis will be presented first, followed by the results in the parallel orientation. In the plots quantifying the signal, there are some data points missing and this will be because the five measurements with greatest deviation from the background level were found in locations spread apart and away from the slot location.

As a reminder, the defect sizes are shown in table 2.1, but the lengths of the slots will be summarised here. There is a single nominally 10 mm long slot on the SS sample, four slots on the TiAl sample and two slots on the Ti sample. The three shortest slots on the TiAl sample are 0.55 mm, 0.79 mm and 1.28 mm long with an uncertainty of 0.05 mm each and the longest slot is nominally 2 mm long. The two slots on the Ti sample are 0.46(5) mm and 0.75(5) mm long with an uncertainty of 0.05 mm each. They will be grouped by their nominal lengths in plots where the experimental and simulation results are combined to help with comparison. To this effect, the 10 mm long slot on the SS sample and the 2 mm slot on the TiAl sample do not have a measured value so they will already be referred to by their nominal lengths. However, the TiAl sample also has slots nominally 0.25 mm, 0.5 mm and 1 mm long. While, the Ti sample has slots with nominal lengths of 0.25 mm and 0.5 mm.

Starting with the results in the perpendicular orientation. The background region is defined to be $[\mathrm{x}, \mathrm{y}, \mathrm{width}, \mathrm{height}] = [1, 1, 5, 5]$ mm for the SS results and $[\mathrm{x}, \mathrm{y}, \mathrm{width}, \mathrm{height}] = [6.5, 1.5, 5, 5]$ mm on the original data set for the TiAl sample, which between the longest (nominally 2 mm) and third-longest slot (1.28(5) mm). For the Ti sample, the background is defined to be$[\mathrm{x}, \mathrm{y}, \mathrm{width}, \mathrm{height}] = [9, 5, 2.5, 2.5]$ mm, which is between the two slots present. To be able to get separate values for each slot on the TiAl and Ti samples, the defect search area is split into the quadrants and halves respectively. Figure 4.9 shows the calculated SNR. As a reminder, the SNR calculations are based on the method in section 2.7.

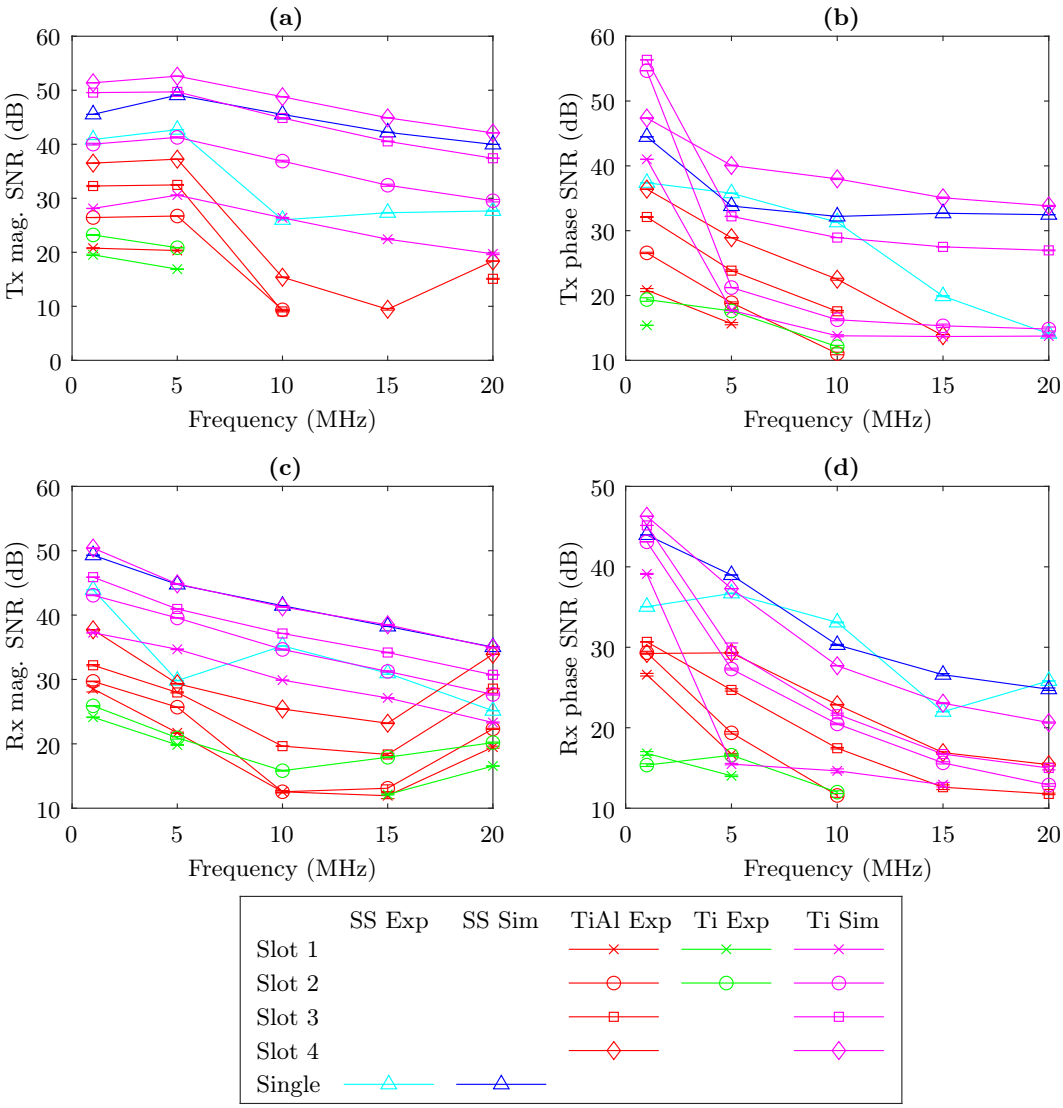

Figure 4.9: Signal-to-noise ratio as a function of frequency for the experimental and simulation results in the parallel orientation. The legend is arranged by row from the shortest to the longest slot. Exp and Sim are short for experimental and simulation results respectively.

From figure 4.9, the SNR is good at 1 MHz even for the smaller slots, which is a significant results as there is a requirement to detect surface-breaking defects and fatigue cracks at the earliest stage of growth in safety-critical components, with an aspirational target of detecting defects of less than 250 µm in length.

The SNR can, however, be seen to generally decreases with increasing frequency. At higher frequencies, this means the SNR cannot be determined for many of the parameter, but even the smallest slots can be seen in the Rx mag. The cause of

the noise in the experimental results will be due to physical factors, rather than the mesh as is the case for the simulation results, but it is sensible to reason that factors contributing to a stronger signal in the simulation may transfer to the experimental results.

Figure 4.10 shows that the voltage constantly increases with frequency in the simulation results whereas the voltage only increases up to 5 MHz in the experimental results before decreasing. This could be because the capacitance of the electronics is taken to be negligible. Accordingly, the impedance of the coils and thus, voltage would be expected to simply increase. The simulation would therefore be expected to be more accurate for lower frequencies.

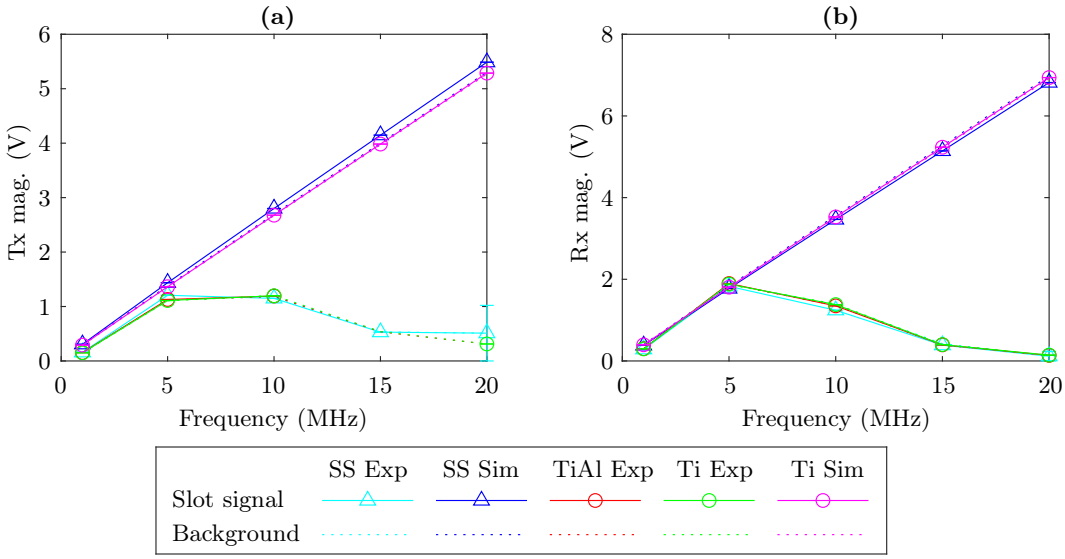

Figure 4.10: Voltage with frequency for experimental and simulation results in the perpendicular orientation. To simplify the plot, just the results for the 0.5 mm slot is shown for the TiAl and Ti samples.

Figure 4.11 shows the defect signal as a percentage of the background signal to get an idea of the general response. A positive value would correspond to the measurement being higher than background value and a negative value would correspond to the measurement being lower than the background value. From this, it can be seen that the direction of the response is the same in both the experimental and simulation results for all variables at 1 MHz. It is positive in both the experimental and simulation results for the Tx mag., Tx phase and Rx phase. As well as, in Rx mag., except for the SS slot and 2 mm long slot, where it is negative for both the experimental and simulation results. This suggests the change in response is due to the size of the slot, where larger slots result in a negative response and smaller slots

have a positive response.

Increasing from 1 MHz to 5 MHz, the experimental and simulation results generally move in the same direction, but the behaviour is starting to diverge. For example, looking at the SS results, values for the experimental and simulation results both either increase or decrease. However, the value for the Rx phase decreases so that it is negative, which produces a response that is different in appearance. The divergence reflects the aforementioned resonance (subsection 3.5.2).

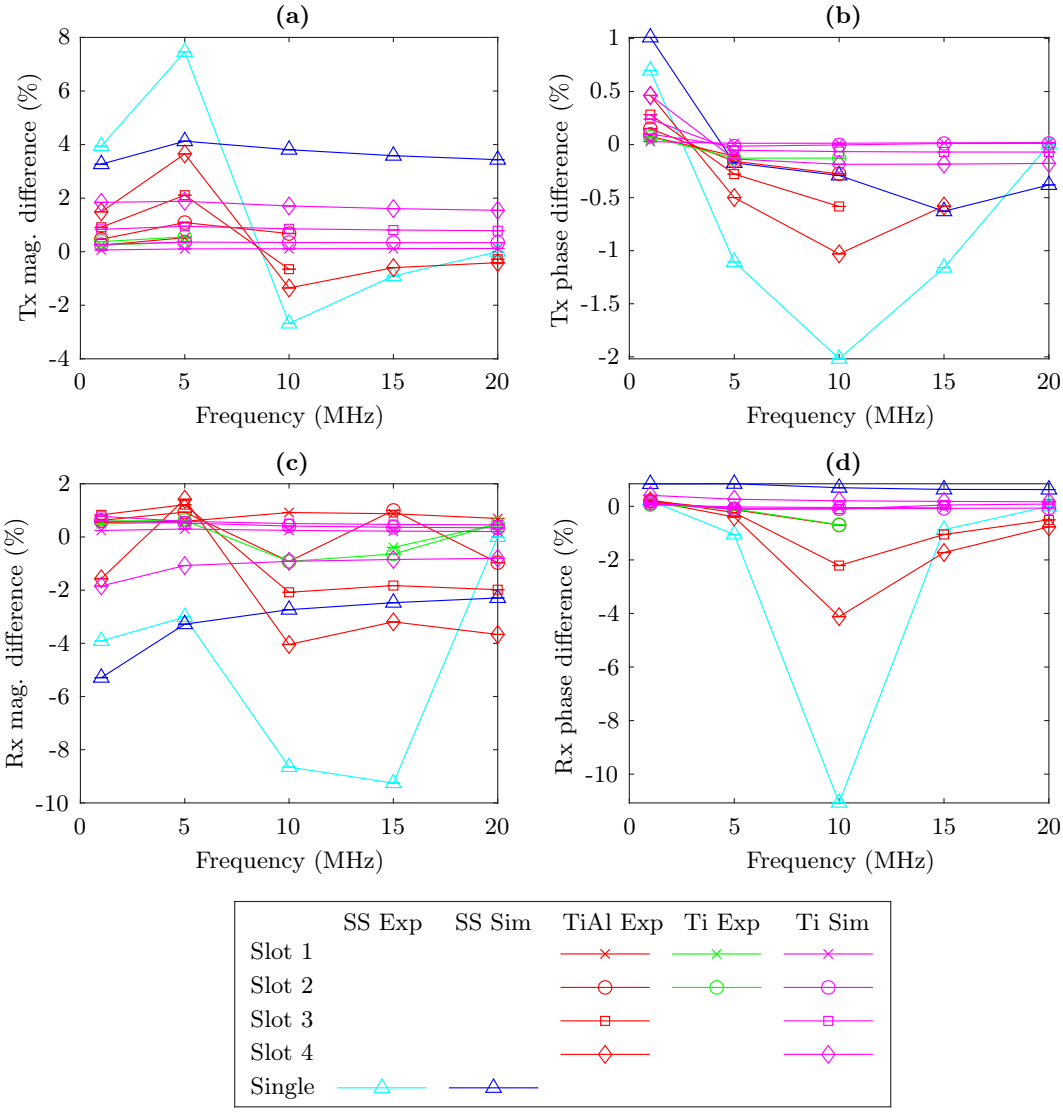

Figure 4.11: Defect signal as a percentage. Calculated by taking the difference between the signal and average of the background region divided by this average. Results for the perpendicular orientation.

The values are not exactly the same, but when combined with similarities in morphology between the experimental and simulation slots signals, the simulations can be used as a tool to try to understand some of the behaviour observed in the experiments. Cross-sections through the slot are shown to demonstrate some of these characteristics.

For the SS slots, the defect signal has a mainly bar-like profile that reflects footprint of slot, the side profiles of which can be seen in the line scans in figures 4.12 and 4.14 for the experimental results, and in its simulated counterpart in figures 4.13 and 4.13.

In figure 4.12, the results at 20 MHz appears noisy due to the banding present. The results are clearer in the 2D scans as more area is covered, which can be interpreted in a fairly intuitive manner as the data is visual in nature. It is worth noting that the experimental results along the y-direction such as in figure 4.14 may look like a continuous line scan. However, they are in fact composed of extracting data from different scan lines. It is, thus, more susceptible to showing lift-off as lift-off mainly occurs between scan lines. It was from this that it was suggested that the Rx phase may be more robust to lift-off, which formed the part of the rational to later study lift-off (section 4.3).

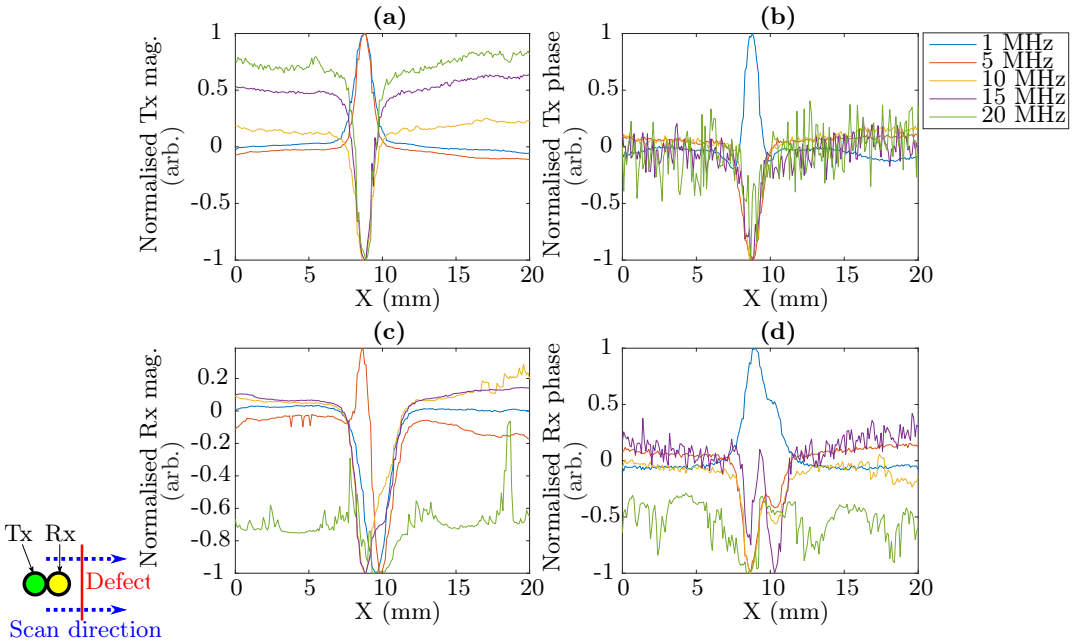

Figure 4.12: Cross-section through the centre of the 2D scan in experimental results for the perpendicular orientation on stainless steel.

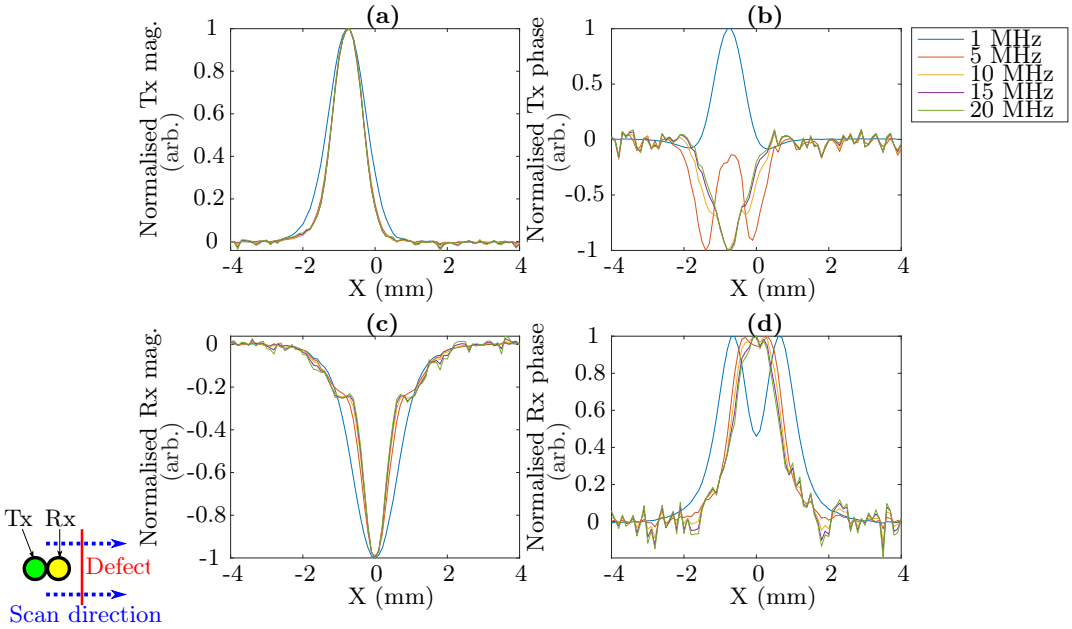

Figure 4.13: Cross-section through the centre of the 2D scan in simulation results for the perpendicular orientation on stainless steel.

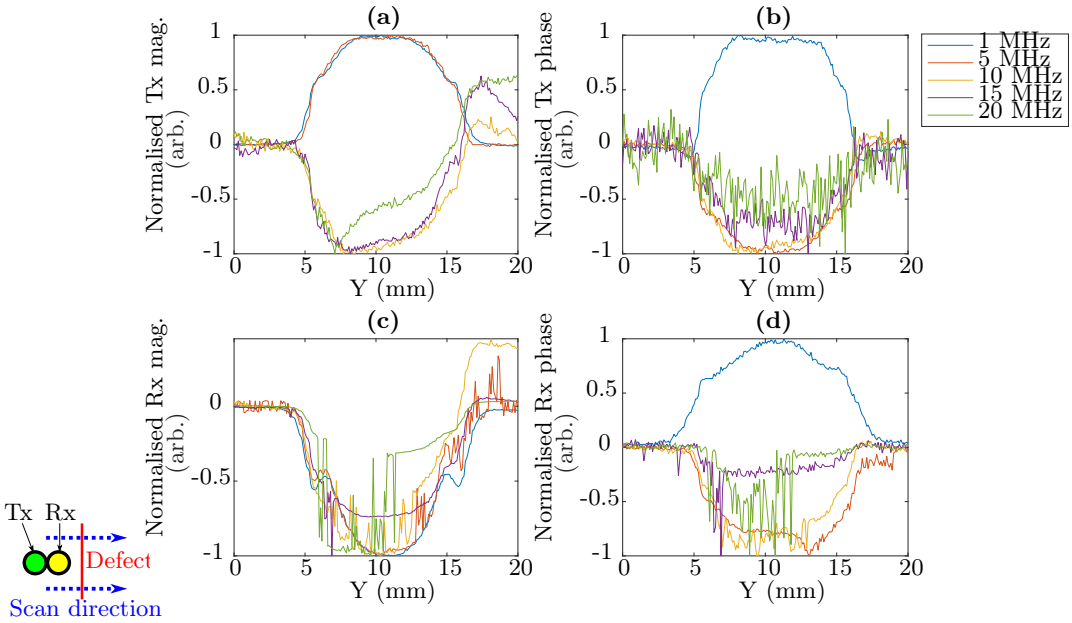

Figure 4.14: Cross-section through location with the maximum measured value in the experimental results for the perpendicular orientation on stainless steel.

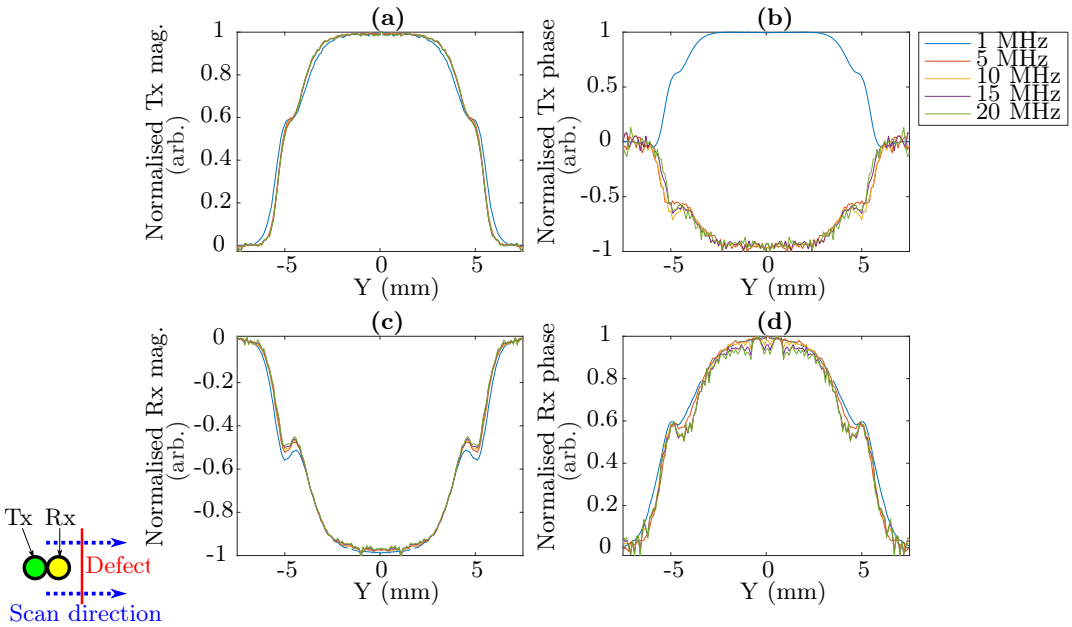

Figure 4.15: Cross-section through location with the maximum measured value in the simulation results for the perpendicular orientation on stainless steel.

Moreover, the signal can be seen to localises with frequency in both the experimental and simulation results (figure 4.16).

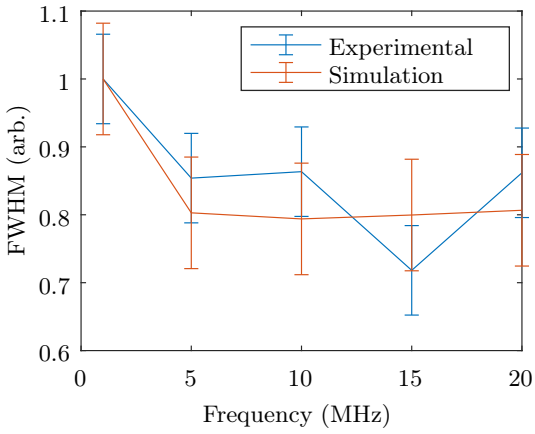

Figure 4.16: Full width half maxima through the width of the slot (through $Y = 10\,\text{mm}$ for the experimental results and $Y = 0\,\text{mm}$ for the simulation results) in the perpendicular orientation on stainless steel.

Cross-sections for select slots on the TiAl and Ti samples will also be presented.

Figure 4.17 shows a cross-section through the longest slot on the TiAl sample (nominally 2 mm long) from the experimental 2D scan, and figure 4.18 shows the simulated counterpart.

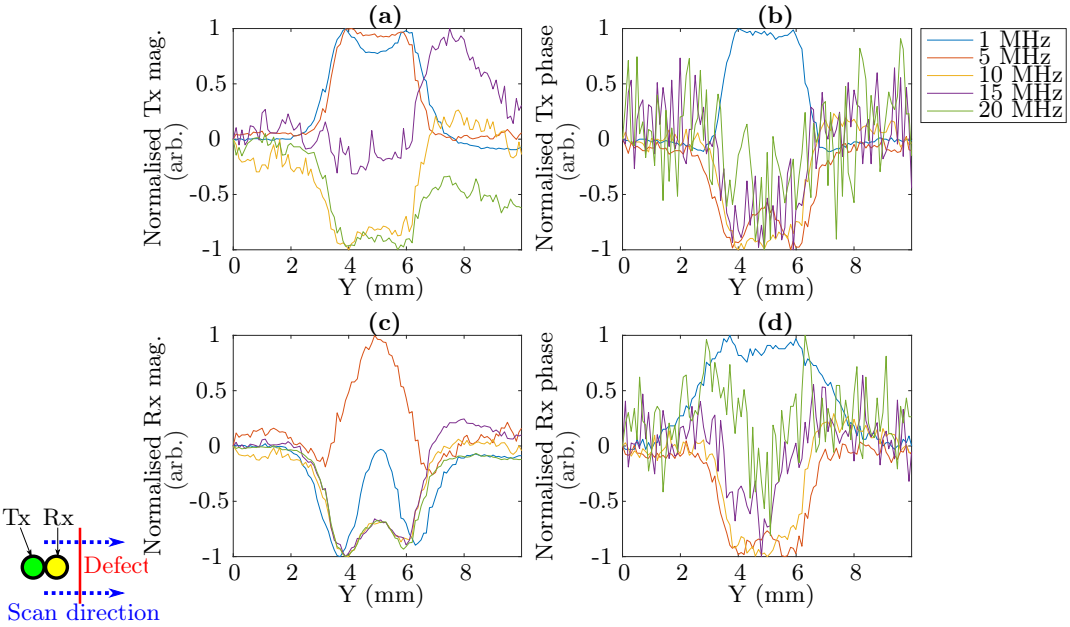

Figure 4.17: Cross-section through the centre of the experimental 2D scan for the perpendicular orientation on the longest slot (nominally 2 mm) on TiAl.

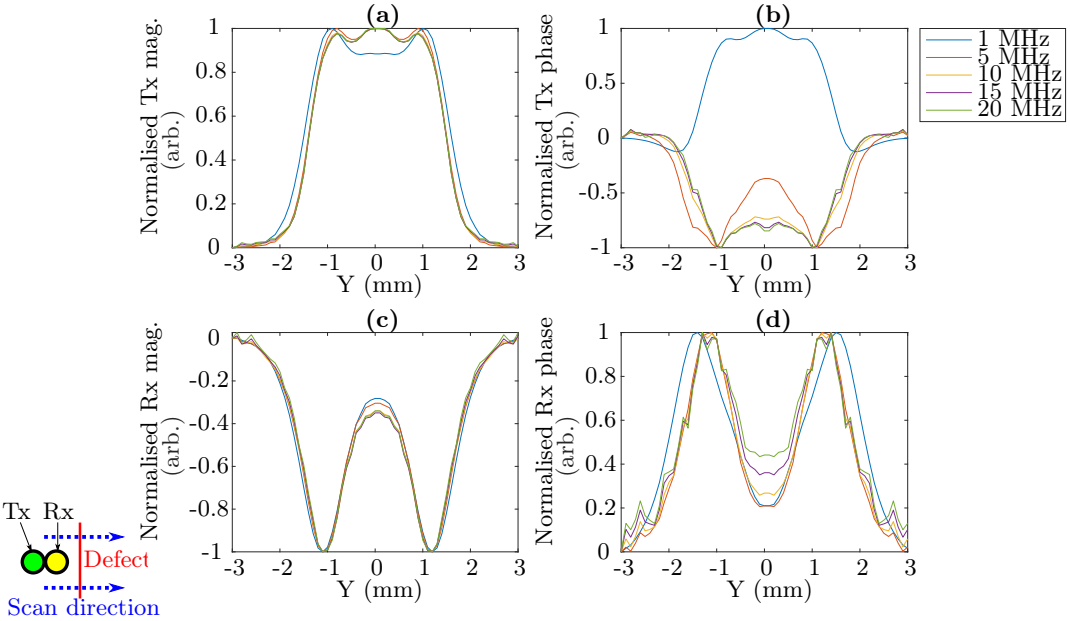

Figure 4.18: Cross-section through the centre of the simulated 2D scan for the perpendicular orientation on the longest slot (nominally 2 mm) on Ti.

While figure 4.19 shows a cross-section through the longest slot on the Ti sample (0.75(5) mm long) from the experimental 2D scan and figure 4.20 shows the simulated counterpart.

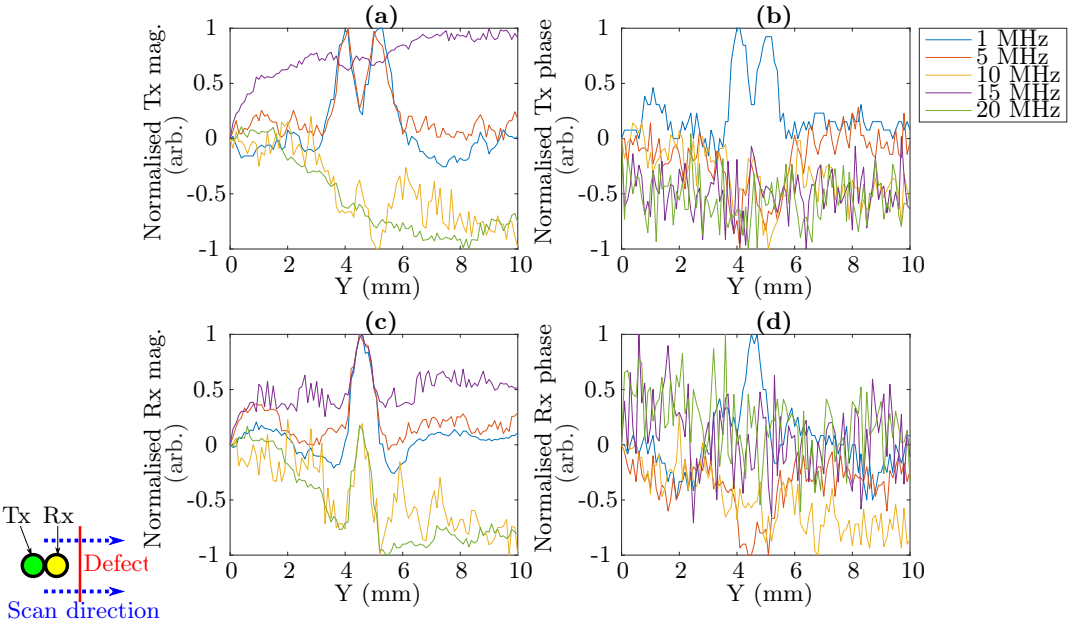

Figure 4.19: Cross-section through the centre of the experimental 2D scan for the perpendicular orientation on the longest slot (0.75(5) mm) on Ti.

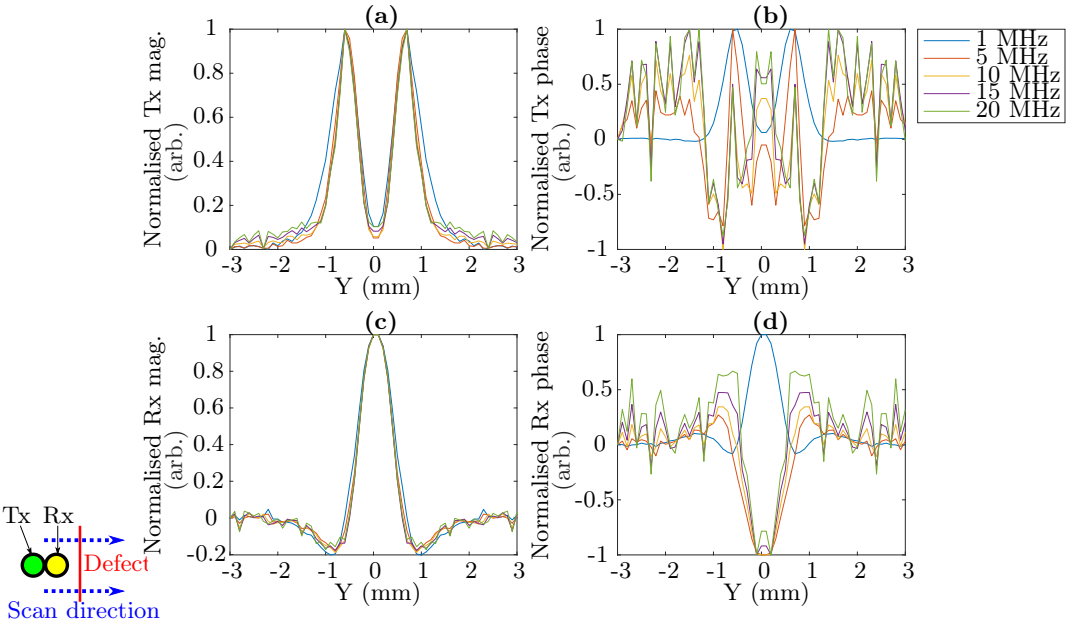

Figure 4.20: Cross-section through the centre of the simulated 2D scan for the perpendicular orientation on the 0.5 mm long slot on Ti.

The signals are well localised, and the the position where the signal is maximum for the Tx and Rx are not expected to coincide. This is a problem for selecting a single cross-section that shows the defect signal well. It is such that at high frequencies, it is difficult to observe the signal in a single cross-section. That being said, it is possible to see some similarities in morphology such as the double peaking in the Tx mag. for both the TiAl and Ti slots, as well as the w-shaped response to the larger TiAl slot and the single peaking response to the Ti slot in the Rx mag. This difference in the Rx mag. is caused by the size of the slot.

Moving on the results in the parallel orientation. Again, to quantify the signal, the defect search region is divided in to quadrants and halves for the TiAl and Ti samples respectively, and the background is set to be $[\mathrm{x}, \mathrm{y}, \mathrm{width}, \mathrm{height}] = [2, 7, 5, 5]$ mm on the original data for the TiAl sample and $[1, 7, 2.5, 2.5]$ mm on the original data for the Ti sample. The resulting SNR is shown in figure 4.21.

The SNRs appears to be high at 1 MHz though it tends to decrease with frequency, similar to the perpendicular results. The SNRs are also generally higher than those in the perpendicular direction. Furthermore, the SNR is improved for both the perpendicular and parallel scan orientations (SNRs shown figures 4.9 and 4.21) when considering the 1 MHz operation that had been previously tested. This suggests that the new resin 3D printed coil holder is helping to improve the scan results.

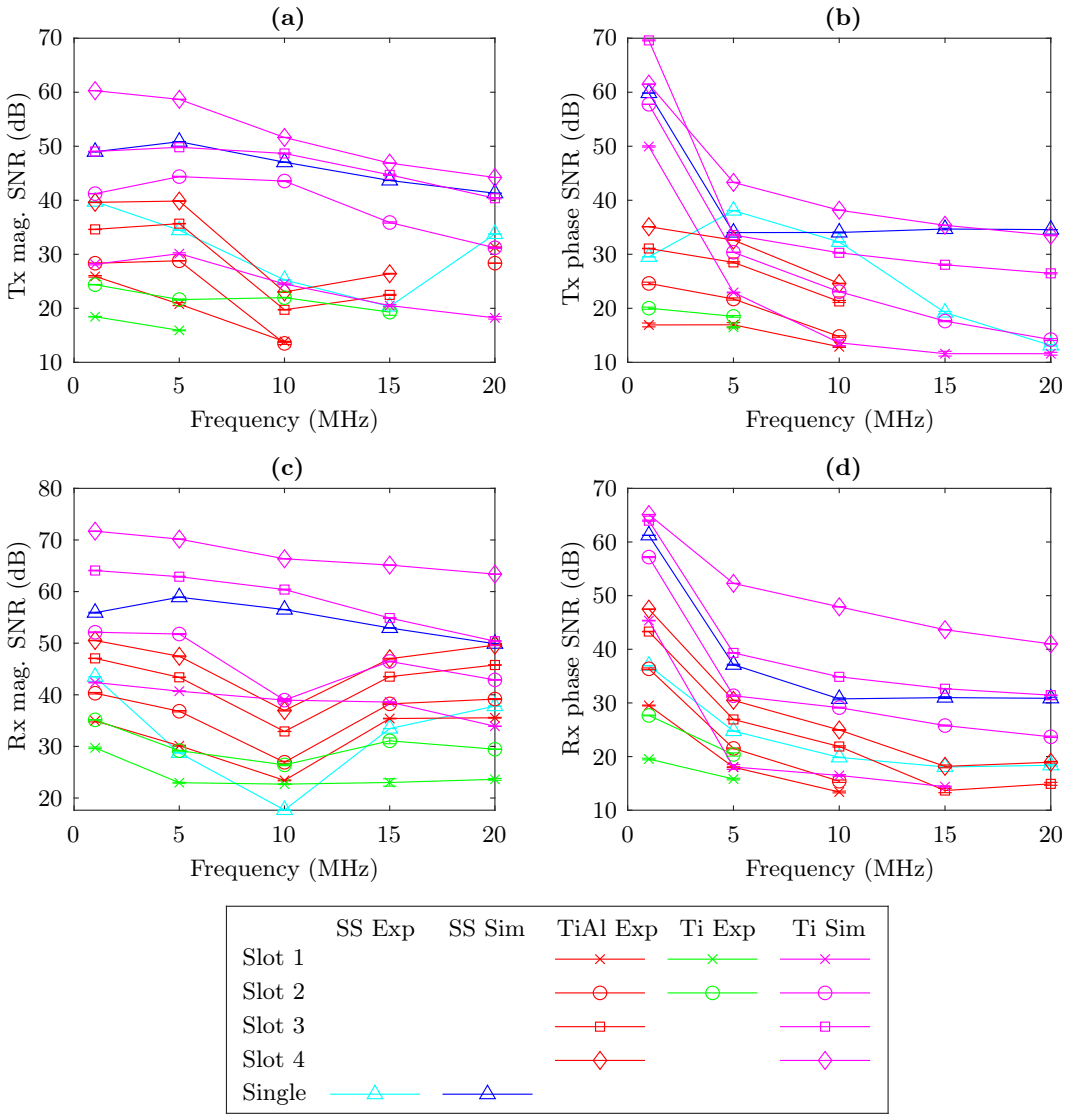

Figure 4.21: Signal-to-noise ratio as a function of frequency for the experimental and simulation results in the parallel orientation. The legend is arranged by row from the shortest to the longest slot. Exp and Sim are short for experimental and simulation results respectively.

From figure 4.22, the same divergence between the experimental and simulation results, seen in the perpendicular orientation, is present in the parallel orientation.

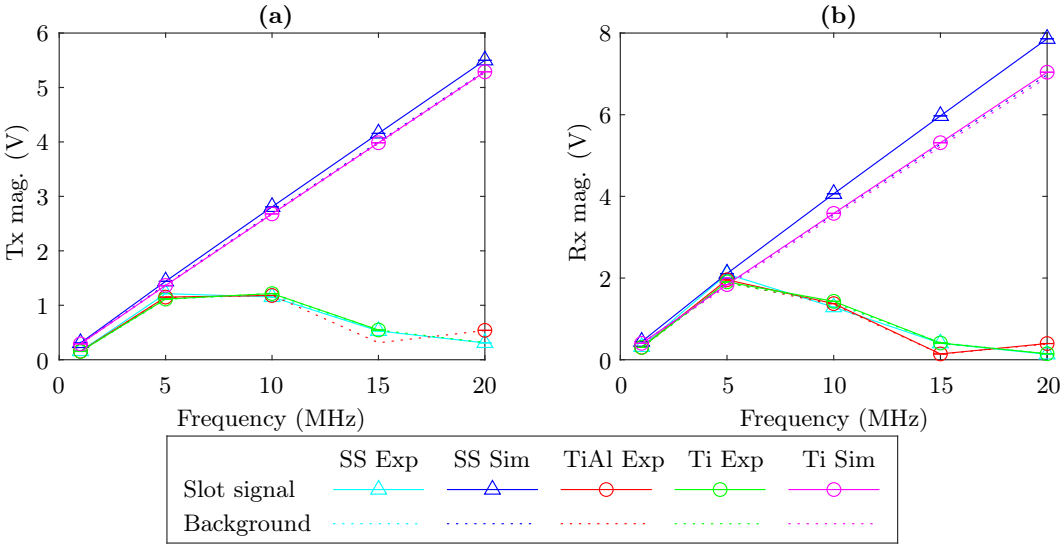

Figure 4.22: Voltage with frequency for experimental and simulation results in the parallel orientation. To simplify the plot, just the results for the 0.5 mm slot is shown for the TiAl and Ti samples.

The defect signal as a percentage of the background signal is shown in figure 4.23. This is the counterpart to figure 4.11 but in the parallel orientation. It can be seen that the plots are similar in Tx mag. and Tx phase compared to equivalent plots in the parallel orientation, which is to be expected, since the defect response would be expected to be just mainly rotated to reflect the different orientation of the slot. In fact, if one were to plot the values from the perpendicular results again the parallel results, the correlation coefficient would be 0.99 for the Tx mag. and 0.94 for the Tx phase. There is also some similarity in the Rx phase (correlation coefficient of 0.83).

The Rx mag. on the other hand differs significantly from the perpendicular results (correlation coefficient of 0.09). The Rx mag. response is to largely increase in response to the slot (positive values) in the parallel orientation, whereas the Rx mag. increases (positive values) for shorter slots and decreases (negative values) for larger slots in the perpendicular orientation.

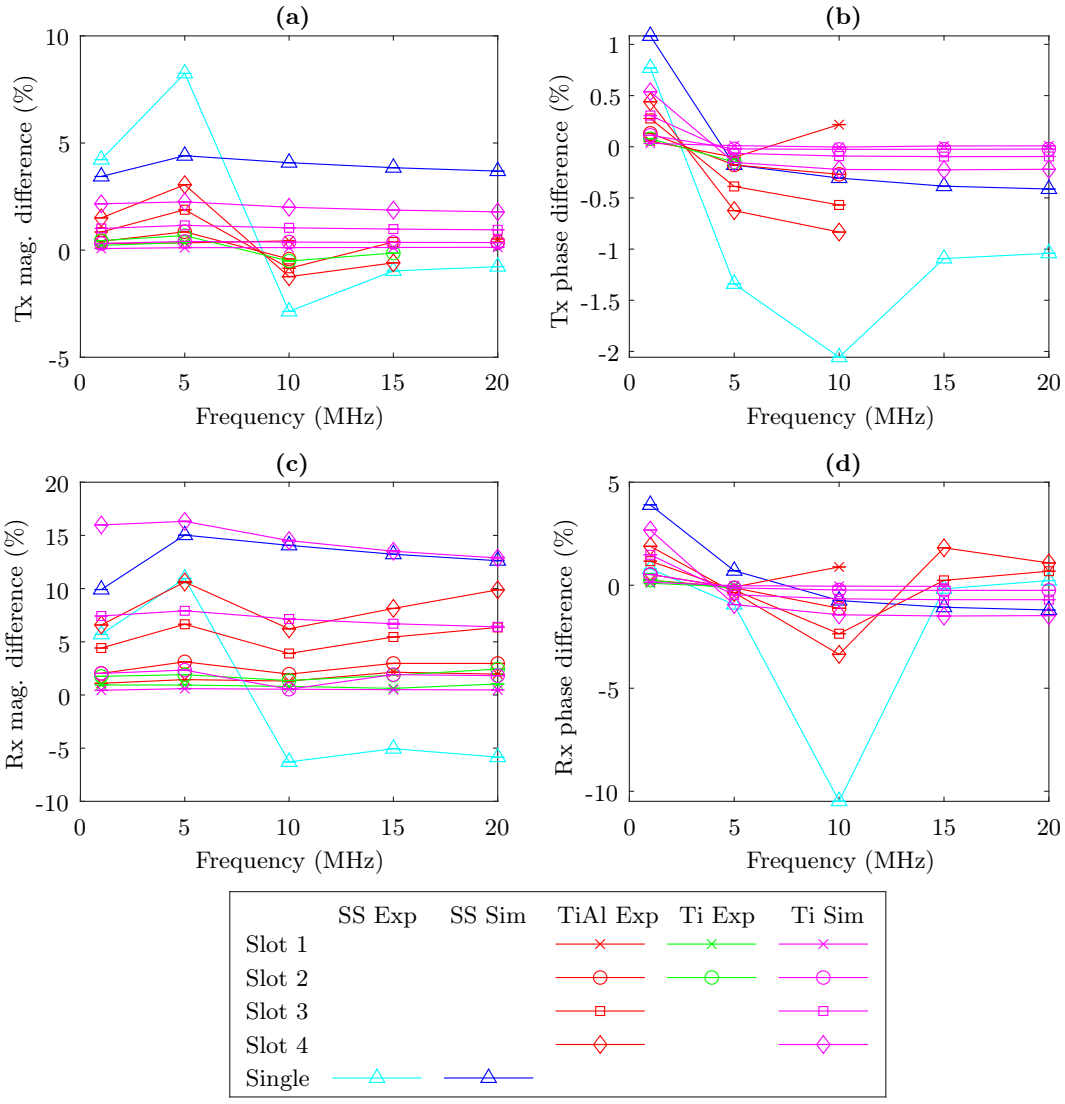

Figure 4.23: Defect signal as a percentage. Calculated by taking the difference between the signal and average of the background region divided by this average. Results for the parallel orientation.

It is possible to see further changes in morphology in the parallel results compared to the previous perpendicular results. For example, on the steel sample, there appears to be a double peaked defect signal in the Rx mag. along the slot length. This can be seen in figures 4.24 and 4.25, which are cross-sections from the experimental scan and the simulated counterpart respectively.

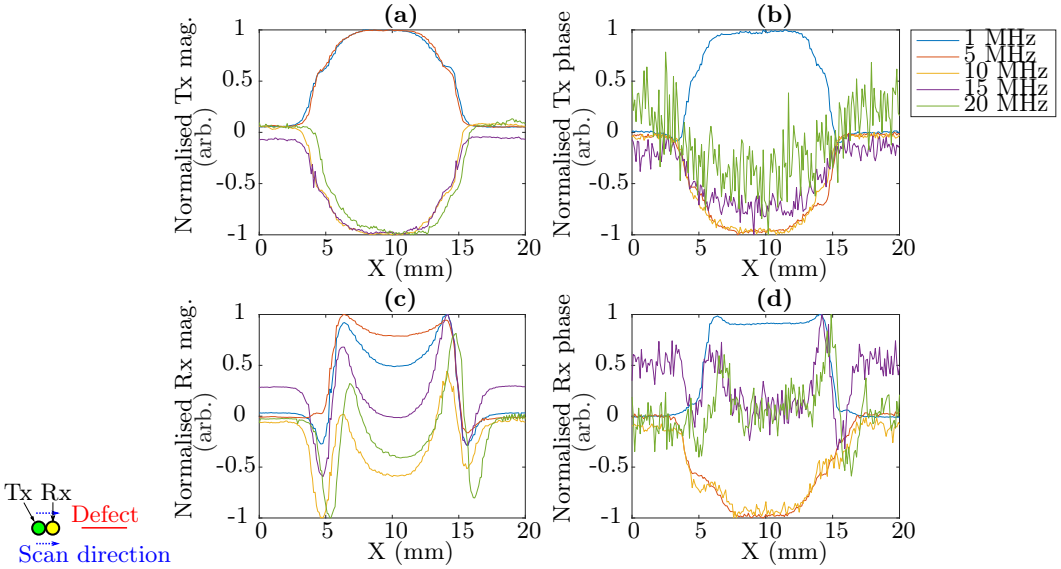

Figure 4.24: Cross-section through the centre of the 2D scan (through $Y = 10\,\text{mm}$) in experimental results for the parallel orientation on stainless steel.

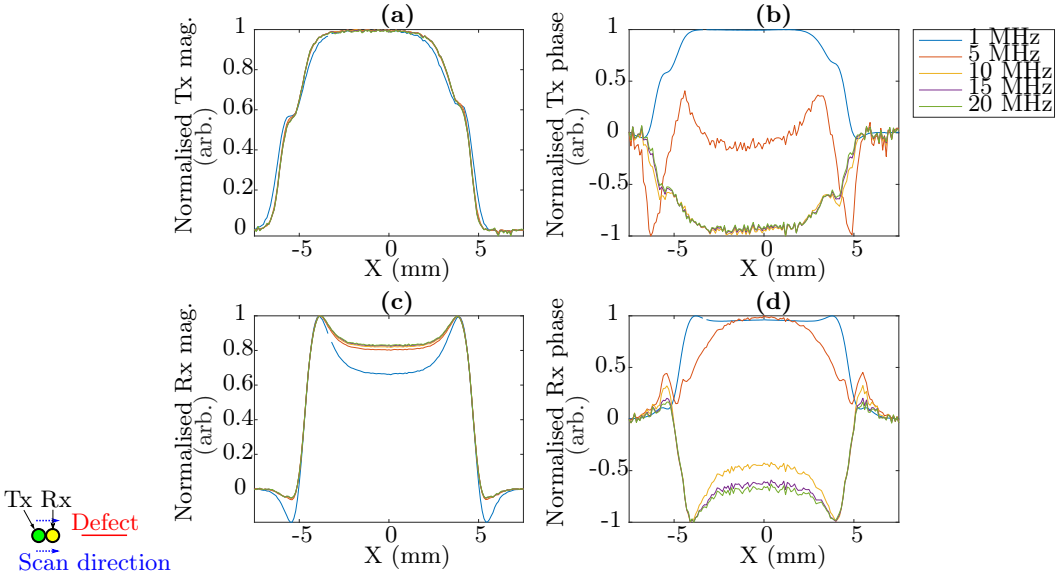

Figure 4.25: Cross-section through the centre of the 2D scan (through $Y = 0\,\text{mm}$) in simulation results for the parallel orientation on stainless steel.

Figure 4.26 and its simulated counterpart in figure 4.27 show the same defect signal but along the slots width.

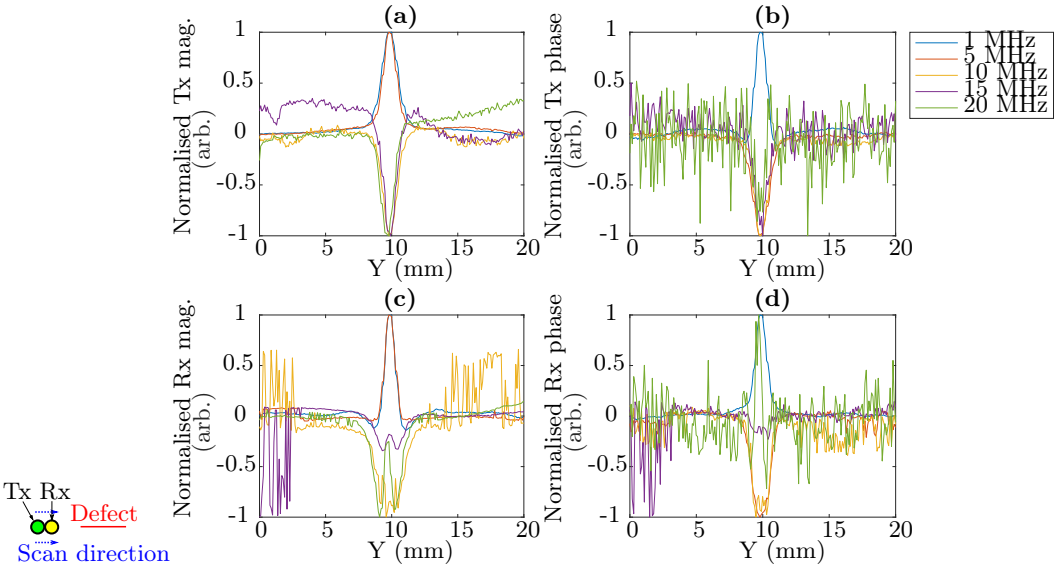

Figure 4.26: Cross-section through the centre of the 2D scan (through $X = 10\,\text{mm}$) in the experimental results for the parallel orientation on stainless steel.

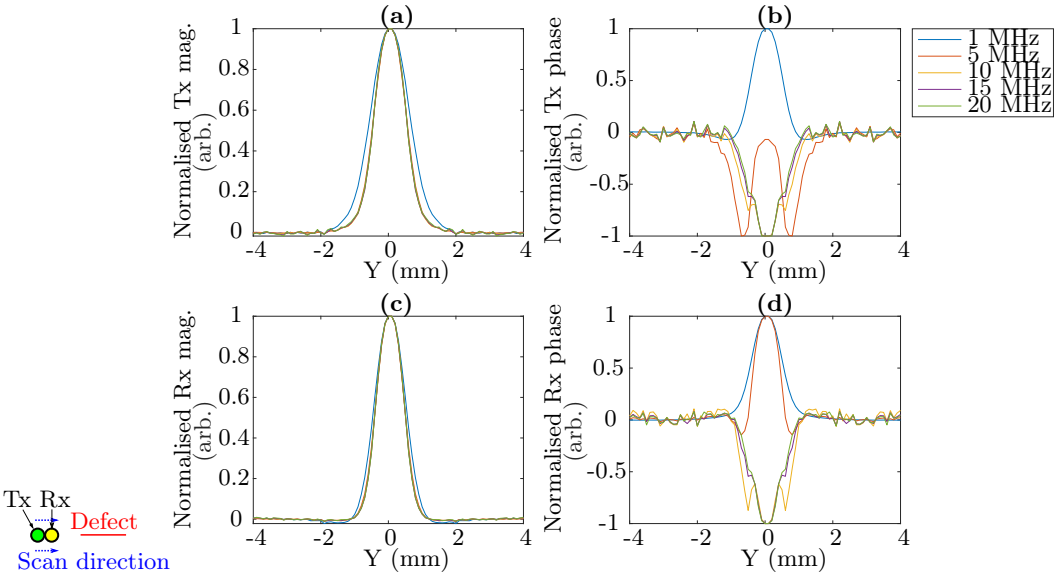

Figure 4.27: Cross-section through the centre of the 2D scan (through $X = 0\,\text{mm}$) in the simulation results for the parallel orientation on stainless steel.

Cross-sections in the parallel orientation are shown below for the TiAl and Ti slots to complement the previous cross-sections for the perpendicular orientation. Figure 4.28 shows the longest slot (nominally 2 mm) on the TiAl sample, while figure 4.29 shows its simulated counterpart.

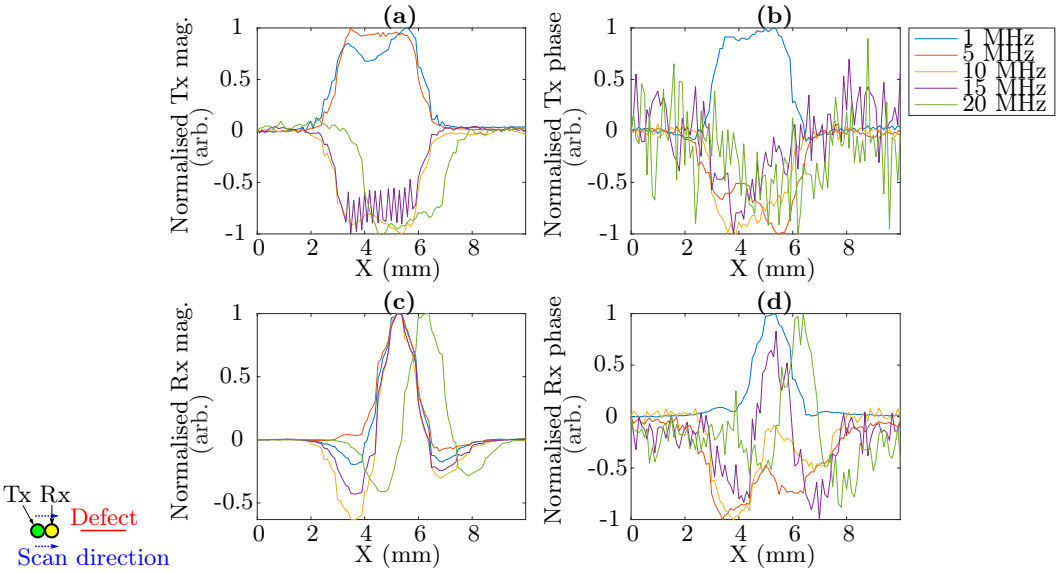

Figure 4.28: Cross-section through the centre of the 2D scan in experimental results for the parallel orientation on the longest slot (nominally 2 mm) on TiAl.

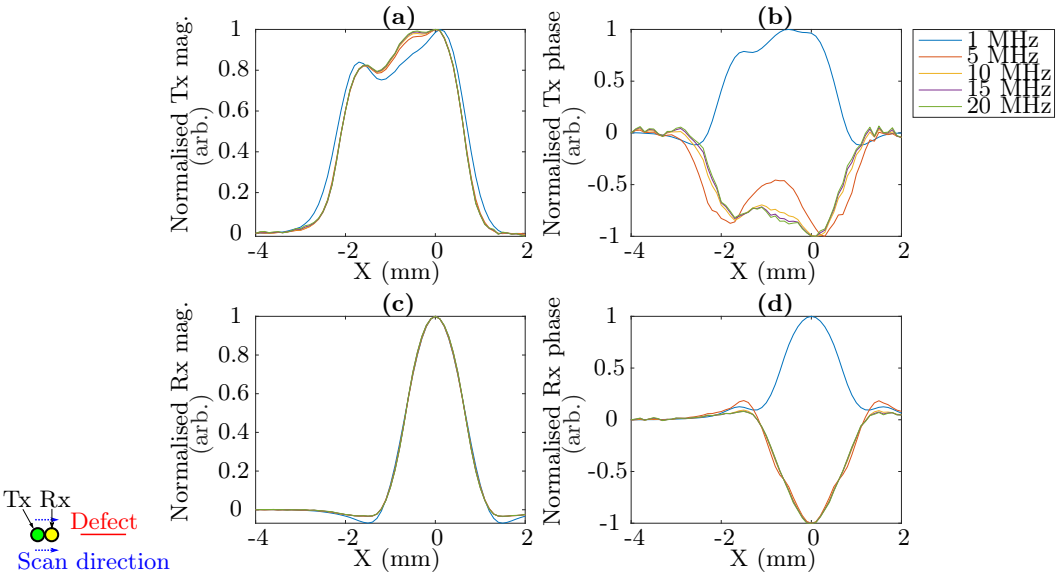

Figure 4.29: Cross-section through the centre of the 2D scan in simulation results for the parallel orientation on the longest slot (nominally 2 mm) on Ti.

While figure 4.30 shows the longest slot (0.75(5) mm long) on Ti and figure 4.31 shows its simulated counterpart.

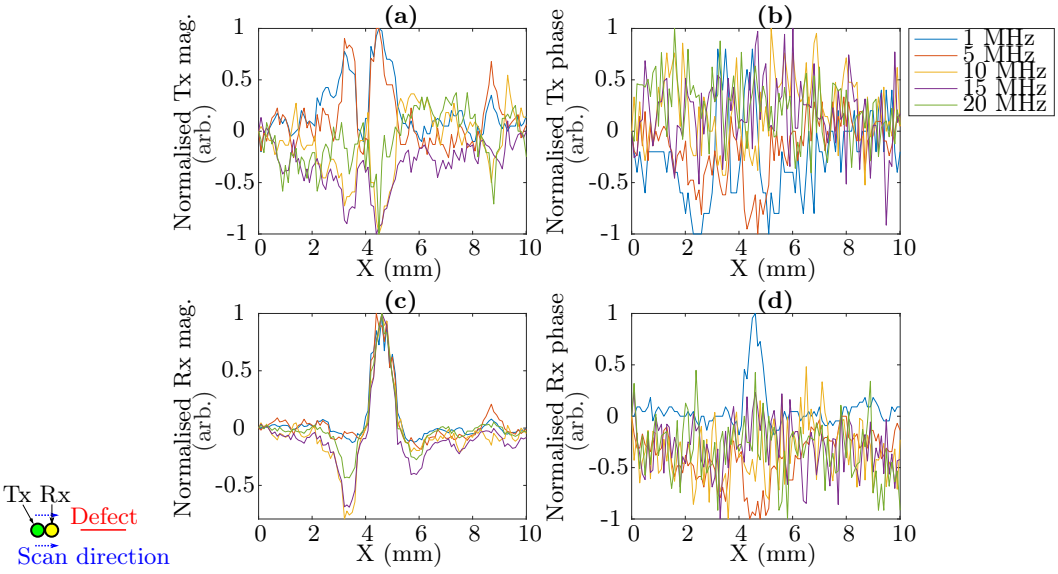

Figure 4.30: Cross-section through the centre of the 2D scan in experimental results for the parallel orientation on the longest slot (0.75(5) mm) on Ti.

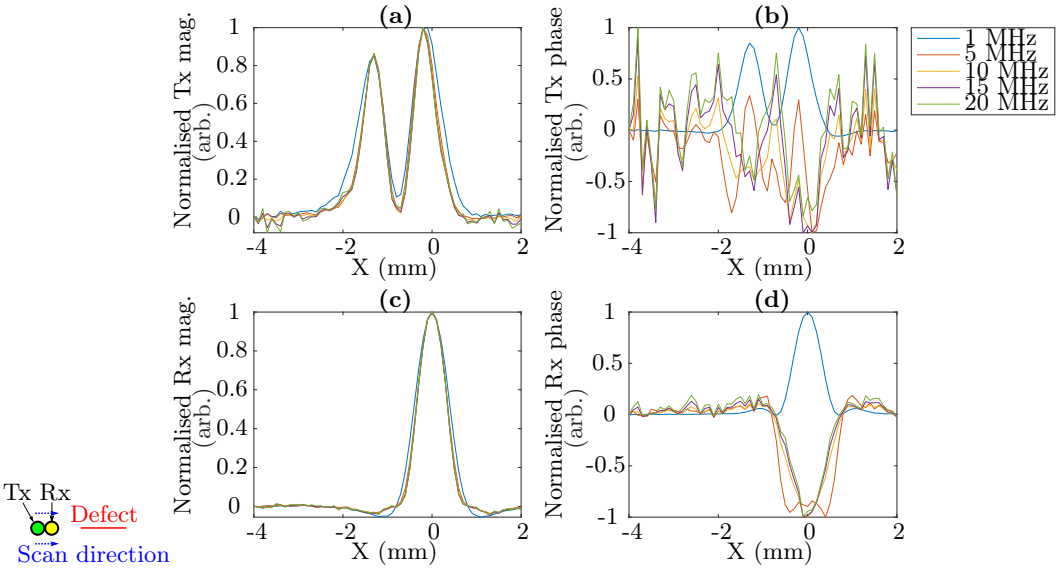

Figure 4.31: Cross-section through the centre of the 2D scan in simulation results for the parallel orientation on the 0.5 mm long slot on Ti.

There are similarities between the experimental and simulated cross-sections for the TiAl and Ti slots (figures 4.28-4.31), particularly in the less noisy magnitude plots and at lower frequencies. It can be seen that for both the TiAl and Ti slot that the Rx mag. response resembles more of a single peak. While, in the Tx mag., the Ti slot has a double peaking response, while the TiAl slot has a broader response from the peaks merging as the TiAl slot is longer. This can also be seen in the 2D scan plots.

Figure 4.32 shows correlation coefficient between the experimental and simulation results for the SNR and the defect signal as a percentage. For these calculations, the Ti simulations are used as the counterpart to the TiAl experimental results. As mentioned, the cause of the noise in the experimental and simulation results are fundamentally different. As such, the correlation coefficient may not be as strong. However, the correlation coefficient for the defect signal as a percentage seems to confirm that there are similarities in the experimental and simulation response to a slot at lower frequencies, but the response diverges at higher frequencies.

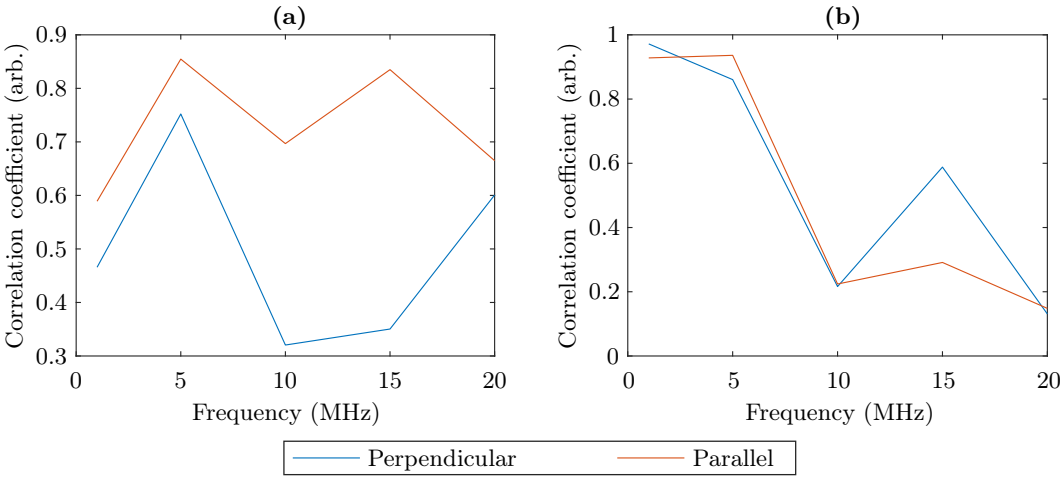

Figure 4.32: Correlation coefficient between the experimental and simulation results for (a) the SNR and (b) the defect signal as a percentage.

To summarise, the experimental results show similarities to the simulation results, particularly at 1 MHz, and the range of slots investigated help show the evolution of the defect profile with defect size. The Tx mag. measurement generally rises in response to the intersection of the slot with the coil wires. For slots that are long compared to the coil diameter, such as the one on the SS sample, this manifests as a region where the Tx mag. measurement increases when both coils are on the slot to form a raised bar on the 2D scan image with steps either side, where the coils are only partially on the slot, and thus are not cutting across the eddy currents as

strongly. Whereas for the slots that are short compared to the coil diameter, for example, those on the Ti sample or the smaller slots on the TiAl sample, there is not a sustained length where the coils are both on the slot, and thus the 2D scan image contains a feature that is more of a raised halo in shape, where the slot blocks the eddy current when underneath the coil's wires. The cause of the behaviour is the same, but the shape is different due to the different slot sizes. The explanation for the Tx phase response is similar.

The Rx mag. measurement appears to dip in the 2D scans when the slot blocks the eddy current as it does for sufficiently long slots, such as the longest slot on the Ti sample or the slot on the SS sample, in the perpendicular orientation. This can be intuitively explained by the diminished eddy current reducing the voltage induced in the Rx coil. On the larger SS slot, there are peaks near the ends of the defect signal in the Rx mag. for the scan in the parallel orientation and a single peak for the smaller slots on the other samples in either orientation. It appears that for these scenarios, the Rx mag. generally rises, which could be because of a build-up in eddy current close to the edge of the slot. Though, there is some dipping around the main signal, which may evolves to be the main signal when the eddy current is more strongly blocked and pushed under the slot.

Furthermore, the greatest SNRs are achieved at 1 MHz in the parallel orientation for TiAl and Ti slots. The SNRs are good even for the shorter slot, though the SNRs rise greatly for the longer slots. Operating at higher frequencies generally results in a lower SNR. However, there is more spatial localisation of the defect signal at higher frequencies; for example, in the perpendicular orientation, the FWHM of the Tx mag. signal reduces from 1.5(2) mm at 1 MHz to 1.3(2) mm at 20 MHz across the width of the SS slot.

There is much less horizontal banding in the 2D scan results with the implementation of the resin 3D printed coil holder, as lift-off is reduced by allowing the sensor to follow the surface of the sample. With this development, the results have much improved SNRs. The system is capable of detecting sub-millimetre sized defects with good SNRs, but the system will be altered further in chapter 6. The system in chapter 6 will use an AD8302 chip to measure the voltage gain/phase, and the chips themselves have the benefit of being relatively inexpensive and compact.

4.3 Varying lift-off of eddy current coils

4.3.1 Experimental setup for varying lift-off

It had been observed that the Rx phase seemed to response less to lift-off in the 2D scans. This is significant since lift-off variation is known to be one of the main factors that can limit effective eddy current testing (ECT) [125], where variations in lift-off have the potential to mask a defect. However, this was more of a suggestion based on our understanding where lift-off was more likely to occur (i.e. from scan line to scan line).

To be confident in the result, a study whereby lift-off is controlled would be needed. To perform this study, a micrometer (Newport 423 series) was added to vary lift-off. The sensor is attached to the micrometer, which is mounted to a horizontal bar that is parallel to the sample surface, a depiction of this is shown in figure 4.33. All the results presented in this chapter are taken with the slot in the parallel orientation (also depicted in figure 4.33).

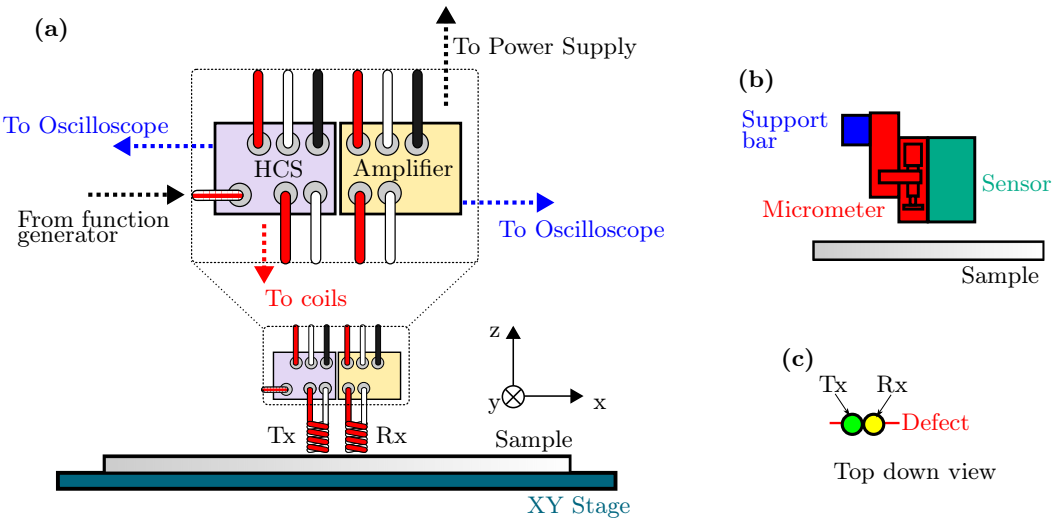

Figure 4.33: Setup for lift-off experiment. (a) General setup. (b) Depiction of the vertical positioning micrometer and how it is mounted to allow lift-off to be varied (z-direction in (a)). The micrometer is mounted to a horizontal support bar and the sample mounted to a table that can be tilted to get the probe and surface of the sample flush. (c) Orientation of slot with respect to the coils.

Additionally, the figures that show only the 1 MHz results (i.e. figures 4.34, 4.37 and 4.40) are taken with the DPO3034 oscilloscope while the remaining figures are taken with the MDO4054C oscilloscope, which will also be the oscilloscope that will be used in all proceeding chapters in this thesis.

4.4 Experimental results from varying lift-off

4.4.1 Results on the stainless steel sample

For the SS sample, there is one slot of length 10 mm, width 60 µm and depth 1.15 mm. Lift-off measurements are taken at a location away from the slot, and at three locations on the slot: the left, middle and right to coincide with where the defect signal peaks (middle location from Tx mag., and left and right from the double-peaked structure in the Rx mag.). Figure 4.34 shows the results for lift-off measurements taken at 1 MHz. The experimental results are plotted alongside the simulation results, and can be seen to respond similarly.

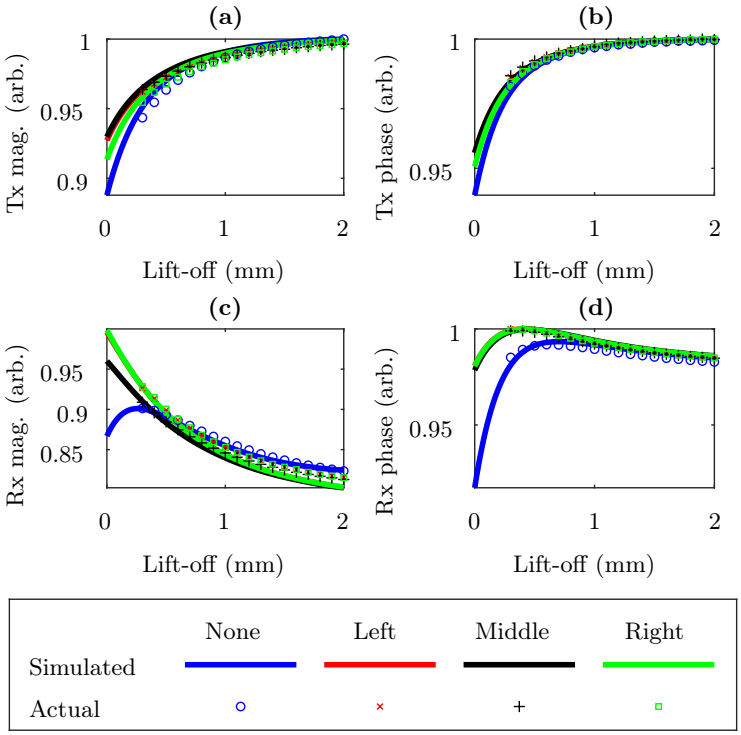

Figure 4.34: Normalised experimental and simulation results showing lift-off response on Stainless Steel (316L) for transmitter (Tx) and receiver (Rx) coils at 1 MHz. Results normalised so that the maximum of the experimental and simulation data are equal to unity with the exception of the experimental Rx magnitude, which is normalised so that the measurement at the closest lift-off (0.3 mm aligns with the theoretical value at the same point to aid with comparison. The measurements are taken at three positions on the slot (left, middle and right) and at one position away from the slot, which are colour coded according to the legend.

Figure 4.35 shows the results for lift-off measurements where the frequency is swept between 1 MHz and 20 MHz for each location. As previously mentioned, the system resonance causes the simulation and experimental results to diverge at higher frequencies. Accordingly, they are not plotted together in this figure.

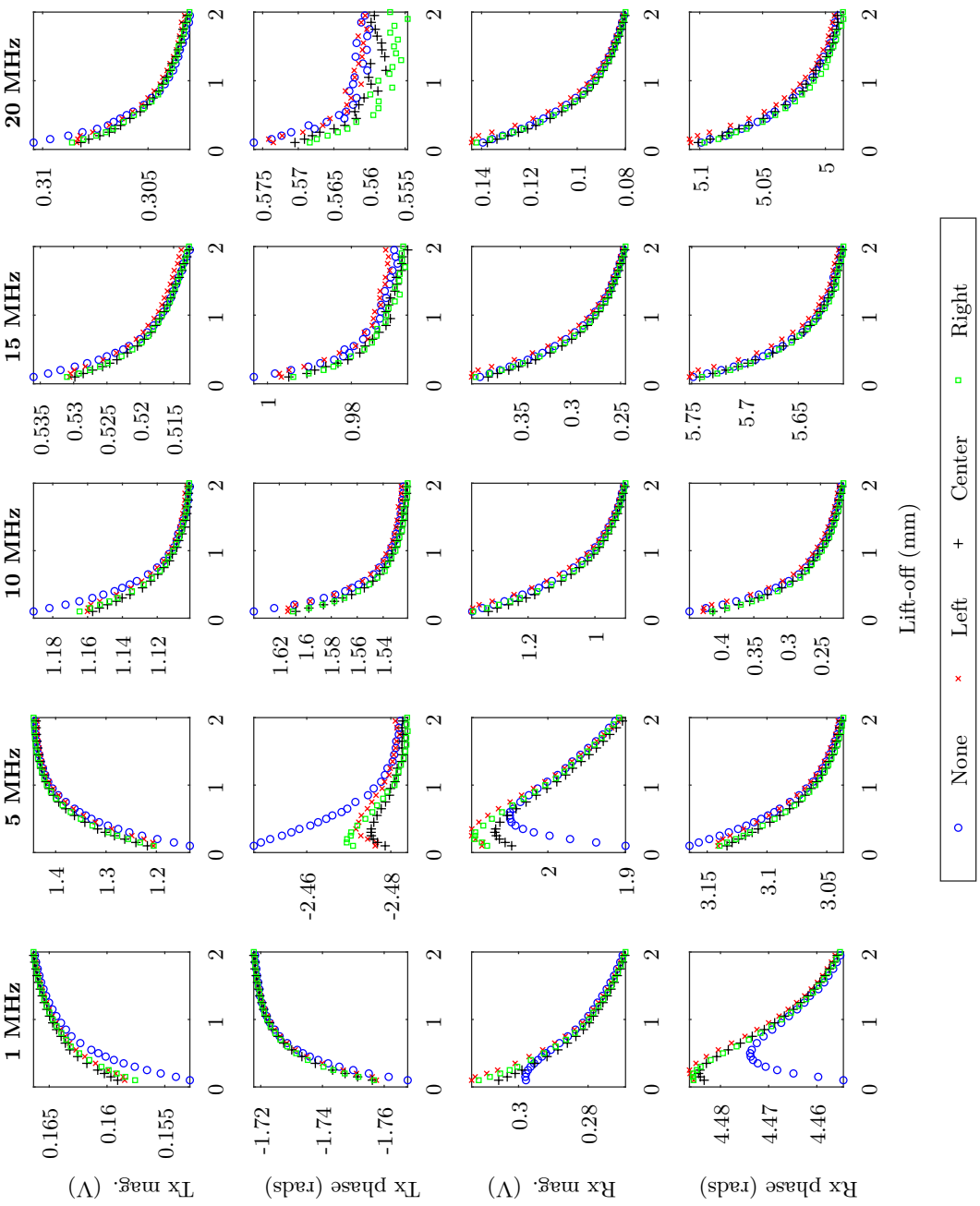

Figure 4.35: Experimental lift-off measurement results on Stainless Steel at several frequencies. Arranged in columns by frequency and in rows by the measured parameter.

For figure 4.34, each subplot is normalised, so that the maximum of each subplot is equal to unity, except for Rx mag. For Rx mag., the simulation result remains normalised to have a maximum equal to unity, but the experimental results are normalised so the maximum at the lowest lift-off considered coincides with the Rx mag. measurement at the same lift-off in the simulation results. This is because the maximum Rx mag. in the simulation results occurs before the lowest lift-off in the experimental results. Normalising in this way allows the simulation and experimental curves to be compared, where the simulation results can be seen to match the experimentally observed behaviour. The correlation coefficients between the experimental and simulation data are 0.99, 1.00, 1.00 and 0.98 for the Tx mag., Tx phase, Rx mag. and Rx phase respectively.

The Rx phase appears more robust to lift-off variation when compared to the other measured parameters. The larger differences in the lift-off curves for defect and defect-free regions compared to the variation due to lift-off is indicative of greater robustness to lift-off. The defect signal should be clearly distinguishable from the lift-off response, where a change in the signal caused by lift-off variation is unlikely to be mistaken for a defect signal, as there is a significant separation between the defect and defect-free curves with the curves not touching for a reasonable lift-off of less than 1 mm. To quantify this, the Rx phase changes by approximately 0.2% with lift-off while the difference between the defect and defect-free regions is around 1.4% at the lowest lift-off. The lift-off curves are relatively closer for the other measured parameters, and a defect is thus more likely to be masked in these parameters. For example, the change due to lift-off is 6.0%, 1.9% and 8.6% for Tx mag., Tx phase and Rx mag. respectively, while the difference between the defect and defect-free locations at the lowest lift-off considered is around 2.1%, 0.4%, and 3.0% for Tx mag., Tx phase and Rx mag. respectively. This is a significant result that we have published [177] since lift-off can often obscure a defect, even if there is a strong response to the defect, since the defect may not be seen if the lift-off response is equally strong. It is however a result specific to this defect size; it may not be universal across all defect parameters and lift-offs. Whilst the gap between the defect and defect-free curves may seem small, the lift-off variations in the scans are evidently gradual enough when using the XY stage so that only a small separation between the defect and defect-free curves is required to detect the defect.

For figure 4.35, the plots are not normalised, but they are plotted in a way where the maximum and minimum values are at the top and bottom of the plot so that the relative gap between the lift-off curves and the variation due to lift-off can be compared. It can be seen that separation between the curves for each

subplot seems to be greatest at 1 MHz-5 MHz and with increasing frequency, the gap between the curves generally reduces. Thus, the signals are less robust to lift-off with increasing frequency. This contributes to the general undulation/horizontal banding in the background of the 2D scans increasing as the frequency increases. To quantify the differences due to a) the defect and b) lift-off, figure 4.36 shows the ratio of the difference between the defect and defect-free locations at the lowest lift-off, and the change due to lift-off, which confirms the separation is better at lower frequencies, particularly for the Rx phase at 1 MHz.

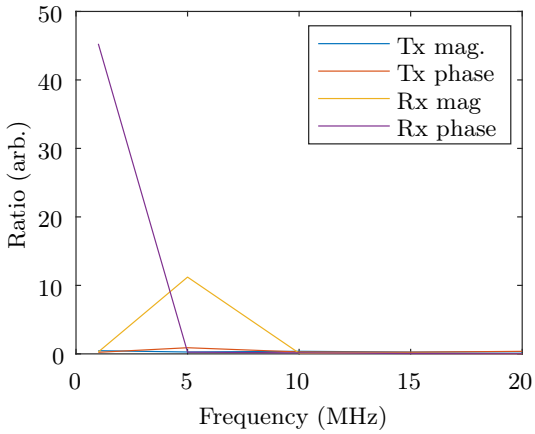

Figure 4.36: Ratio of difference in signal due to the defect and lift-off for stainless steel slot.

Additionally, the curves are less stable with increasing frequency, particularly in the Tx phase data. This is likely related to the salt and pepper like noise in the 2D scans at increasing frequency, and could (as discussed previously) be caused by electrical noise from increased shunt capacitance and unwanted inductance in connecting wires. At these frequencies, the electrical instabilities seem to be more of a limiting factor for defect detection.

4.4.2 Results on the TiAl sample

For each slot, lift-off measurements will be taken at one location. This location was chosen to be where the Rx mag. peak arises. The reasoning for taking lift-off measurements at this location was discussed in subsection 4.4.2. It was identified to be a good reference point for consistent lift-off measurements, and it happens to occur when the centre of the slot and centre of the two coils coincide in the simulated 2D scans. The slots will be referred to by their nominal lengths and as a reminder, the full set of slot sizes is given in table 2.1.

The normalised experimental results are plotted for 1 MHz in figure 4.37 and at different frequencies in figure 4.38. All the plots are all normalised by dividing by the maximum value and there are no simulation results plotted alongside due to uncertainty in the exact conductivity of the TiAl sample.

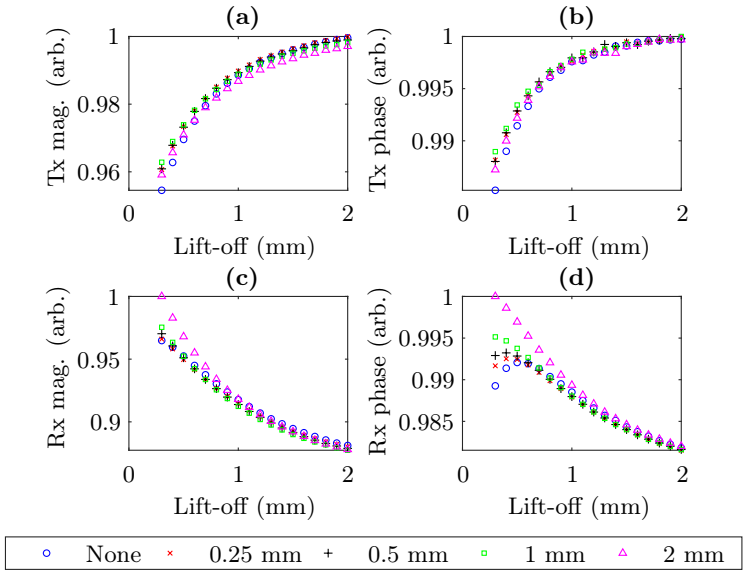

Figure 4.37: Experimental results showing lift-off response on titanium aluminide for the transmitter (Tx) and receiver (Rx) coils. The purpose of this plot is to determine the lift-off change that would be required to give the same reading as a measurement above a defect or defect-free region. Results are normalised so that the maximum value on any plot is unity. The values on the legend represent the length of the defect. There is a particularly large separation between the defect-free and defect curves in the Rx phase. Note that although the separation in plot (c) appears to be small, the high signal-to-noise ratio means that the separation is clear at the low lift-offs.

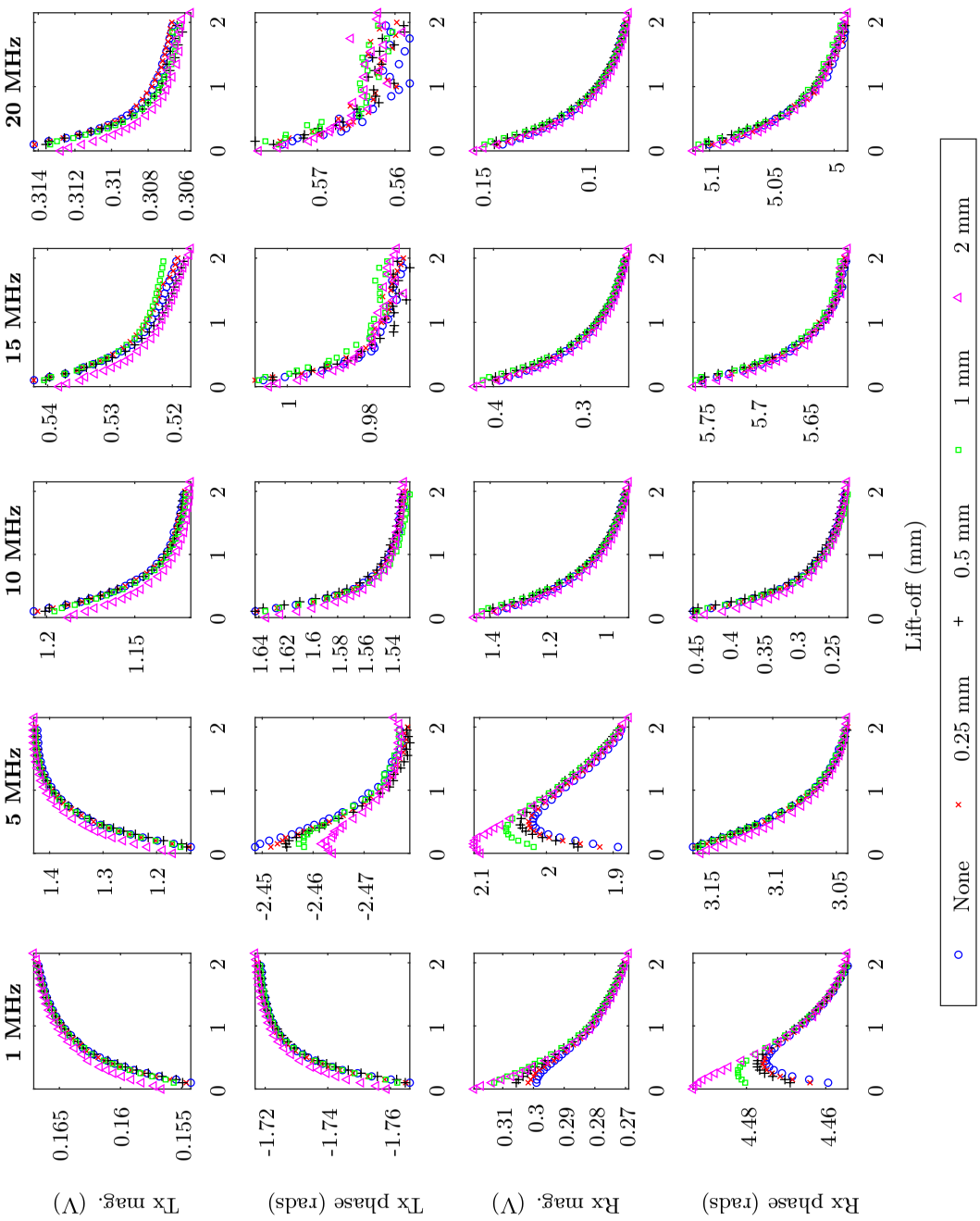

Figure 4.38: Experimental lift-off on TiAl at several frequencies. Arranged in columns by frequency and in rows by the measured parameter.

The lift-off curves for the TiAl slots in figure 4.37 look similar in shape to the ones for the SS slot, though different slot sizes are presented, where the difference between defect and defect-free regions is most apparent for the longest slot (nominally 2 mm), although is also a significant difference for the shortest slot (nominally 0.25 mm).

The largest observed gap between the curves is in the Rx phase measurement, indicating it is more robust to lift-off variation. Accordingly, the Rx phase measurement again appears to be more robust to lift-off variations, where there is a larger variation in the measurement between a defect and defect-free region up to a lift-off of 0.5 mm than would be caused by any variation in lift-off when compared to the other parameters.

In figure 4.38, the curves appear generally better separated between 1 MHz-5 MHz, as seen in the SS results. They become closer at higher frequencies, which results in less robustness to lift-off and more banding. To quantify the difference due to a) the defect and b) lift-off, figure 4.39 shows the ratio of a) the difference between the defect and defect-free values at the lowest lift-off and b) the change due to lift-off, which confirms that the separation is best between 1 MHz-5 MHz.

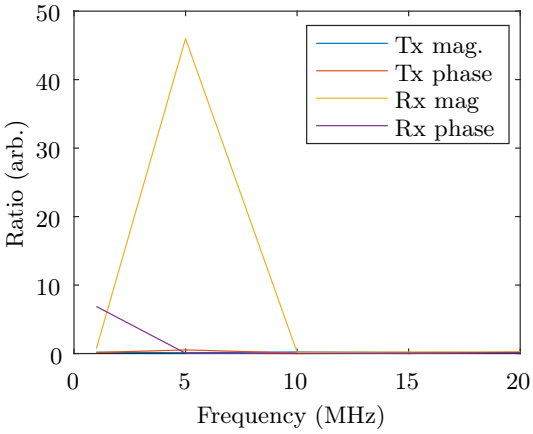

Figure 4.39: Ratio of difference due to the defect and lift-off for TiAl slot.

Moreover, the instability in the curves, especially for the Tx phase data, appear to increase with increasing frequency, which may be related to the salt and pepper like noise caused by the electronics.

4.4.3 Results on the Ti sample

The experimental and simulation results normalised by their maximum value are shown in figure 4.40, and the experimental lift-off results from sweeping the frequency is shown in figure 4.41. Only figure 4.40 has the simulation and experimental results on a single plot, since the simulation results diverge from the experimental results at higher frequencies. In figure 4.40, the simulation results appear similar to the experimental results. The correlation coefficients are 1.00, 1.00, 1.00 and 0.73 for Tx mag., Tx phase, Rx mag. and Rx phase respectively.

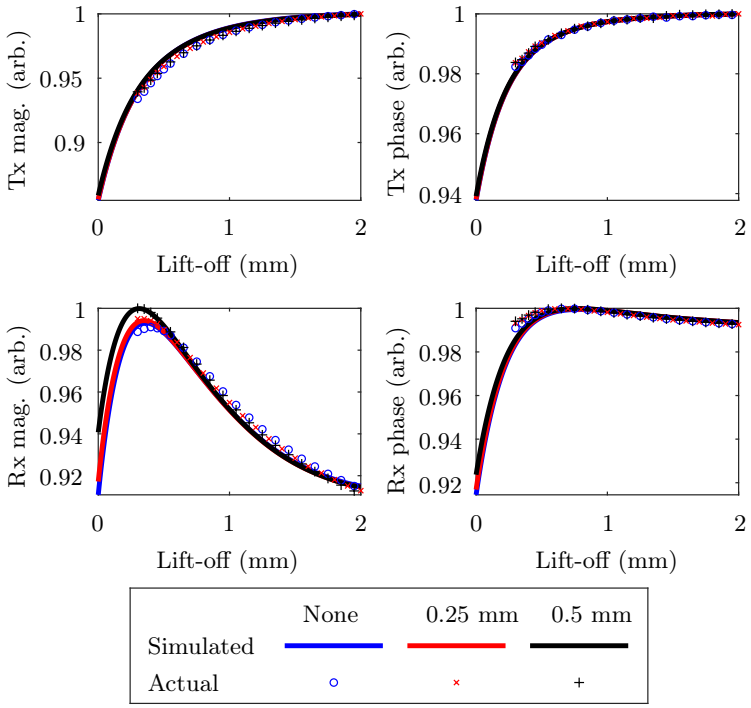

Figure 4.40: Simulation and experimental results showing lift-off response on titanium for the transmitter (Tx) and receiver (Rx) coils at 1 MHz. Results normalised so that the maximum of the experimental and simulation data are equal to unity. Experimental and simulation data show a similar response between the defect-free and defect regions.

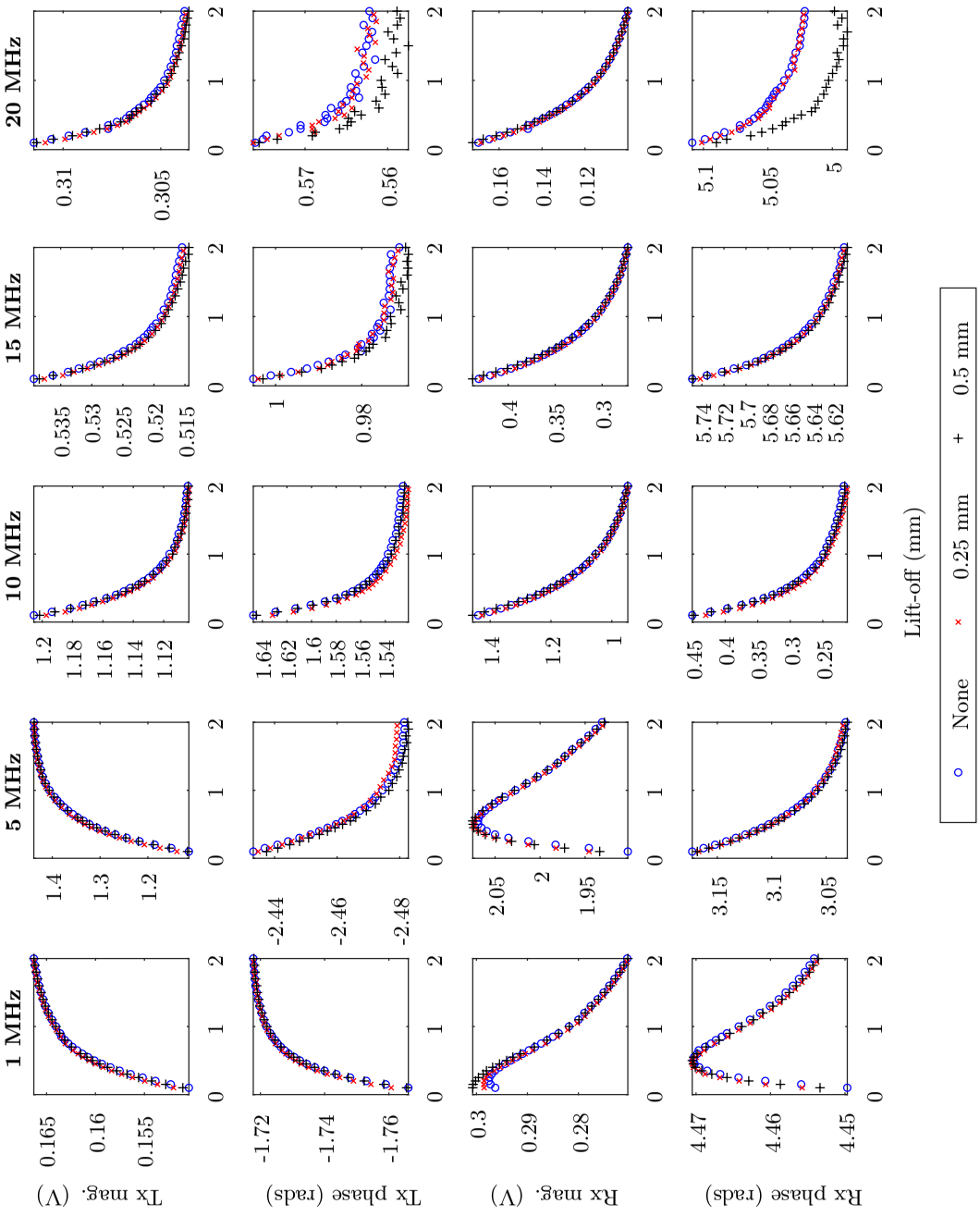

Figure 4.41: Experimental lift-off on Ti at several frequencies. Arranged in columns by frequency and in rows by the measured parameter.

There are many similarities to the results from the other sample, including the general shape of the curves and the largest defect having the largest response. As before, the ratio of the difference between the defect and defect-free locations at the lowest lift-off, and the change due to lift-off will be plotted. The result is shown in figure 4.42. The ratios suggest that the Rx mag. and Rx phase are the most robust to lift-off. Though, the generally lower ratio, also suggest that measurements on the Ti sample are generally more susceptible to lift-off.

Additionally, at higher frequencies (figure 4.38), the lift-off curves are more unstable, which is likely related to the increased noise in the 2D scans at higher frequencies, where increasing the frequency seems to have no particular benefit for the sensor used on these samples. However, in chapter 5, it will be seen that increasing the frequency may help with the detection of edge defects and, in particular, the Rx phase measurement may again be useful when searching for defects close to the edge of a sample.

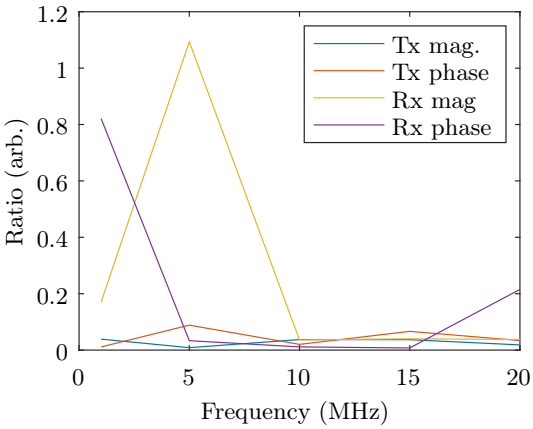

Figure 4.42: Ratio of difference in signal due to the defect and lift-off for Ti slot.

4.5 Summary of experimental results

Overall, the experimental results seem to share similarities with the simulation results, and through these results, it has been shown that Rx phase measurements can aid with finding defects, and in some cases can be the most robust to lift-off and therefore, the most reliable parameter to measure, although it obviously makes sense to still capture and analyse all the measured parameters. The signal variation in the Rx phase measurement when on and off the defect region does not overlap for reasonable/practical lift-off variations of less than 1 mm, where the curves converge for SS and TiAl. As such, variation in the signal due to lift-off is unlikely to be mistaken for a defect. This was shown for a wide variety of slot sizes and it was possible to reliably see the shortest slot on TiAl, which is nominally 0.25 mm in length but measured to be 0.55(5) mm in length, despite its low electrical conductivity. Using the phase measurement and/or combining it with amplitude measurements may provide an approach to help distinguish lift-off from a defect signal. Later, edge defects will be considered in chapter 5, where the large change in the response of the eddy current sensor at the sample edge introduces different considerations.

Chapter 5

Edge defect detection on a Ti sample

5.1 Setup for detecting edge defects using 2D scans

The setup is shown in figure 5.1.

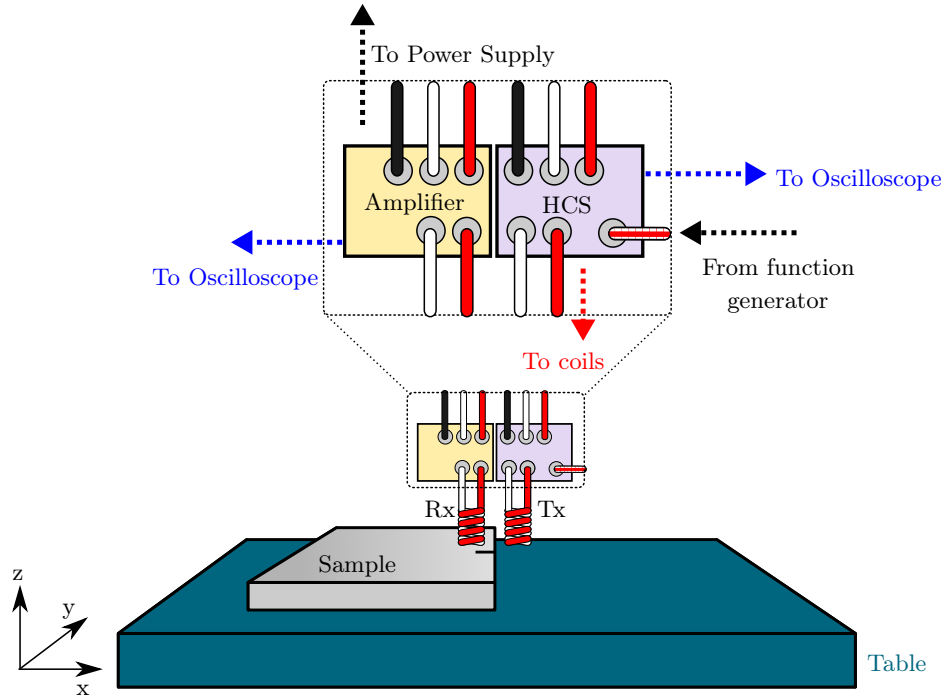

Figure 5.1: Setup for edge defect detection. The part within the dotted box is directly behind the coils and along with the coils, they are mounted onto the XY stage. Not to scale - coils are much smaller compared to the rest of the components shown and are in close proximity to each other.

The setup is based on chapter 2, which includes details of the defect dimensions (table 2.2). The Tx and Rx coils are made with 100 turns of wire with an inner diameter of 0.315 mm, an outer diameter of 0.55 mm and a height of 1 mm. These coils are air-cored and are made using copper wire with a diameter of 0.025 mm. An AFG3052C function generator drives the HCS and an MDO4054C oscilloscope is used to measure the voltage across each coil. The XY stage is a Zaber X-LSM, and thus the custom table previously implemented in chapter 4 was not used. Also, the coils holder is not resin printed as they are in chapter 4, thus there was a reversion to leaving a paper-thin gap between the coils and the sample for this chapter.

Detecting edge defects is a known challenge for eddy current testing, whereby it can be more difficult to detect a defect near an edge, due to the way the edge modifies the electromagnetic field from the coils. The change in signal due to the sensor's response to the edge can mix with the response due to a defect. This can potentially mask the defect response, especially as the edge response is often larger than the defect response. In going to higher frequencies, the eddy current is more localised under the footprint of the coils. In doing so, the extent to which the eddy current response is affected by the edge is expected to reduce, while the sensitivity to more surface-level changes such as shallower defects is expected to improve. To help with this, the coils were made to have a particularly small, sub-millimetre sized diameter (dimensions mentioned in previous paragraph). The dimensions are significantly smaller than the coils used in the rest of this thesis. The smaller coils would be expected to help confine the extent of the eddy current.

Another driving factor to use smaller, air-cored coils, is that with the coils used in previous chapters, the system seems to reach resonance at just 7 MHz (see subsection 3.5.2). This means the system is behaving capacitively rather than inductively at frequencies above 7 MHz, which is clearly undesirable. Air-cored coils would be expected to have a lower inductance than ferrite-cored coils. In this case, the inductance is $\sim$1.8 µΩ. This may help, as the HCS needs to have a larger output impedance than the load impedance, but this is an issue at higher frequencies, as not only do the coil's impedance increase as the frequency increases but so does the stray capacitance from cables and circuitry, which act to reduce the output impedance and compounded the issue. This is significant as it is thought that this issue may be the limiting factor in the hardware restricting the ability to get good SNR at higher frequencies.

5.2 Experimental results for detecting edge defects

The experimental results were taken by Zhichao Li, but all other work such as processing and analysing the results as well as the simulation work was performed by myself. Results will be taken in the range of 1 MHz to 20 MHz. In this range, the system does not appear to go through resonance; the mag. does not peak and the phase does not transition (figure 5.2).

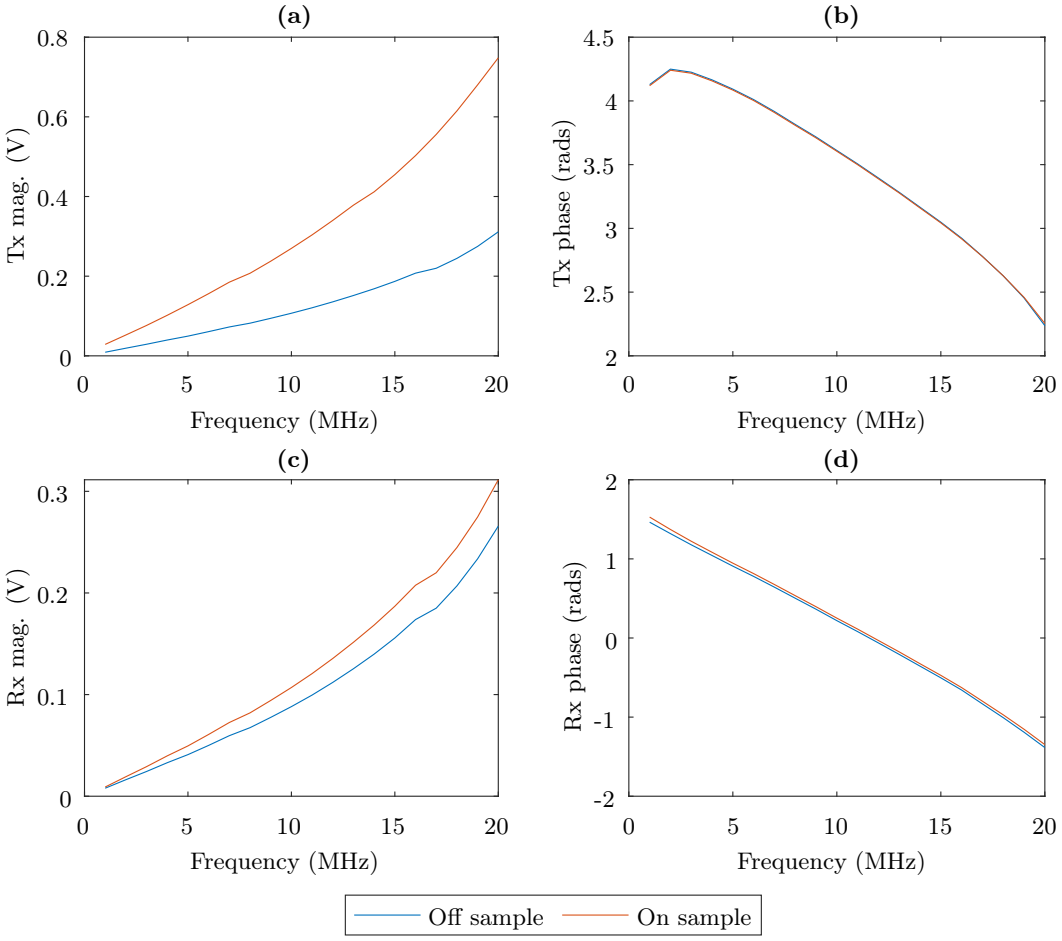

Figure 5.2: Measured parameter as a function of frequency. MATLAB functions wrapTo2Pi and wraptoPi are used for Tx phase and Rx phase since phase wraps around.

Scans from 1 MHz to 20 MHz in increments of 1 MHz were taken, but just a selection of frequencies are shown. Figure 5.3 show the experimental results for a 2D scan of an edge defect at selected frequencies and figure 5.4 shows the simulated counterpart. For the experimental results, 19 MHz is shown instead of 20 MHz.

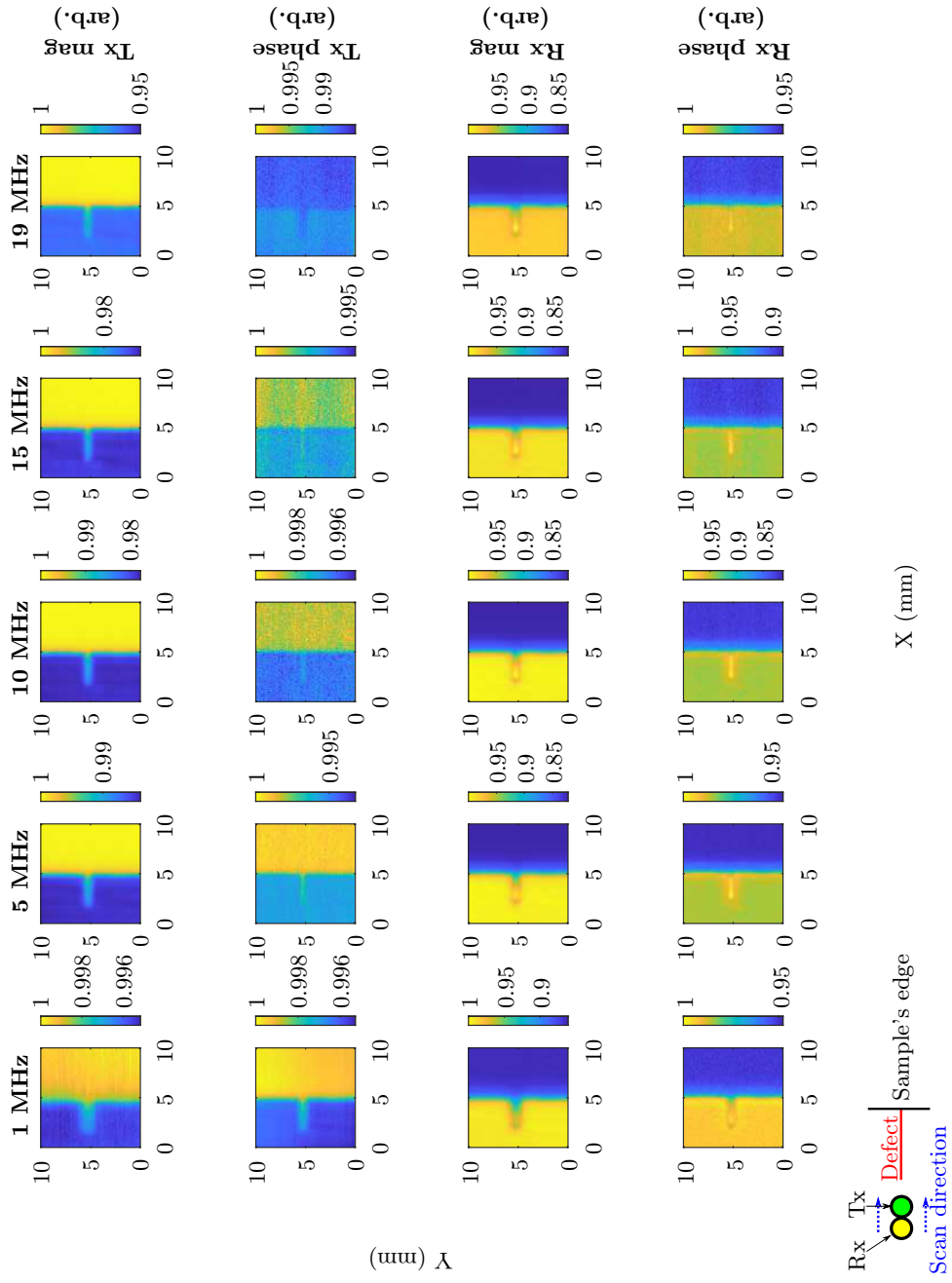

Figure 5.3: Normalised experimental results for 2D scans on titanium near an edge at selected frequencies (1 MHz, 5 MHz, 10 MHz, 15 MHz and 19 MHz). The bottom and left labels are for the x-axis and y-axis respectively. The plots are organised into columns of the same frequency, given by the labels on the top edge. The plots are organised into rows according to the parameter being measured as labelled on the right edge. A depiction of the scan orientation is in the bottom left corner.

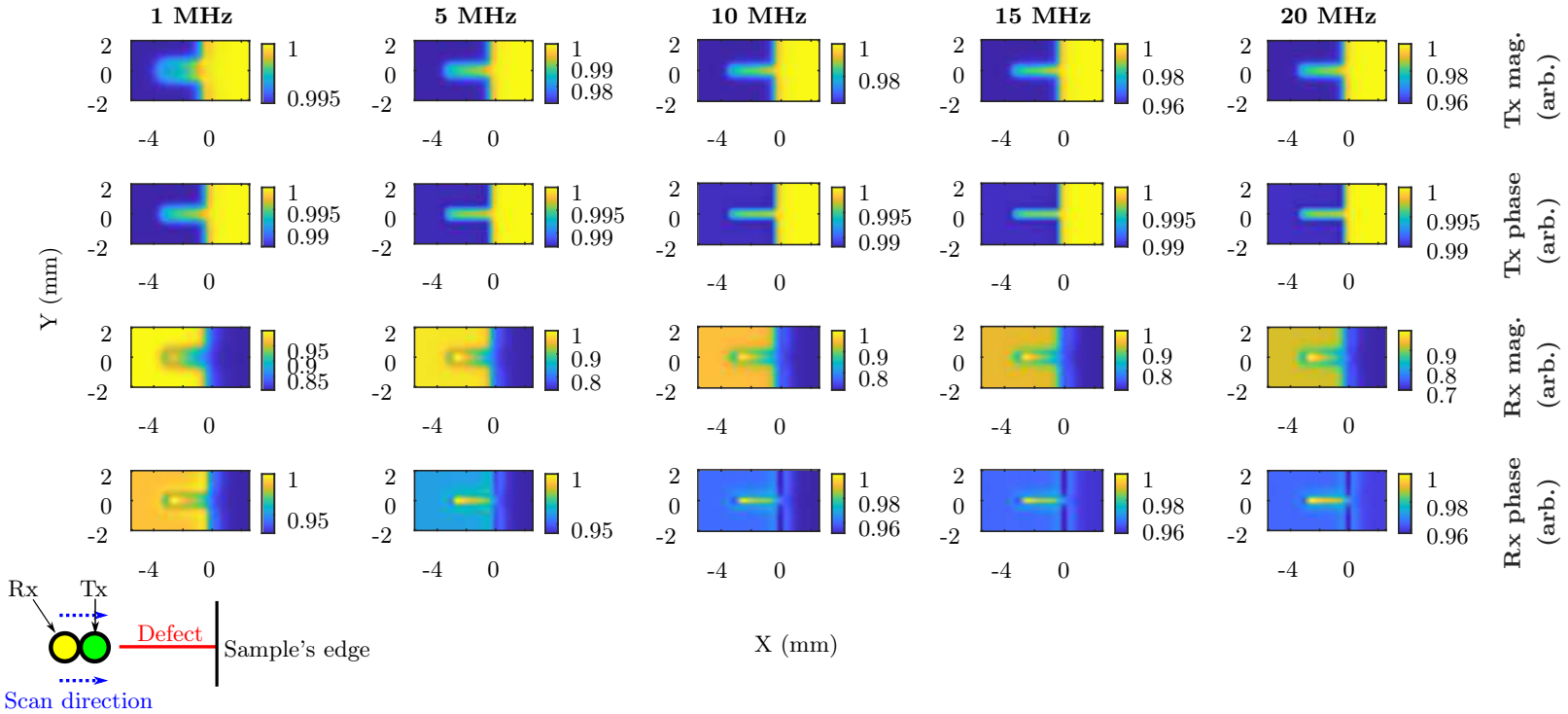

Figure 5.4: Normalised simulations for defects near an edge on Ti. Grouped in columns by frequency and row by measured parameters. $x = 0\,\text{mm}$ is where the centre of the coils and edge coincide. The horizontal centre line of the defect and the centre line through both coils coincide at $y = 0\,\text{mm}$. A depiction of the scan orientation is in the bottom left corner.

There are similarities to the experiment on SS slots in the parallel orientation, as the defect length is much larger than the coil diameter and the coils lie parallel to the defect. Consequently, there is some common behaviour in the observed response to a defect. Again, the Tx mag. and Rx mag. rise in response to a defect forming a raised bar. For the data from the SS sample, in the Rx mag., there was peaking near the ends of the bar, to form a double-peaked structure along the defect length and a lower surrounding region. For the edge defect, one observes something that looks like the left half of this response, as the right side is cut-off by being over the sample edge. The phase data is more interesting, whereby in the SS data, the Tx and Rx phases both change their main response to a defect, from rising to dipping as the frequency is increased, but this change does not appear to occur for these edge defect results. In these scans, the general signal does not invert when the frequency is increased unlike in previous chapters. Thus, the experimental results appear more consistent with the simulation results even up to higher frequencies.

In the Tx mag. and Tx phase measurements, the edge behaves like the defect as one might intuitively expect [98], where the response to both the defect and the edge is to increase, as, in both scenarios, there is less material under the probe. However, the Rx mag. and Rx phase display an interesting behaviour, whereby the response to the defect in the Rx mag. and Rx phase differs to the response when moving off the sample, by increasing instead of decreasing. The behaviour means the defect region is where the maximum signal is located, and this helps the defect and edge effects to be distinguished from each other, in a consistent and well-defined way. This behaviour is clearer in the Rx phase than in the Rx mag. measurements, where the raised defect signal extends further towards the edge of the sample, and one can also see a trend where regions on the sample and off the sample become more similar in the Rx phase with increasing frequency, which helps the defect to stand out.

It may initially seem odd that the Rx mag. and Rx phase measurements reduce over the edge of the sample, since the defect signal rises, and both are essentially equivalent to a reduction in the amount of material underneath the coil. But, the situation of there being less material beyond the edge is in fact more like the SS slot in the perpendicular orientation, which acts to block the eddy current.

The signal also seems to be more spatially localised with increasing frequency like the simulation results. This is most easily quantified for the Tx mag. and to some extent the Tx phase where the signal cross-section along the width of the defect looks like a single peak. The FWHM for the Tx mag. and Tx phase through the defect (at $X = 4.5\,\text{mm}$ in the experimental result and $X = -1.5\,\text{mm}$ in the simulation result)

as the frequency is increased is given in figure 5.5. In these plots, it can be seen that the signal becomes increasingly spatially localised as the frequency increases, although with diminishing gains. Another indication of this localisation is that the apparent edge position, particularly in the simulated results, appears to move closer to the actual edge ($X = 0\,\text{mm}$ in the simulated results).

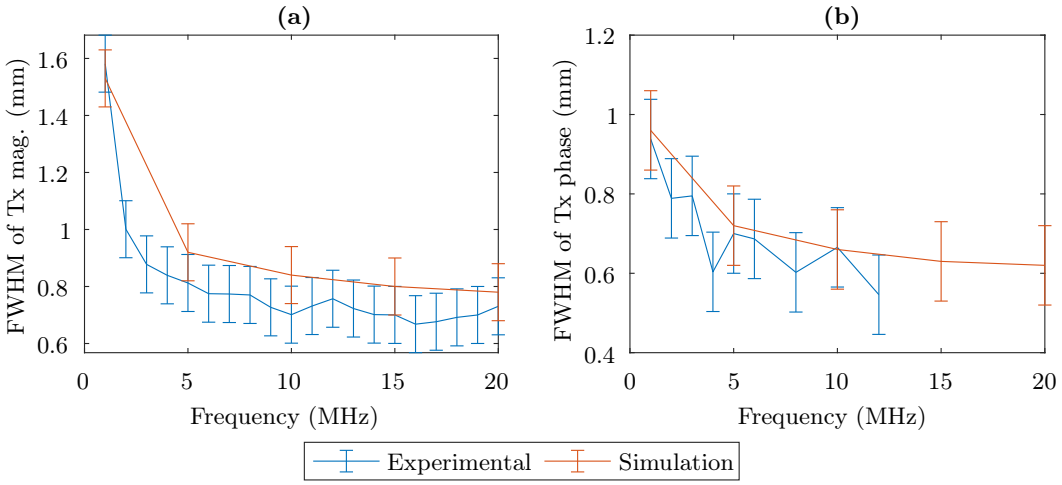

Figure 5.5: Full width at half maxima plot for edge defect through $\text{X} = 4.5\,\text{mm}$. Error bars based on scanning interval. Some Tx phase results in the experimental plot were excluded as the highest point in the cross-section were not in the defect region.

The increased localisation with increased frequency can be intuitively understood to arise from the localisation of the eddy current, where the eddy current would be expected to be more directly focused under the footprint of the wires of the eddy current coil with increasing frequency. It is also possible that one may only be able to benefit from improved resolution with increasing frequency up to a certain point, as the returns diminish and at the highest frequencies, the defect signal may be broadened by noise.

The process for calculating SNR in section 2.7 involves picking a section away from the defect that is fairly representative of the defect-free region. This works well when the background is fairly consistent. However, for the edge defects, the background region varies greatly depending on if it is on the sample, off the sample or between the two (the edge region). Thus, the process of calculating SNR will be altered by defining the defect search region and background region with the same x position and moving this x position. The defect search area defined to be $[\text{x}, \text{y}, \text{width}, \text{height}] = [\text{x}, 7, 0.5, 2]\,\text{mm}$ and the background area is defined as $[\text{x}, \text{y}, \text{width}, \text{height}] = [\text{x}, 4.2, 0.5, 2]\,\text{mm}$. The x position was moved along the defect

where at $X = 1\,\text{mm}$ the sensor is closer to the left of the defect signal on the 2D plot and away from the defect edge, and at $X = 5\,\text{mm}$, it is closer to the right of the defect and closer to the edge. This is akin to looking down a couple of lines of constant x to see the variation and would be somewhat akin to what the eye would do to try to find the defect, whereby it would be trying the compare sections next to each other along the edge.

Detecting the defect is a complex process of distinguishing the sample and the edge with the problem being made more difficult by the fact the edge can respond similarly to the defect. As before, what matters is obtaining a consistent and repeatable means of calculating SNR, and being careful with the interpretation of this value. After all, SNR is just an attempt to quantify how good the signal is, something that is difficult to completely quantify in a meaningful way in a 2D scan. Inspecting the image for evidence of a defect is in fact a complex process and the reader is obviously drawing on a wider set of data than a simple number would suggest. Spotting patterns is something humans do well and defects may be easier to "see" than a simple quantification might imply. The conclusions drawn from the calculated SNR values should be meaningful so long as care is taken in the interpretation of the values.

The results of the SNR calculations are shown in figure 5.6. From this, it can be seen that SNR is generally greater at $X = 3\,\text{mm}$. That being said $X = 4\,\text{mm}$ is closer to the edge region that is of interest.

In the Tx mag. measurement at $X = 3\,\text{mm}$, the SNR looks like it initially increases as the frequency increases then decreases near the end. It is nearer to the edge, at $X = 4\,\text{mm}$, where the SNR mainly increases as the frequency increases, perhaps benefitting from the increased localisation of the signal, although the SNR decreases at the highest frequency 20 MHz, which is in line with the general salt and pepper like noise that can be seen in the 2D plot.

The Tx phase SNR seems to mainly decrease with frequencies. Tx phase tends to have more salt and pepper like noise, which is reflected in the lower SNR and this makes it difficult to benefit from going to higher frequencies. The Rx mag. and phase results are more interesting, as there appears to be a peak in the SNR at 4 MHz and 5 MHz respectively. This peak is more defined for the Rx phase than the Rx mag. The peak in SNR seems linked to a behaviour whereby the defect signal seems to go from a more of a dip to more of a peak in the 2D scans.

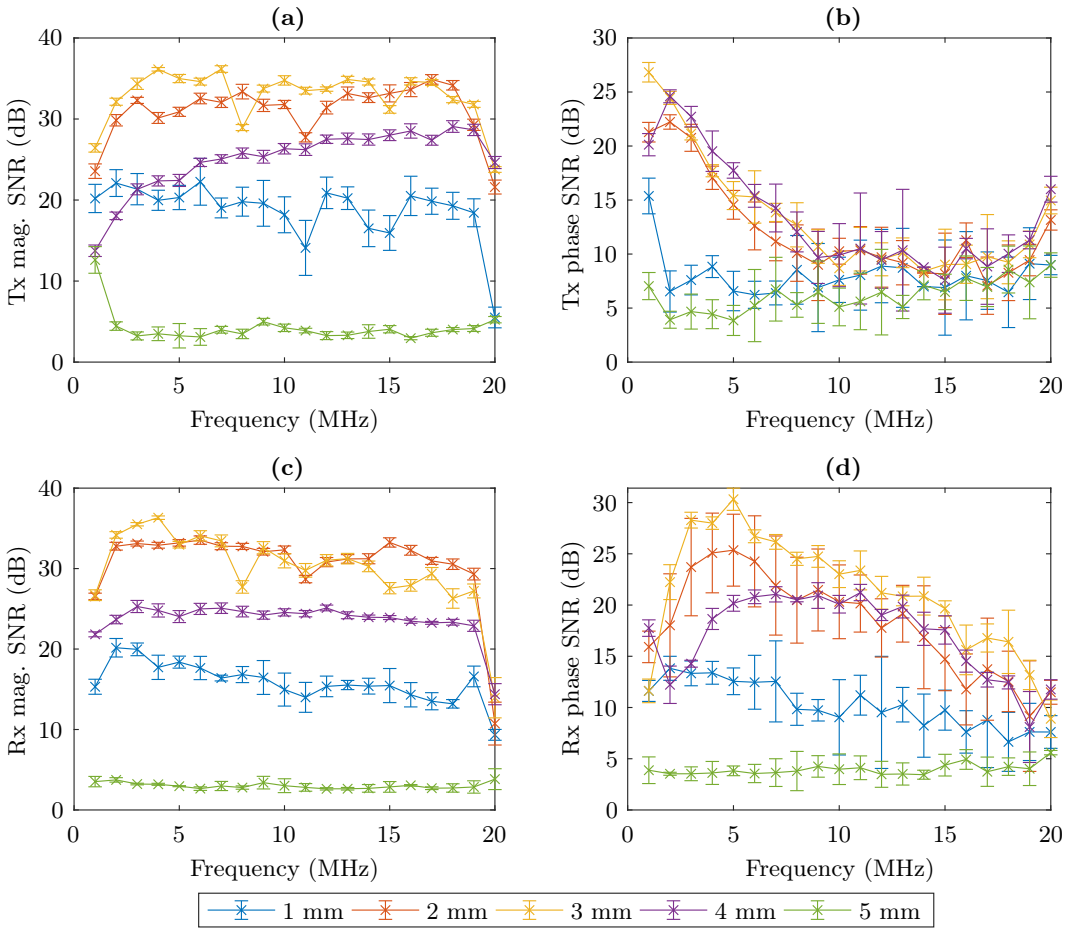

Figure 5.6: Signal-to-noise ratio at different x positions, as given by the key. The background area is defined as $[\mathrm{x}, \mathrm{y}, \mathrm{width}, \mathrm{height}] = [\mathrm{x}, 7, 0.5, 2]$ mm and the defect search area is defined as $[\mathrm{x}, \mathrm{y}, \mathrm{width}, \mathrm{height}] = [\mathrm{x}, 4.2, 0.5, 2]$ mm. At 14 MHz, the Tx phase wrapped around thus, the wrapTo2Pi function was used in MATLAB.

The above process of calculating SNR is helpful, but it focuses more on the difference between the defect area and defect-free area on the sample. It does not capture the improvement to signal detection that would arise from the interesting behaviour of the defect signal rising above both the sample and off-sample regions in the Rx mag. and Rx phase measurement at some frequencies. The behaviour whereby the defect signal becomes the maximum signal means that the defect signal can just be picked out as the highest points. If a similar approach to the one described before is used but the signal is taken to be located at the maximum, the resulting SNR is as shown in figure 5.7. To clarify, there are two signal-to-noise ratios since there are two background regions considered per plot. One background region is on the sample ($[\mathrm{x}, \mathrm{y}, \mathrm{width}, \mathrm{height}] = [0, 0, 3, 3]$ mm) and the other is off the sample

$[\mathrm{x}, \mathrm{y}, \mathrm{width}, \mathrm{height}] = [7, 7, 3, 3]$ mm. This is because the task of distinguishing the defect is a combination of comparing of defect signal with the defect-free sample and the off-sample regions. However, the SNR values based on the sample region could be argued to be more important than that based on the off-sample region since the defect signal is very clearly above the off-sample region for all the plots considered, which makes the task of defect detection more about distinguishing the defect from the sample.

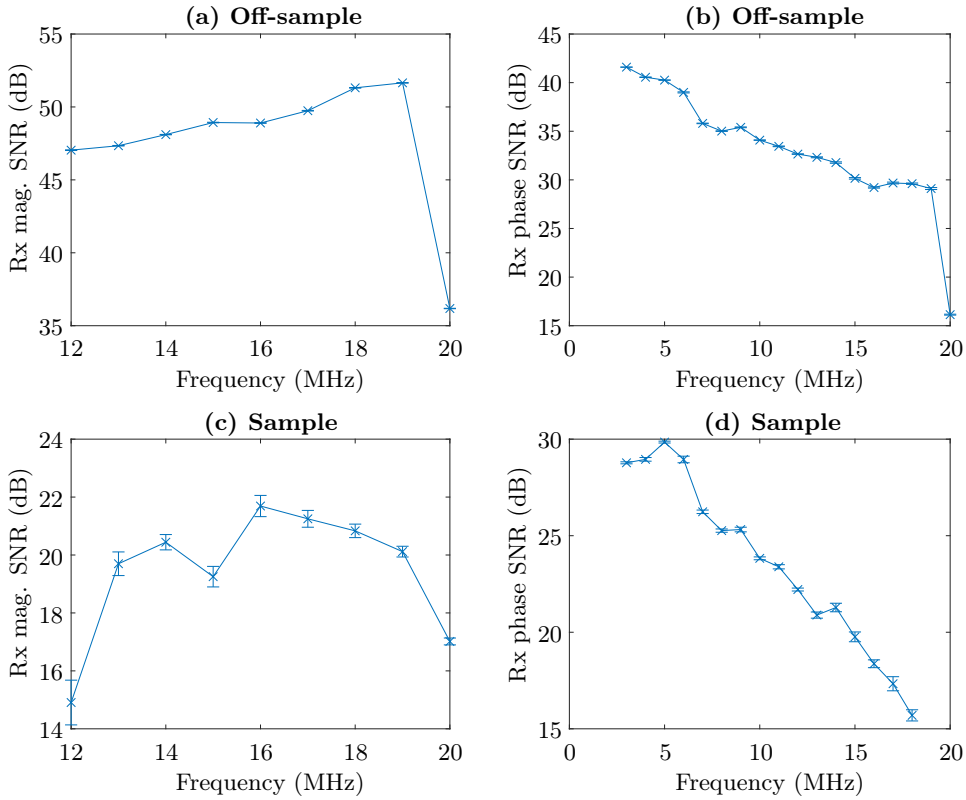

Figure 5.7: Signal-to-noise ratio where signal is defined to be at the five highest locations. The plots labelled air are based on a background region off the sample ($[\mathrm{x}, \mathrm{y}, \mathrm{width}, \mathrm{height}] = [7, 7, 3, 3]$ mm) and the plots labelled sample are based on a background area on the sample region ($[\mathrm{x}, \mathrm{y}, \mathrm{width}, \mathrm{height}] = [0, 0, 3, 3]$ mm). Some frequencies are not plotted, since the maximum location did not coincide with the defect location. For low frequencies, this was often because the defect signal has not risen above the sample level yet and for higher frequencies, this was because of the noise, which affects phase worse.

A few SNR values are not present, as for these results not all the five of the maximum points are located on the defect, and for lower frequencies, the defect signal has not sufficiently risen above the sample, and thus the maximum values

would not be on the defect. For Rx mag., it is more of a case whereby the signal is largely a dip, but part of the defect signal rises within the dip with increasing frequency, which can be seen in the 2D plot and somewhat in the cross-sections. At the lowest frequencies, the maximum five points are simply not on the defect as the rising part is not high enough and this is in line with the simulation results. Going up in frequency to 10 MHz, some but not all the five maximum points are on the defect for the experimental results even though all five of the maximum points are on the defect in the simulation results, which appears to be caused by lift-off variation. For example at 10 MHz, it is possible to see that the value of Rx mag. at the top is generally larger than the bottom, and by removing the top 1 mm strip of the plot, the largest two points are on the defect and by removing the top 2 mm strip, the largest three points are on the defect. It is possible to get all the defects to be on the defect with further cropping. This suggest the sample lift-off varies from the top to the bottom of the scan.

For the Rx phase, the defect rises above the sample at an earlier point than Rx mag. For the Rx phase, three of the highest points are already on the defect at 1 MHz while five of the highest points are all on the defect at 3 MHz. For the Rx phase measurement, the defect signal increases to be above the sample region up to 5 MHz and declines past this point.

Considering all the calculated SNR values and the 2D plots themselves for the single edge, a frequency around 5 MHz may be a good frequency to consider. Visually, it is a good compromise between getting the morphology that helps the defect to stand out, while avoiding increased noise that comes with higher frequencies, whereby the effect of lift-off and electrical noise are expected to become more of an issue. That being said a multi-frequency approach may be best as it is clear that the best frequency to consider is different for different parameters.

Following a similar process used for the edge defect, 2D scans were performed on two corner defects. This is a natural extension, essentially, going from one edge to two edges. The experimental results are shown in figures 5.8 and 5.10 for select frequencies. There was the issue that much of the apparent low contrast between the sample and off-sample regions was caused by the probe is still stabilising near the start of the scan, which is on the bottom edge of the 2D plots. Consequently, the measured value near the start can be quite different from the rest of the plot, which means much of the plot is plotted on a limited range. The simulated counterparts are shown in figures 5.9 and 5.11

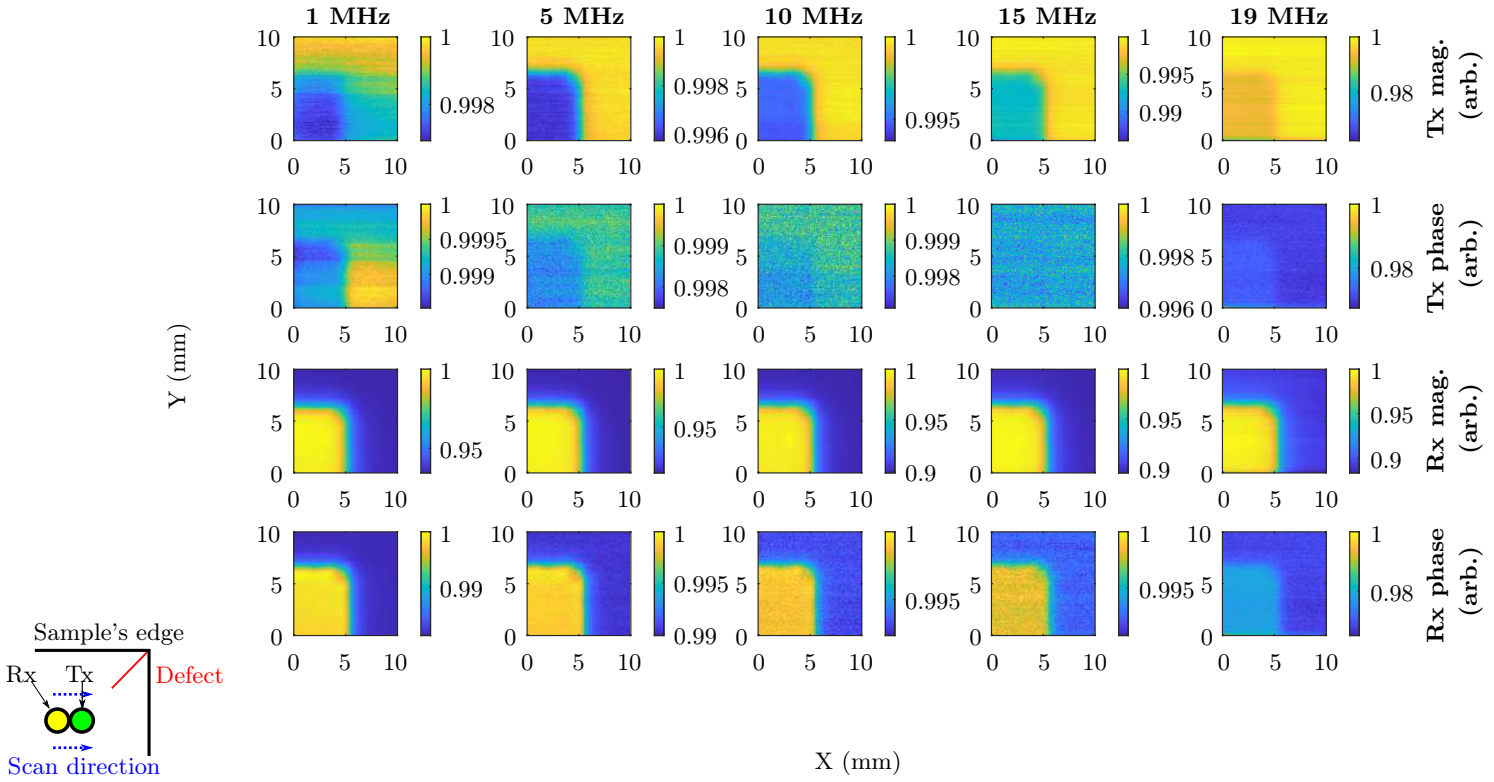

Figure 5.8: Normalised experimental results for notch 1 for selected frequencies (1 MHz, 5 MHz, 10 MHz, 15 MHz and 19 MHz). The bottom and left labels are for the x-axis and y-axis respectively. The plots are organised into columns of the same frequency as labelled on the top edge. The plots are organised into rows according to the measured parameter as labelled on the right edge. The sample is located in the bottom left corner and is surrounded by the air region. A depiction of the scan orientation is in the bottom left corner.

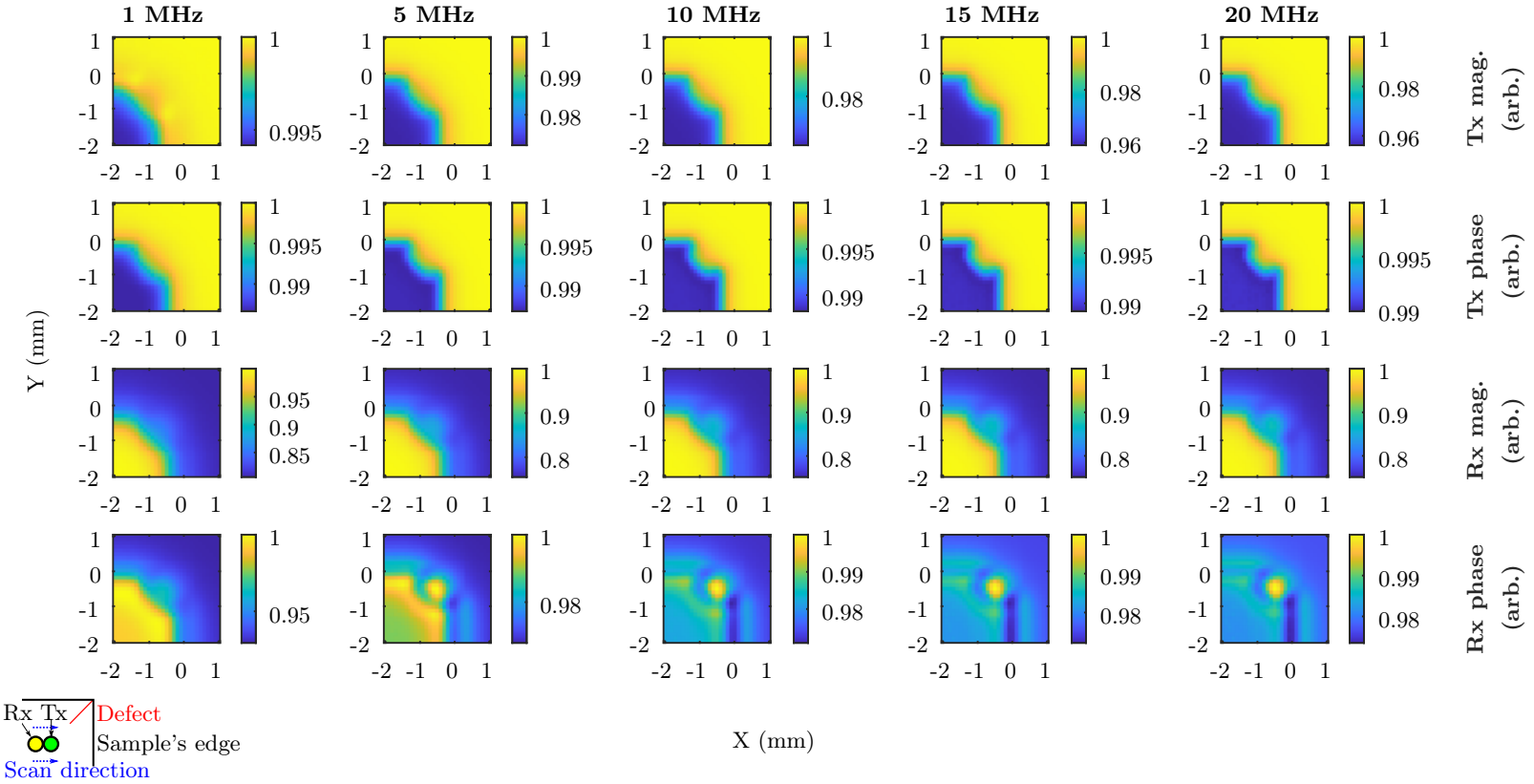

Figure 5.9: Normalised simulation of notch 1 near the corner on Ti. Grouped in columns by frequency and row by measured parameters. (0,0) is where the centre of the coils and corner coincide. A depiction of the scan orientation is in the bottom left corner.

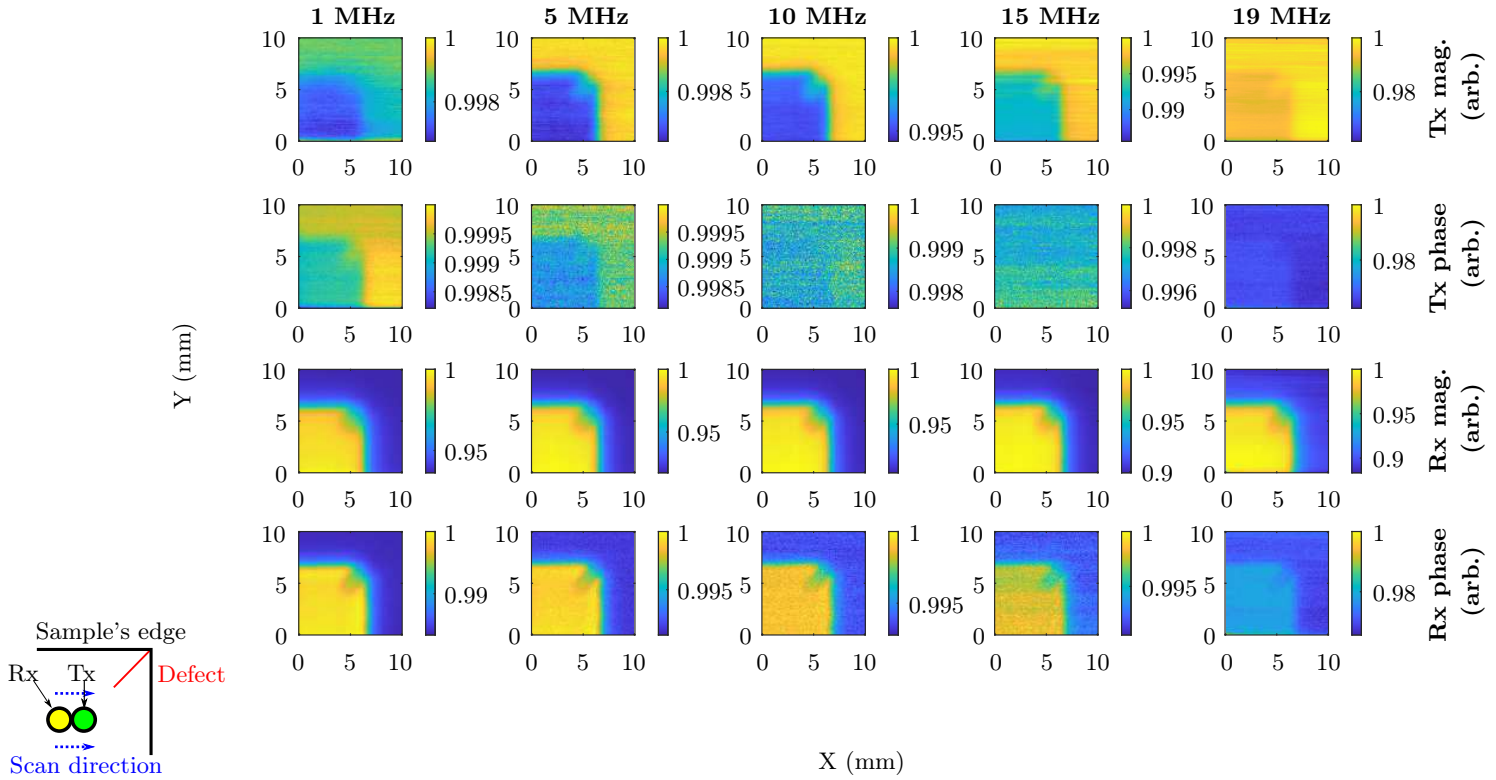

Figure 5.10: Normalised experimental results for notch 2 for selected frequencies (1 MHz, 5 MHz, 10 MHz, 15 MHz and 19 MHz). The bottom and left labels are for the x-axis and y-axis respectively. The plots are organised into columns of the same frequency as labelled on the top edge. The plots are organised into rows according to the measured parameter as labelled on the right edge. The sample in located on the bottom left corner and is surrounded by the air region. A depiction of the scan orientation is in the bottom left corner.

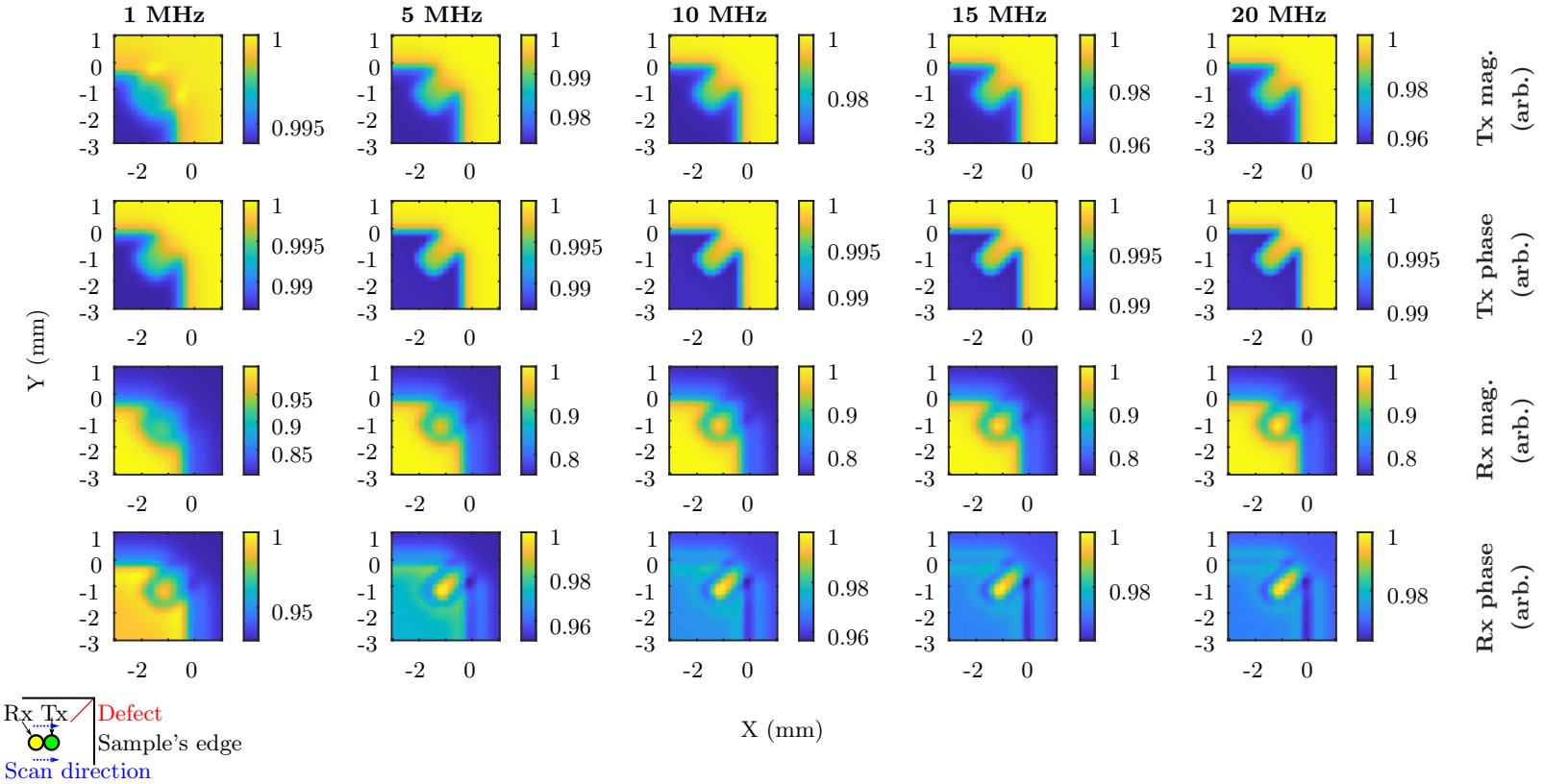

Figure 5.11: Normalised simulation of notch 2 near the corner on Ti. Grouped in columns by frequency and row by measured parameters. (0,0) is where the centre of the coils and corner coincide. A depiction of the scan orientation is in the bottom left corner.

The results for notch 1 and 2 are similar, as there are a lot of similarities in the geometry, however notch 2 has a longer defect indication to coincide with its longer length. In the Tx mag. and Tx phase measurements, the response to the defect looks very similar to the response observed for the sample edge. However, the defect signal in the Rx mag. and Rx phase has a slightly raised region inside the slot, which is clearer to see in the simulation results. This helps distinguish the defect signal. Additionally, like for the edge defect, the corner defect appears to localise with increasing frequency.

Like the single edge results, detecting the defect is again a complex process of distinguishing the sample, defect and air region, where the problem is made more difficult by the fact the edge can respond similarly to the defect. As before, the SNR will be calculated by limiting the search area. The defect search areas are $[\mathrm{x}, \mathrm{y}, \mathrm{width}, \mathrm{height}] = [3, 4, 2, 2]$ mm and $[4, 4, 2, 2]$ mm notch 1 and 2 respectively, while the background region is taken to be $[1, 4, 2, 2]$ mm for both notches. The resulting SNR is plotted in figure 5.12 for notch 1 and figure 5.13 for notch 2.

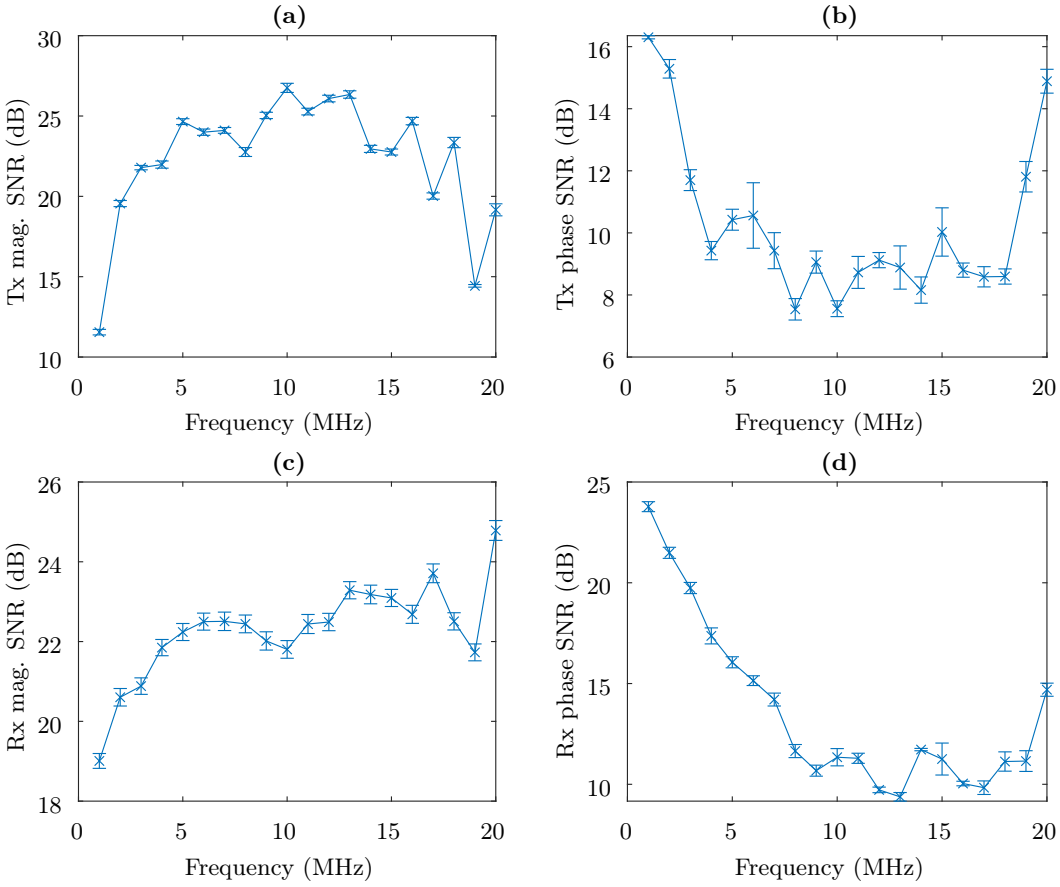

Figure 5.12: Indicative signal-to-noise ratio for notch 1.

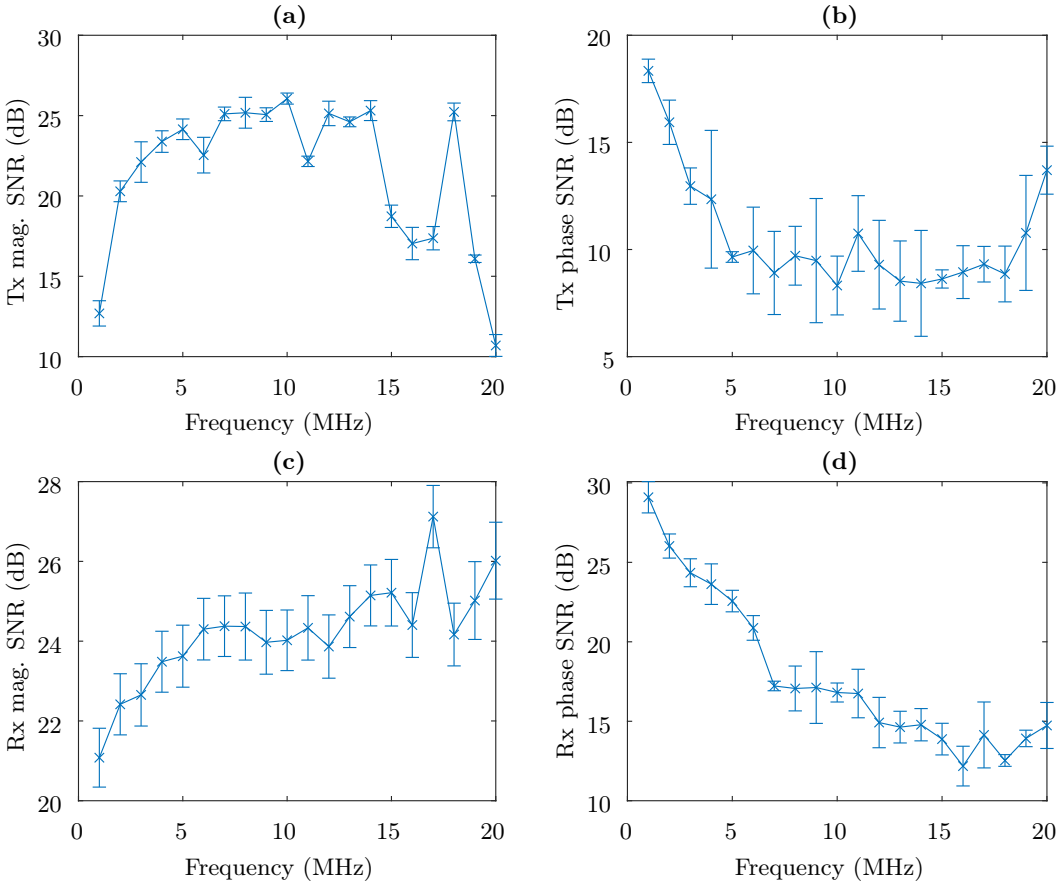

Figure 5.13: Indicative signal-to-noise ratio for notch 2.

It can be seen that the SNR generally decreases for the phase measurements with increasing frequency. Conversely, the Rx mag. measurement SNR seems to be optimal around 10 MHz, initially benefitting from the increased localisation of the eddy current with higher frequencies before it becomes too noisy, whilst, the SNR for the Rx mag. measurements seem to continue to increase as the frequency increases, suggesting it is less affected by the noise at higher frequencies. As the SNR for each parameter is optimal at different frequencies, choosing the best frequency is a complex decision. Simply looking at the phase, lower frequencies should be used. While, the increasing SNR in the Rx mag. measurements as the frequency increases, due to the localisation of the signal, suggests that one should push to higher frequencies. Looking at the scans, the change in the signal strength in the Rx mag. measurement is less perceptible to the eye than for the Tx mag. measurement. This is perhaps because the SNR range is larger for Tx mag. compared to Rx mag. (e.g. approximately 15 dB and 6 dB for notch 1) whereby the SNR goes from a relatively low SNR to a higher one in the Tx mag. while for Rx mag., it always stays

above a reasonable SNR. From this, one may conclude by looking at the scans that the 10 MHz frequency may be the best frequency if one had to choose a particular fixed frequency. However, the approach used here allows one to sweep frequencies or switch between different frequencies.

Here, the defect signal does not become the maximum signal for the Rx mag. and Rx phase measurements even at higher frequencies, unlike for the edge defects, and thus it does not make sense to apply the SNR calculation based on the maximum locations that occurred for the edge results. The simulation does show this behaviour, suggesting that the difference is not caused by the change from an edge to a corner defect and more so because the corner notches are not as sharply cut as that used in the simulation. The simulation assumes a rectangular slot when in fact, the defect depth varies and it is possible to see that going into the sample, the depth reduces below what is measured on the exterior. Nevertheless, what is important is that it is possible to see from these results and the previous single edge defect results that small defects near the edge(s) of the sample can be detected with this approach.

5.3 Summary of experimental results

Detecting small defects near the edge of a sample is a known challenge, where it can be more difficult to detect defects due to the influence of the sample edge on the signal. It has been shown that it is possible to detect defects using this method, where operating at high frequencies with small coils, less than 1 mm in diameter, enables the identification of small defects. The SNR values are reasonable, but the measurement of both the mag. and phase of the Tx and Rx coils improves the confidence in the detection of defects, particularly as each parameter has a unique response. Rx phase has a particularly interesting response giving the highest resolution of defect shape and the most reliable result for distinguishing the defect from the sample edge.

Chapter 6

New phase difference and signal amplitude meter based on the AD8302 chip

6.1 Setup for testing new meter by performing 2D scans

As mentioned at the end of subsection 4.1.1, the setup used will be modified further to use a new meter based on the AD8302 chip. This new meter was built to a requested design and specification by Robert Day (Physics Department Electronics Technician). The AD8302 chip is an inexpensive device, that is essentially a signal analyser on a chip; it is capable of measuring gain and phase differences at radio frequencies/intermediate frequencies, and it works from low frequencies up to 2.7 GHz. Its range allows it to be used in various applications from low frequency (Hz) [178] to high frequency (GHz) [179], where its low cost and compactness are major draws. It converts gain and phase information into voltage output levels, and the phase accuracy is independent of signal level over a wide range [180].

The new meter was used to measure the gain and phase of the Rx coil. The setup is the same as the one used in chapter 4, but the output to the oscilloscope from the amplifier on the Rx coil is instead connected to the new meter as the signal to be measured (as a reminder, the setup in chapter 4 uses the setup in section 3.5 with the addition of a custom tilt table and resin printed coil holder. While the setup in section 3.5 uses the general setup in chapter 2 with the addition of a benchtop oscilloscope and function generator).

To use the meter, the signal from the signal generator in the previous setup, that went to the HCS, is split between the HCS and the new meter, as the reference

signal for the new meter needs to be comparable to the measured signal i.e. both inputs are ideally sinusoidal, which means the TTL signal cannot be used. The MDO4054C oscilloscope will be used to measure the output from the new meter, but a DC voltage data logger would also be capable of this simple task. Despite the ability of the device to measure very high frequency (GHz) signals, the system resonance meant the frequencies considered were limited to those below the system's resonance. As such, measurements for just 1 MHz and 5 MHz were taken.

Since the process for measuring the Tx signal is kept the same, the signal-to-noise ratio is expected to be similar. It provides a reference, whereby if the SNRs of the Tx mag. and Tx phase are similar, an improvement or deterioration in the Rx mag. or Rx phase measurement is more likely to be due to the new measurement system rather than extraneous factor such as lift-off. That being said the actual Tx values might differ from before as to use these new meters, the function generator had to be varied to keep the output within a certain range.

The meter was designed so that one could change the gain of the signal to be measured and the gain for the reference signal along with the phase difference between them. This is to improve sensitivity, and keep the signal to be measured and reference signal within the input ranges of the chip, where the phase discrimination works best for a phase difference of around 0°. It is important to remember what matters is the variation in magnitude or phase rather than their absolute values in defect detection. The components are inexpensive but it takes some effort to ensure good performance and layout of the circuit.

In the first iteration, the meter is a relatively large box positioned away from the coils as a proof of concept. The setup for the this first iteration is shown in figure 6.1. The chip itself is, however, relatively small (4.4 mm×5.0 mm×1 mm [181]), and a second iteration was made that was much more compact. The compact version was 65 mm x 40 mm x 3 mm in size, which allowed it to be placed directly behind the coils with the other electronic circuits (setup shown in figure 6.2). An image showing the printed circuit board is shown in figure 6.3, and it can be seen to be smaller than the original less compact version in figure 6.4, which was designed to be a bench-top unit. The more compact form would confer some advantages in reducing the amount of cabling between the signal generated and the measuring device.

As mentioned the function generator voltage had to be varied. The function generator voltage was kept to 200 mV for 1 MHz and 30 mV for 5 MHz on the first iteration, and to 1 V for 1 MHz and 400 mV for 5 MHz on the second iteration.

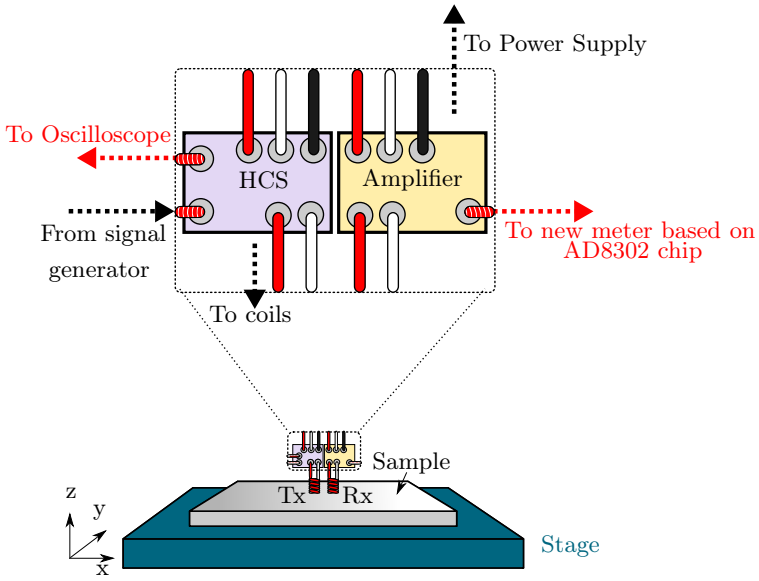

Figure 6.1: Setup with new meter based on AD8302 chip. The part within the dotted box is directly behind the coils. The reference signal for the AD8302 meter is from the signal generator. Not to scale - coils are much smaller compared to the rest of the components shown and are in close proximity to each other.

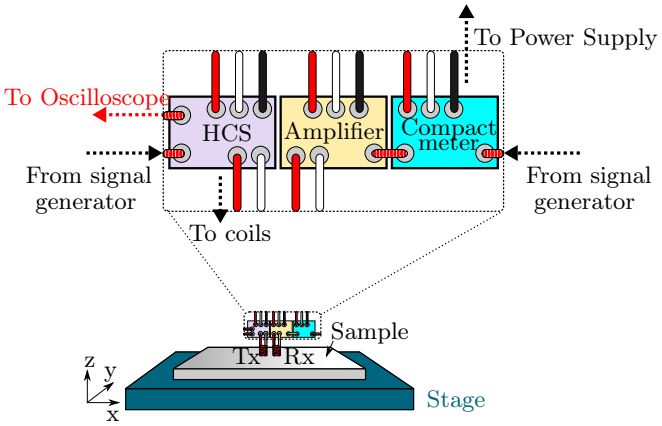

Figure 6.2: Setup with compact version of new meter based on AD8302 chip ("compact meter" in diagram). The part within the dotted box is directly behind the coils. Not to scale - coils are much smaller compared to the rest of the components shown and are in close proximity to each other.

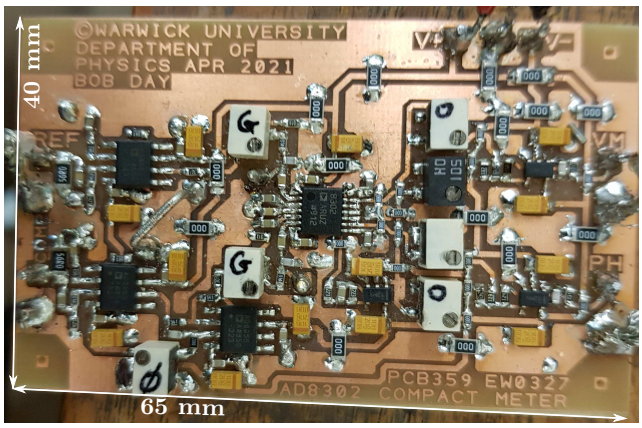

Figure 6.3: Image of printed circuit board for compact meter showing dimensions.

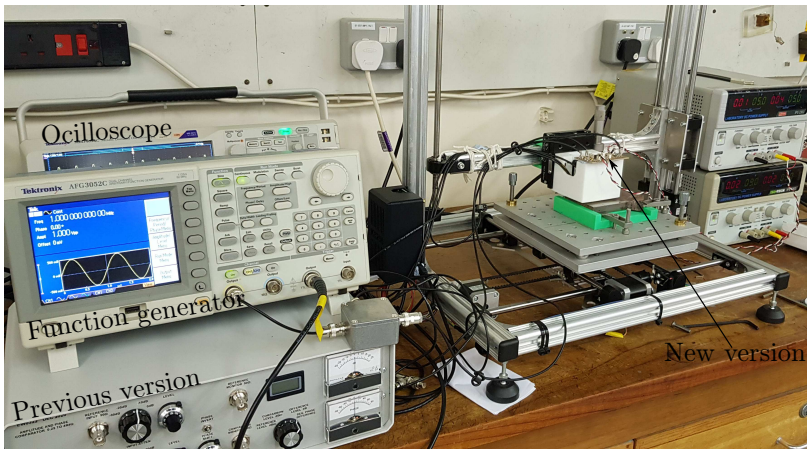

Figure 6.4: Image of setup including previous benchtop version in view, the circuit inside the unit being much larger than the newer, compact design.

6.2 Experimental results from testing new meter

Following the analysis in section 4.1, plots of the 2D scans at 1 MHz for each material will be shown alongside plots of the SNR. The other previously used metrics make less sense to apply here as these results were taken with a device whereby the background level was set to be as close as possible to zero, as this is the most sensitive range (though in the compact version, it was sometimes not possible to achieve this for the phase as the level could not be adjusted far enough).

Starting with the 2D plots. Figure 6.5-6.10 show the plots in the perpendicular and parallel orientation on each sample using the first iteration of the meter.

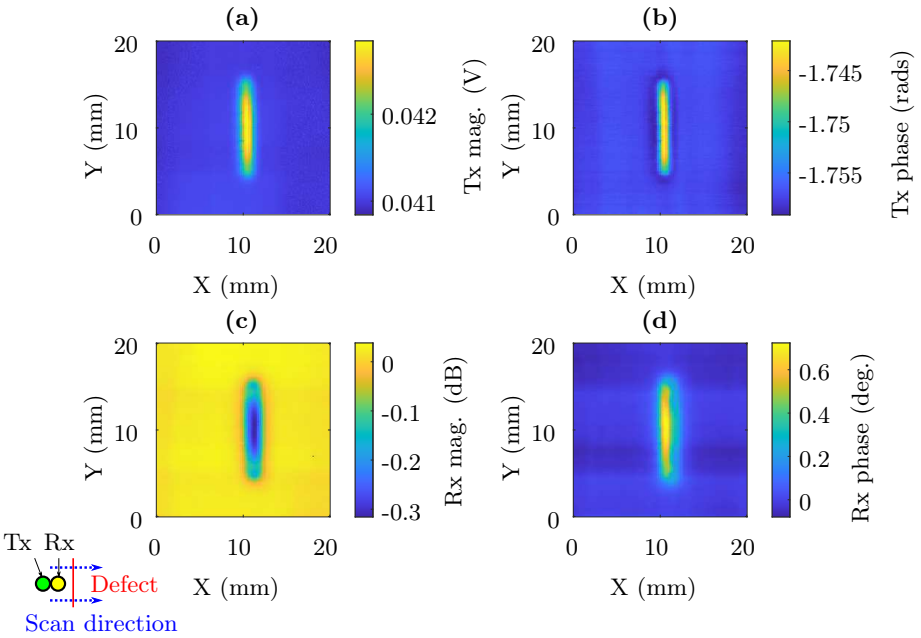

Figure 6.5: 2D scan on stainless steel with defect in perpendicular orientation (as depicted in the bottom left corner). Measurement taken with a 1 MHz driving current and a meter based on the AD8302 chip for the Rx measurements.

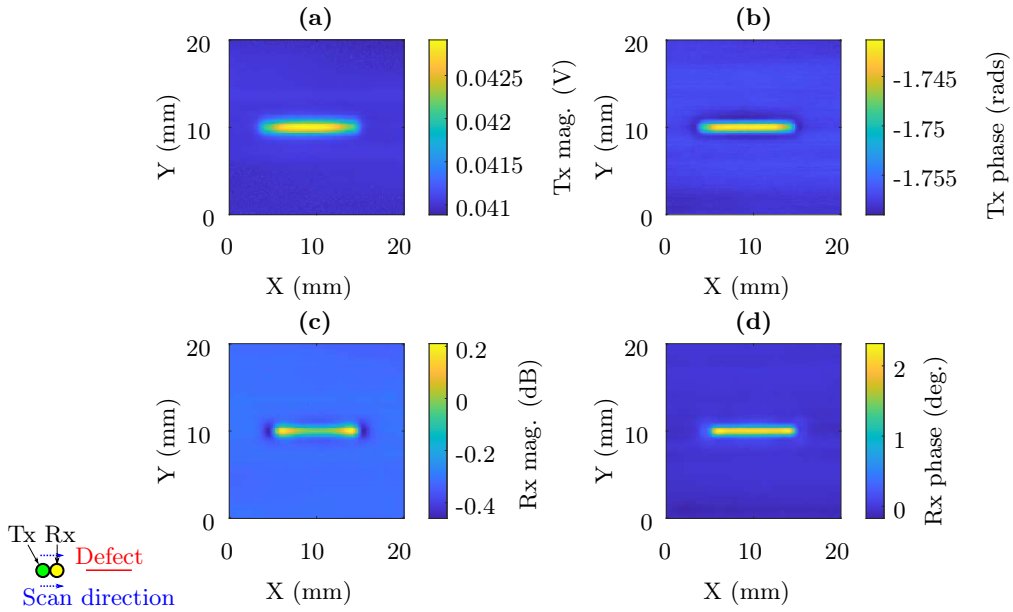

Figure 6.6: 2D scan on stainless steel with defect in parallel orientation (as depicted in the bottom left corner). Measurement taken with a 1 MHz driving current and a meter based on the AD8302 chip for the Rx measurements.

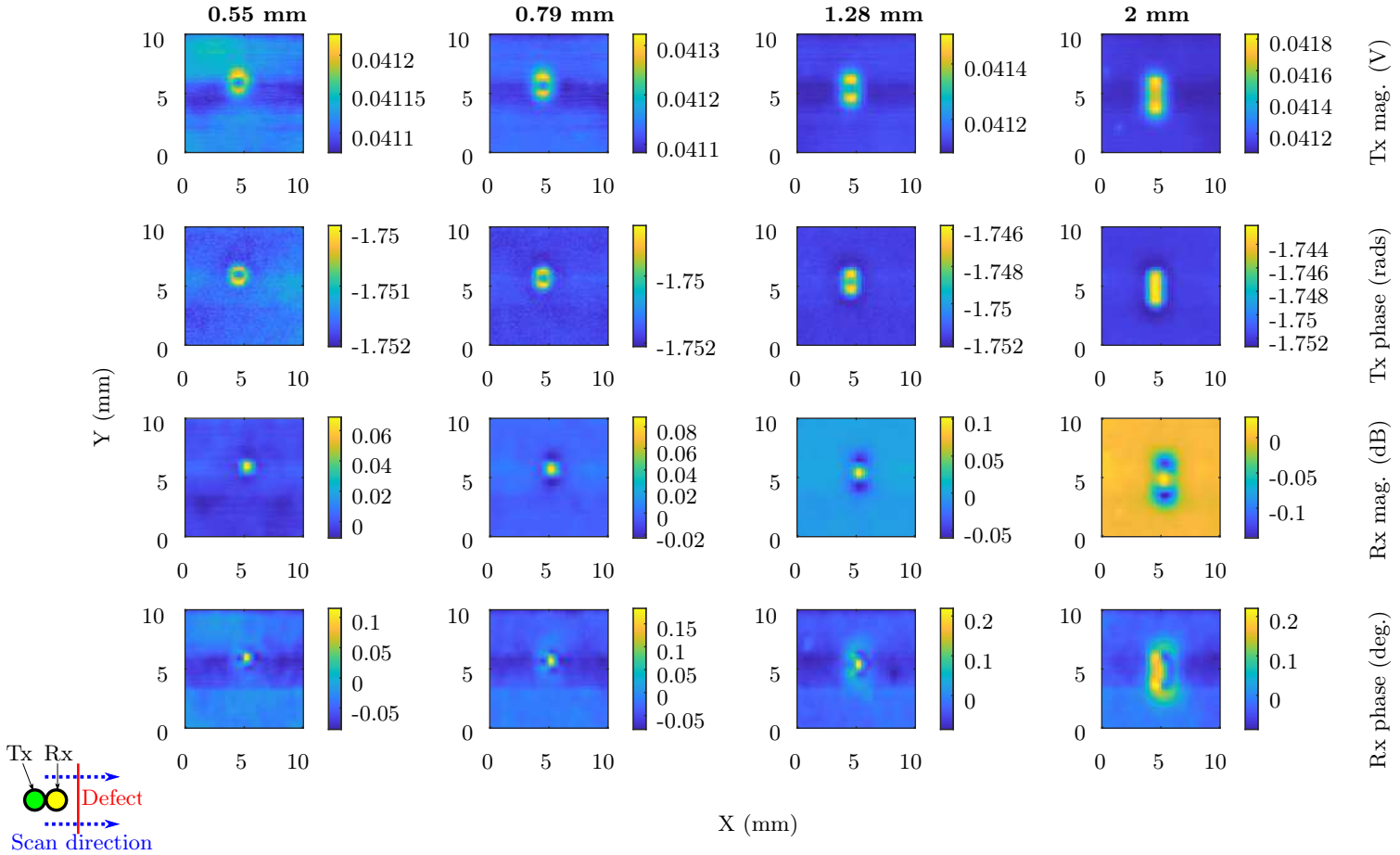

Figure 6.7: 2D scan on TiAl with defects in perpendicular orientation (as depicted in the bottom left corner). Measurement taken with a 1 MHz driving current and a meter based on the AD8302 chip for the Rx measurements. Grouped in rows by the measured parameter and columns by the slot length.

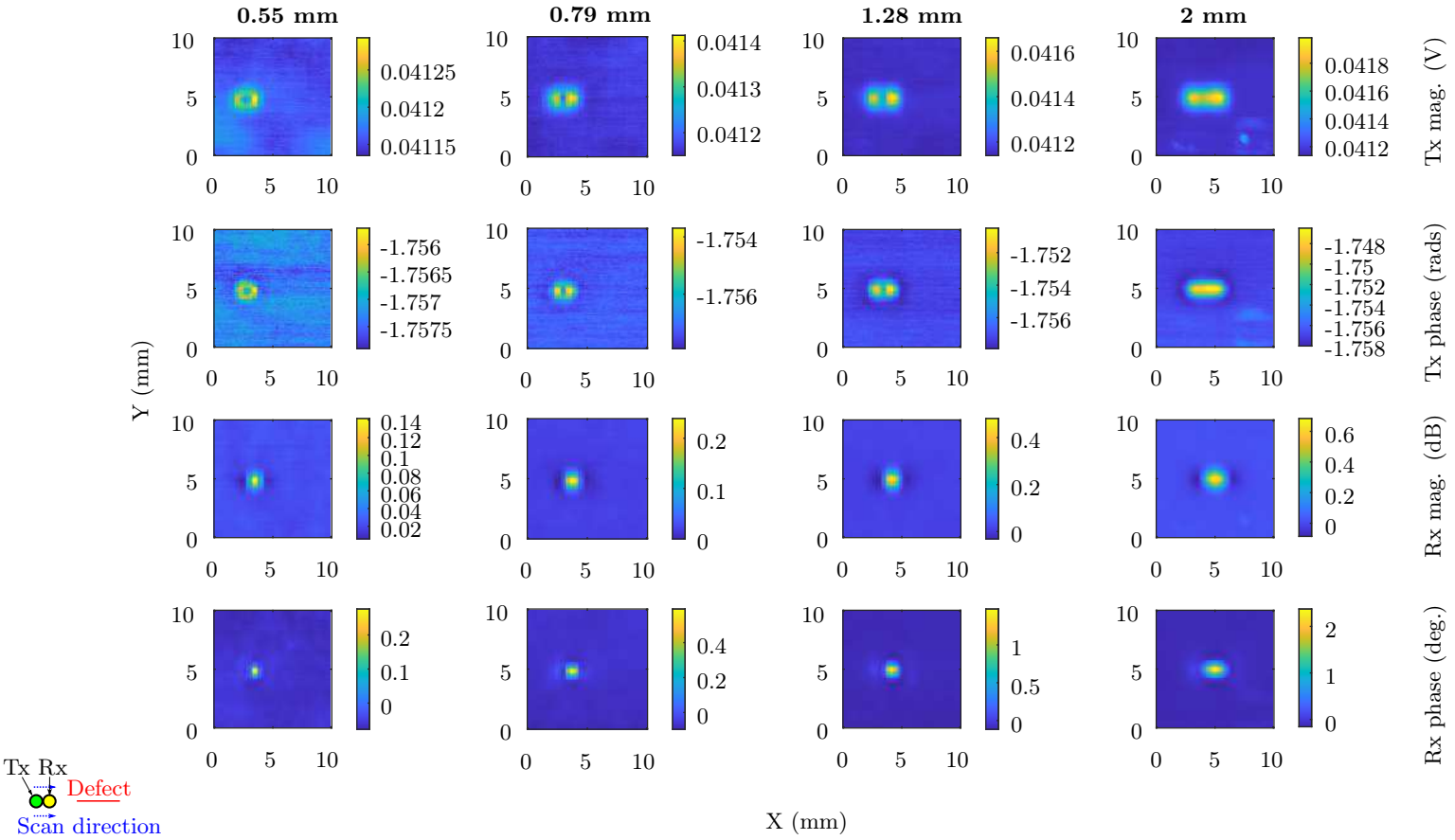

Figure 6.8: 2D scan on TiAl with defects in parallel orientation (as depicted in the bottom left corner). Measurement taken with a 1 MHz driving current and a meter based on the AD8302 chip for the Rx measurements. Grouped in rows by the measured parameter and columns by the slot length.

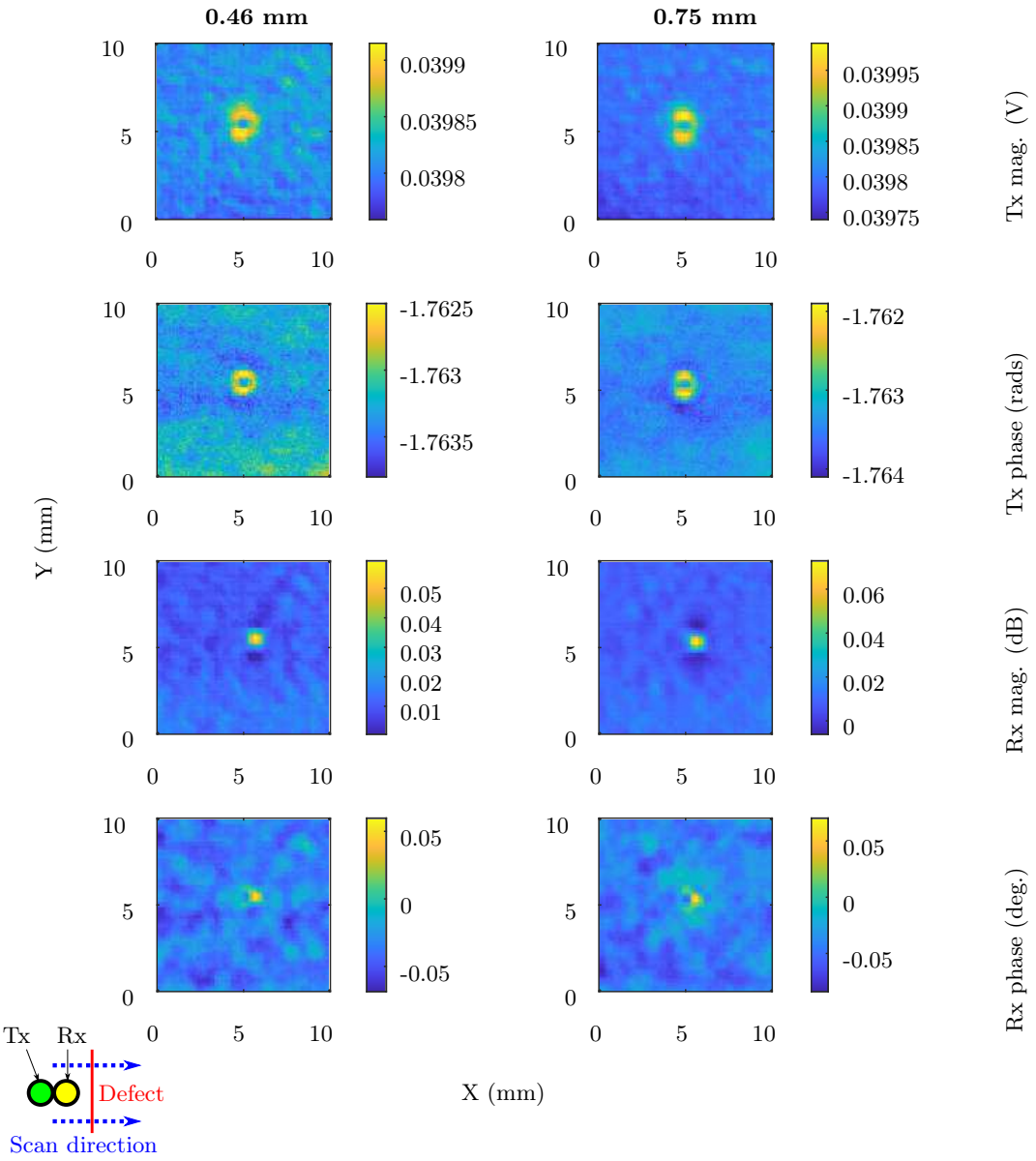

Figure 6.9: 2D scan on Ti with defects in perpendicular orientation (as depicted in the bottom left corner). Measurement taken with a 1 MHz driving current and a meter based on the AD8302 chip for the Rx measurements. Grouped in rows by the measured parameter and columns by the slot length.

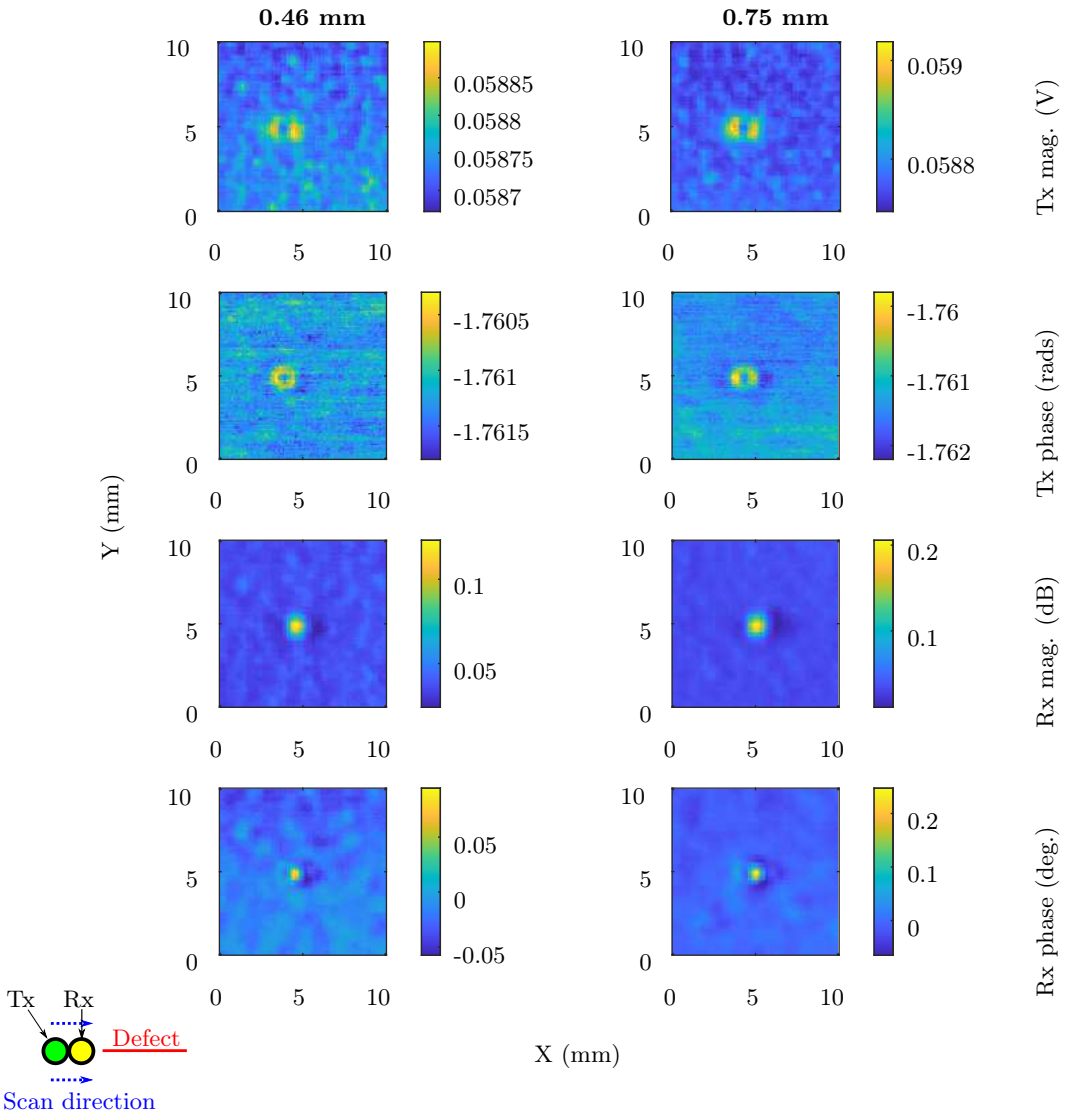

Figure 6.10: 2D scan on Ti with defects in parallel orientation (as depicted in the bottom left corner). Measurement taken with a 1 MHz driving current and a meter based on the AD8302 chip for the Rx measurements. Grouped in rows by the measured parameter and columns by the slot length.

The results at 1 MHz using the compact version are shown in figures 6.11-6.16.

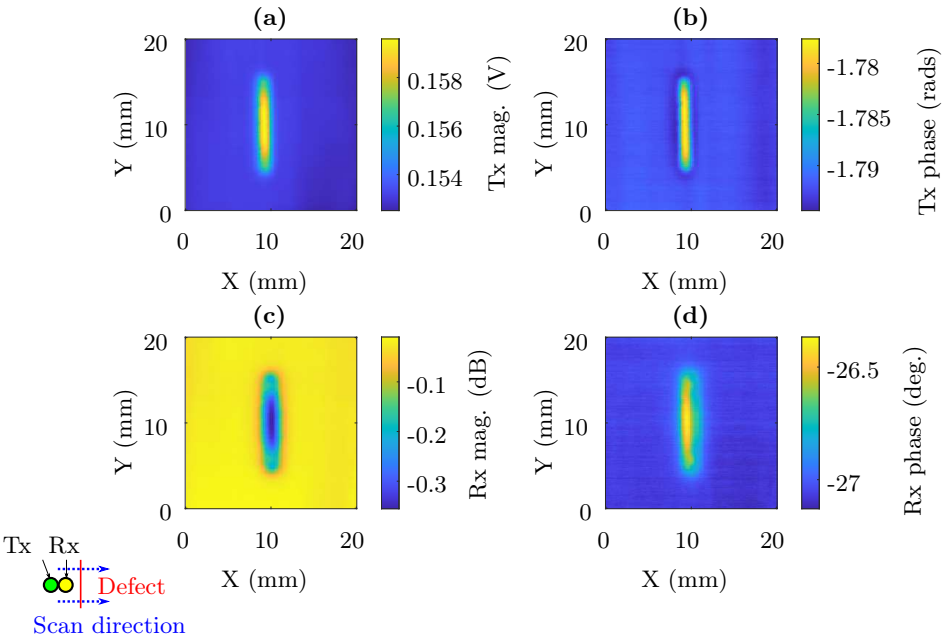

Figure 6.11: 2D scan on stainless steel with defect in perpendicular orientation (as depicted in the bottom left corner). Measurement taken with a 1 MHz driving current and the compact version of the meter based on the AD8302 chip for the Rx measurements.

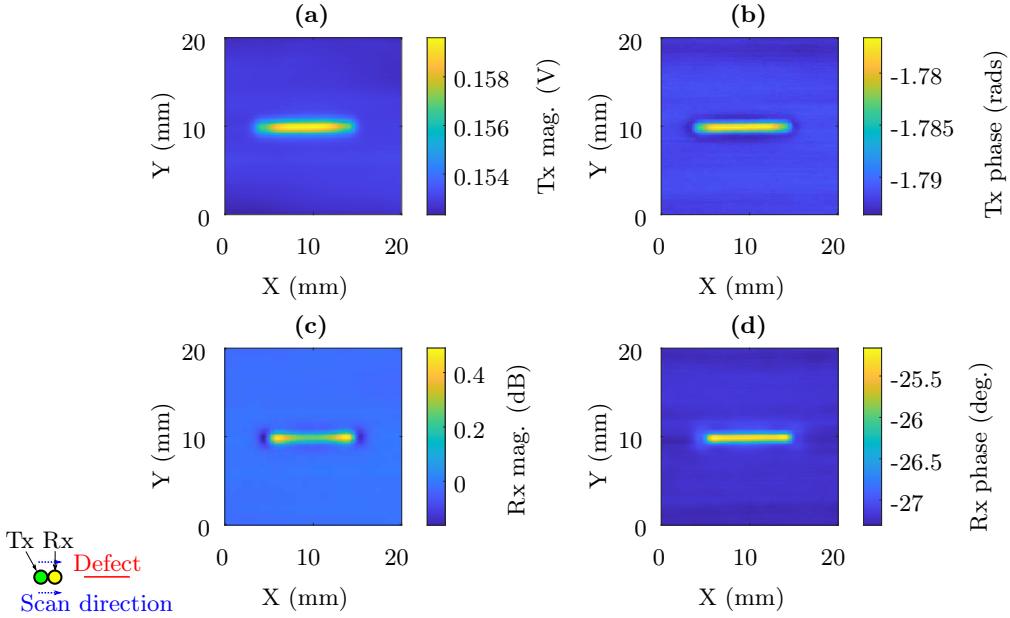

Figure 6.12: 2D scan on stainless steel with defect in parallel orientation (as depicted in the bottom left corner). Measurement taken with a 1 MHz driving current and the compact version of the meter based on the AD8302 chip for the Rx measurements.

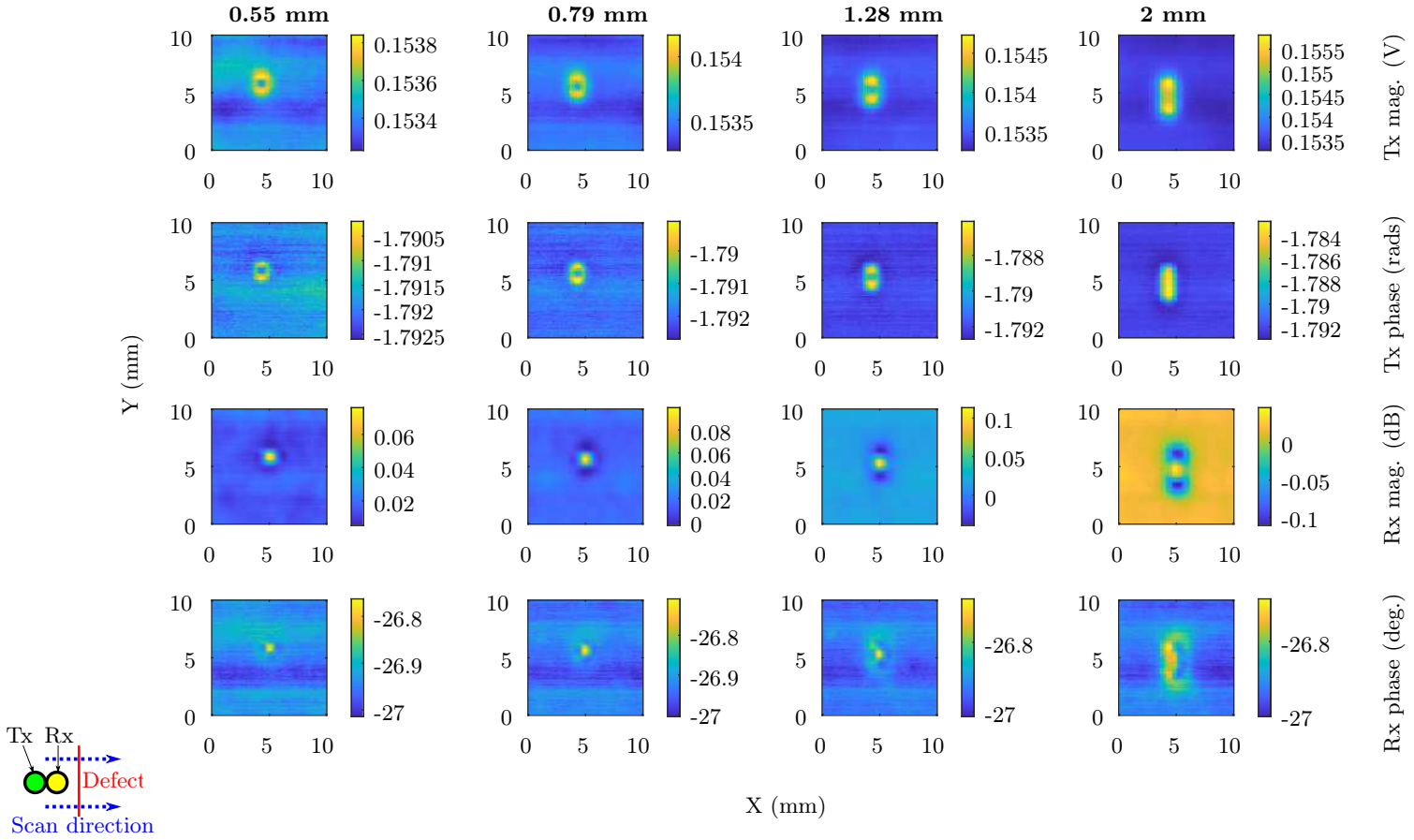

Figure 6.13: 2D scan on TiAl with defect in perpendicular orientation (as depicted in the bottom left corner). Measurement taken with a 1 MHz driving current and the compact version of the meter based on the AD8302 chip for the Rx measurements. Grouped in rows by the measured parameter and columns by the slot length.

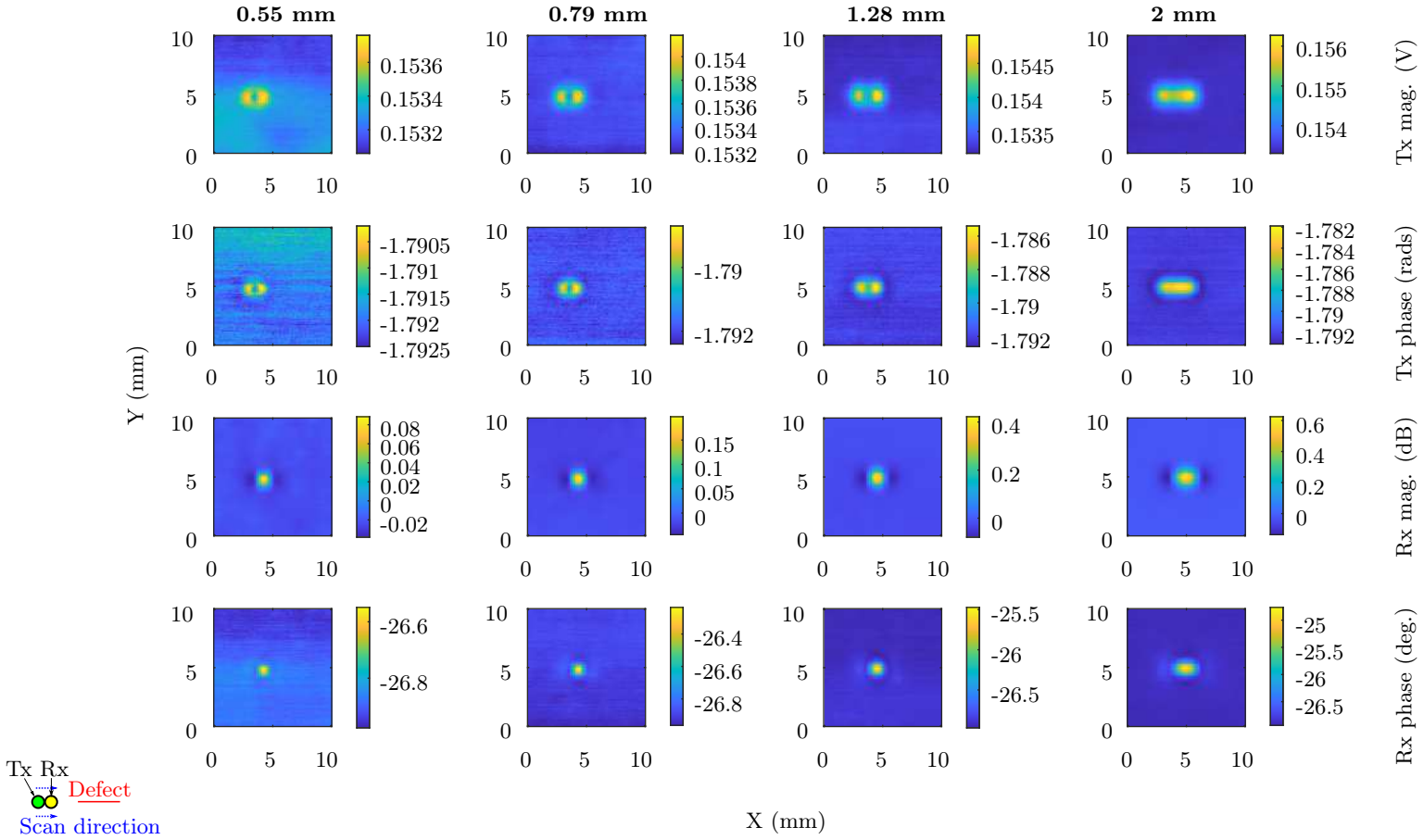

Figure 6.14: 2D scan on TiAl with defect in parallel orientation (as depicted in the bottom left corner). Measurement taken with a 1 MHz driving current and the compact version of the meter based on the AD8302 chip for the Rx measurements. Grouped in rows by the measured parameter and columns by the slot length.

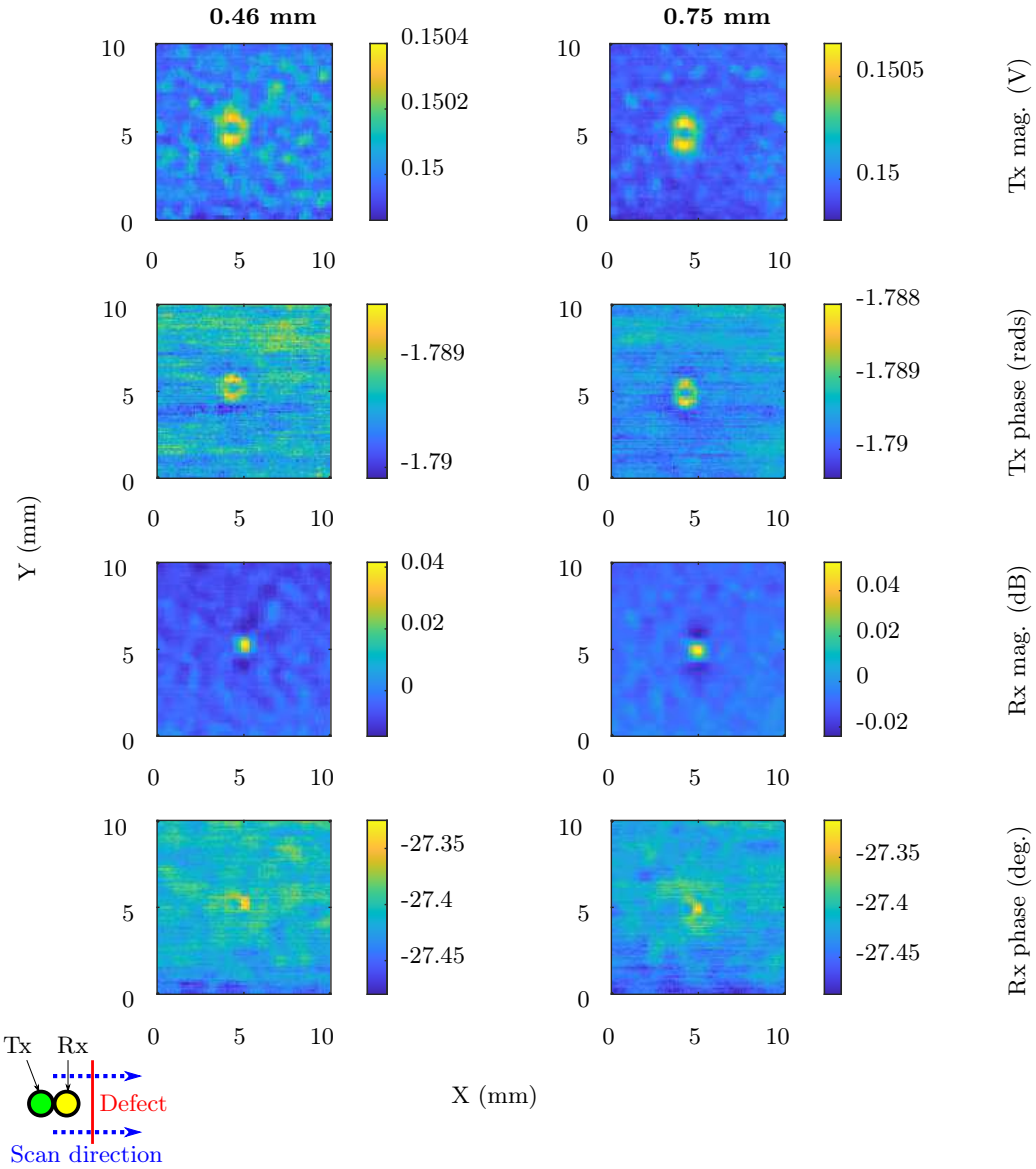

Figure 6.15: 2D scan on Ti with defect in perpendicular orientation (as depicted in the bottom left corner). Measurement taken with a 1 MHz driving current and the compact version of the meter based on the AD8302 chip for the Rx measurements. Grouped in rows by the measured parameter and columns by the slot length.

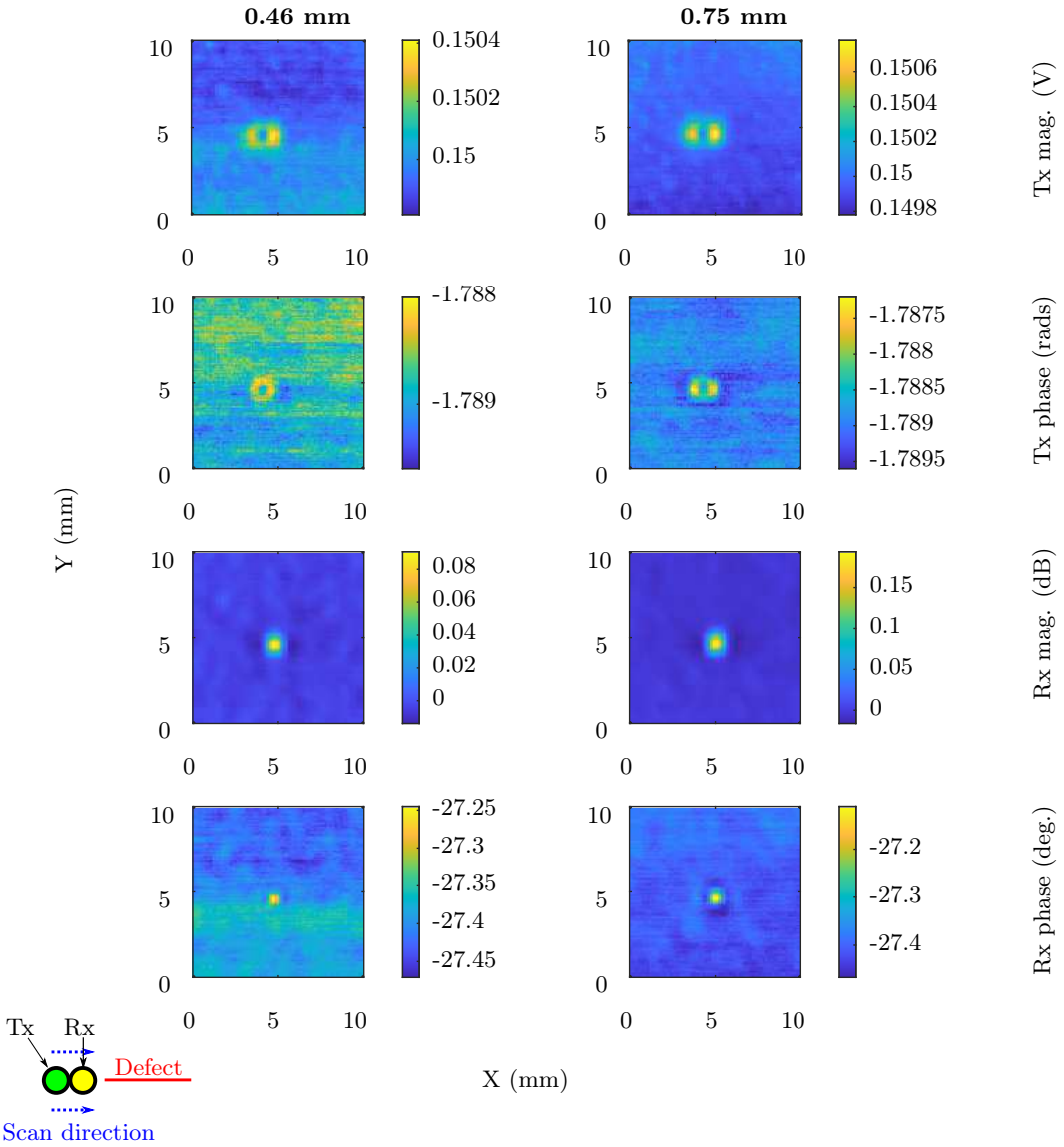

Figure 6.16: 2D scan on Ti with defect in parallel orientation (as depicted in the bottom left corner). Measurement taken with a 1 MHz driving current and the compact version of the meter based on the AD8302 chip for the Rx measurements. Grouped in rows by the measured parameter and columns by the slot length.

These results look similar to the previous experimental results in section 4.1 and to the simulation results. However, the signal response will be quantified, where a SNR calculation similar to section 4.1 is performed. The Rx mag. values from the simulation were also converted to decibels prior to the SNR calculation as the new meter measures magnitude in decibels.For the SNR in the perpendicular orientation, the background region is taken to be $[\mathrm{x}, \mathrm{y}, \mathrm{width}, \mathrm{height}] = [1, 1, 5, 5]$ mm

for the SS sample, $[\mathrm{x}, \mathrm{y}, \mathrm{width}, \mathrm{height}] = [7, 1.5, 5, 5]$ mm for the TiAl sample and $[\mathrm{x}, \mathrm{y}, \mathrm{width}, \mathrm{height}] = [9, 1, 2.5, 2.5]$ mm for the Ti sample. This results in the plot shown in figure 6.17. The correlation coefficient between the experimental and simulation results is 0.51 at 1 MHz and 0.71 at 5 MHz.

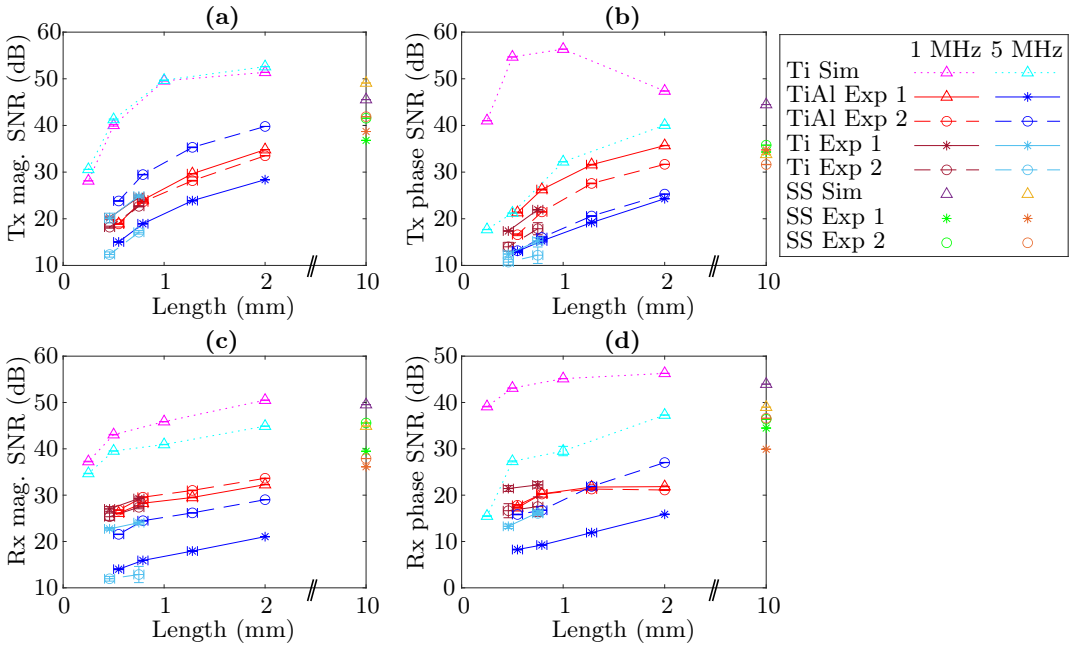

Figure 6.17: Signal-to-noise ratio as a function of frequency for the experimental and simulation results in the perpendicular orientation. The legend is arranged by row from the shortest to the longest slot. Exp and Sim are short for experimental and simulation results respectively. The experimental results are also categorised by whether they come from the first iteration of the meter or the second more compact iteration.

The counterpart in the parallel orientation is shown in figure 6.18. For this plot, the background region is taken to be $[\mathrm{x}, \mathrm{y}, \mathrm{width}, \mathrm{height}] = [1, 1, 5, 5]$ mm for the SS sample,$[\mathrm{x}, \mathrm{y}, \mathrm{width}, \mathrm{height}] = [2, 7, 5, 5]$ mm for the TiAl results and $[\mathrm{x}, \mathrm{y}, \mathrm{width}, \mathrm{height}] = [1, 7, 2.5, 2.5]$ mm for the Ti sample. The correlation coefficient between the experimental and simulation results is 0.59 at 1 MHz and 0.77 at 5 MHz.

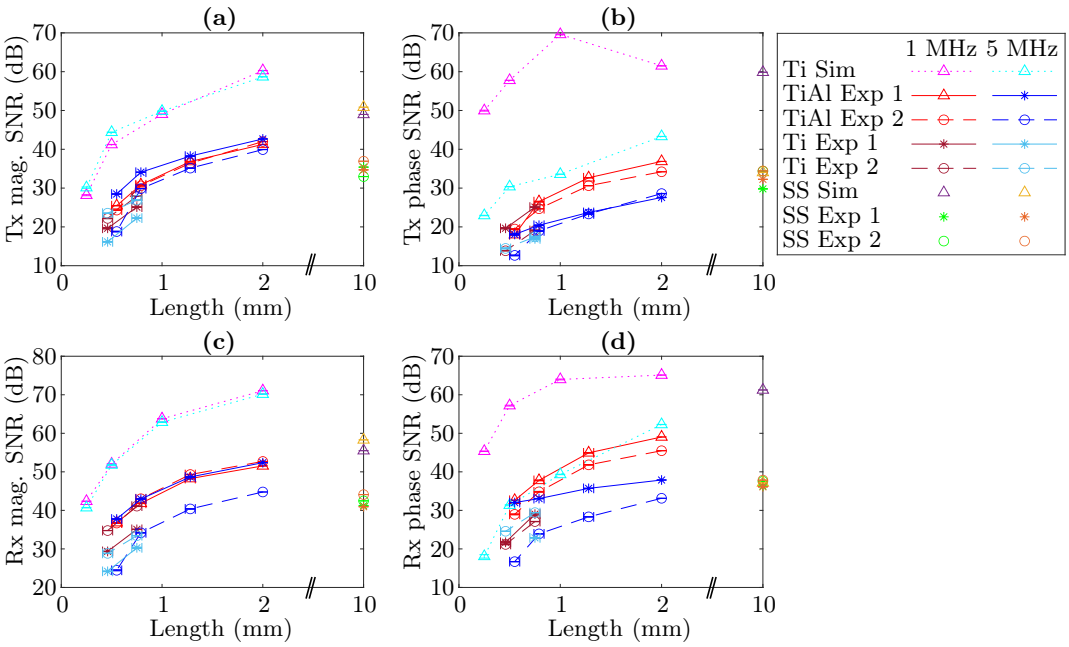

Figure 6.18: Signal-to-noise ratio as a function of frequency for the experimental and simulation results in the parallel orientation. The legend is arranged by row from the shortest to the longest slot. Exp and Sim are short for experimental and simulation results respectively. The experimental results are also categorised by whether they come from the first iteration of the meter or the second more compact iteration.

From these SNR results, it can be seen the that the SNR generally increases with size. There is the issue that it is hard to exactly replicate the previous conditions, particularly as the system is sensitive to small changes. This makes it difficult to do a straightforward comparison with previous results, but the results are nevertheless similar. The Tx magnitude and Tx phase measurements are taken in the same way as before and help to act as a reference. Given this, the Rx magnitude and Rx phase measurements look similar in magnitude. This is significant as these chips are relatively inexpensive compared to the much more expensive and bulky hardware that was used before. Additionally, by putting together all of the electronics, there may be more flexibility to alter the measuring system further down the line.

6.3 Summary of experimental results

The AD8302 chip, identified as a potentially suitable device for performing the phase and magnitude measurements of the signals from the eddy current coils, has been shown to work at least as well as a more bulky and expensive, high specification oscilloscope with similarities in the 2D scans and the SNR values compared to their counterparts in section 4.1.

The signal processing for magnitude and phase measurement is also performed within the chip, increasing measurement speed. Finally, it has been demonstrated that the AD8302 is also suited for incorporation onto the small electrical circuit mounted directly behind the coils, for improved performance at high frequencies. This proof of concept design opens the door to a more "open source" design for making eddy current systems compact and capable of operating at high frequencies.

Chapter 7

Conclusion

This thesis details the development of an eddy current probe system, including a novel compact meter capable of detecting and quantifying sub-millimetre defects whilst achieving SNRs in the detected voltage amplitude across the receiver coil (Rx mag.) of 34.76(2) dB and 36.7(1) dB for the shortest defects (0.46(5) mm and 0.55(5) mm) on Ti and TiAl respectively. The compact nature of the eddy current sensor makes it more convenient to use and allows electrical components and circuits to be integrated closer to the eddy current coils, reducing the need to use long connecting cables, which can potentially introduce noise. As discussed, this proof of concept design opens the door to a more "open source" design for making eddy current systems compact and capable of operating at high frequencies. Moreover, the novel compact sensor expands on the capabilities of earlier versions of the hardware by being able to also measure phase.

Additionally, it was found that the measurement of the phase difference on the receiving coil compared to the reference driving current (Rx phase) could potentially be more robust to lift-off variations, a well-known problem for defect detection.

Moreover, using small coils and high frequency of operation facilitates the detection of small surface defects that are close to the edge of a sample. A defect 3.0(1) mm long has been detected at the edge of a Ti sample with an SNR in the Rx mag. of up to 36.5(1) dB. Interesting behaviour was also observed in the Rx phase near the edge of a Ti sample in comparison to the response from a defect, which has the potential to help with detection of defects close to a sample edge. These main findings are broken down into sections below, and opportunities for further work will be discussed.

7.1 Designing and developing a new eddy current probe

Two main EC systems were developed in this thesis: one based on benchtop laboratory equipment to generate the reference signal and to measure the voltage from both coils, and another based on measuring the Rx mag. and Rx phase instead with a new magnitude and phase meter, based on the AD8302 chip. The systems were tested on defects machined on materials such as SS 316L and Ti as well as TiAl, which is likely to see increased use in the aerospace industry. The defects on the Ti and TiAl samples are especially small, being laser-machined sub-millimetre slot defects; the shortest slots on the Ti and TiAl have measured lengths of 0.46(5) mm and 0.55(5) mm respectively, and measured widths of 0.22(5) mm and 0.29(5) mm respectively. Moreover, the systems are capable of measuring both the magnitude and phase of the transmitter and receiver coils in the eddy current sensor.

With the system that uses benchtop laboratory equipment (AFG3052C function generator and MDO4054C oscilloscope), the greatest SNR values for Ti and TiAl are achieved at 1 MHz and with the coils in the parallel orientation relative to the defect (see section 2.6). Good SNRs are achieved for the smallest defects (e.g. SNR for the Rx mag. is 29.7(1) dB and 35.0(2) dB for the shortest slots on Ti and TiAl respectively), but the SNR is much improved for larger defects (e.g. SNR for the Rx mag. is 50.53(5) dB for the nominally 2 mm long defect on TiAl). While going to a higher frequency generally results in a lower SNR, probably due to stray capacitance, there is more spatial localisation of the defect signal at higher frequencies.

For the other system, a new compact meter was designed to a requested design and specification in this thesis. This meter uses a small and inexpensive chip (AD8302), with dimensions 4.4 mm x 5.0 mm x 1 mm, to measure magnitude and phase. A 65 mm x 40 mm x 3 mm PCB was fabricated to integrate the chip with the current electronics and was designed so that the gain for both the signal to be measured and the reference signal from the signal generator could be changed, along with the phase difference between them to improve sensitivity. There are certain advantages associated with this small design, including portability and the ability to fit the measuring electronics behind the coils to facilitate high-frequency operation.

The new compact meter was used to measure the Rx voltage, where the Tx coil voltage continues to be measured by extracting the magnitude and phase from signal measured by the oscilloscope as a baseline. With this, the SNR is again generally greater at 1 MHz in the parallel orientation like for the benchtop laboratory equipment. Here, the new Rx mag. SNRs are 29.35(6) dB and 36.81(2) dB for

the shortest slots on Ti and TiAl respectively. Again, the SNR is much improved for larger defects (e.g. the SNR for the nominally 2 mm long defect on TiAl is 51.54(3) dB). The SNR values obtained are similar to those for the benchtop laboratory equipment setup. This suggests that the compact meter with new electronics has a similar ability to measure the magnitude and phase.

While the SNR is generally largest for Rx mag. compared to the other measured parameters for the systems developed in this thesis, by measuring other parameters apart from Rx mag., it may be possible to combine them or use them together to increase confidence in defect detection, particularly as some parameters show interesting features such as the robustness of the Rx phase measurement to lift-off.

7.2 Comparison with EddySense prototype

The EC systems developed in this thesis were able to perform much better than the evaluation prototype from EddySense. With this, the best SNR is again at 1 MHz with an Rx mag. SNR of 23.86(8) dB for the smallest defect and 42.57(4) dB for the largest defect on the TiAl sample. Both of these measurements are again in the parallel orientation like the SNR values quoted in section 7.1, but for these SNR values, background subtraction was used because of the observed issues with lift-off variation. The SNR values from the Eddysense probe are good, but the SNR values achieved using the systems developed in this thesis are better. Another bonus is that the systems developed in this thesis can also measure phase.

7.3 Robustness of Rx phase to lift-off

The Rx phase measurement potentially appears more robust to lift-off variations, as the horizontal banding in the 2D scans was less visible than in scans of other parameters. This is significant as lift-off is a well-known issue in defect detection, where sensitivity to defects often is linked to sensitivity to lift-off since both are associated with a loss of material underneath the eddy current coils. Lift-off variation thus has the potential to obscure the detection of defects.

The natural progression was therefore to perform lift-off measurements, which was done with the system that uses the benchtop laboratory equipment. This showed that for 1 MHz eddy current measurements, the Rx phase has the largest response to a defect compared to the response to lift-off for the parameters measured. This manifests as a more visible gap in the normalised lift-off for the Rx phase compared

to the other parameters. The robustness of the Rx phase measurement for defect detection with varying lift-off is a novel result and is the subject of a published paper [177].

7.4 Edge defect detection

For the edge defects, the eddy current frequency was swept between 1 MHz and 20 MHz in steps of 1 MHz. Higher frequencies were expected to confine the eddy current spatial extent, thus emphasising variations in the sample that are closer to the eddy current coils, which is to be balanced with the increased electrical noise at higher frequencies. For the 3.0(1) mm long micromachined edge defect with a width of 0.5(1) mm and depth of 2.0(1) mm, it could be seen that the edge and the defect respond similarly in the Tx parameters (Tx mag. and Tx phase). The response to both the edge and the defect in these parameters is to rise. The similar response in these signals to both the edge and defect can make the defect difficult to distinguish from the response to the sample's edge.

For the Rx mag. and Rx phase measurements, the defect signal rises above the signal on the sample for frequencies above 12 MHz for the Rx mag. measurement, and for frequencies above 3 MHz for the Rx phase, despite the Rx mag. measurement and Rx phase measurement falling in response to the edge. Taking the signal value for the SNR calculation to be the average of the five highest points and the background as a defect-free region on the sample, the highest SNR in the Rx mag. measurement is achieved at 16 MHz and the highest SNR in the Rx phase measurement is achieved at 5 MHz. The defect signal in the Rx phase measurement stands out further, as unlike in the Rx mag. measurement defect signal, the Rx phase defect signal does not have visible sloping of the signal down towards the edge, dropping below the signal on the sample before the apparent edge is reached. For the corner defects, this behaviour was not seen, perhaps as the defect is more crudely cut.

Nevertheless, it can be seen that operating at certain frequencies can improve defect detection. Given that the best SNR is achieved at different frequencies for the different parameters, a multi-frequency approach may be beneficial. Furthermore, the spatial resolution generally increases as the frequency increases, which can be seen in the FWHM, though it does so at a decreasing rate, and considering that the SNR can decrease at higher frequencies due to electrical noise, one may need to strike a balance. The possibility of improving edge detection by increasing frequency and measuring the various parameters, especially the Rx phase, is an interesting result and the subject of another paper [182].

7.5 Finite element analysis of interaction of the eddy current coils with defects

To support the experimental results and provide insight to those results, finite element simulations were performed using COMSOL that have helped to validate and explain the observations made. At lower frequencies, these simulation results match well with the experimental results, although they deviated at higher frequencies, due to resonance of the electronic system that was not accounted for. The simulation has, however, helped confirm that some of the features seen in the experiment are indeed expected from the underlying physics of the system. For example, the increase in the Rx mag. and Rx phase measurements in response to a defect, despite these signals decreasing over the edge.

7.6 Final notes

The eddy current probes that have been designed and developed in this thesis are capable of measuring sub-millimetre defects with a high probability of detection due to the favourable level of SNR. This was achieved using benchtop laboratory equipment and using a compact circuit that is 65 mm x 40 mm x 3 mm in size, based on the AD8302 chip. The compact circuit was shown to work at least as well as a more bulky and expensive, high specification oscilloscope combined with PC processing of the data. The signal processing for magnitude and phase measurement is also performed within the chip, increasing measurement speed. It has been demonstrated that the AD8302 is also suited for incorporation onto the small electrical circuit mounted directly behind the coils, for improved performance at high frequencies. This proof of concept design opens the door to a more "open source" design for making eddy current systems compact, and capable of operating at high frequencies.

In addition to designing and developing new eddy current probes, some interesting behaviour was identified that may be used to improve defect detection, such as the potential robustness of the Rx phase measurement to lift-off variation, as well as there being a particularly interesting response to a defect in the Rx phase, which helps to distinguish it from the edge. These observations are the subject of two published papers [177, 182].

New eddy current probes and several interesting and novel results have been presented, but there are opportunities for further work. For example, there is scope to develop the compact circuit based on the AD8302 chip further and work on a stable and compact signal generator for driving the HCS to complement the compact

meter. Additionally, work could be carried out to try to accurately measure the profile of the defect so that more accurate simulations can be performed and the defect response can be better understood. This would however require capabilities that were not available in the development of this thesis, or the use of destructive methods. Moreover, a wider range of defect sizes could be tested to better establish a trend between the defect characteristics and signal observed, in particular, smaller defects may be of interest for safety-critical applications, where it is crucial to find defects at their earliest stage of development. There are opportunities to stretch the capabilities of the current technique and see the limits of what the technique is capable of.

References

[1] F Hughes, R Day, N Tung, and S Dixon. High-frequency eddy current measurements using sensor-mounted electronics. *Insight-Non-Destructive Testing and Condition Monitoring*, 58(11):596–600, 2016.

[2] A Egbeyemi. *Eddy Current Array Optimisation*. EngD thesis, University of Warwick, 2018.

[3] R Hussin, N Ismail, and S Mustapa. A study of foreign object damage (FOD) and prevention method at the airport and aircraft maintenance area. *IOP Conference Series: Materials Science and Engineering*, 152:012038, 2016.

[4] BL Boyce, X Chen, JW Hutchinson, and RO Ritchie. The residual stress state due to a spherical hard-body impact. *Mechanics of Materials*, 33(8):441–454, 2001.

[5] Ahmed F El-Sayed. *Bird strike in aviation: statistics, analysis and management*, page 51. John Wiley & Sons, 2019.

[6] Samuel A Howard, Jeremiah T Hammer, Kelly S Carney, and J Michael Pereira. *Jet engine bird ingestion simulations: comparison of rotating to non-rotating fan blades*, volume 55133, page 1. American Society of Mechanical Engineers, 2013.

[7] John J Ruschau, Theodore Nicholas, and Steven R Thompson. Influence of foreign object damage (FOD) on the fatigue life of simulated Ti-6Al-4 V airfoils. *International journal of impact engineering*, 25(3):233–250, 2001.

[8] Rhys Jones, Alan A Baker, Neil Matthews, and Victor K Champagne. *Aircraft sustainment and repair*, page 1. Butterworth-Heinemann, 2017.

[9] Xi Chen. Foreign object damage on the leading edge of a thin blade. *Mechanics of Materials*, 37(4):447–457, 2005.

[10] Trevor S Harding and J Wayne Jones. Effect of foreign object damage on the fatigue strength of an xd^{TM} γ-tial alloy. *Scripta Materialia*, 43(7):631, 2000.

[11] Ravi Prakash. *Non-destructive testing techniques*, pages 2,20,86. New Academic Science, 2011.

[12] Ian Baker. *Titanium*, page 243. Springer International Publishing, 2018.

[13] BP Bewlay, S Nag, A Suzuki, and MJ Weimer. Tial alloys in commercial aircraft engines. *Materials at High Temperatures*, 33(4-5):549–559, 2016.

[14] Adrian P Mouritz. *Introduction to aerospace materials*, pages 216–218, 255. Elsevier, 2012.

[15] Paul Breeze. *Gas-Turbine power generation*, page 45. Academic Press, 2016.

[16] Ikuhiro Inagaki, Tsutomu Takechi, Yoshihisa Shirai, and Nozomu Ariyasu. Application and features of titanium for the aerospace industry. *Nippon steel & sumitomo metal technical report*, 106(106):22–27, 2014.

[17] Stefano Gialanella and Alessio Malandruccolo. *Aerospace alloys*, pages 180–186. Springer, 2020.

[18] Thywill Cephas Dzogbewu. Additive manufacturing of tial-based alloys. *Manufacturing Review*, 7:35, 2020.

[19] Philip G Tipping. *Understanding and mitigating ageing in nuclear power plants: materials and operational aspects of plant life management (PLiM)*, pages 3–10, 59. Elsevier, 2010.

[20] Romney Duffey and Igor Pioro. Ensuring the future of nuclear power. *Mechanical Engineering*, 141(11):30–35, 2019.

[21] HM Hashemian. Aging management of instrumentation & control sensors in nuclear power plants. *Nuclear Engineering and Design*, 240(11):3781–3790, 2010.

[22] Minyu Fan, Mingya Chen, Min Yu, Wenqing Jia, Yuanfei Li, Yu Cao, Fei Xue, and Weiwei Yu. Long-term thermal aging performance of welding structures in primary coolant pipes for nuclear power plants. *Annals of Nuclear Energy*, 149:107793, 2020.

[23] Emilio Neri, Amanda French, Maria Elena Urso, Marc Deffrennes, Geoffrey Rothwell, Ivan Rehak, Inge Weber, Simon Carroll, and Vladislav Daniska. Costs of decommissioning nuclear power plants. Technical report, Organisation for Economic Co-Operation and Development, 2016.

[24] Andrew King, G Johnson, D Engelberg, Wolfgang Ludwig, and J Marrow. Observations of intergranular stress corrosion cracking in a grain-mapped polycrystal. *Science*, 321(5887):382–385, 2008.

[25] Karan Sotoodeh. Chapter twelve - material selection and corrosion. In Karan Sotoodeh, editor, *Subsea Valves and Actuators for the Oil and Gas Industry*, page 431. Gulf Professional Publishing, 2021.

[26] Ulla Ehrnstén. 2 - environmentally-assisted cracking of stainless steels in light water reactors. In Stefan Ritter, editor, *Nuclear Corrosion*, European Federation of Corrosion (EFC) Series, page 19. Woodhead Publishing, 2020.

[27] Noritaka Yusa, Zhenmao Chen, and Kenzo Miya. Sizing of stress corrosion cracking on austenitic stainless piping in a nuclear power plant from eddy current ndt signals. *Nondestructive Testing and Evaluation*, 20(2):103–114, 2005.

[28] Maurice G Silk, Arthur Marshall Stoneham, and J Andrew G Temple. *The reliability of non-destructive inspection: assessing the assessment of structures under stress*, pages 1–87. Adam Hilger, 1987.

[29] Jean-Paul Balayssac and Vincent Garnier. *Non-destructive testing and evaluation of civil engineering structures*, pages 1, 2. Elsevier, 2017.

[30] N. Faith. *Derail: Why Trains Crash*, page 144. Pan Macmillan, 2001.

[31] Jack Blitz. *Electrical and magnetic methods of non-destructive testing*, pages 2, 137, 160. Chapman & Hall, 2 edition, 1997.

[32] Andrew Starr, Basim Al-Najjar, Kenneth Holmberg, Erkki Jantunen, Jim Bellew, and Alhussein Albarbar. Maintenance today and future trends. In *E-maintenance*, pages 11–16. Springer, 2010.

[33] Milan Janic. An assessment of risk and safety in civil aviation. *Journal of Air Transport Management*, 6(1):43–50, 2000.

[34] Daniel J Inman, Charles R Farrar, Vicente Lopes Junior, and Valder Steffen Junior. *Damage prognosis: for aerospace, civil and mechanical systems*, page 8. John Wiley & Sons, 2005.

[35] I Virkkunen, M Kemppainen, JM Tchilian, and J Martens. Advances in production of realistic cracks to ndt development and qualification purposes of steam generator tubes. In *6th CNS International Steam Generator Conference, Toronto*, 2009.

[36] Zhenmao Chen, Noritaka Yusa, and Kenzo Miya. Enhancements of eddy current testing techniques for quantitative nondestructive testing of key structural components of nuclear power plants. *Nuclear engineering and design*, 238(7): 1651–1656, 2008.

[37] P Cawley. Non-destructive testingâĂŤcurrent capabilities and future directions. *Proceedings of the Institution of Mechanical Engineers, Part L: Journal of Materials: Design and Applications*, 215(4):213–223, 2001.

[38] W. Karwowski and W.S. Marras. *Occupational Ergonomics: Principles of Work Design*, chapter 17, page 21. Principles and Applications in Engineering. CRC Press, 2003.

[39] B. Raj, T. Jayakumar, and M. Thavasimuthu. *Practical Non-destructive Testing*, pages 4, 29. Woodhead, 2002.

[40] S Rajeswari, MR Vijaya Lakshmi, MV Shubhanjali, Jis Mathew, KR Raghu, and Sreelal Sreedhar. Applications of visual inspection in NDE of aero engine components–case studies. *Indian National Seminar & Exhibition on Non-Destructive Evaluation NDE 2015*, 2015.

[41] Jeff Tollefson et al. Nuclear power plants prepare for old age. *Nature*, 537 (7618):16–17, 2016.

[42] BINDT. Non-destructive testing (ndt) – guidance document: An introduction to ndt common methods, 11 2015.

[43] Mark Rice, Liyuan Li, Gu Ying, Marcus Wan, Eng Thiam Lim, Gao Feng, Jamie Ng, MT Jin Li, and VS Bab. Automating the visual inspection of aircraft. In *Aerospace technology and engineering conference*, 2018.

[44] T Armitt. The requirement for training of visual test personnel. *CINDE Journal*, 24(2):6–12, 2003.

[45] Lei Geng, YuXiang Wen, Fang Zhang, YanBei Liu, et al. Machine vision detection method for surface defects of automobile stamping parts. *American Academic Scientific Research Journal for Engineering, Technology, and Sciences*, 53(1):128–144, 2019.

[46] Bence Bartha. Nondestructive evaluation applications for failure analysis. *Journal of Failure Analysis and Prevention*, pages 1–8, 2022.

[47] L. Cartz. *Nondestructive testing: radiography, ultrasonics, liquid penetrant, magnetic particle, eddy current*, pages 16, 128, 187. ASM International, 1995.

[48] O. Glasser. *Wilhelm Conrad Röntgen and the Early History of the Roentgen Rays*, pages 99–100. Norman Radiology Series. Norman Pub., 1993.

[49] Wilhelm Conrad Röntgen. On a new kind of rays. *Science*, 3(59):227–231, 1896.

[50] Sanjay Kumar and DG Mahto. Recent trends in industrial and other engineering applications of non destructive testing: a review. *International Journal of Scientific & Engineering Research*, 4(9), 2013.

[51] D.E. Bray and D. McBride. *Nondestructive Testing Techniques*, pages 5–18, 113, 450–451, 503–532. New Dimensions In Engineering Series. Wiley, 1992.

[52] Matthew W Kozak. Radiation protection and safety in industrial radiography, international atomic energy agency safety series number 13, 2000.

[53] A.S. Paipetis, T.E. Matikas, D.G. Aggelis, and D. Van Hemelrijck. *Emerging Technologies in Non-Destructive Testing V*, page 225. Taylor & Francis, 2012.

[54] D Cerniglia, M Scafidi, A Pantano, and J Rudlin. Inspection of additive-manufactured layered components. *Ultrasonics*, 62:292–298, 2015.

[55] Rainer Pohl, Anton Erhard, H-J Montag, H-M Thomas, and Hermann Wüstenberg. Ndt techniques for railroad wheel and gauge corner inspection. *NDT & e International*, 37(2):89–94, 2004.

[56] Elias Klein. Some background history of ultrasonics. *The Journal of the Acoustical Society of America*, 20(5):601–604, 1948.

[57] Warren P Mason. Piezoelectricity, its history and applications. *The Journal of the Acoustical Society of America*, 70(6):1561–1566, 1981.

[58] Earl N Mallory. *Nondestructive testing: methods, analyses and applications*, page 63. Nova Science Publishers, 2010.

[59] M.G. Silk. *Ultrasonic Transducers for Nondestructive Testing*, pages 111–114. Adam Hilger, 1984.

[60] Dale Ensminger and Leonard J Bond. *Ultrasonics: fundamentals, technologies, and applications*, page 210. CRC press, 2011.

[61] SJ Davies, Chris Edwards, GS Taylor, and Stuart B Palmer. Laser-generated ultrasound: its properties, mechanisms and multifarious applications. *Journal of Physics D: Applied Physics*, 26(3):329, 1993.

[62] TL Moran, P Ramuhalli, AF Pardini, MT Anderson, and SR Doctor. Replacement of radiography with ultrasonics for the nondestructive inspection of welds-evaluation of technical gaps-an interim report. *US Department of Energy*, 2010.

[63] Jeffrey P Milligan, Daniel T Peters, and Jason K Van Velsor. Advanced NDE techniques and their deployment on high pressure equipment. In *ASME 2012 Pressure Vessels and Piping Conference*, pages 89–95. American Society of Mechanical Engineers, 2012.

[64] C. Matthews. *Handbook of Mechanical In-Service Inspection: Pressure Systems and Mechanical Plant*, page 111. Professional Engineering Publishing handbook. Wiley, 2003.

[65] M.J. Lovejoy. *Magnetic Particle Inspection: A practical guide*, pages 172–174. Springer Netherlands, 2012.

[66] NP Migoun and NV Delenkovskii. Improvement of penetrant-testing methods. *Journal of Engineering Physics and Thermophysics*, 82(4):734–742, 2009.

[67] IAEA Training Course Series. Liquid penetrant and magnetic particle testing at level 2, 2000.

[68] Charles Babbage and John Frederick William Herschel. Xxi. account of the repetition of m. arago's experiments on the magnetism manifested by various substances during the act of rotation. *Philosophical Transactions of the Royal Society of London*, 115:467–496, 1825.

[69] Irene Arias and Jan D Achenbach. A model for the ultrasonic detection of surface-breaking cracks by the scanning laser source technique. *Wave Motion*, 39(1):61–75, 2004.

[70] YiLai Ma, JinZhong Chen, Yang Jin, and RenYang He. Simulation and experimental research on 316l liner of bimetal composite pipe with eddy current testing. *Insight-Non-Destructive Testing and Condition Monitoring*, 64 (3):131–137, 2022.

[71] Michael Faraday. Experimental researches in electricity. *Philosophical Transactions of the Royal Society of London*, 122:125–162, 1832.

[72] DE Hughes. Induction-balance and experimental researches therewith. *Proceedings of the Physical Society of London*, 3(1):81, 1879.

[73] Robert C McMaster. The origins of electromagnetic testing. *Mater. Eval*, 43 (8):946–956, 1985.

[74] HL Libby. Miscellaneous eddy current techniques. Technical report, Battelle-Northwest, Richland, Wash. Pacific Northwest Lab., 1969.

[75] DL Waidelich and CJ Renken Jr. The impedance of a coil near a conductor. *Proceedings of the national electronics conference*, 12:188, 1956.

[76] CV Dodd and WE Deeds. Analytical solutions to eddy-current probe-coil problems. *Journal of applied physics*, 39(6):2829–2838, 1968.

[77] CC Cheng, CV Dodd, and WE Deeds. Int testing. *J. Nondestr*, 3:109, 1971.

[78] Erol Uzal, John C Moulder, Sreeparna Mitra, and James H Rose. Impedance of coils over layered metals with continuously variable conductivity and permeability: Theory and experiment. *Journal of Applied Physics*, 74(3):2076–2089, 1993.

[79] Yoseph Bar-Cohen. Emerging NDE technologies and challenges at the beginning of the 3rd millennium—part i. *Material Evaluation*, 58(1):17–30, 2000.

[80] A McNab and J Thomson. An eddy current array instrument for application on ferritic welds. *NDT & E International*, 28(2):103–112, 1995.

[81] W Yin, SJ Dickinson, and AJ Peyton. A multi-frequency impedance analysing instrument for eddy current testing. *Measurement Science and Technology*, 17 (2):393, 2006.

[82] Foz Hughes, R Day, N Tung, and S Dixon. High-frequency eddy current measurements using sensor-mounted electronics. *Insight-Non-Destructive Testing and Condition Monitoring*, 58(11):596–600, 2016.

[83] Henning Heuer, Martin H Schulze, et al. Eddy current testing of carbon fiber materials by high resolution directional sensors. *Proc NDT Canada*, pages 1–13, 2011.

[84] Vistasp M Karbhari. *Non-destructive evaluation (NDE) of polymer matrix composites*, page 40. Elsevier, 2013.

[85] Bassam A Abu-Nabah and Peter B Nagy. High-frequency eddy current conductivity spectroscopy for residual stress profiling in surface-treated nickel-base superalloys. *Ndt & E International*, 40(5):405–418, 2007.

[86] Carsten Schmidt, Cedric Schultz, Patricc Weber, and Berend Denkena. Evaluation of eddy current testing for quality assurance and process monitoring of automated fiber placement. *Composites Part B: Engineering*, 56:109–116, 2014.

[87] Yew San Hor, Vinod K Sivaraja, Yu Zhong, Bui V Phuong, and Christopher Lane. Modelling and evaluation of electrical resonance eddy current for submillimeter defect detection. *Progress In Electromagnetics Research C*, 89:101–110, 2019.

[88] E Rau, J Bamberg, J Burchards, P Berwig, and W Voelkl. High resolution crack detection on turbine blade roots by the use of eddy current and ultrasonic rayleigh waves. *World Conference on Non-Destructive Testing*, 2016.

[89] Gerhard Mook, Rolf Lange, and Ole Koeser. Non-destructive characterisation of carbon-fibre-reinforced plastics by means of eddy-currents. *Composites science and technology*, 61(6):865–873, 2001.

[90] Jun Cheng, Jinhao Qiu, Xiaojuan Xu, Hongli Ji, Toshiyuki Takagi, and Tetsuya Uchimoto. Research advances in eddy current testing for maintenance of carbon fiber reinforced plastic composites. *International Journal of Applied Electromagnetics and Mechanics*, 51(3):261–284, 2016.

[91] Robert R Hughes, BW Drinkwater, and RA Smith. Characterisation of carbon fibre-reinforced polymer composites through radon-transform analysis of complex eddy-current data. *Composites Part B: Engineering*, 148:252–259, 2018.

[92] Dehui Wu, Fang Cheng, Fan Yang, and Chao Huang. Non-destructive testing for carbon-fiber-reinforced plastic (cfrp) using a novel eddy current probe. *Composites Part B: Engineering*, 177:107460, 2019.

[93] Jun Cheng, Jinhao Qiu, Hongli Ji, Enrong Wang, Toshiyuki Takagi, and Tetsuya Uchimoto. Application of low frequency ect method in noncontact detection and visualization of cfrp material. *Composites Part B: Engineering*, 110: 141–152, 2017.

[94] A Ruosi. Nondestructive detection of damage in carbon fibre composites by squid magnetometry. *physica status solidi (c)*, 2(5):1533–1555, 2005.

[95] C Carr, D Graham, JC Macfarlane, and GB Donaldson. Squid-based nondestructive evaluation of carbon fiber reinforced polymer. *IEEE transactions on applied superconductivity*, 13(2):196–199, 2003.

[96] Seyed Masoud Marandi, Kh Rahmani, and Mehdi Tajdari. Foreign object damage on the leading edge of gas turbine blades. *Aerospace Science and Technology*, 33(1):65–75, 2014.

[97] B Sasi, BPC Rao, and T Jayakumar. Dual-frequency eddy current nondestructive detection of fatigue cracks in compressor discs of aero engines. *Defence Science Journal*, 54(4):563, 2004.

[98] Sarit Sharma, Ibrahim Elshafiey, Lalita Udpa, and Satish Udpa. Finite element modeling of eddy current probes for edge effect reduction. In *Review of Progress in Quantitative Nondestructive Evaluation*, pages 201–208. Springer, 1997.

[99] Nathan Ida and Norbert Meyendorf. *Handbook of advanced nondestructive evaluation*, page 665. Springer International Publishing Cham, Switzerland, 2019.

[100] Theodoros Theodoulidis and John R Bowler. Interaction of an eddy-current coil with a right-angled conductive wedge. *IEEE Transactions on Magnetics*, 46(4):1034–1042, 2009.

[101] John R Bowler, Theodoros P Theodoulidis, and Nikolaos Poulakis. Eddy current probe signals due to a crack at a right-angled corner. *IEEE transactions on magnetics*, 48(12):4735–4746, 2012.

[102] Yuedong Xie, Jiyao Li, Yang Tao, Shupei Wang, Wuliang Yin, and Lijun Xu. Edge effect analysis and edge defect detection of titanium alloy based on eddy current testing. *Applied Sciences*, 10(24):8796, 2020.

[103] Yibo Wang, Qian Bai, Wei Du, and Bi Zhang. Edge effect on eddy current detection for subsurface defects in titanium alloys. In *Proceedings of the 8th International Conference on Computational Methods, Guilin, China*, pages 25–27, 2017.

[104] Teodor Dogaru· and Stuart T Smith. Edge crack detection using a giant magnetoresistance based eddy current sensor. *Nondestructive Testing and Evaluation*, 16(1):31–53, 2000.

[105] J Fava and M Ruch. Design, construction and characterisation of ect sensors with rectangular planar coils. *Insight-Non-Destructive Testing And Condition Monitoring*, 46(5):268–274, 2004.

[106] N Eua-Anant, Lalita Udpa, and J Chao. Morphological processing for crack detection in eddy current images of jet engine disks. In *Review of Progress in Quantitative Nondestructive Evaluation*, pages 751–758. Springer, 1999.

[107] WE Gardner. *Improving the effectiveness and reliability of non-destructive testing*, page 62. Elsevier, 2013.

[108] Javier García-Martín, Jaime Gómez-Gil, and Ernesto Vázquez-Sánchez. Non-destructive techniques based on eddy current testing. *Sensors*, 11(3):2525–2565, 2011.

[109] J Hansen. The eddy current inspection method. *Insight*, 46(8):1–4, 2004.

[110] Ian S Grant and William Robert Phillips. *Electromagnetism*, pages 221, 388–390. John Wiley & Sons, 2013.

[111] Hyo J. Eom. *Maxwell's Equations*, page 117. Springer Netherlands, Dordrecht, 2013.

[112] Nicola Bowler and N Bowler. *Eddy-current nondestructive evaluation*, page 61. Springer, 2019.

[113] D.J. Hagemaier. *Fundamentals of Eddy Current Testing*, pages 35–46. American Society for Nondestructive Testing, 1990.

[114] Zhenmao Chen, Cherdpong Jomdecha, and Shejuan Xie. *Eddy Current Testing*, page 2. Springer International Publishing, Cham, 2019.

[115] Gerhard Mook, Olaf Hesse, and Valentin Uchanin. Deep penetrating eddy currents and probes. *Materials Testing*, 49(5):258–264, 2007.

[116] FHe Froes. *Titanium: physical metallurgy, processing, and applications*, page 27. ASM international, 2015.

[117] Michael De Podesta. *Understanding the properties of matter*, page 217. CRC Press, 2020.

[118] Pasquale Cavaliere. *Spark plasma sintering of materials: advances in processing and applications*, page 282. Springer, 2019.

[119] JC Li, Y Wang, and DC Ba. Characterization of semiconductor surface conductivity by using microscopic four-point probe technique. *Physics Procedia*, 32:347–355, 2012.

[120] N. S. Stoloff. *Fatigue*, chapter 17, page 347. John Wiley & Sons, Ltd, 2002.

[121] Fernando Franco, Filipe A Cardoso, Luís S Rosado, Ricardo Ferreira, Susana Cardoso, Moisés Piedade, and Paulo P Freitas. Advanced ndt inspection tools for titanium surfaces based on high-performance magnetoresistive sensors. *IEEE Transactions on Magnetics*, 53(4):1–5, 2016.

[122] VS Cecco, G Van Drunen, and FL Sharp. Eddy current testing, volume 1. Technical report, Atomic Energy of Canada Ltd., 1981.

[123] James William Nilsson and Susan A Riedel. *Electric circuits*, page 357. Pearson, 2020.

[124] Kenneth L Kaiser. *Electromagnetic compatibility handbook*, pages 19–48. CRC press, 2004.

[125] Robert R Hughes and Steve Dixon. Analysis of electrical resonance distortion for inductive sensing applications. *IEEE Sensors Journal*, 18(14):5818–5825, 2018.

[126] Bryan H Suits. *Electronics for Physicists: An Introduction*, page 37. Springer Nature, 2020.

[127] G Van Drunen and VS Cecco. Recognizing limitations in eddy-current testing. *NDT international*, 17(1):9–17, 1984.

[128] R Winston Revie. *Oil and gas pipelines: integrity and safety handbook*, page 538. John Wiley & Sons, 2015.

[129] Klara Capova, Ivo Cap, Ladislav Janousek, and Milan Smetana. Recent trends in electromagnetic non-destructive sensing. *Advances in Electrical and Electronic Engineering*, 7(1-2):322–325, 2011.

[130] Tribikram Kundu. *Ultrasonic and electromagnetic NDE for structure and material characterization: engineering and biomedical applications*, page 193. CRC Press, 2012.

[131] John Hansen. The eddy current inspection method. part 2: The impedance plane and probes. *Insight*, 46(6):364–365, 2004.

[132] LS Obrutsky, VS Cecco, SP Sullivan, and D Humphrey. Transmit-receive eddy current probes for circumferential cracks in heat exchanger tubes. *NDT and E International*, 3(30):172, 1997.

[133] H Wong, YM Foong, and DHC Chua. Improving the conductivity of diamond-like carbon films with zinc doping and its material properties. *Applied surface science*, 257(22):9616–9620, 2011.

[134] SL Kakani. *Material science*, page 432. New Age International (P) Ltd., Publishers, 2004.

[135] John R Bowler. Eddy-current interaction with an ideal crack. i. the forward problem. *Journal of Applied Physics*, 75(12):8128–8137, 1994.

[136] Anastassios Skarlatos and Theodoros Theodoulidis. Analytical treatment of eddy-current induction in a conducting half-space with a cylindrical hole parallel to the surface. *IEEE transactions on magnetics*, 47(11):4592–4599, 2011.

[137] Theodoros Theodoulidis and John Bowler. Eddy-current interaction of a long coil with a slot in a conductive plate. *IEEE Transactions on Magnetics*, 41(4): 1238–1247, 2005.

[138] AG Mackie. Green's functions and riemann's method. *Proceedings of the Edinburgh Mathematical Society*, 14(4):293–302, 1965.

[139] M. V. K. Chari. Finite-element solution of the eddy-current problem in magnetic structures. *IEEE Transactions on Power Apparatus and Systems*, PAS-93 (1):62–72, 1974.

[140] Kazuhisa Ishibashi. Eddy current analysis by boundary element method utilizing impedance boundary condition. *IEEE transactions on magnetics*, 31(3): 1500–1503, 1995.

[141] N. A. Demerdash and T. W. Nehl. An evaluation of the methods of finite elements and finite differences in the solution of nonlinear electromagnetic fields in electrical machines. *IEEE Transactions on Power Apparatus and Systems*, PAS-98(1):74–87, 1979.

[142] Kevin W Cassel. *Matrix, Numerical, and Optimization Methods in Science and Engineering*, pages 382–383. Cambridge University Press, 2021.

[143] John T Katsikadelis. *The boundary element method for engineers and scientists: theory and applications*, page 3. Academic Press, 2016.

[144] Kok Hwa Yu, A Halim Kadarman, and Harijono Djojodihardjo. Development and implementation of some bem variants—a critical review. *Engineering Analysis with Boundary Elements*, 34(10):884–899, 2010.

[145] Joost van der Weijde, Erik Vlasblom, Peter Dobbe, Heike Vallery, and Michael Fritschi. Force sensing for compliant actuators using coil spring inductance. In *2015 IEEE/RSJ International Conference on Intelligent Robots and Systems (IROS)*, pages 2692–2697. IEEE, 2015.

[146] Hantaro Nagaoka. The inductance coefficients of solenoids. *The journal of the College of Science, Imperial University of Tokyo, Japan*, 27:1–33, 1909.

[147] Duck-Gun Park, C Sekar Angani, BPC Rao, Gabor Vértesy, Duk-Hyun Lee, and Kyung-Ho Kim. Detection of the subsurface cracks in a stainless steel plate using pulsed eddy current. *Journal of Nondestructive Evaluation*, 32(4): 350–353, 2013.

[148] Z Mottl. The quantitative relations between true and standard depth of penetration for air-cored probe coils in eddy current testing. *NDT international*, 23(1):11–18, 1990.

[149] S Majidnia, R Nilavalan, and J Rudlin. A numerical study of the depth of penetration of eddy currents. *Insight-Non-Destructive Testing and Condition Monitoring*, 58(3):129–134, 2016.

[150] Mark Blodgett, Hassan Waled, and Peter B Nagy. Theoretical and experimental investigations of the lateral resolution of eddy current imaging. *Materials Evaluation*, 58(5):647–654, 2000.

[151] GD Hammond, CC Speake, and M Stiff. Noise analysis of a howland current source. *International journal of electronics*, 95(4):351–359, 2008.

[152] Fair-rite. Fair-rite catalog 17th edition. *Fair-Rite Products Corp., PO Box*, Accessed 15 September 2021.

[153] Fair-rite. Material safety data sheet (MSDS). *Fair-Rite Products Corp., PO Box*, Accessed August 2021.

[154] Fair-rite. 67 material complex permeability vs. frequency. *Fair-Rite Products Corp., PO Box*, Accessed November 2017.

[155] R Hughes, Y Fan, and S Dixon. Investigating electrical resonance in eddy-current array probes. In *AIP Conference Proceedings*, volume 1706, page 090001. AIP Publishing LLC, 2016.

[156] Krishna Naishadham. Closed-form design formulas for the equivalent circuit characterization of ferrite inductors. *IEEE transactions on electromagnetic compatibility*, 53(4):923–932, 2011.

[157] Theodoros P Theodoulidis. Model of ferrite-cored probes for eddy current nondestructive evaluation. *Journal of applied physics*, 93(5):3071–3078, 2003.

[158] Ronald Halmshaw. *Non-destructive testing*, pages 36.1, 36.2. Edward Arnold, 1991.

[159] Harold M Cobb. *The history of stainless steel*, pages 7, 185. ASM International, 2010.

[160] G.F. Vander Voort, ASM International. Handbook Committee, and ASM International. *Metallography and Microstructures*, page 683. ASM handbook. ASM International, 2004.

[161] Lei Bi. Institute of metal research, chinese academy of sciences: aiming to achieve breakthroughs in the development of materials. *National Science Review*, 4(2):269–282, 2017.

[162] RJ Schaeffer and GM Janowski. Phase transformation effects during hip of TiAl. *Acta Metallurgica et Materialia*, 40(7):1645–1651, 1992.

[163] Ilio Miccoli, Frederik Edler, Herbert Pfnür, and Christoph Tegenkamp. The 100th anniversary of the four-point probe technique: the role of probe geometries in isotropic and anisotropic systems. *Journal of Physics: Condensed Matter*, 27(22):223201, 2015.

[164] Ilham Zainal Abidin, Gui Yun Tian, John Wilson, Suixian Yang, and Darryl Almond. Quantitative evaluation of angular defects by pulsed eddy current thermography. *NDT & E International*, 43(7):537–546, 2010.

[165] Yashar Javadi, Nina E Sweeney, Ehsan Mohseni, Charles N MacLeod, David Lines, Momchil Vasilev, Zhen Qiu, Randika KW Vithanage, Carmelo Mineo, Theodosia Stratoudaki, et al. In-process calibration of a non-destructive testing system used for in-process inspection of multi-pass welding. *Materials & Design*, 195:108981, 2020.

[166] RE Beissner. Slots vs. cracks in eddy current NDE. *Journal of Nondestructive Evaluation*, 13(4):175–183, 1994.

[167] George A Matzkanin and H Thomas Yolken. Probability of detection (pod) for nondestructive evaluation (nde). Technical report, NONDESTRUCTIVE TESTING INFORMATION ANALYSIS CENTER AUSTIN TX, 2001.

[168] MathWorks. Matlab R2020a, 2020.

[169] Ifan Hughes and Thomas Hase. *Measurements and their uncertainties: a practical guide to modern error analysis*, page 38. OUP Oxford, 2010.

[170] Yuichi Sekine and Hitoshi Soyama. Using an eddy current method with inverse analysis to determine the thickness of the layer modified by cavitation peening at the surface of type 316 l austenitic stainless steel. *NDT & E International*, 46:94–99, 2012.

[171] David A Litvin. Titanium for marine applications. *Naval Engineers Journal*, 83(5):37–44, 1971.

[172] Noritaka Yusa, Hidetoshi Hashizume, Tetsuya Uchimoto, Toshiyuki Takagi, and Kunihiro Sato. Evaluation of the electromagnetic characteristics of type 316l stainless steel welds from the viewpoint of eddy current inspections. *Journal of Nuclear Science and Technology*, 51(1):127–132, 2014.

[173] Mark Blodgett and Peter B Nagy. Anisotropic grain noise in eddy current inspection of noncubic polycrystalline metals. *Applied Physics Letters*, 72(9): 1045–1047, 1998.

[174] Analog Devices. AD9850 CMOS 125MHz complete DDS synthesizer. *Analog Devices, One Technology Way, PO Box*, 9106, 2004.

[175] VM Uchanin. Specific features of the space distribution of the signal of an eddy-current converter caused by cracks of different lengths. *Materials Science*, 43 (4):591–595, 2007.

[176] Tektronics. AFG3000C Series Datasheet, August 2021. URL `https://uk.tek.com/datasheet/afg3000c-arbitrary-function-generator-datasheet`.

[177] A To, Z Li, and S Dixon. Improved eddy current testing sensitivity using phase information. *Insight - Non-Destructive Testing & Condition Monitoring*, 63 (10):578–584, 2021.

[178] Youssoufa Mohamadou, Foutse Momo, Lealea Theophile, C Njike Kouekeu Landry, Tueche Fabrice, and Simeu Emmanuel. Accuracy enhancement in low frequency gain and phase detector (ad8302) based bioimpedance spectroscopy system. *Measurement*, 123:304–308, 2018.

[179] YF Yee and Chandan Kumar Chakrabarty. Phase detection using ad8302 evaluation board in the superheterodyne microwave interferometer for line average plasma electron density measurements. *Measurement*, 40(9-10):849–853, 2007.

[180] Analog Devices. datasheet AD8302: RF/IF gain and phase detector. *Rev. A*, 2002.

[181] Analog devices. 14-lead thin shrink small outline package [TSSOP]. *Analog devices*, Accessed 7 September 2021.

[182] A To, Z Li, and S Dixon. Improved detection of surface defects at sample edges using high-frequency eddy current amplitude and phase measurements. *Nondestructive Testing and Evaluation*, pages 1–25, 2022.